FACULDADE DE ENGENHARIA DA UNIVERSIDADE DO PORTO

Optimization and accuracy of numerical methodologies applied to sheet metal forming with experimental validation

Sara Esmeralda Silva Correia de Miranda



Programa Doutoral em Engenharia Mecânica

Supervisor: Rui Loureiro Amaral

Co-supervisors: Abel Dias dos Santos
José César de Sá

December, 2023

© Sara Miranda, 2023

Optimization and accuracy of numerical methodologies applied to sheet metal forming with experimental validation

Sara Esmeralda Silva Correia de Miranda

Programa Doutoral em Engenharia Mecânica

Approved by:

President: Dr. Renato Manuel Natal Jorge
Professor at Department of Mechanical Engineering, Faculty of Engineering of University of Porto

Referee: Dr. Gabriela Tamara Vincze
Professor at Department of Mechanical Engineering, University of Aveiro

Referee: Dr. Francisco José Gomes da Silva
Professor at Department of Mechanical Engineering, Porto School of Engineering

Referee: Dr. Pedro Manuel Cardoso Teixeira
Researcher at Frezite High Performance Lda.

Referee: Dr. Marco Paulo Lages Parente
Professor at Department of Mechanical Engineering, Faculty of Engineering of University of Porto

Referee: Dr. Rui Ricardo Loureiro Amaral
Researcher at Institute of Science and Innovation in Mechanical and Industrial Engineering

(This page was deliberately left blank)

Abstract

Sheet metal forming techniques are extensively applied across various manufacturing sectors. The increasing complexity of products, the reduction in development times and current increasing for employing lighter and stronger materials create challenges to forming processes. In response to these demands, a virtual try-out evaluation is made based on finite element numerical simulation. Taking this into account, the successful application of numerical simulation in sheet metal forming relies on accurate material models to capture the complex deformation behavior of metallic materials. Ongoing research efforts are dedicated to improve these models and enhancing their predictive capabilities.

The main objective of this thesis is to improve and establish methodologies that will allow a further step on new numerical modeling tools for accurate and better prediction capabilities of material behavior using constitutive models. Sheet metal materials include aluminum alloys (AA5182 and AA6016) and advanced high strength steels (DP500 and DP780). For mechanical characterization, a suitable set of experimental tests corresponding to different strain paths and loading stress states has been defined and performed in order to improve the material behavior definition and, as a result, the accuracy of the numerical results.

Additionally, a series of benchmark tests, corresponding to a variety of conditions in which a material can be subjected during the deformation process, including the deep drawing tests (cylindrical cup and cross-die forming test) were carried out, as well as, a springback analysis based on a split ring for a cylindrical cup.

The anisotropic behavior has been one of the leading research topic of the sheet metal forming processes. The variation of mechanical properties as a function of the loading direction of sheet materials are a key aspect in the accuracy of numerical results. So, an implementation of both associated (AFR) and non-associated plastic flow rules (NAFR) are considered, being the Hill'48 and Yld91 anisotropic yield criteria the basis models to describe the material anisotropic behavior, as well as, Yld2004-18p.

Finite element numerical simulations were applied to evaluate the capabilities for predicting the anisotropic behavior of metallic sheets for the different constitutive models under study. The obtained numerical results were evaluated and compared with the data provided from the experiments. The non-associated plastic flow rule approach shows a good correlation with experimental results and an improvement in accuracy of anisotropic and springback behaviors.

Keywords: Sheet metal forming, Numerical simulation, Benchmark tests, Yield criteria, Experimental validation

(This page was deliberately left blank)

Resumo

Os processos de conformação de chapas metálicas desempenham um papel essencial em diversos setores da indústria transformadora. O aumento da complexidade dos produtos, a necessidade de encurtar os prazos de desenvolvimento e o crescente uso de materiais mais leves e/ou resistentes representam desafios significativos para os processos de conformação. Para responder a estas solicitações, surge a necessidade de analisar e avaliar os processos por meio da simulação numérica com base em elementos finitos. Neste contexto,o sucesso da aplicação da simulação numérica na conformação de chapas metálicas está diretamente ligado a modelos matemáticos capazes de capturar o comportamento dos materiais metálicos durante a sua deformação.

O principal objetivo desta tese é estabelecer procedimentos que permitirão o desenvolvimento de novas metodologias de modelação numérica, com o intuito de melhorar a capacidade de previsão do comportamento dos materiais utilizando modelos constitutivos. Os materiais metálicos estudados incluem ligas de alumínio (AA5182 e AA6016) e aços avançados de alta resistência (DP500 e DP780). Para a caraterização mecânica, foi definido e realizado um conjunto adequado de ensaios experimentais correspondentes a diferentes trajetórias de deformação e estados de tensão, de modo a melhorar a definição do comportamento do material e, consequentemente, a precisão dos resultados numéricos.

Adicionalmente, foi efetuada uma série de ensaios de referência, correspondentes a uma variedade de condições a que um material pode ser sujeito durante o processo de conformação, incluindo os ensaios de estampagem profunda (copo cilíndrico e *cross die forming*), bem como uma análise de retorno elástico baseada num anel dividido proveniente de um copo cilíndrico.

O comportamento anisotrópico tem sido um dos principais tópicos de investigação dos processos de conformação de chapas metálicas. A variação das propriedades mecânicas em relação à direção de solicitação é um aspeto fundamental para o rigor dos resultados numéricos. Assim, considera-se a implementação de leis de plasticidade associadas e não associadas, tendo como base os critérios de cedência anisotrópicos de Hill'48, Yld91 e Yld2004-18p.

Para avaliar as capacidades de previsão do comportamento anisotrópico dos materiais foram realizadas simulações numéricas para os diferentes modelos constitutivos em estudo. Os resultados numéricos obtidos foram avaliados e comparados com os dados experimentais. A abordagem da lei de plasticidade não-associada apresenta uma boa correlação com os resultados experimentais e por conseguinte uma melhoria no rigor das previsões numéricas.

Palavras-chave: Conformação plástica, Simulação numérica, *Benchmarks* experimentais, Critérios plasticidade, Validação experimental

(This page was deliberately left blank)

Acknowledgments

I am deeply grateful to Professor Doctor Abel Dias dos Santos for affording me the opportunity to pursuit on this scientific journey through this thesis. His guidance, insights, continuous support, accessibility, and thorough review of this manuscript were fundamental to ensure the flow and successful completion of this thesis.

I want to express my profound gratitude to Professor José Manuel de Almeida César de Sá for his constant availability, invaluable assistance, and meticulous review of this text, which ensured its coherence and consistency.

Additionally, I would like to thank to Doctor Rui Loureiro Amaral for his critical sense and analysis of the experimental part. The valuable guidance, support and clarifications have guided me throughout all the difficulties and contribuited to the achievement of this thesis.

I extend my appreciation to the Institute of Science and Innovation in Mechanical and Industrial Engineering (INEGI) for their support and provision of resources throughout the duration of this study. The easy and comprehensive access to a wide range of scientific and technological resources provided by INEGI (Institute of Science and Innovation in Mechanical and Industrial Engineering) was instrumental in enabling the extensive experimental research upon which this thesis is built.

I express my sincere appreciation to the members of UTAF (Advanced Manufacturing Processes) for their invaluable fellowship and support throughout the course of this research. Their contributions have been instrumental in the successful execution of this study. Furthermore, I would like to extend my appreciation to all individuals who have directly or indirectly committed their time and effort, as their contributions have played a vital role in the successful completion of this research project.

To my beloved family, I would like to express my deepest gratitude for your understanding and friendship, which have allowed me to successfully complete this long journey. Your support and encouragement have been essentials to achieve success. Words are not enough to express my appreciation.

Finally, I gratefully acknowledge the financial support of the Portuguese Foundation for Science and Technology (FCT) for the Doctoral grant SFRH/BD/146083/2019 provided under the program POCH, co-financed by the European Social Fund (FSE) and Portuguese National Funds from MCTES.



(This page was deliberately left blank)

À Maria Antónia

"Learning never exhausts the mind."
Leonardo da Vinci

(This page was deliberately left blank)

Contents

1 Introduction **1**
- 1.1 Motivation . . . 3
- 1.2 Objectives . . . 4
- 1.3 Outline of the thesis . . . 6

2 Sheet metal forming challenges **7**
- 2.1 Introduction . . . 9
- 2.2 Forming phenomena . . . 11
- 2.3 Numerical simulation accuracy . . . 14
  - 2.3.1 Hardening laws - isotropic evolution . . . 16
  - 2.3.2 Yield criteria . . . 18
  - 2.3.3 Interaction between contact surfaces . . . 29
- 2.4 Experimental benchmarks . . . 32
  - 2.4.1 Swift test . . . 33
  - 2.4.2 Modified Demeri test . . . 37
  - 2.4.3 Cross die forming test . . . 40

3 Materials, characterization and constitutive modeling **43**
- 3.1 Introduction . . . 45
  - 3.1.1 Aluminum alloys . . . 45
  - 3.1.2 Advanced high strength steels . . . 47
- 3.2 Mechanical Characterization . . . 49
  - 3.2.1 Stress-strain flow curves . . . 49
- 3.3 Anisotropic plastic strain ratios . . . 59
  - 3.3.1 Anisotropic r-values . . . 59
  - 3.3.2 Biaxial plastic anisotropy . . . 61
- 3.4 Material modeling . . . 65
  - 3.4.1 Hardening . . . 66
  - 3.4.2 Yield criteria . . . 68

4 Experimental benchmark tests **75**
- 4.1 Swift test . . . 77
  - 4.1.1 Punch force . . . 79
  - 4.1.2 Earing profile . . . 82
  - 4.1.3 Cup wall thickness profiles . . . 83

4.2 Modified Demeri Benchmark test (Split Ring test) . . . 86
4.2.1 Split ring opening . . . 88
4.3 Cross die test . . . 92
4.3.1 Punch force evolution with displacement . . . 95
4.3.2 Blank draw-in . . . 97
4.3.3 Thickness distribution . . . 100

5 Numerical simulation benchmark tests 103
5.1 Numerical models . . . 105
5.2 Swift test . . . 107
5.2.1 Evolution of punch force . . . 107
5.2.2 Earing evolution - cup height . . . 109
5.2.3 Cup wall thickness profiles . . . 110
5.2.4 Modeling elastic tools . . . 119
5.3 Split ring test . . . 126
5.4 Cross die forming test . . . 129
5.4.1 Punch force evolution . . . 130
5.4.2 Draw-in . . . 132
5.4.3 Thickness Distribution . . . 136

6 Conclusions 141
6.1 Final remarks . . . 143
6.2 Future work . . . 145

References 147

A Lubricant conditions - FERROCOAT N6130 157
A.1 Applications . . . 159
A.2 Properties . . . 159
A.3 Benefits . . . 159

B Split-ring test 161
B.1 Split-ring test . . . 163
B.1.1 AA5182 . . . 163
B.1.2 AA6016 . . . 164
B.1.3 DP500 . . . 165
B.1.4 DP780 . . . 166

C Cross die forming test 167
C.1 Cross shape component . . . 169
C.2 Plus shape component . . . 177

List of Figures

1.1 Relationship between experimental data and finite element analysis (FEA). 4

2.1 Products obtained by sheet metal forming process (adapted from [2]). . . 9
2.2 Multi-material design used in body-in-white of a vehicle (adapted from [4]). 10
2.3 Common phenomena in sheet metal forming processes [12, 13]. 12
2.4 Schematic representation of the plastic behavior of materials in tension-compression on $\sigma_1 - \sigma_2$ plane and corresponding stress *vs.* plastic strain curves for isotropic hardening. 16
2.5 Plastic flow directionality: associated (AFR) and non-associated (NAFR) flow rules (adapted from [53]). 29
2.6 Scheme with different possibilities to model blankholder boundary conditions. 30
2.7 Comparison between the friction coefficient (CoF) and the contact pressure at different sliding velocities [55]. 31
2.8 Scheme of deep drawing cylindrical cup tools - Swift test. 33
2.9 Ring Location in a deep drawn cylindrical cup (adapted from [ASTM E2492]). 37
2.10 Different stages of a split ring procedure: X - length of section removed during cutting; C - length measured between the tips of the split ring [ASTM E2492]. 38
2.11 Illustration of cross die test tools. 40

3.1 Flow curves of aluminum alloys AA5182 (left) and AA6016 (right). . . . 51
3.2 Flow curves for aluminum alloys DP500 (left) and DP780 (right). 52
3.3 Hydraulic bulge test scheme and its key variables (dimensions in mm) - adapted from [90]. 54
3.4 Biaxial stress-strain curve (left) and hydraulic pressure-height profiles (right) obtained for the materials in study. 56
3.5 Equivalent stress-strain curves for the studied materials by combining the converted biaxial bulge data with results tensile tests. 58
3.6 Evolution of plastic strain transverse and thickness strain for five directions relative to the rolling direction. 60
3.7 Experimental setup used for stacked compression test. 62
3.8 Experimental assembly with location of specimens for testing. 62

3.9 Force vs. displacement curve used to defined the applied load range for 5 stacked circular disks, 11 mm diameter. 64
3.10 Relationship between longitudinal and transverse strain by axial compression tests on five stacked circular disks for the aluminum and steel specimens in the study. 64
3.11 Comparison of disk compression specimens (before and after) the forming test. 65
3.12 Comparison between the equivalent stress-strain curves generated by combining the converted biaxial data with uniaxial tensile test and hardening laws for the different materials. 68
3.13 Predicted yield surfaces and evolution of yield stresses and r-values of Hill'48 and Yld91 models for AA5182. 70
3.14 Predicted yield surfaces and evolution of yield stresses and r-values of Hill'48 and Yld91 models for AA6016. 71
3.15 Predicted yield surfaces and evolution of yield stresses and r-values of Hill'48 and Yld91 models for DP500 stress. 72
3.16 Predicted yield surfaces and evolution of yield stresses and r-values of Hill'48 and Yld91 models for DP780 stress. 73

4.1 Cylindrical cup test schematic representation and tool dimensions. 77
4.2 Procedure used for measuring the sheet blank diameter. 78
4.3 Obtained experimental cylindrical cups. 79
4.4 Experimental punch force vs. displacement for the materials under study. 80
4.5 Ironing effect on punch force curve for aluminum alloys. 80
4.6 Stages of deep drawing cylindrical cup forming process. 81
4.7 Ironing and the material flow representation. 81
4.8 Selected points to obtain the earing profiles of the cylindrical cups. 82
4.9 Earing profiles for the aluminum alloys and dual-phase steel cups. 83
4.10 Cup thickness profile sections and measurement strategy utilized. 84
4.11 Cup thickness measurements for vertical section for the aluminum alloys and steel. 84
4.12 Cup thickness measurements for vertical section for the aluminum alloys and steel. 85
4.13 Profile sections measured for the cylindrical cup test. 86
4.14 Strategy of split ring test. 87
4.15 Measurement of the opening, before and after vertical cut, the split ring. . 87
4.16 Location of the rings for analysis on the cylindrical cup drawing. 88
4.17 Springback opening measured in the rings cutted for the different materials in study. 89
4.18 Comparison of rings R1 after springback for the different materials. . . . 90
4.19 Opening rings for the AA5182 and AA6016, left and right respectively. . 91
4.20 Opening rings for the DP500 and DP780, left and right respectively. . . . 91
4.21 Press machine and tools used in Cross die test. 92
4.22 Cross-die test assembly and tool dimensions. 93
4.23 Different obtained component shapes based on blank orientation. 93

4.24 Cross die test blank-holder force behavior. 94
4.25 Measurement system used to obtain the three-dimensional coordinates of the deformed cross shaped components. 95
4.26 Comparison of experimental results of punch force *vs.* displacement for the materials in study for cross die forming test. 95
4.27 Obtained samples from cross die test in the rolling direction - cross shape ("X"). 96
4.28 Obtained samples from cross die test in the rolling direction - plus shape ("+"). 97
4.29 Points used to measure the blank draw-in. 98
4.30 Measured draw-in in cross-die forming test using aluminum alloys and dual-phase steels for the cross "X" specimen. 98
4.31 Measured draw-in in cross-die forming test using aluminum alloys and dual-phase steels for the plus "+" specimen. 99
4.32 Measured strategy followed for the thickness distribution in cross die forming test for the "x" shape. 100
4.33 Thickness distribution in cross-die forming test for the "X" specimen. . . 100
4.34 Measured strategy followed for the thickness distribution in cross die forming test for the plus "+" shape. 101
4.35 Thickness distribution in cross-die forming test for the plus "+" specimen. 101

5.1 Finite element 3D models: Swift test (a); Cross die forming test - cross shape (b) and plus shape (c). 105
5.2 Considered blank discretization: a) Swift test; b) cross die forming test. . 106
5.3 Finite element cross die test tools discretization. 107
5.4 Punch force vs displacement for the materials in study using different yield criteria. 108
5.5 Comparison of numerical earing height profiles of the materials in study with experimental data using different implemented yield criteria. 109
5.6 Comparison of profile geometry and wall thickness distribution for the AA5182 aluminum alloy using different yield criteria. 111
5.7 Comparison of profile geometry and wall thickness distribution for the AA6016 aluminum alloy using different yield criteria, with rigid tools. . . 112
5.8 Comparison of profile geometry and wall thickness distribution for the DP500 steel alloy using different yield criteria. 113
5.9 Comparison of profile geometry and wall thickness distribution for the DP780 steel alloy using different yield criteria. 114
5.10 Outer (top) and inner (bottom) equivalent stress contours for AA5182 cylindrical cup using the different yield criteria: a) Hill'48 r-based, Hill'48 s-based, Yld91; b) Hill'48, Yld91 (from left to right, respectively). 116
5.11 Outer (top) and inner (bottom) equivalent plastic strain contours for AA5182 cylindrical cup using the different yield criteria: a) Hill'48 r-based, Hill'48 s-based, Yld91; b) Hill'48, Yld91 (from left to right, respectively). 116

5.12 Outer (top) and inner (bottom) equivalent stress contours for AA6016 cylindrical cup using the different yield criteria: a) Hill'48 r-based, Hill'48 s-based, Yld91, Yld2004; b) Hill'48, Yld91 (from left to right, respectively). 117
5.13 Outer (top) and inner (bottom) equivalent plastic strain contours for AA6016 cylindrical cup using the different yield criteria: a) Hill'48 r-based, Hill'48 s-based, Yld91, Yld2004; b) Hill'48, Yld91 (from left to right, respectively). 117
5.14 Outer (top) and inner (bottom) equivalent stress contours for DP500 cylindrical cup using the different yield criteria: a) Hill'48 r-based, Hill'48 s-based, Yld91; b) Hill'48, Yld91 (from left to right, respectively). 117
5.15 Outer (top) and inner (bottom) equivalent plastic strain contours for DP500 cylindrical cup using the different yield criteria: a) Hill'48 r-based, Hill'48 s-based, Yld91; b) Hill'48, Yld91 (from left to right, respectively). 118
5.16 Outer (top) and inner (bottom) equivalent stress contours for DP780 cylindrical cup using the different yield criteria: a) Hill'48 r-based, Hill'48 s-based, Yld91; b) Hill'48, Yld91, Yld2004 (from left to right, respectively). 118
5.17 Outer (top) and inner (bottom) equivalent plastic strain contours for DP780 cylindrical cup using the different yield criteria: a) Hill'48 r-based, Hill'48 s-based, Yld91; b) Hill'48, Yld91, Yld2004 (from left to right, respectively). 118
5.18 Swift test numerical model with deformable tools. 119
5.19 Punch force *vs* displacement for the AA6016 using different yield criteria. 120
5.20 Outer (top) and inner (bottom) equivalent stress contours for AA6016 for elastic tools using the different yield criteria: a) Hill'48 r-based, Hill'48 s-based, Yld91; b) Hill'48, Yld91 (from left to right, respectively). 120
5.21 Outer (top) and inner (bottom) equivalent plastic strain contours for AA6016 for elastic tools using the different yield criteria: a) Hill'48 r-based, Hill'48 s-based, Yld91; b) Hill'48, Yld91 (from left to right, respectively). 121
5.22 Comparison of numerical earing height profiles of the AA6016 in study with experimental data for the different implemented yield criteria. 121
5.23 Comparison of profile geometry and wall thickness distribution for the AA6016 aluminum alloy for the different yield criteria, with elastic tools. 122
5.24 Contact pressure distribution in a AA6016 cylindrical cup for different moments of the ironing phase. 123
5.25 Contact pressure distribution in a AA6016 cylindrical cup for different moments of the ironing phase. 124
5.26 Comparison of numerical punch force and earing height profiles of the AA6016 for elastic tools, with a constant and pressure dependent friction coefficient. 124
5.27 Comparison of wall thickness distribution of the AA6016 for elastic tools, with a constant and pressure dependent friction coefficient. 125
5.28 Comparison of numerical punch force and earing height profiles of the AA6016 using rigid and elastic tools, with a constant and pressure dependent friction coefficient. 125

5.29 Outer (top) and inner (bottom) equivalent plastic strain contours for AA6016 for elastic tools using the different friction conditions, $\mu = 0.06$, $\mu = 0$ and $\mu = f(P)$. 126
5.30 Outer (top) and inner (bottom) equivalent stress contours for AA6016 for elastic tools using the different friction conditions, $\mu = 0.06$, $\mu = 0$ and $\mu = f(P)$. 126
5.31 Adopted numerical strategy of split ring springback analysis. 127
5.32 Split ring springback comparison using the first ring (R1) for the aluminum alloys and dual-phase steels. 128
5.33 Split ring experimental (left) and numerical (right) comparison of the first ring (R1) for the materials in the study. 128
5.34 Split ring equivalent stress contours for AA5182 (Yld91), AA6016 (Hill'48-NAFR), DP500 (Yld91-NAFR) and DP780 (Hill'48-NAFR), left to right, respectively. 129
5.35 Comparison of cross shape between experimental, 3D scan and numerical simulation. 129
5.36 Comparison of plus shape between experimental, 3D scan and numerical simulation. 130
5.37 Punch force-displacement curves of the cross die test, for 'X' shape component. 130
5.38 Punch force-displacement curves of the cross die test, for the plus shape '+' component. 131
5.39 Draw-in results of the cross die test, for the 'X' shape component 132
5.40 Draw-in 'X' shape results of cross die test, for the AA5182. 132
5.41 Draw-in 'X' shape results of cross die test, for the AA6016. 133
5.42 Draw-in 'X' shape results of cross die test, for the DP500. 133
5.43 Draw-in 'X' shape results of cross die test, for the DP780. 133
5.44 Draw-in results of the cross die test, for the '+' shape component 134
5.45 Draw-in '+' shape results of cross die test, for the AA5182. 135
5.46 Draw-in '+' shape results of cross die test, for the AA6016. 135
5.47 Draw-in '+' shape results of cross die test, for the DP500. 135
5.48 Draw-in '+' shape results of cross die test, for the DP780. 135
5.49 Comparison of profile geometry for the AA5182 aluminum alloy for the different yield criteria for 'X' result. 136
5.50 Comparison of profile geometry for the AA6016 aluminum alloy for the different yield criteria for 'X' result. 137
5.51 Comparison of profile geometry for the DP500 dual-phase steel for the different yield criteria for 'X' result. 137
5.52 Comparison of profile geometry for the DP780 dual-phase steel for the different yield criteria for 'X' result. 137
5.53 Stress triaxility distribution of the DP780 cross shape component. 138
5.54 Comparison of profile geometry for the AA5182 aluminum alloy for the different yield criteria for '+' result. 139

5.55 Comparison of profile geometry for the AA6016 aluminum alloy for the different yield criteria for '+' result.. 139
5.56 Comparison of profile geometry for the DP500 dual-phase steel for the different yield criteria for '+' result. 139
5.57 Comparison of profile geometry for the DP780 dual-phase steel for the different yield criteria for '+' result. 139

B.1 Split-Ring equivalent plastic stress contours for AA5182 using the yield point as a limit for different yield criteria a) Hill'48 r-based, Hill'48 s-based, Yld91; b) Hill'48 and Yld91(left to right, respectively). 163
B.2 Split-Ring opening evaluation for different yield criteria a) Hill'48 r-based, Hill'48 s-based, Yld91; b) Hill'48 and Yld91(left to right, respectively). . 163
B.3 Split-Ring equivalent plastic stress contours for AA6016 using the yield point as a limit for different yield criteria a) Hill'48 r-based, Hill'48 s-based, Yld91; b) Hill'48 and Yld91(left to right, respectively). 164
B.4 Split-Ring opening evaluation of AA6016 for different yield criteria a) Hill'48 r-based, Hill'48 s-based, Yld91; b) Hill'48 and Yld91(left to right, respectively). 164
B.5 Split-Ring equivalent plastic stress contours for DP500 using the yield point as a limit for different yield criteria a) Hill'48 r-based, Hill'48 s-based, Yld91; b) Hill'48 and Yld91(left to right, respectively). 165
B.6 Split-Ring opening evaluation of DP500 for different yield criteria a) Hill'48 r-based, Hill'48 s-based, Yld91; b) Hill'48 and Yld91(left to right, respectively). 165
B.7 Split-Ring equivalent plastic stress contours for DP780 using the yield point as a limit for different yield criteria a) Hill'48 r-based, Hill'48 s-based, Yld91; b) Hill'48 and Yld91(left to right, respectively). 166
B.8 Split-Ring opening evaluation of DP780 for different yield criteria a) Hill'48 r-based, Hill'48 s-based, Yld91; b) Hill'48 and Yld91(left to right, respectively). 166

C.1 Equivalent plastic strains contours for AA5182 X shape of cross die, using the different yield criteria: a) Hill'48 r-based, Hill'48 s-based, Yld91; b) Hill'48, Yld91 (from left to right, respectively). 169
C.2 Equivalent stress contours for AA5182 X shape of cross die, using the different yield criteria: a) Hill'48 r-based, Hill'48 s-based, Yld91; b) Hill'48, Yld91 (from left to right, respectively). 170
C.3 Equivalent plastic strains contours for AA6016 X shape of cross die, using the different yield criteria: a) Hill'48 r-based, Hill'48 s-based, Yld91; b) Hill'48, Yld91 (from left to right, respectively) 171
C.4 Equivalent stress contours for AA6016 X shape of cross die, using the different yield criteria: a) Hill'48 r-based, Hill'48 s-based, Yld91; b) Hill'48, Yld91 (from left to right, respectively). 172

C.5 Equivalent plastic strains contours for DP500 X shape of cross die, using the different yield criteria: a) Hill'48 r-based, Hill'48 s-based, Yld91; b) Hill'48, Yld91 (from left to right, respectively). 173
C.6 Equivalent stress contours for DP500 X shape of cross die, using the different yield criteria: a) Hill'48 r-based, Hill'48 s-based, Yld91; b) Hill'48, Yld91 (from left to right, respectively). 174
C.7 Equivalent plastic strains contours for DP780 X shape of cross die, using the different yield criteria: a) Hill'48 r-based, Hill'48 s-based, Yld91; b) Hill'48, Yld91 (from left to right, respectively). 175
C.8 Equivalent stress contours for DP780 X shape of cross die, using the different yield criteria: a) Hill'48 r-based, Hill'48 s-based, Yld91; b) Hill'48, Yld91 (from left to right, respectively). 176
C.9 Equivalent plastic strains contours for AA5182 plus shape ("+") of cross die, using the different yield criteria: a) Hill'48 r-based, Hill'48 s-based, Yld91; b) Hill'48, Yld91 (from left to right, respectively). 177
C.10 Equivalent stress contours for AA5182 plus shape ("+") of cross die, using the different yield criteria: a) Hill'48 r-based, Hill'48 s-based, Yld91; b) Hill'48, Yld91 (from left to right, respectively). 178
C.11 Equivalent plastic strains contours for AA6016 plus shape ("+") of cross die, of cross die using the different yield criteria: a) Hill'48 r-based, Hill'48 s-based, Yld91; b) Hill'48, Yld91 (from left to right, respectively). 179
C.12 Equivalent stress contours for AA6016 plus shape ("+") of cross die, using the different yield criteria: a) Hill'48 r-based, Hill'48 s-based, Yld91; b) Hill'48, Yld91 (from left to right, respectively). 180
C.13 Equivalent stress contours for DP500 plus shape ("+") of cross die, using the different yield criteria: a) Hill'48 r-based, Hill'48 s-based, Yld91; b) Hill'48, Yld91 (from left to right, respectively). 181
C.14 Equivalent stress contours for DP500 plus shape ("+") of cross die, using the different yield criteria: a) Hill'48 r-based, Hill'48 s-based, Yld91; b) Hill'48, Yld91 (from left to right, respectively). 182
C.15 Equivalent stress contours for DP780 plus shape ("+") of cross die, using the different yield criteria: a) Hill'48 r-based, Hill'48 s-based, Yld91; b) Hill'48, Yld91 (from left to right, respectively). 183
C.16 Equivalent stress contours for DP780 plus shape ("+") of cross die, using the different yield criteria: a) Hill'48 r-based, Hill'48 s-based, Yld91; b) Hill'48, Yld91 (from left to right, respectively). 184

(This page was deliberately left blank)

List of Tables

3.1 Strength ranges for different wrought aluminum alloys [81]. 45
3.2 Experimental conditions of uniaxial tensile test for the aluminum alloys. . 50
3.3 Experimental conditions of uniaxial tensile test for dual-phase steels. . . . 50
3.4 Uniaxial tensile test material properties. 53
3.5 Tools dimensions of the hydraulic bulge test. 54
3.6 Experimental conditions used on the hydraulic bulge test for the AA and AHSS. 56
3.7 Aluminium alloys and dual-phase steels properties obtained form hydraulic bulge test. 57
3.8 Parameter k value for the transformation of biaxial data. 58
3.9 Experimental conditions used to measure anisotropic properties of AA and AHSS. 60
3.10 Identified anisotropic properties for the selected materials 61
3.11 Experimental conditions used on the stacked compression tests. 63
3.12 Hardening laws parameters of AA5182 using uniaxial and biaxial stress-strain data. 67
3.13 Hardening laws parameters of AA6016 using uniaxial and biaxial stress-strain data. 67
3.14 Hardening laws parameters of DP500 using uniaxial and biaxial stress-strain data. 67
3.15 Hardening laws parameters of DP780 using uniaxial and biaxial stress-strain data. 67
3.16 Parameters used in yield criteria. 69
3.17 Summary of experimental data used for yield criteria parameters identification. 69
3.18 Identified yield criteria parameters for AA5182. 70
3.19 Identified yield criteria parameters for AA6016. 71
3.20 Identified yield criteria parameters for DP500. 72
3.21 Identified yield criteria parameters for DP780. 73

4.1 Experimental conditions of deep drawing cylindrical cup tests. 78
4.2 Rings extracted from the cylindrical cups. 88
4.3 Split ring opening measurements. 89
4.4 Experimental conditions of cross die forming test. 94

5.1 Results of split ring. 127

A.1 FERROCOAT N6130 159

Acronyms and Nomenclature

Acronyms

AA	Aluminum Alloy
AFR	Associated Flow Rule
AHSS	Advanced High Strength Steels
BCC	Body Centered Cubic
CPB	Cazacu, Plunkett and Barlat yield criterion
DIC	Digital Image Correlation
DP	Dual-phase
FCC	Face Centered Cubic
FEA	Finite Element Analysis
FEM	Finite Element Method
HSS	High Strength Steels
H48R	Hill (1948) yield criterion r-based
H48S	Hill (1948) yield criterion σ-based
NAFR	Non-associated Flow Rule
RD, DD, TD	Rolling, Diagonal and Transverse Directions
Yld91	Barlat et al. (1991) yield criterion
Yld2004-18p	Barlat et al. (2004) yield criterion

Nomenclature

α	Swift+Voce hardening law weighting parameter
$\Delta\overline{\varepsilon}^p$	Equivalent plastic strain increment
$\Delta\lambda$	Plastic multiplier increment
Δr	Planar anisotropic coefficient
$\boldsymbol{\varepsilon}$	Strain tensor
ε_b	Biaxial strain
$\boldsymbol{\varepsilon}^e$	Elastic strain tensor
$\boldsymbol{\varepsilon}^p$	Plastic strain tensor
ϕ	Yield Condition
λ	Plastic multiplier
ρ	Radius of curvature
$theta$	angle relative to the rolling direction
μ	Friction coefficient
$\boldsymbol{\sigma}$	Cauchy stress tensor
σ_1, σ_2, σ_3	Principal stresses
$\overline{\sigma}$	Equivalent yield stresses
σ_θ	Yield stress corresponding to the direction with the angle θ relative to the RD
σ_b	Biaxial yield stress
σ_Y	Flow stress
σ_m	Mean stress
σ_0, K, n	Ludwik law parameters
A, B, C	Voce law parameters
a, b, c, f, g, h, m	Yld91 yield criterion anisotropic parameters
c_i for i=1:10, m	Yld2004-18p yield criterion

Chapter 1

Introduction

This chapter introduces the overall structure and needs associated with sheet metal forming technology, emphasizing the importance of finite element numerical simulation. Furthermore, it outlines the primary goals of the research conducted within this thesis. Additionally, the structure and the objectives of this thesis are also outlined.

(This page was deliberately left blank)

1.1 Motivation

Metal forming processes face numerous challenges that require careful consideration and expertise to overcome. One of the primary challenges is selecting the appropriate material for a specific forming process. The material must possess the necessary properties, including ductility, strength and formability, to meet the requirements of the desired shape and the forming technique employed.

Designing an efficient and cost-effective metal forming process poses another challenge. Factors such as tooling design, die material selection, lubrication and process parameters must be meticulously analyzed and optimized. Achieving the desired shape without defects, such as cracks or wrinkles, is also a considerable challenge. This requires understanding and managing formability, which refers to the materials ability to undergo shaping without failure, as well as, addressing springback, which is the elastic recovery of the material after forming that can lead to deviations from the intended shape.

Lastly, the emergence of advanced materials, such as advanced high strength steels and aluminum alloys, presents new challenges. These materials often have unique characteristics that require specialized forming techniques and tooling. Extensive research and understanding of their behavior during forming are necessary to overcome these challenges. For example, the automotive industry has experienced a significant growth in demand of such materials, leading to a substantial increase in its application to vehicles.

Among these technological processes, sheet metal forming operations occupy a prominent position in industry, which are commonly characterized by the application of large strains involving strain path changes. These processes induce substantial plastic deformations in a variety of metals. The forming process is influenced by various parameters, including material properties, geometric factors and process parameters. Therefore, a comprehensive understanding of these parameters is essential to gain deep insights into the process.

In this context, numerical simulation has emerged as a valuable and cost-effective tool for optimizing the forming process, addressing design and manufacturing challenges, figure 2.1. Achieving accurate numerical modeling of sheet metal forming processes requires the use of appropriate material models that accurately describe material behavior. This requirement stands as a fundamental necessity for ensuring the precision and reliability of the simulation results.

However, to achieve consistent and accurate results, numerical simulation techniques must be employed in conjunction with validated material constitutive models. The key is to develop a realistic model that effectively describes the material behavior. This model

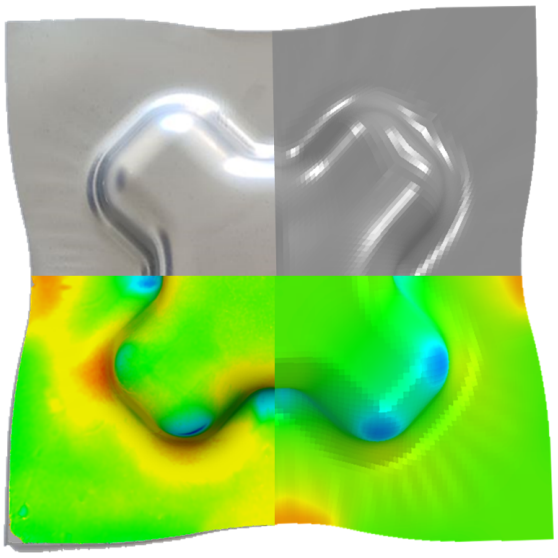


Figure 1.1: Relationship between experimental data and finite element analysis (FEA).

must take into account the influence of material changes resulting from the complex loading paths encountered during sheet metal forming, since the accuracy of simulations is highly influenced by the material model adopted to represent the behavior of the metal during the forming process. The reliability and precision of this material model rely on the quality and quantity of experimental data used for model calibration. If the material model fails to accurately capture the behavior of the metal sheet during the forming process, the simulation results will inevitably exhibit inaccuracies.

To address this challenge, it is essential to meticulously characterize and identify the material model specific to the material under investigation. This can be accomplished by carrying out experimental benchmark tests that generate stress-strain data responses for various loading paths. By using such data, a comprehensive understanding of the material behavior can be achieved, enabling the development of robust and accurate models for sheet metal forming processes.

1.2 Objectives

The plastic deformation present in the technological processes of sheet metal forming allows the production of different components, with different geometries. Such processes have been the subject of research, due to their current use in a wide variety of industries, since most of the products obtained by plastic forming are present in our daily life.

This study aims to contribute to the deepening of knowledge in the field of numerical simulation of technological processes, with a particular focus on the study of anisotropic

constitutive models for describing the behavior of metallic alloys. The research incorporates diverse methodologies to accurately determine the mechanical behavior of metallic materials, with a specific emphasis on Aluminum Alloys (AA) and Advanced High Strength Steels (AHSS). The main objective is to address industrial applications effectively. To accomplish these objectives, a comprehensive finite element analysis (FEA) program, namely the ABAQUS software, is utilized. This work seeks to make significant contributions to the advancement of numerical simulation capabilities. The chosen methodology will focus on characterizing the impact of material anisotropic effects on the behavior of specific materials under specific loading conditions. This analysis aims to provide insights into the mechanisms that contribute to defects during the processing stage.

The integration of numerical modeling has become an essential stage in the preproduction phase of metal forming operations. However, to use reliable and valid material constitutive models, the accuracy of the input parameters is of greatest importance. For that, a set of experimental mechanical characterization test is performed to identify the constitutive model parameters, to ensuring accurate predition by numerical modelling.

Additionally, the numerical simulation will be employed to analyze various experimental benchmarks that represent different types of loading conditions encountered in the sheet metal forming field. The main aim is to investigate and evaluate the capacity of each constitutive model to predict the material behavior under deformation. For this purpose, a predefined set of parameters, identified through data obtained from experimental characterization tests, will be utilized and implemented in the numerical simulation of the benchmark test. It is expected that this deepened knowledge will contribute to a more appropriate prediction of the material behavior in metal forming processes and enable virtual tool tryouts using finite element method (FEM) codes.

In summary, this work focuses on modeling material and process conditions, taking advantage of the continuously expanding capabilities of computers. It not only explores new methodologies in simulation-based engineering science through the use of constitutive models but also emphasizes the importance of interdisciplinary research and experimental validation. By combining these approaches, the study aims to advance the field and enhance our understanding of material and process behavior.

1.3 Outline of the thesis

This thesis aims to apply the finite element method in the numerical simulation of the sheet metal forming process, using the ABAQUS analysis program. In addition to current chapter (Chapter 1), where a brief introduction to numerical simulation and sheet metal forming is presented, this thesis consists of other five chapters and appendixes.

In chapter 2, the challenges of sheet metal plastic forming are presented and the correspondent forming challenges using different experimental tests such as the cylindrical cup forming test which allows to acquire the limits of the material in deep drawing. A modified Demeri split ring test was selected in order to analyze the springback behavior after forming of the cutted rings from the deep drawing cylindrical cup, and finally the cross die forming test, used in the industry, to observe the forming capabilities of the metallic material. A brief revision of the works published in this field was also made. Additionally a review of the hardening laws and yield criteria applied in this thesis was presented.

Chapter 3 introduces the materials employed in this study. A series of experimental mechanical characterization tests were conducted to determine fundamental properties and establish reliable input data for numerical simulations. Furthermore, the parameters of the constitutive models, including hardening laws and yield criteria, are identified and presented.

In chapter 4, the benchmark of the selected forming tests was made. The experimental procedure was fully described and the correspondent results of the experimental part of this work, was presented.

The chapter 5 explores the results of numerical simulations conducted based on the experimental benchmark tests. These simulations are used to evaluate the prediction capabilities of such constitutive models regarding the material behavior obtained through plastic deformation processes. Also, the obtained results are compared with the experimental ones presented in chapter 4.

Chapter 6 presents the main conclusions of this thesis and suggestions for future works.

Chapter 2

Sheet metal forming challenges

This chapter presents a brief description of the forming challenges and the importance of accurate numerical simulation to fully reproduce the material behavior. Constitutive models applied to sheet metal materials are presented, concerning its mechanical properties and plasticity in the numerical simulation. Additionally, benchmark tests used to evaluate the materials anisotropic and forming capabilities are described.

(This page was deliberately left blank)

2.1 Introduction

Sheet metal forming is a highly versatile and widely employed manufacturing process, and also one of the oldest manufacturing methods, in which metal sheets are shaped into desired geometries, using various techniques such as bending, stretching, deep drawing or stamping. The initial shape of the blank is changed by the application of external mechanical forces that combine tensile and compressive loading states, resulting in the material undergoing plastic deformation. The choice of a specific forming process is determined by the desired specifications of the final component, aiming to deliver a product with the appropriate functionality and properties while keeping costs to a minimum [1].

When the in-plane dimensions significantly exceed the thickness of the initial sheet, denoted as sheet deformation, it becomes practical to assume the existence of plane stress conditions. Furthermore, deep drawing processes enable the production of parts with exceptional mechanical properties. Figure 2.1 presents some examples of sheet metal formed parts.



Figure 2.1: Products obtained by sheet metal forming process (adapted from [2]).

Some advantages of these sheet metal forming processes can include the design flexibility, allowing for the creation of complex shapes, contours and elaborated details. This enables the production of components with varying sizes, geometries and functional requirements. The cost efficiency is a key variable where this process often results in minimal material waste since it involve plastic deformation rather than material removal, like machining operations. This leads to cost savings in terms of raw material usage. Additionally, these processes are highly efficient for producing high-volume quantities, further reducing production costs. The lightweight and strength are also an advantage of this process. Sheet metal components produced through forming processes exhibit

high strength-to-weight ratios, making them ideal for applications where lightweight and strong structures are desired. This advantage is particularly relevant in industries such as automotive, aerospace and construction. The precision and consistency in this process are very accurate because the sheet metal forming processes can achieve higher levels, ensuring tight tolerances and uniformity across the produced components. This is crucial for applications where precise fit, functionality and interchangeability are essential.

Although sheet metal forming processes offer design flexibility, achieving highly complex shapes with feature details and imposed design constraints on sheet metal components that require multiple forming operations or specialized equipment, which increases the production time and cost. Due to material flow and tooling limitations, features like sharp corners, deep indentations or thin ribs can be difficult to achieve [3]. Designers need to consider these constraints and make appropriate modifications to ensure manufacturability. For example, the development of materials for automobile applications, specially for body-in-white (BiW) (figure 2.2), results from multiple and often contradictory constraints.

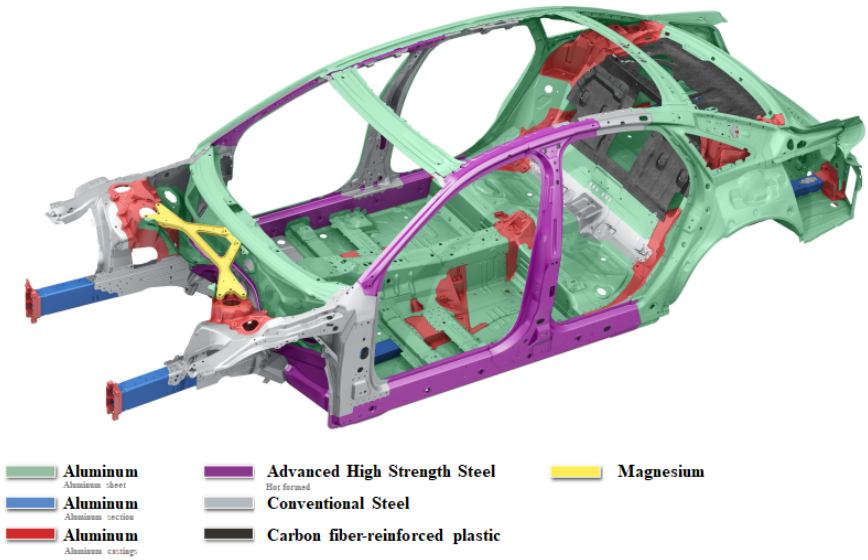


Figure 2.2: Multi-material design used in body-in-white of a vehicle (adapted from [4]).

The implementation of a lightweight design, high formability to satisfy the need and renewed designs, sufficient stiffness for vehicle handling, high mechanical strength for safety reasons, production possibilities in large quantities with increased productivity, excellent ease of assembly, a durable surface when subject to a severe environment, are all aspects that have to be achieved under severe economic constraints [5].

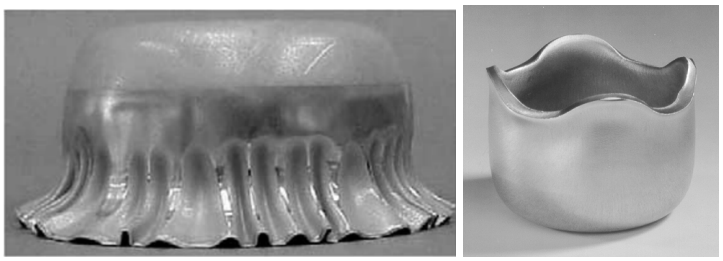
Additionally, sheet metal forming processes often require specialized tooling, such as dies, punches, to shape the metal. Designing, manufacturing and maintaining these tools can be expensive, particularly for complex or custom components. The initial investment in tooling can be a significant cost consideration, especially for low-volume production series. Another crucial point is that these types of processes may end up introducing surface imperfections, such as wrinkles, scratches or tool marks, especially in deep drawing operations. These imperfections may require additional finishing operations like grinding, polishing, or coating, adding time and cost to the production process [6, 7].

2.2 Forming phenomena

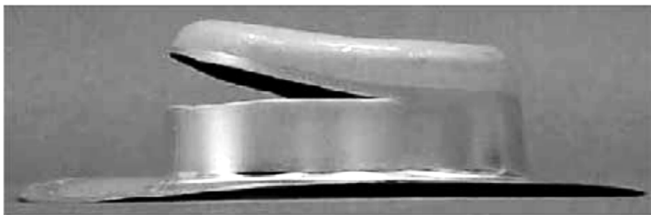
The versatility of sheet metal components obtained through the forming process is noteworthy. Deep drawing or stamping operations allow for a wide range of shapes, sizes and designs to be achieved with precision and consistency. Whether producing simple flat parts or complex three-dimensional geometries, these processes can accommodate various requirements. In case of stamping, the process enables the creation of details, such as embossed features, perforations or raised surfaces, enhancing the aesthetics and functionality of the components. Additionally, stamping supports the production of high-volume quantities efficiently and cost-effectively. This versatility makes stamping an indispensable technique for manufacturing sheet metal components across various industries, including automotive, aerospace, electronics and household appliances [8, 9].

On the other hand, deep drawing is a specialized metal forming process used also to manufacture complex, three-dimensional shapes from a flat sheet metal. It is particularly suitable for producing parts with a high depth-to-initial size ratio, such as cups, cans, automotive components, etc. The process involves placing a flat sheet of metal, typically steel, aluminum, or copper, over a die, which is a tool with a cavity that matches the desired shape of the final product. A punch is then forced into the sheet, applying radial forces that draw the material into the die's contours. As a result, the sheet undergoes plastic deformation, stretching and reshaping until it assumes the desired form. As a widely used manufacturing technique, deep drawing continues to play a vital role in various industries, contributing to the creation of countless everyday used items. This process offers numerous advantages, including high production efficiency, consistency in part quality and minimal material waste. However, it demands skilled operators and well-designed tooling to achieve optimal results. The success of deep drawing depends on the ductility of the metal, as well as precise control of factors such as blank size, lubrication and material thickness [10, 11]. While deep drawing is a highly effective and efficient

technique, it has also its challenges, while various defects, such as wrinkling, tearing or excessive thinning, can occur during the process, affecting the quality and integrity of the final product, as shown in figure 2.3.



(a) Wrinkling (b) Earing



(c) Tearing



(d) Springback

Figure 2.3: Common phenomena in sheet metal forming processes [12, 13].

Wrinkling is a common defect observed during deep drawing and occurs when the sheet metal develops unwanted surface undulations, resembling wrinkles or folds. This defect is primarily influenced by the material's mechanical properties, including its thickness, ductility, and anisotropy [14]. When subjected to the compressive stresses imposed during the drawing process, certain regions of the sheet metal may experience insufficient resistance to deformation, resulting in localized buckling or wrinkling. Additionally, the design of the die geometry, as well as the process parameters such as the punch-die clearance and lubrication, can significantly impact the occurrence and severity of wrinkling defects [15].

Excessive thinning of the material is a common concern in deep drawing operations, particularly in regions that undergo significant stretching. Thin areas can compromise the structural integrity and mechanical properties of the drawn component, making it more

susceptible to failure under load. Thinning is mainly influenced by the draw ratio (ratio of the final blank diameter to the initial blank diameter), the material's strain-hardening behavior, and the punch-die clearance [16]. Minimizing thinning often involves adjusting the draw ratio, selecting suitable materials, and optimizing the die geometry.

Ear formation, also known as earing, is a defect where small protrusions or ears form around the periphery of the drawn component, usually near the flange region [17]. This phenomenon arises from the anisotropic nature of the material, causing preferential deformation along specific crystallographic orientations during drawing. Earing is a more significant concern in materials with strong crystallographic textures, such as certain aluminum alloys and steels. To mitigate earing defects, manufacturers can employ special blank shapes or control the orientation of the blank relative to the die during the drawing process.

Inconsistent wall thickness is a defect that results in variations in the thickness of the drawn component. This defect can be caused by uneven material flow, improper blank holder force, or non-uniform deformation characteristics of the material. To achieve uniform wall thickness, manufacturers must carefully design the die geometry, control the blank holder force, and select materials with desirable formability characteristics [18].

Tearing is a severe defect characterized by partial or complete fracture of the material during the deep drawing operation. It occurs when the tensile stresses exceed the material's ultimate tensile strength, leading to localized failure. Tearing can result from various factors, including excessive drawing speed, inadequate lubrication, improper punch-die clearance, or the use of suboptimal materials. To prevent tearing, it is crucial to carefully select the appropriate material and optimize the process parameters to avoid exceeding the material's mechanical limits [19].

Surface imperfections, such as scratches, gouges, or abrasions, can occur during the deep drawing process, especially if the sheet metal comes into contact with abrasive materials or damaged die surfaces. These imperfections not only compromise the part's aesthetics but can also act as stress concentration points, potentially leading to premature failure. Proper handling, appropriate die maintenance, and adequate protection of the sheet metal surface can help avoid surface imperfections [19].

Deep drawing induces residual stresses in the drawn component due to plastic deformation and elastic recovery. These residual stresses can cause dimensional instability, warpage, or distortion in the final product. The magnitude and distribution of residual stresses are influenced by the material mechanical properties, the drawing process parameters, and the cooling conditions after forming [20]. Heat treatment or stress relieving

processes may be employed to minimize residual stresses and improve the part dimensional stability.

Springback is a phenomenon where the drawn component tends to return partially or entirely to its original shape after the deep drawing process is completed. This effect occurs due to the elastic recovery of the material after the removal of forming stresses. Springback can be particularly challenging to predict and control, as it is influenced by various factors such as the material's elastic modulus, yield strength, and the extent of plastic deformation experienced during drawing. Advanced simulation techniques and experimentation are often employed to predict and compensate for springback, ensuring the final part conforms to the intended design specifications.

To mitigate these defects and ensure the production of high-quality deep-drawn components, manufacturers typically employ a combination of advanced simulation techniques, experimental testing, and process optimization. The use of specialized materials, proper die design, lubrication and tool maintenance are critical factors in achieving successful deep drawing operations [2]. Additionally, comprehensive quality control measures, including regular inspections and material testing, are essential to identify and address defects early in the manufacturing process, leading to improved product reliability and performance.

2.3 Numerical simulation accuracy

The ability to efficiently and accurately predict the behavior of sheet metal during forming processes is of vital importance to ensure the final product quality, reducing costs and optimizing manufacturing operations.

Traditionally, the design and optimization of sheet metal forming processes heavily relied on physical prototypes and trial-and-error approaches. These methods, while effective, are time-consuming and labor-intensive, as well as expensive. Moreover, they do not provide insights into the detailed internal deformation and strain distribution within the material during forming. To overcome these limitations, numerical simulation techniques have emerged as powerful tools for predicting and analyzing the behavior of sheet metal during forming processes [21].

Numerical simulation, specifically finite element analysis (FEA), has revolutionized the field of sheet metal forming by offering virtual modeling and analysis capabilities. FEA enables the prediction of various aspects of the forming process, including deformation, stress and strain distribution, as well as, prevents phenomena such as excessive thinning, splits, wrinkles, surface damage and inconsistent or uncontrolled springback. It

simulates the behavior of sheet metal by discretizing the continuous geometry into a mesh of small elements, each governed by specific material properties, contact and boundary conditions. Through the solution of complex mathematical equations, FEA calculates the mechanical response of the sheet metal as it undergoes deformation.

The application of numerical simulation in sheet metal forming offers numerous advantages. It allows engineers and researchers to evaluate and compare different forming strategies and process parameters virtually, reducing the need for costly physical experiments. By simulating multiple solutions, it is possible to optimize the forming process by minimizing defects, improving product performance and reducing material waste. Also, numerical simulation provides valuable insights into the internal behavior of the sheet metal, such as the occurrence of localized necking, strain distribution and potential failure areas. This information is essential for understanding and controlling the forming process, leading to enhanced product quality and reliability [22].

Additionally, numerical simulation facilitates the exploration of innovative forming techniques and the development of advanced materials. By virtually testing new designs, materials and process variations, researchers can accelerate the development cycle and reduce time-to-market for new products [23]. Furthermore, it can support in the design of specialized tools, optimizing their geometry and shape to ensure uniform deformation and minimize material thinning. This level of control and predictability can significantly enhance the overall productivity and efficiency of sheet metal forming operations [24, 25].

However, despite the numerous benefits, the successful application of numerical simulation in sheet metal forming requires accurate material models, appropriate meshing techniques and reliable analysis to capture the complex deformation behavior. These models describe the mechanical properties of the material, such as its stress-strain evolution behavior, strain rate sensitivity, anisotropy, and hardening characteristics. The development of accurate material models involves characterizing the material properties through experimental testing and incorporating the results into mathematical constitutive formulations. Still, accurately reproducing the mechanical behavior of metallic materials can be challenging due to its non-linear and anisotropic response. Ongoing research focuses on refining material models to better capture these complexities and improve the predictive capabilities of numerical simulations [26].

To ensure the accuracy and reliability of the constitutive material models, careful experimental benchmark tests are performed to evaluate the performance of numerical simulation methodologies predictions. These tests involve the deformation of sheet metal using specific experimental setups and under controlled conditions, in order to measure

several parameters such as thickness distribution, final component shape springback, failure and comparing the experimental results with the simulation predictions.

By comparing simulation results with benchmark test data, researchers can identify discrepancies, improve model accuracy, and gain a deeper understanding of the underlying deformation mechanisms and establish confidence in the predictive capabilities of constitutive models. Common benchmark tests in sheet metal forming include the deep drawing cylindrical cup, cross die tests, U-rail, among others. These tests cover a range of forming processes and loading stress states, considering standardized methodologies.

Taking this into account, the successful application of numerical simulation in sheet metal forming relies on accurate material models to capture the complex deformation behavior of metallic materials. Ongoing research efforts are dedicated to improve these models and enhancing their predictive capabilities.

2.3.1 Hardening laws - isotropic evolution

During plastic deformation the yield surface evolves with the increase of plastic deformation, which is known as hardening behavior. Typically, the evolution of the yield surface can be of two types: (i) isotropic, which corresponds to the homothetic expansion of the yield surface and (ii) kinematic, corresponding to the translational movement of the surface's center. Kinematic hardening allows describing the mechanical behavior of materials presenting a decrease of the yield stress with a reverse strain path change, i.e. presenting Bauschinger effect, these two laws combined in the so-called mixed isotropic-kinematic hardening law [27, 28]. The isotropic type is schematically presented in figure 2.4, highlighting the correspondence between the yield surfaces and stress *vs.* plastic strain curves.

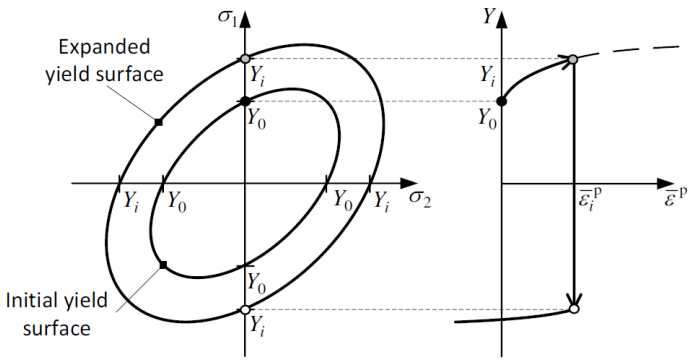


Figure 2.4: Schematic representation of the plastic behavior of materials in tension-compression on $\sigma_1 - \sigma_2$ plane and corresponding stress *vs.* plastic strain curves for isotropic hardening.

Isotropic hardening is a material property that describes how a material's yield strength changes due to plastic deformation. When a material undergoes plastic deformation, the material's yield strength typically increases, making it more difficult to continue deforming the material. Isotropic hardening occurs when the yield strength increases uniformly in all directions, regardless of the direction of previous deformation.

Mathematically, isotropic hardening can be described by an equation that relates the material yield stress to the accumulated equivalent plastic strain. Isotropic hardening can be contrasted with kinematic hardening, which describes how a material yield stress changes due to the direction of previous deformation. In kinematic hardening, the yield strength increases more in the direction of preceding deformation, whereas in isotropic hardening, the yield stress increases uniformly in all directions.

One of the first hardening laws was proposed by Ludwik in 1909 [29], giving the evolution of the yield stress, Y, as a function of the equivalent plastic strain, $\overline{\varepsilon}^p$, in the form

$$Y = Y_0 + K(\overline{\varepsilon}^p)^n \tag{2.1}$$

where Y_0, K and n represent the initial yield stress, the hardening modulus and the hardening coefficient, respectively.

Different hardening laws were proposed by several authors, to better reproduce the experimentally observed hardening behavior. The most well-known are the ones proposed by:

Hollomon, 1945 [30]:

$$\sigma = K(\overline{\varepsilon}^p)^n \tag{2.2}$$

Voce, 1948 [31]:

$$\sigma = A + B\left(1 - e^{C\cdot\varepsilon_p}\right) \tag{2.3}$$

Swift, 1952 [32]:

$$\sigma = K(\varepsilon_0 + \overline{\varepsilon}^p)^n \tag{2.4}$$

Hockett and Sherby, 1975 [33]:

$$\sigma = A + B\left(1 - e^{C\cdot\varepsilon_p^n}\right) \tag{2.5}$$

where ε_0, a, C_y, H, σ_{sat} and σ_S are material parameters.

The most used laws are the Voce 2.3 and Swift 2.4 where the Voce law is used to describe the behavior of materials exhibiting hardening with saturation, which occurs in face centered cubic metallic materials like aluminum and the Swift law, which is the most adopted for exhibiting hardening without saturation, like steels. Combining the Swift and Voce laws, it becomes possible to represent the mechanical behavior of a material that demonstrates a pronounced initial hardening response and reaches a state of saturation at higher levels of plastic deformation [34].

$$\sigma_Y = \alpha\left[K(\varepsilon_0+\varepsilon_p)^n\right] + (1-\alpha)\cdot\left[A + B\left(1-e^{C\cdot\varepsilon_p}\right)\right] \tag{2.6}$$

where $\alpha \in [0,1]$ corresponds to the weighting coefficient between the power and saturation laws.

2.3.2 Yield criteria

Yield criteria are mathematical equations or models used to describe the behavior of materials under plastic loading conditions. A simple yield criterion, such as the von Mises criterion, can accurately describe the behavior of materials under simple loading, but cannot take into account the anisotropic behavior of sheet metal materials. For that, complex yield criteria are used to model the behavior of materials under more complex loading conditions, such as multi-axial loading, strain path changes or when different material properties are exhibited in tension and compression.

There are many different types of anisotropic yield criteria, each with their own mathematical equations and assumptions. Some examples include the series of Hill criterion, Barlat formulations [35, 36, 37, 38, 39], Banabic et. al [40] models (BCC), Cazacu, Plunkett and Barlat (CPB) [41] yield criterion and other. These criteria take into account additional material properties, such as anisotropy, because when a metal undergoes significant plastic deformations, it experiences changes in grain sizes and orientations along the direction of deformation. As a consequence, the plastic yield behavior of the material exhibits a dependency on the loading direction, resulting in directional anisotropy.

The investigation of anisotropic behavior, which refers to the variation in mechanical properties concerning the loading direction, is a prominent research area in the mechanical characterization of sheet metal materials used in forming processes [42].

The anisotropic behavior is influenced by several factors, particularly in the context of metal sheets. In cold-rolled and non-recrystallized materials, the primary cause of anisotropy is the heterogeneous plastic deformation that occurs during the manufacturing process. Additional factors include crystallographic texture, chemical composition,

and the influence of thermal and mechanical treatments to which the material has been subjected.

The impact of anisotropy has been assessed and measured using various parameters that characterize the distribution of deformations when the material is subjected to external forces [43]. One widely employed and standardized parameter is the plastic anisotropic coefficient, denoted as r. It is defined as the ratio (equation 2.7) of the strain in the transverse direction (ε_2) to the strain in the thickness direction (ε_3).

$$r = \frac{\varepsilon_2}{\varepsilon_3} = -\frac{\varepsilon_2}{\varepsilon_1 + \varepsilon_2} \tag{2.7}$$

A fundamental requirement of a yield function is its ability to describe and predict the evolution of the plastic anisotropic coefficient and yield stresses within the plane of the sheet metal. To assess this capability, it is essential to establish relationships that define the dependence of the previously mentioned parameters on the angle θ.

2.3.2.1 Hill'48 yield function

Hill's 1948 [44] mathematical model is a constitutive model used to describe the anisotropic behavior of materials. It provides a mathematical representation of the stress-strain relationship taking into account the materials directional dependence. The model assumes that the materials yield behavior can be described by an ellipsoidal yield surface in the stress space, where the shape and orientation of the ellipsoid depend on the material's anisotropic properties.

Hill's model incorporates the concept of yield functions, which are mathematical expressions that determine when the material undergoes plastic deformation. The model aims to capture the anisotropic yield behavior by defining a yield function based on the stress components and the material's anisotropic coefficients. The model parameters are typically determined through experimental testing or obtained from material characterization data.

In the case where the axes of the coordinate system align with the axes of orthotropy, the yield criterion is defined by the following equation:

$$\begin{aligned} 2\phi(\boldsymbol{\sigma}) = F(\sigma_{yy} - \sigma_{zz})^2 + G(\sigma_{zz} - \sigma_{xx})^2 + H(\sigma_{xx} - \sigma_{yy})^2 + \\ 2\left(L \cdot {\sigma_{yz}}^2 + M \cdot {\sigma_{zx}}^2 + N \cdot {\sigma_{xy}}^2\right) = {\overline{\sigma_f}}^2 \end{aligned} \tag{2.8}$$

where F, G, H, L, M, and N are the material anisotropic parameters of the Hill's 1948 model. σ_{xx}, σ_{yy}, and σ_{zz} represent the stresses in the rolling direction (x), transverse

direction (y), and thickness direction (z), respectively. Additionally, σ_{xy}, σ_{yz}, and σ_{zx} correspond to the shear stress components.

In the specific case where $F = G = H = 0.5$ and $N = 1.5$, the Hill's 1948 criterion simplifies to the *von Mises* criterion. Assuming $L = M = 1.5$ as well, the yield criterion can be further simplified.

The yield criterion can be expressed as follows under the plane stress state condition ($\sigma_{zz} = \sigma_{yz} = \sigma_{zx} = 0$):

$$F \cdot \sigma_{yy}^2 + G \cdot \sigma_{xx}^2 + H\left(\sigma_{xx} - \sigma_{yy}\right)^2 + 2 \cdot N \cdot {\sigma_{xy}}^2 = \overline{\sigma_f}^2 \tag{2.9}$$

Applying the plastic multiplier (λ) relationship to the yield criterion (equation 2.8), the following associations are obtained, relating the strain increment components with the stress components.

$$\begin{bmatrix} d\varepsilon_x^p \\ d\varepsilon_y^p \\ d\varepsilon_z^p \\ d\gamma_{xy}^p \\ d\gamma_{yz}^p \\ d\gamma_{zx}^p \end{bmatrix} = d\lambda \begin{bmatrix} H+G & -H & -G & 0 & 0 & 0 \\ -H & H+F & -F & 0 & 0 & 0 \\ -G & -F & G+F & 0 & 0 & 0 \\ 0 & 0 & 0 & 2N & 0 & 0 \\ 0 & 0 & 0 & 0 & 2L & 0 \\ 0 & 0 & 0 & 0 & 0 & 2M \end{bmatrix} \begin{bmatrix} \sigma_{xx} \\ \sigma_{yy} \\ \sigma_{zz} \\ \sigma_{xy} \\ \sigma_{yz} \\ \sigma_{zx} \end{bmatrix} \tag{2.10}$$

where $1/2\gamma_{ij} = \varepsilon_{ij}$.

Defining σ_θ as the yield stress corresponding to the direction at an angle θ relative to the rolling direction, the tensor components for uniaxial loading can be expressed as follows:

$$\begin{cases} \sigma_{xx} = \sigma_\theta \cdot cos^2(\theta) \\ \sigma_{yy} = \sigma_\theta \cdot sin^2(\theta) \\ \sigma_{xy} = \sigma_{xy} = \sigma_\theta \cdot cos(\theta) \cdot sin(\theta) \end{cases} . \tag{2.11}$$

Considering the established relationships in equation 2.9 with 2.11, the effective stress can be expressed as follows:

$$\overline{\sigma_f}^2 = \sigma_\theta^2 \left[F sin^4\theta + G cos^4\theta + H\left(cos^2\theta - sin^2\theta\right)^2 + 2 \cdot N cos^2\theta \cdot sin^2\theta \right] \tag{2.12}$$

In the case where $\overline{\sigma_f} = \sigma_0$, the evolution of the effective stress with the angle relative to the rolling direction can be described as follows:

$$\sigma_\theta = \sigma_0 \left[F sin^4\theta + G cos^4\theta + H \left(cos^2\theta - sin^2\theta \right)^2 + 2 \cdot N cos^2\theta \cdot sin^2\theta \right]^{-\frac{1}{2}} \tag{2.13}$$

Using a similar approach, the evolution of the anisotropy coefficient with the orientation (angle relative to the rolling direction) of the sheet metal, under the assumption of volume consistency ($\varepsilon_{xx} + \varepsilon_{yy} + \varepsilon_{zz} = 0$), can be described as follows:

$$r_\theta = \frac{F sin^4\theta + G cos^4\theta + H \left(cos^2\theta - sin^2\theta \right)^2 + 2 \cdot N cos^2\theta \cdot sin^2\theta}{F sin^2\theta + G cos^2\theta} - 1 \tag{2.14}$$

The method for identifying the parameters of the Hill'48 criterion is based on yield stresses, using equation 2.15, and assuming that $G + H = 1$.

$$\begin{cases} F = \dfrac{\sigma_0^2}{2} \cdot \left(\dfrac{1}{\sigma_{90}^2} + \dfrac{1}{\sigma_b^2} - \dfrac{1}{\sigma_0^2} \right) \\ G = \dfrac{\sigma_0^2}{2} \cdot \left(-\dfrac{1}{\sigma_{90}^2} + \dfrac{1}{\sigma_b^2} + \dfrac{1}{\sigma_0^2} \right) \\ H = \dfrac{\sigma_0^2}{2} \cdot \left(\dfrac{1}{\sigma_{90}^2} - \dfrac{1}{\sigma_b^2} + \dfrac{1}{\sigma_0^2} \right) \\ N = \dfrac{1}{2} \cdot \dfrac{\sigma_0^2}{\tau_{xy}^2} \end{cases} \tag{2.15}$$

In the present methodology, the identification of the parameters for the Hill'48 criterion is based on the yield stresses, as expressed in equation 2.15. It is assumed that the sum of the parameters G and H is equal to 1, ensuring volume consistency. The yield stresses used for parameter determination are denoted as σ_0 and σ_{90}, corresponding to the angles 0° and 90° relative to the rolling direction, respectively. However, it should be noted that measuring the tensile yield stress in the through-thickness direction is challenging for thin metal sheets. As an alternative, the biaxial yield stress, denoted as σ_b, is utilized due to the difficulty in obtaining precise measurements in the through-thickness direction.

In some studies [45, 46], researchers have explored an alternative approach for estimating the parameter N by considering the yield stress σ_{45}, as described in equation 2.16. This methodology is particularly employed when conducting shear tests and obtaining accurate data present challenges. By utilizing the yield stress at an angle of 45° relative to the rolling direction, the parameter N can be estimated without relying on shear test results.

$$N = \frac{\sigma_0^2}{2} \cdot \left(\frac{4}{\sigma_{45}^2} - \frac{1}{\sigma_b^2} \right) \tag{2.16}$$

An alternative and a commonly employed approach for the determination of the Hill'48 parameters involves utilizing the plastic anisotropy coefficients associated with specific angles relative to the rolling direction, namely 0°, 45°, and 90°. These coefficients, denoted as r_0, r_{45}, and r_{90} respectively, quantify the degree of anisotropy in the material's plastic response. The identification of the Hill'48 parameters using this method can be formulated as follows:

$$G+H=1 \Rightarrow G=\frac{1}{r_0+1}; \quad \frac{H}{G}=r_0; \quad F=\frac{H}{r_{90}}; \quad N=(F+G)\left(r_{45}+\frac{1}{2}\right) \tag{2.17}$$

With the proposed yield function, it is also feasible to predict the material behavior under a biaxial stress state. In this scenario, the yield stress (σ_{biax}) and the biaxial anisotropy coefficient (r_{biax}) are given by the following expressions:

$$\begin{cases} \sigma_{biax} = \sigma_0 \sqrt{\frac{1}{F+G}} \\ \\ r_{biax} = \frac{F}{G} \end{cases} \tag{2.18}$$

2.3.2.2 Yld91 yield function

To predict the evolution of the equivalent stress with respect to the angle relative to the rolling direction, the Yld91 function offers a suitable expression. This function, proposed by Barlat et al. in 1991 [36], extends Hershey's isotropic function to capture the orthotropic anisotropy present in metallic materials. The Yld91 function is a non-quadratic yield criterion composed of six components, and it can effectively describe the anisotropic behavior of these materials.

$$\phi(\boldsymbol{\sigma}) = |S_1 - S_2|^m + |S_2 - S_3|^m + |S_3 - S_1|^m = 2\overline{\sigma_f}^m \tag{2.19}$$

where S_1, S_2, and S_3 represent the principal values of the isotropic equivalent stress tensor $\boldsymbol{S}$, and σ_1, σ_2, and σ_3 are the corresponding yield strengths in the respective material directions. The exponent m is recommended to be set to 6 for materials with a body-centered cubic (BCC) crystal structure and 8 for materials with a face-centered cubic (FCC) crystal structure.

By employing the Yld91 function, researchers can effectively analyze and predict the evolution of equivalent stress as the angle relative to the rolling direction varies. This function provides valuable insights into the anisotropic behavior of metallic materials, facilitating the characterization and understanding of their mechanical response. The Yld91 function has been widely used in the field of material science and engineering to accurately model the complex behavior of orthotropic materials subjected to various loading conditions.

To calculate the stress tensor $\boldsymbol{S}$, a linear transformation $\boldsymbol{L}$ is applied to the Cauchy stress tensor $\boldsymbol{\sigma}$ according to the relationship:

$$\boldsymbol{S} = \boldsymbol{L} \cdot \boldsymbol{\sigma} \Leftrightarrow \begin{bmatrix} S_{xx} \\ S_{yy} \\ S_{zz} \\ S_{yz} \\ S_{zx} \\ S_{xy} \end{bmatrix} = \frac{1}{3} \begin{bmatrix} c+b & -c & -b & 0 & 0 & 0 \\ -c & a+c & -a & 0 & 0 & 0 \\ -b & -a & b+a & 0 & 0 & 0 \\ 0 & 0 & 0 & f & 0 & 0 \\ 0 & 0 & 0 & 0 & g & 0 \\ 0 & 0 & 0 & 0 & 0 & h \end{bmatrix} \cdot \begin{bmatrix} \sigma_{xx} \\ \sigma_{yy} \\ \sigma_{zz} \\ \sigma_{yz} \\ \sigma_{zx} \\ \sigma_{xy} \end{bmatrix} \tag{2.20}$$

a, b, c, f, g and h are the anisotropic material coefficients

The principal values of $\boldsymbol{S}$ can be obtained from the determination of the eigenvalues or using the following approach:

$$\begin{cases} S_1 = 2\sqrt{I_2}cos\left(\dfrac{\theta}{3}\right) = z^{\frac{1}{3}} + \overline{z}^{\frac{1}{3}} \\ S_2 = 2\sqrt{I_2}cos\left(\dfrac{\theta}{3} - \dfrac{2\pi}{3}\right) = w \cdot z^{\frac{1}{3}} + \overline{w} \cdot \overline{z}^{\frac{1}{3}} \\ S_3 = 2\sqrt{I_2}cos\left(\dfrac{\theta}{3} + \dfrac{2\pi}{3}\right) = \overline{w} \cdot z^{\frac{1}{3}} + w \cdot \overline{z}^{\frac{1}{3}} \end{cases} \tag{2.21}$$

where

$$\begin{cases} \theta = arccos\left(\dfrac{I_3}{I_2^{3/2}}\right) \\ z = I_3 + i\sqrt{I_2 - I_3} = I_2^{3/2}\left[cos(\theta) + isin(\theta)\right] \\ w = e^{-2i\pi/3} \end{cases} \tag{2.22}$$

The second (I_2) and third (I_3) stress invariants are given by:

$$\begin{aligned} I_2 &= \frac{S_{xx}^2 + S_{yy}^2 + S_{zz}^2 + 2\left(S_{yz}^2 + S_{zx}^2 + S_{xy}^2\right)}{6} \\ I_3 &= \frac{S_{xx}S_{yy}S_{zz} + 2S_{yz}S_{zx}S_{xy} - \left(S_{xx}S_{yz}^2 + S_{yy}S_{zx}^2 + S_{zz}S_{xy}^2\right)}{2} \end{aligned} \tag{2.23}$$

To predict the evolution of the equivalent stress with respect to the angle relative to the rolling direction, the following expression can be considered:

$$\sigma_\theta = \sigma_0 \cdot \left(\frac{|S_1 - S_2|^m + |S_2 - S_3|^m + |S_3 - S_1|^m}{2}\right)^{-\frac{1}{m}} \tag{2.24}$$

The calculation of the strain increment components, which are essential for determining the plastic anisotropy coefficient as a function of the orientation angle, involves taking

derivatives of the yield function as a function of stress tensor components. This can be expressed as follows:

$$\phi(\boldsymbol{\sigma}) = 2\overline{\sigma_f}^m \Longrightarrow \frac{\partial \overline{\sigma_f}}{\partial \sigma_{ij}} = \frac{1}{2m \cdot \overline{\sigma_\theta}^{m-1}} \frac{\partial \phi}{\partial \sigma_{ij}} \tag{2.25}$$

where:

$$\frac{\partial \phi}{\partial \sigma_{ij}} = \sum_{k=1}^{3} \sum_{l=2}^{3} \sum_{m=1}^{6} \frac{\partial \phi}{\partial S_k} \frac{\partial S_k}{\partial I_l} \frac{\partial I_l}{\partial s_m} \frac{\partial s_m}{\partial \sigma_{ij}} \tag{2.26}$$

Since the Yld91 function is more complex than the functions previously presented, partial derivatives were determined accordingly to each variable.

By utilizing this expression, the Yld91 function enables the estimation of the equivalent stress evolution as the angle relative to the rolling direction changes, providing insights into the anisotropic behavior of metallic materials.

2.3.2.3 Yld2004 yield function

In 2004, Barlat et al. proposed an enhanced version of the Yld91 yield function, known as the Yld2004-18p function [47]. It is used to predict the onset of plastic deformation in metals subjected to complex loading conditions, particularly in sheet metal forming processes.

The Yld2004 model is an improvement over the Yld2000-2d model, as it incorporates additional parameters to account for the effect of plastic anisotropy and strain path changes during forming. With this hardening law, it is possible to describe the anisotropic behavior of metals in a full three-dimensional stress state. It is based on a combination of anisotropic and isotropic hardening rules and takes into account the effect of strain rate, temperature, and multiaxial stress states on the yield strength of metals. It is particularly useful for predicting the behavior of metals under biaxial and triaxial stress states, which are commonly encountered in sheet metal forming processes.

This yield criterion has been validated for a wide range of metallic materials and can be used in industry for the evaluation of sheet metal components. When large numbers of experimental data are available, typically, uniaxial tension data for seven test directions between the rolling (RD) and transverse (TD) directions, as well as balanced biaxial data, the following yield function ϕ, is proposed:

$$\begin{aligned}\phi = \phi(\overline{\mathbf{S}'}, \overline{\mathbf{S}''}) = |\overline{S'_1} - \overline{S''_1}|^m + |\overline{S'_1} - \overline{S''_2}|^m + |\overline{S'_1} - \overline{S''_3}|^m + |\overline{S'_2} - \overline{S''_1}|^m + |\overline{S'_2} - \overline{S''_2}|^m \\ + |\overline{S'_2} - \overline{S''_3}|^m + |\overline{S'_3} - \overline{S''_1}|^m + |\overline{S'_3} - \overline{S''_2}|^m + |\overline{S'_3} - \overline{S''_3}|^m \\ = 4\overline{\sigma}^m\end{aligned} \tag{2.27}$$

In the equation 2.27, $\overline{\sigma}$ is the flow stress, and $\tilde{S}'_i$ and $\tilde{S}'_j$ are the principal values of the tensor $\tilde{\mathbf{s}}'$ and $\tilde{\mathbf{s}}''$ defined by two linear transformations on the stress deviator s.

$$\tilde{\mathbf{s}}' = \mathbf{C}'\mathbf{s} = \mathbf{C}'\mathbf{T}\sigma = \mathbf{L}'\sigma \tag{2.28}$$

$$\tilde{\mathbf{s}}'' = \mathbf{C}''\mathbf{s} = \mathbf{C}''\mathbf{T}\sigma = \mathbf{L}''\sigma \tag{2.29}$$

In the equations 2.28 and 2.29, σ represents the Cauchy stress tensor, and $\mathbf{C}'$ and $\mathbf{C}''$, shown the associated linear transformations on the stress deviators, the anisotropy coefficients.

$$\mathbf{C}' = \begin{bmatrix} 0 & -c_1 & -c_2 & 0 & 0 & 0 \\ -c_3 & 0 & -c_4 & 0 & 0 & 0 \\ -c_5 & -c_6 & 0 & 0 & 0 & 0 \\ 0 & 0 & 0 & -c_7 & 0 & 0 \\ 0 & 0 & 0 & 0 & -c_8 & 0 \\ 0 & 0 & 0 & 0 & 0 & -c_9 \end{bmatrix}, \tag{2.30}$$

$$\mathbf{C}'' = \begin{bmatrix} 0 & -c_{10} & -c_{11} & 0 & 0 & 0 \\ -c_{12} & 0 & -c_{13} & 0 & 0 & 0 \\ -c_{14} & -c_{15} & 0 & 0 & 0 & 0 \\ 0 & 0 & 0 & -c_{16} & 0 & 0 \\ 0 & 0 & 0 & 0 & -c_{17} & 0 \\ 0 & 0 & 0 & 0 & 0 & -c_{18} \end{bmatrix} \tag{2.31}$$

The transformation matrix, $\mathbf{T}$, transforms the stress tensor to its deviator s,

$$\mathbf{T} = \frac{1}{3}\begin{bmatrix} 2 & -1 & -1 & 0 & 0 & 0 \\ -1 & 2 & -1 & 0 & 0 & 0 \\ -1 & -1 & 2 & 0 & 0 & 0 \\ 0 & 0 & 0 & 3 & 0 & 0 \\ 0 & 0 & 0 & 0 & 3 & 0 \\ 0 & 0 & 0 & 0 & 0 & 3 \end{bmatrix} \tag{2.32}$$

This is an isotropic and convex function with respect to its arguments. The two linear transformations provide 18 coefficients that can be used to capture the material anisotropy. When the coefficients are all equal to one, this function reduces to Hershey's isotropic yield function proposed to reproduce the yield surface calculated with a self-consistent polycrystal model. Also, for m=2 (or 4) and all the coefficients c_i are equal to 1, the yield function reduces to *von Mises*. Note that when $\mathbf{C}'' = \mathbf{C}'$ (or $\mathbf{L}'' = \mathbf{L}'$), i.e., when the formulation accounts for only one linear transformation, Yld2004-18p reduces to Yld91.

2.3.2.4 Flow rules

The application of novel, lightweight and high-strength materials in various sheet metal industries, particularly the automotive sector, poses significant manufacturing challenges. Traditional materials predictive behaviors may not apply to these newer materials, such as HSS steels and aluminum alloys, thereby necessitating precise predictions of their mechanical behavior. Accurate assessment and analysis of material behavior in the context of sheet metal forming entail multiple challenges encompassing material properties, mechanical testing, numerical modeling, and methodological approaches. Specifically, the decoupling of the yield function and potential function is recognized as the Non-Associated Flow Rule (NAFR).

This work, focuses on the identification of yield function parameters using planar yield stresses and establishes the plastic potential function based on r-values. The explicit separation of the yield function and the potential function represents the application of the NAFR.

Within the framework of plasticity theory, the associated and non-associated flow rules cover two distinct concepts that clarify the interaction between stress and strain during the occurrence of plastic deformation in a material. These principles form the basis for understanding the mechanical behavior and response of materials under external loading conditions.

The associated and non-associated flow rules stand as fundamental concepts in plasticity theory, offering distinct perspectives on the stress-strain relationship during plastic deformation in materials. The associated flow rule assumes a direct proportionality between the plastic strain rate and the deviatoric stress tensor, independent of the material stress history. This assumption simplifies the analysis of plastic deformation of materials by neglecting the influence of prior stress states [37, 38, 48, 49].

For the non-associated flow rule, the plastic strain rate takes into account the deviatoric stress tensor and hydrostatic stresses. This more comprehensive relationship is essential for accurately capturing the plastic deformation behavior of anisotropic materials or materials exhibiting substantial strain hardening characteristics. By considering the influence of both deviatoric and hydrostatic stresses, the non-associated flow rule accommodates a broader range of material behaviors, enabling a more realistic representation of plastic deformation phenomena. The NAFR offers a broader and more generalized reproduction of plastic flow phenomena in materials, as it permits to describe the direction of plastic flow to be independent of the rate of deformation. This distinctive attribute allows materials to exhibit dissimilar behaviors under varying loading conditions. This flow rule accommodates the inherent complexities of these materials, characterized by anisotropy and strain-rate sensitivity, enabling a more precise and comprehensive representation of their plastic deformation response [50, 51, 52].

In general, the formulation of plasticity criteria predominantly relies on the associated flow rule (AFR), wherein the yield and plastic potential functions are assumed to be equivalent and follow the normality assumption, as shown in figure 2.5. The numerical simulation of sheet metal forming processes often employs criteria governed by the AFR, resulting in favorable agreement with experimental observations. However, investigations have demonstrated that the predictive accuracy of plastic behavior in certain anisotropic materials, such as steel and aluminum alloys, necessitates improvement.

This limitation arises from the AFR's incapacity to effectively capture both the yield stresses and the plastic anisotropic coefficients simultaneously through a single function.

The ability to accurately reproduce the sheet metal material behavior is directly dependent on the methodology used to identify the constitutive parameters. For example, the AFR can describe the yield stresses evolution and the plastic anisotropic coefficients evolution for different angles relative to the rolling direction, using one function but based only on stress parameters or on r-values. In the case of the NAFR, it is possible to describe both yield stresses and anisotropy coefficients since there are two functions and two sets of constitutive coefficients, one set for the yield surface and another for the potential surface.

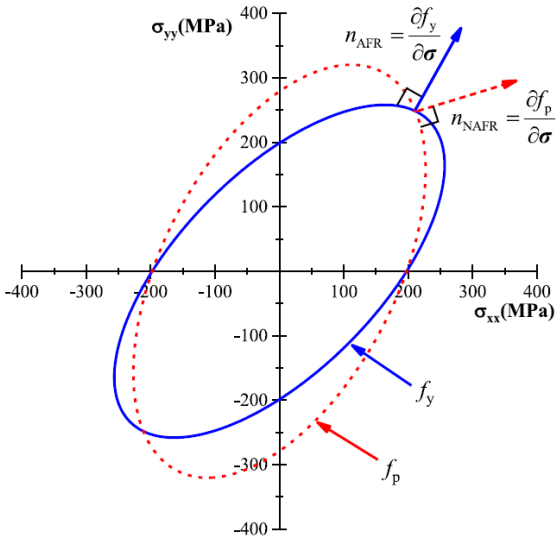


Figure 2.5: Plastic flow directionality: associated (AFR) and non-associated (NAFR) flow rules (adapted from [53]).

While the accuracy can be enhanced, the process of parameter identification becomes inherently more complex. This complexity arises due to the increased need for experimental data, leading to additional efforts, extended verification time and increased computational costs.

2.3.3 Interaction between contact surfaces

The force that results from the friction between sheet metal blank and forming tools is crucial because it influences the process performance and final product quality. In finite element modeling, friction behavior is frequently considered by employing a constant coefficient of friction, usually using the classic Coulomb model. However, sometimes this could result in an inadequate representation of the actual friction behavior. The use of a local variable blankholder force in deep drawing is an example of the influence of friction forces on sheet material flow.

If the deep drawing of a cylindrical or square cup is considered without a blankholder force, the material in the corners must be compressed before it flows into the die. As a result, there is regional thinning or tearing of the material and substantial thickness variances in the finished cup. A potential solution to this issue is to employ a blank holder that is divided into separate sections. Each of these components may be loaded individually with a distinct variable force. It is feasible to affect the friction force by decreasing or increasing the mean contact pressure locally.Additional practical instances of local friction

control involve incorporating elements such as sandpaper or thin teflon foils in designated areas, and/or implementing selective lubricant delivery to specific locations.

To simulate a blank holder interaction, various possibilities can be considered, some of which involve associated simplifications. Figure 2.6 presents a schematic representation of different modeling options.

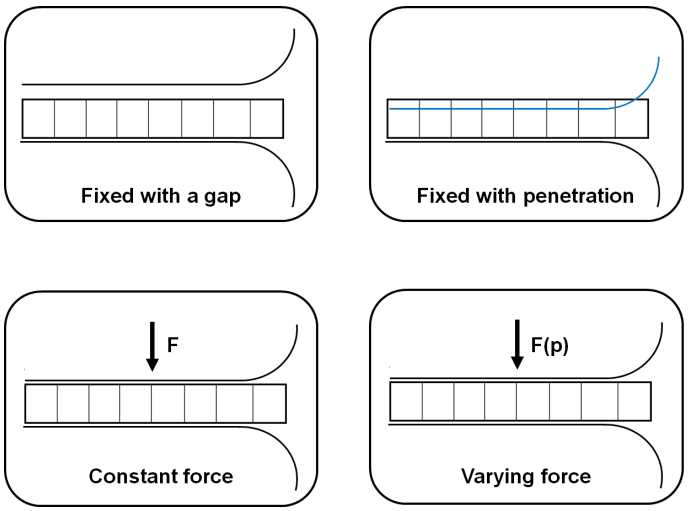


Figure 2.6: Scheme with different possibilities to model blankholder boundary conditions.

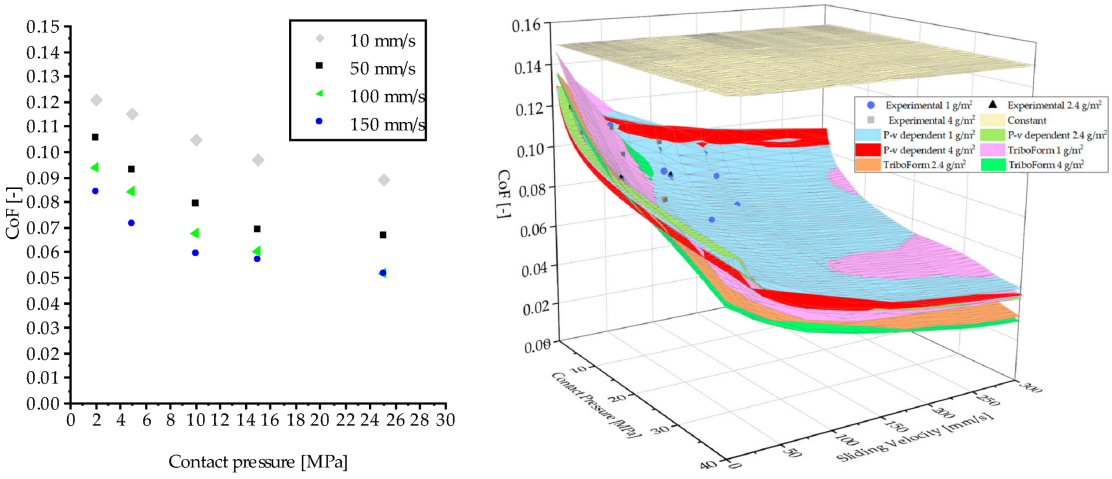
Modeling the blankholder with a fixed gap, corresponds to have a boundary condition where there is always a distance between the die and the blankholder, which remains constant during all of the simulation. In case of a constant force condition, a pre-defined force value is applied to the blankholder. The more of the blank flows into the die, the smaller contact area between blank and blankholder will be, which can lead to higher contact pressures in the end of the process since the contact area has been reduced.

Another alternative is the blankholder force being a function of the contact surface area. As the contact are decreases over time, the blankholder force should decrease as well in order to provide a constant contact pressure on the sheet.

However, most sheet metal forming simulations use the fricion coefficient (μ) as a constant, ignoring the fact that the variables on which this value is dependent may change during the process, needing sometimes the use of a model that characterizes μ as a function of local contact conditions. Plastic deformation, in addition to elastic deformation, plays a key role in sheet metal forming, therefore, the effects of both elastic and plastic deformation on the friction behavior of surface contacts must be considered. Friction under lubricated conditions is known to be pressure dependent and experimental evaluation of this dependency has traditionally defined pressure as a uniform value throughout the

contact area [54]. However, non-uniform pressure distributions at the contact surfaces have been documented in numerous experiments and models.

Muñiz et al. [55] evaluated the friction coefficient (CoF) as a function of contact pressure, sliding velocity and lubricant quantity. Results showed that the CoF decreases with increasing contact pressure, as observed in figure 2.7. This phenomenon was also studied by Karupannasamy et al. [56], who concluded that the surface deformation had an effect on CoF evolution at low contact pressure. Moreover, when compared to the constant friction model, the use of friction coefficient as a function of contact pressure significantly improved the numerical simulation accuracy. This highlights the need to sometimes use tribological models that take into account other variables that may change during the forming process.



(a) (b)

Figure 2.7: Comparison between the friction coefficient (CoF) and the contact pressure at different sliding velocities [55].

In the work of Kim et al. [57] the impact of non-uniform pressure distribution during the drawbend friction test was investigated. The study focuses on how variations in pressure distribution across the material surfaces during the test can affect the accuracy of friction measurements. By analyzing these effects, the research enhanced the reliability and precision of friction measurements in various applications. The results showed that non-uniform pressure distribution during the drawbend friction test significantly impacts friction measurements, leading to inaccurate results. Addressing these pressure variations was crucial for improving the reliability of friction data. Additionally, the same authors quantified the pressure-friction relationship through experimental trials, which

was directly applied to the cup drawing process, leading to an improved simulation accuracy [58].

Kraus et al. [59] investigated how a single sheet metal compression test can effectively study friction behavior under varying contact pressures. This method provided practical insights into friction in sheet metal materials during deformation. The study emphasized the influence of contact pressure on friction coefficients. The obtained friction coefficients were observed to change with different contact pressures, highlighting the importance of considering contact pressure as a significant factor that can influence friction behavior in sheet metal forming processes.

2.4 Experimental benchmarks

The application of new materials in sheet metal forming processes can introduce new challenges. The behavior observed in the manufacturing of a well known component may not be directly applicable when working with high-strength steels or aluminum alloys. Consequently, numerical codes must accurately capture and model these distinct material behaviors. Various constitutive equations have been developed to enhance the accuracy of material behavior modeling in such cases. As a result, there is an increased demand for higher experimental reliability to facilitate numerical validation, which has reached an advanced level of result quality.

To ensure this reliability, a consistent approach involves selecting a benchmark model, establishing a standardized procedure for conducting experiments, defining appropriate measurement methods for selected results and carried out the benchmark (if possible, across multiple institutions). This process of benchmarking, standardization and collaboration allows a higher level of experimental accuracy, enabling effective validation of the numerical developments.

A standardized method is provided by the benchmark test for simulating springback in sheet metal forming. This allows for a comparison of springback predictions between different numerical simulation codes and experimental results. To measure the gap caused by splitting a ring taken from a drawn cup, the test is utilized. The test does not require the use of measurement fixtures or sophisticated profiling equipment. Additionally, it produces significant springback, which enhances measurement accuracy and reduces experimental error.

The NUMISHEET conference series is one the most significant international conference on the area of the numerical simulation of sheet metal forming processes and usually

at each conference different challenges are proposed to the participants, some of them being industrial problems, through benchmarks. A common benchmark is the cylindrical cup forming test in different variants regarding blank initial size, tools dimensions, or even a reverse operation. It is also used to address the springback behavior after forming by determining the opening of a ring cut from the sidewall of a drawn cylindrical cup, known as the split ring test, as first presented by Demeri et al. [60].

2.4.1 Swift test

Deep drawing tests are commonly employed to evaluate the formability and mechanical characteristics of sheet materials. The test assesses the material ability to withstand stretching and compressive forces without cracking, wrinkling, or other phenomena. It also provides insights into the material strain distribution, thinning and potential for springback after forming. Usually, the tools used in deep drawing operations rely on three distinct components: a punch (used to apply a controlled force to draw the blank), a die (used to give the final component shape) and a blank holder (where a flat sheet metal blank is clamped between the die). The blank undergoes significant plastic deformation as it takes the shape of the die, resulting in the formation of a structure. The depth of the drawn part is dependent on the material formability.

Among the deep drawing tests, the Swift test has been widely used and is considered as a standard test, which consists on forming a cylindrical cup from a circular blank, using a flat bottom cylindrical punch.

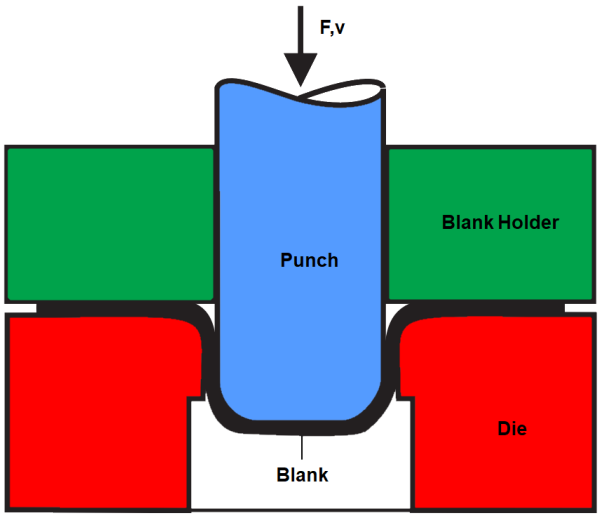


Figure 2.8: Scheme of deep drawing cylindrical cup tools - Swift test.

It has been broadly studied as a reference test to evaluate the formability limit of the materials, by measuring the limit drawing ratio (LDR) [1], but also as a reference test to evaluate the capabilities of constitutive models to predict the anisotropic behavior during deformation.

To ensure the quality of the final component and avoid defects, various factors related to the blank size and contact conditions need to be carefully adjusted. The flow of the blank into the die is influenced by the contact interaction with the tools. However, the interaction between tribological (friction and wear) and mechanical properties of the contacting bodies complicates the development of analytical expressions to support and reproduce the real behavior of sheet metal forming process [58].

The deep drawing cylindrical cup test is influenced by various variables that affect the final result and quality of the formed part. These variables can be grouped into material-related parameters, tooling and process parameters. The common defects in the deep drawing cylindrical cup include wrinkling, ironing, tearing, earing and galling. Due to the complexity of the deep drawing cylindrical test and all the variables involved, several studies were conducted to understand the influence of the different parameters in the success of the experimental test.

Ghafar et al. [61] investigated the impact of misalignment severity in the square cup deep drawing process on drawing force and wall thickness distribution. They used a 1 mm electrolytic zinc-coated steel sheet (SECC) as a blank and simulated the conditions with Abaqus/Explicit software. The study considered the anisotropic nature of the material and utilized the Hill'48 model based on testing data in different directions. Tensile and forming tests were conducted to obtain stress–strain and forming limit diagrams. Using a circular blank, they drew sheet metal to a depth of 16 mm. Validation using a drawing jig and a universal tensile machine confirmed that misalignment increases drawing force and reduces wall thickness distribution.

Amaral et al. [62] studied the earing height profile, wall thickness distribution and punch force evolution for dual-phase steel sheets, using a deep drawing cylindrical cup test. Finite element simulations and experimental tests was performed in order to evaluate and compare the obtained results for this kind of advanced high strength steels. The numerical simulation of the cylindrical cup test was carried out using a user subroutine in the FE code with different implemented anisotropic yield criteria, namely Hill'48, Barlat 91 and CPB06. The results for earing height profile and wall thickness distribution showed that Hill'48 and CPB06 give similar predictions and close to experimental points. On the

[1] LDR - corresponds to the ratio between the maximum diameter of the blank that can be stamped without breaking, and the diameter of the punch.

other hand, the predicted punch force evolution is not very sensitive to the selected yield criteria and their results was very closer to experimental data.

Arab and Javadimanesh [63] studied the analysis of deep drawing of circular blanks into axi-symmetric cylindrical cup using numerical modeling. The blank drawability has been related both theoretically and experimentally with the initial diameter of the blank and deep drawing parameters. The strains in the radial and circumferential directions have been measured. A correlation on the flange thickness variation by taking into account the work hardening with the analytical and experimental values have also been searched.

Barros et al [64] investigated a cup drawing of an Alcoa AA3104 aluminum alloy by using the FEM. The earing profile, thickness and punch forces evolutions as well as stress and strain states are analyzed. A proper experimental procedure was adopted to characterize the material mechanical behavior and to perform the cylindrical cup deep drawing. Additionally numerical simulations were performed considering the CB2001 and CPB06ex2 yield criteria, both implemented in DD3IMP in-house code. The results confirmed that the earing profile trend is primarily influenced by the directionality of in-plane yield stresses and r-values.

Evin et al. [65] studied the influence of the friction coefficient in the simulation of stamping processes. Analytical models were verified by an experimental strip drawing test under the same contact conditions. Steel sheets for the automotive industry were used in experiments and simulations extra deep drawing quality DC 05 and austenitic stainless steel AISI 304. The friction coefficients were also evaluated when the cup test was performed. A regression model of drawing to the blankholding force was also applied. The results confirmed the conformity of friction coefficients when measured by cup tests and strip tests.

Dwivedi et al. [66] studied a new technique for the deep drawing process of cylindrical cups through a conical die without a blank holder. The cylindrical cups were produced by pushing a circular blank using a flat-headed cylindrical punch through a conical die with a cylindrical throat in a single punch stroke. In the traditional deep drawing process, a blank holder is required to press the blank over the die to prevent wrinkling and to control the material flow into the die cavity but, on the other way is responsible for fracture on the sheet. The optimization of blank holder pressure is very critical. Aditionally a 3-D parametric FE model was built using the commercial FE package ANSYS/APDL-19. Two different aluminum alloys were used, a AA8011 and AA1200 with 1 to 2 mm initial thicknesses respectively, and the diameters which varies from 45 to 65 mm. The results of the finite element models showed good agreement with experimental test and a cylindrical cup with a LDR of 2.5 has been successfully achieved.

Lăzărescu et al. (2015) conducted experiments and finite element simulations to explore the impact of constant and time-variable blank-holding forces on drawing force and thickness distribution in the deep drawing process for cylindrical and square cups using AA6016-T4 aluminum alloy sheets. Their finite element model, developed in AutoForm software, was validated with experiments. The study revealed that employing a variable blank-holding force, as opposed to a constant one, decreased drawing force but resulted in wall thickening.

For cylindrical cups, drawing force was influenced more by the amount of blank-holding force than its type (constant or time-variable). In square cups, both the amount and type of blank-holding force affected drawing force. The variable force only reduced drawing force in the second stage of the drawing process.

The study found that wall thinning in the punch shoulder part was unaffected by the type of blank-holding force. However, thickening at the side wall of deep-drawn cups was influenced by both constant and variable blank-holding forces. Increasing blank-holding force led to decreased thickening of the side wall. Conversely, adopting a time-variable blank-holding force, decreasing throughout the punch stroke, could increase thickening of the side wall.

2.4.2 Modified Demeri test

Over the past decades, the automotive industry has witnessed a significant rise in the use materials that led to one of the most prominent issues, springback. Springback refers to the elastic recovery of the material after it has been subjected to forming forces, leading to a deviation from the desired final shape. This phenomenon makes it challenging to accurately predict and achieve the intended part shape, often necessitating numerous experimental trials and adjustments in tool design.

A standard test method (ASTM E2492-07) [60] for evaluating springback behavior of metals in a test that simulates a stretch-draw forming process is the Demeri split ring test.

The Demeri split ring test addresses the quantification and provides insight into how the metal behaves regarding springback, which refers to the difference of cylindrical cup ring between the final (after split) and initial shape. Compared to other methods, the amount of springback observed in this test is significant. This enhances measurement precision and decreases experimental errors across all ductile metals. The precise measurement of springback can be achieved without the need for complex measurement fixtures or sophisticated profiling equipment. Simple length measuring instruments are all that is required to perform the necessary measurements accurately.

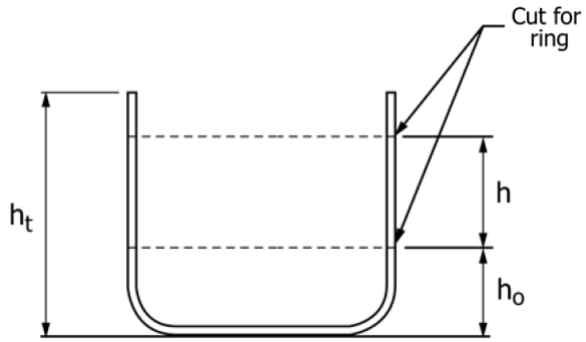


Figure 2.9: Ring Location in a deep drawn cylindrical cup (adapted from [ASTM E2492]).

The Demeri split ring test has been suggested as a benchmark test for springback because it eliminates the challenges associated with precise springback measurement [67]. The change in the ring outer diameter from its original size indicates the amount of residual circumferential stress that has been released. This enables the calibration of numerical and constitutive model parameters to achieve a satisfactory correlation with benchmark test results. This methodology to characterize springback behavior has been already applied by other researchers [68, 69, 70]. The accuracy of springback predictions is influenced by the stress state achieved after forming, which is dependent on the particular combination of forming parameters used during the drawing operation.

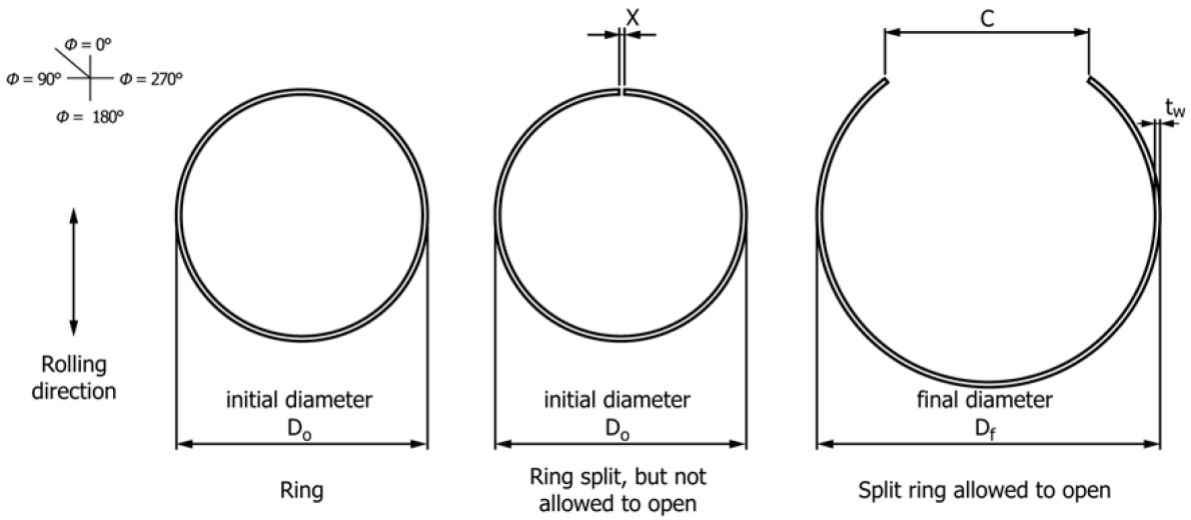


Figure 2.10: Different stages of a split ring procedure: X - length of section removed during cutting; C - length measured between the tips of the split ring [ASTM E2492].

The spilt ring test gained significant exposure and recognition when it was introduced as a benchmark test during the Numisheet conference in 2016. At the conference, researchers evaluated the springback behavior of an AA5086 alloy under warm forming conditions using this test approach. This significant advancement facilitated researchers from diverse backgrounds to adopt and implement the spilt ring test in their studies, development valuable contributions to the advancement of knowledge in this particular field. Because of its adoption, the spilt ring test has become a method for investigate and understand springback phenomena in the deep drawing of a cylindrical cup.

Laurent et al. [71] investigated the capability of different yield criteria (von Mises, Hill'48, Barlat Yld91), with both isotropic and mixed hardening, to represent the behavior of an aluminum alloy during a forming process and springback evolution using the split ring test. As a conclusion of the study, the authors refer a good correlation between the experimental data during forming analysis which demonstrates that simulations are able to predict certain aspects of the forming process fairly well, such as evolution of force during forming, thickness distribution and deformation profile. Numerical results also showed that the constitutive model has a minor influence on drawing operations. The results of springback indicate a higher impact of the yield criteria than the hardening law. The predicted opening using von Mises and Hill'48 criteria with kinematic hardening was less accurate than those obtained using Barlat'91 model.

Simões et al. [72] studied numerically, the impact of the ironing on the residual stress distributions in the cylindrical cup, and consequently, in the split ring test. The analysis was performed considering a 6016-T4 aluminum alloy, for which experimental results

were used as a reference. The results show that the ironing of the vertical wall changes the characteristic distribution of the axial and circumferential residual stresses in all areas of the cup wall, even for relatively small ironing strains. This affects the trend observed for the ring opening value, when rings are cut at different heights.

Lee et al. [73] investigated the effect of anisotropic plasticity and nonlinear elasticity on deep drawing cylindrical cup and corresponding springback prediction based on a split ring test, using a dual-phase DP490 steel. The anisotropic Hill'48 yield criteria, considering also a NAFR approach, and Yld2000-2D non-quadratic yield function, were considered in the numerical analysis. Additionally, both yield surfaces evolve as a function of equivalent plastic strain. The study revealed that by incorporating an effective constitutive model capable of representing anisotropy and nonlinearity during plastic deformation, the finite element simulations exhibited considerable accuracy in predicting both the deformed shapes after forming and springback.

Coer et al. [74] study focus on the experimental and numerical analyses of Swift cup test, followed by the Demeri split ring test, performed with an AA5754-O alloy at room temperature, where a detailed analysis of the punch force evolution, the thickness evolution along the cup wall, the earing profile, the strain paths and ring opening was made. The numerical model adopted in the implicit version of ABAQUS, where the aim is to compare the computational efficiency of solid and solid-shell elements for the constitutive models available. The results demonstrate that the solid-shell element proves to be a more cost-effective alternative than the solid element, presenting global accurate predictions, except for the thinning zones. The von Mises and Hill'48 yield criteria perform well in predicting strain distributions in the final cup. However, improved knowledge concerning the stress states is still required, because the Hill'48 criterion showed difficulties in the correct prediction of the springback, whatever the type of finite element adopted.

2.4.3 Cross die forming test

Cross die forming test, also known as cross tool test, is an experiment used to evaluate the formability and deformation behavior of a sheet metal material under specific conditions. With its unique combination of tool and blank geometry (figure 2.11), this test allows the generation of a diverse range of loading stress states and strain paths, similar to those experienced in industry, within a single experiment.

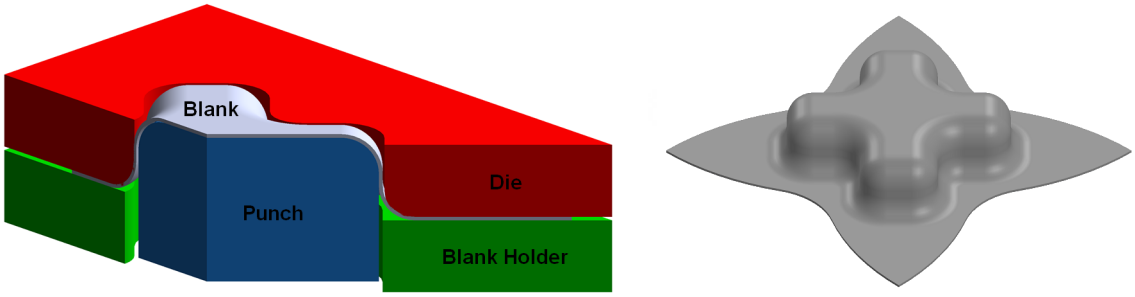


Figure 2.11: Illustration of cross die test tools.

The material ability to undergo complex deformation without failure, such as tearing or fracture, can provide valuable information about the material formability, stretchability and susceptibility to defects during manufacturing processes like stamping or deep drawing.

The cross die test results in the production of a deep drawn component that demonstrates substantial levels of uniaxial, plane strain and biaxial deformation. This test serves the fundamental objective of determining the material ability to withstand the prescribed levels of deformation necessary for the forming process. Several authors used this deep drawing test, in order to study the influence of the variables in the process.

Khalfallah et al. [75] investigated the effect of the number and type of experimental input data used in parameter identification of Hill'48, Barlat'91 (Yld91) and Cazacu and Barlat'01 (CB2001) yield criteria on the accuracy of the finite element simulation results. For that the evaluation of the predictive capacity of the studied yield criteria, calibrated using different sets of experimental data, is made by comparing finite element simulation results with experimental tests for the deep drawing of a cross-shaped part. Different sets of experimental data are used to identify the anisotropy parameters of two metal sheets, exhibiting different anisotropic behavior and hardening characteristics: a mild steel (DC06) and an aluminium alloy (AA6016-T4). As a result a satisfying agreement is observed between experimental and numerical thickness distributions, with a negligible effect of the number and type of experimental data for the Hill'48 and Yld91 yield criteria. On the contrary, CB2001 calibration is quite sensitive to the experimental data available,

particularly biaxial values. Nevertheless, CB2001 calibration based on the combination of effective and artificial experimental data achieves satisfying results, which in the worst case are similar to the ones obtained with the Yld91.

Nakwattanaset et al. [76] developed and analized experimental and numerical forming limit curves (FLC) and forming limit stress curves (FLSC) for DP440 high-strength steel (HSS). The material properties were determined through a group of standard tests like the uniaxial tensile test, hydraulic bulge test and disk compression test. The influence of the applied yield criteria was studied. Eventually, to verify an applicability of all developed curves, the cross-die forming test was conducted both experimental and by numerical simulation. The results showed that the FLSCs could more precisely define the formability behavior of DP440 than the FLCs.

Ramazani et al. [77] applied a Gurson–Tvergaard–Needleman (GTN) model to predict the failure behavior of DP600 steel during the cross-die test, which has been used extensively in the automotive industry to assess the formability of sheet metals. GTN model parameters were identified through the response surface methodology (RSM), and were verified by the comparison of predicted and experimental forming limit curves (FLCs). The good agreement between the simulation and experimental results concerning failure behavior during the cross-die test, indicates that the GTN model can be applied to predict the forming characteristics of DP600 steel. It was also concluded that RSM is a proper method of predicting GTN model parameters.

Lingbeek et al. [78] used the cross die forming test to study the interaction between blank and tools, which is complex in any industrial deep drawing process. The objective was to increase the blank-size in a series of forming tests until fracture occurs. The numerical simulations carried out using ABAQUS, showed that the cross die benchmark is specifically sensitive to tool deformations. Based on these findings, authors point out the importance of conducting further scientific research regarding contact and friction modeling, to improve the accuracy of numerical forming results.

Resende et al. [79] investigated a developed elasto-plastic constitutive model and was used to simulate the cross die deep drawing test. The experiments and numerical simulations were conducted for five interstitial free steels and seven dual-phase (DP) steels, each of them having a different thickness and strength. The main interest of the adopted model was the efficient parameter identification procedure, due to the physical background of the model and the physical significance of some of its parameters and state variables. The numerical simulations were compared to experiments in terms of thickness distributions. The results suggested that the accuracy of the numerical simulations is very satisfactory

despite the scarce experimental input data. Furthermore, the modeling of the transient behavior due to strain-path changes may have a significant impact on the simulation results.

Chapter 3

Materials, characterization and constitutive modeling

An introduction of sheet metal materials that were used in this research, is made in this chapter. A description of their mechanical characterization is also presented, including the approach employed for identifying the corresponding constitutive models parameters. Moreover, it contains a defined set of experimental tests results that have been used to calibrate such parameters.

(This page was deliberately left blank)

3.1 Introduction

In this study, two distinct classes of materials, namely Aluminum Alloys (AA) and Advanced High Strength Steels (AHSS), are used to evaluate the numerical predictions of materials behavior of different constitutive models. These materials are of considerable interest due to their extensive usage in key industries, such as aerospace, automotive and construction sectors. Moreover, the subsequent section provides a comprehensive overview of the materials employed and the experimental test methodologies employed for characterizing the mechanical properties.

3.1.1 Aluminum alloys

The specific properties offered by aluminum and its alloys classified this material as a versatile, lightweight and aesthetically appealing for a diverse range of applications. From its utilization as a highly ductile wrapping foil to its integration in the most demanding engineering scenarios, aluminum alloys hold a significant position as structural metals, second only to steels in terms of usage.

Aluminum alloys (AA) are materials that are made by combining aluminum with one or more metallic or non-metallic elements. The resulting alloy often has improved mechanical properties, such as increased strength, hardness, and corrosion resistance, compared to pure aluminum [80]. Table 3.1 summarizes some common strength levels of aluminum alloys, the type of alloy compositions and the strengthening methods.

Table 3.1: Strength ranges for different wrought aluminum alloys [81].

Aluminum series	Type of alloy composition	Strengthening method	UTS range
1xxx	Al	Cold work	70-175 [MPa]
2xxx	Al-Cu-Mg (1-2.5% Cu)	Heat treat	170-310 [MPa]
	Al-Cu-Mg-Si (3-6% Cu)	Heat treat	380-520 [MPa]
3xxx	Al-Mn-Mg (3-6% Cu)	Cold work	140-280 [MPa]
4xxx	Al-Si	Cold work (some heat treat)	105-350 [MPa]
5xxx	Al-Mg	Cold work (1-2.5% Mg)	140-280 [MPa]
	Al-Mg-Mn	Cold work (3-6 % Mg)	280-380 [MPa]
6xxx	Al-Mg-Si	Heat treat	150-380 [MPa]
7xxx	Al-Zn-Mg	Heat treat	380-520 [MPa]
	Al-Zn-Mg-Cu	Heat treat	520-620 [MPa]
8xxx	Al-Li-Cu-Mg	Heat treat	280-560 [MPa]

As can been seen on table 3.1, the AA can exhibit a wide range of strength levels depending on their composition and processing, in which the different types of aluminum alloys are classified based on their primary alloying element, such as copper, zinc, magnesium, or silicon. They are widely used in a variety of applications due to their favorable combination of properties, including lightweight, high strength-to-weight ratio, good ductility, and excellent thermal and electrical conductivity. Additionally, aluminum alloys can be further modified by various heat treatment methods, which can enhance their mechanical properties even further. The values of tensile strength are approximate and can vary depending on the specific alloy, quenching (heat treatment), and processing conditions, where a specific designation is employed. The common used letters are listed in the following:

- **O**: Annealed condition. The alloy is heated to a high temperature and then allowed to cool slowly, resulting in maximum softness and ductility.
- **H**: Strain-hardened condition. The alloy is subjected to cold working or deformation to increase its strength. The number following the "H" indicates the level of strain hardening, with higher numbers indicating greater hardness and strength.
- **T**: Heat-treated condition. The alloy is subjected to a specific combination of heating and cooling to achieve desired properties. The number following the "T" represents the specific treatment process and its effects on the material. For example T4 is a quenching designation in aluminum alloys indicating that the material has undergone solution heat treatment and natural aging, resulting in good formability and moderate strength. It is commonly used for aluminum sheets and extrusions requiring a balance between strength and workability. T6 is a quenching designation in aluminum alloys indicating that the material has undergone solution heat treatment and artificial aging, resulting in high strength and hardness. It is commonly used for applications requiring excellent mechanical properties, such as structural components and aerospace parts.
- **F**: As-fabricated condition. The alloy is used in its "as-fabricated" state without any additional heat treatment or significant mechanical processing.
- **W**: Solution heat-treated condition. The alloy is heated to a specific temperature and then rapidly cooled (quenched) to achieve solid solution strengthening.

For this study the two selected grades are AA5182-O and AA6016-T4 rolled sheets with 1 mm nominal thickness.

The AA5182-O is an aluminum-magnesium alloy that belongs to the 5xxx series where the "O" designation indicates that it is in the annealed or fully soft condition. This material is known for its good formability and weldability, being commonly used in applications that requires moderate strength, such as automotive body panels, fuel tank, and heat exchanges. The annealing process involves heating the alloy to a high temperature and then allowing it to cool slowly. This promotes the formation of a uniform microstructure with minimal strain and deformation. The resulting microstructure of AA5182-O exhibits fine grains without any significant preferred crystallographic orientation. As a result, the AA5182-O grade demonstrates relatively low tensile strength but exhibits high ductility, rendering it well-suited for various forming and shaping processes [82, 83].

The AA6016-T4 is an aluminum-magnesium-silicon alloy that belongs to the 6xxx series. It is a wrought aluminum alloy that offers a combination of strength, formability and corrosion resistance. This material is commonly used in automotive applications, particularly for body panels and structural components due to its high strength-to-weight ratio and excellent surface finish. The alloy also provides good resistance to corrosion, making it suitable for outdoor and automotive environments [84]. In the T4 temper, AA6016 undergoes a solution heat treatment, which involves heating the material to a specific temperature and then rapidly cooling it to dissolve any soluble phases or precipitates. After solution heat treatment, the material is naturally aged, which allows precipitation hardening to occur over time at room temperature, the process provides a balance of strength and formability, making it suitable for various forming processes, such as stamping and roll forming. This grade is preferred for external parts, as it presents good formability characteristics, with no deterioration of surface aspect quality after forming.

3.1.2 Advanced high strength steels

Due to their high strength-to-weight ratio, advanced high strength steels (AHSS) became increasingly popular in weight reduction efforts, along with other materials. However, there are still many challenges associated with manufacturing automotive parts using AHSS [85]. One major obstacle is the distinct behavior of AHSS, which differs from both mild and conventional high strength steels (HSS). Consequently, empirical knowledge accumulated over the years cannot be directly applied to these materials. New operating settings must be defined to ensure successful forming processes and to facilitate the further implementation of AHSS.

3.1.2.1 Dual-phase steels

The dual-phase (DP) steels belong to the first generation of AHSS materials and are known for their superior mechanical properties compared to traditional steels. Their unique combination of high strength, good formability and hardening behavior allows for the production of automotive components that are thinner yet more durable than before. DP steels also exhibit exceptional energy absorption capacity, making them ideal for use in crash zones of vehicles. The microstructure of DP steels is made of a soft ferrite matrix that ensures good formability and by hard martensite particles that provide strength [86].

The strength level of DP steels can be tailored by adjusting the ratio of martensite to ferrite and grain refinement. This results in a yield point ranging from 400 to 1000 MPa and a tensile strength of 600 to 1200 MPa. These steels are made from low-carbon steel with conversion retarders, such as manganese, chromium, and molybdenum. They are characterized by high tensile strength and low yield point, which gives rise to a low yield strength ratio and high hardening. Moreover, DP steels exhibit a high degree of uniformity and elongation at fracture. However, the transition zones between ferrite and martensite can have a disadvantageous effect, as there is strongly localized elongation in the deformation state in these areas [87].

In this study two grades of dual-phase (DP) steel sheets, DP500 and DP780, with an initial thickness of 0.8 mm are used.

The DP500 is a specific grade of dual-phase steel, which has a minimum ultimate tensile strength of 500 MPa. It is designed to provide a balance of high strength and good formability, making it suitable for various structural and automotive applications that require both strength and impact resistance. Commonly, DP500 is employed in automotive structural components such as body reinforcements, chassis parts, and crash structures. Its high strength allows for weight reduction while simultaneously ensuring structural integrity and crashworthiness.

The DP780 steel is another type of advanced high-strength steel that offers excellent mechanical properties and is commonly used in various industries. Similar to other dual-phase steels, DP780 consists of two distinct phases: a soft ferrite phase and a hard martensite phase and typically has a minimum ultimate tensile strength of 780 MPa. The common applications include automotive components such as body reinforcements, structural parts, and safety-related components. Its high strength allows for lightweight construction while maintaining structural integrity and crash performance.

Comparing both dual-phase steels in terms of formability, DP500 is known for its good formability and ductility, allowing it to be easily formed into complex shapes. On

the other hand, DP780 tends to have slightly lower formability compared to DP500 due to its higher level of martensite particles. Although, both grades offer a good balance between strength and formability for many applications, the attributes of DP steels do not exclusively exhibit only positive qualities. Despite considerable accomplishments, a prominent technological challenge in design and production of sheet metal components, which require precise shape and dimensional accuracy, is the increased springback that occurs during the forming stages, in addition to the significant changes in formability with increasing strength. This phenomenon is more noticeable in higher strength grades, like DP780, DP980 and DP1180 [88].

3.2 Mechanical Characterization

The following section describes the experimental test methodologies used to obtain the mechanical properties of the different metallic materials, in order to identify the constitutive models parameters that will be used in numerical simulations.

3.2.1 Stress-strain flow curves

3.2.1.1 Uniaxial tensile test

A uniaxial tensile test is a standard mechanical test used to determine the mechanical properties of a material under tension. It involves applying a uniaxial (single-axis) tensile force to a specimen. The load is gradually increased until the sample reaches its maximum load-carrying capacity, the ultimate tensile strength (UTS). At this point, the sample fractures, and the test is complete. By analyzing the load-elongation data obtained during the test, various mechanical properties of the material can be determined which include the modulus of elasticity (E), Poisson's ratio (ν), yield stress (Re or $Rp_{0.2}$), ultimate tensile strength (Rm), elongation after rupture (A), and anisotropy coefficients (important for metal sheets due to the manufacturing process). These properties are crucial in understanding the behavior and performance of materials in various applications.

The AA were tested on a 100 kN eletromecanic testing machine (Instron 5900R) at room temperature using a constant crosshead speed, resulting in an initial strain rate of about $16e^{-3}$ s^{-1} until the material fracture. An extensometer with an initial length of 50 mm was utilized to acquire elongation in the uniform section of the specimen and measure corresponding strains.

To ensure result repeatability, multiple tests were conducted for each material and loading direction, totaling 60 tests. To ensure a clear analysis of the stress-strain flow

curves obtained from the uniaxial tensile tests, only one result for each loading direction is presented.

Table 3.2 and table 3.3 contain the experimental conditions for the tensile tests conducted on the chosen materials, following the standard ASTM E8 [89] procedure. The specimens were tested in five distinct loading conditions, which corresponded to different angles relative to the rolling direction (0^o, 22.5^o , 45^o , 67.5^o and 90^o). To obtain the required geometry for the specimens, a rectangular strip was machined to the established geometry.

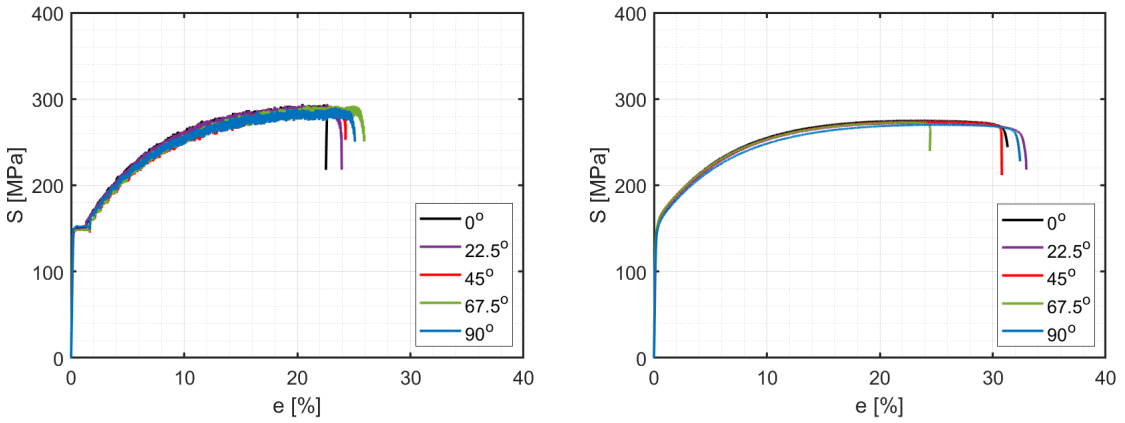
Table 3.2: Experimental conditions of uniaxial tensile test for the aluminum alloys.

Loading directions	5
Number of experiments for each direction	3
Crosshead speed	5 mm/min
Data acquisition	20 Hz
Clip gage initial length - l_0	50 mm
Temperature	22^oC
Relative humidity	53 %

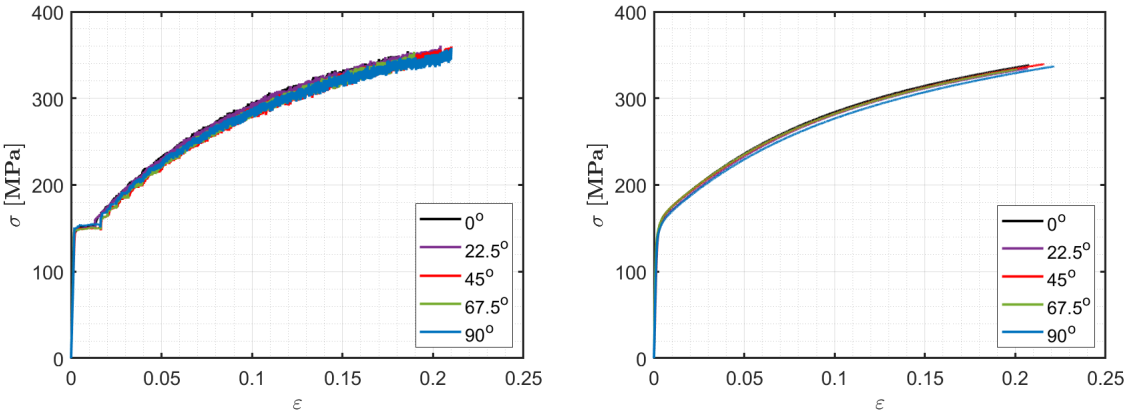
Table 3.3: Experimental conditions of uniaxial tensile test for dual-phase steels.

Loading directions	5
Number of experiments for each direction	3
Crosshead speed (grip)	5 mm/min
Data acquisition	20 Hz
Clip gage initial length - l_0	50 mm
Temperature	23^oC
Relative humidity	56 %

The obtained stress-strain curves from the uniaxial tensile test of the aluminum alloys are present in figure 3.1. As can be seen, the obtained results show that AA5182 a exhibits yield strength but also a strong Portevin-Le Chatelier (PLC) effect which is expected for 5xxx series aluminum alloys.



(a) Engineering stress-strain curves

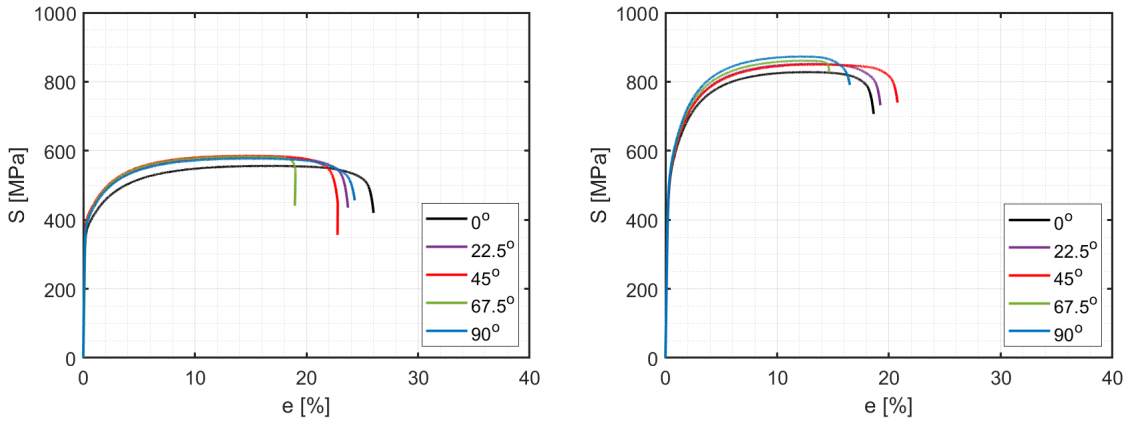


(b) True stress-strain curves

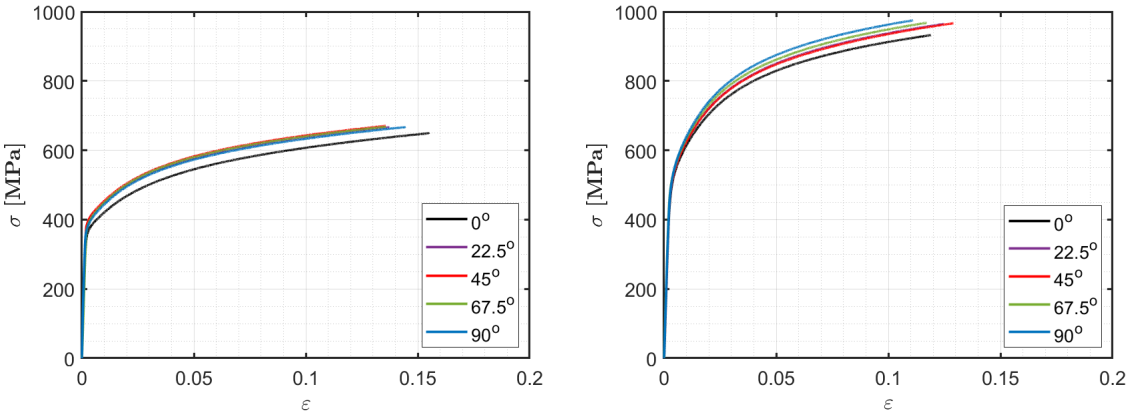
Figure 3.1: Flow curves of aluminum alloys AA5182 (left) and AA6016 (right).

This phenomenon is observed in certain metallic materials during plastic deformation. It is characterized by the occurrence of serrated behavior in the stress-strain curve, particularly in the form of stress drops. These serrations are attributed to dynamic strain aging, which is influenced by various factors, such as temperature, strain rate, and solute concentration in the material and can have significant implications on the mechanical properties and behavior of the material. Additionally, both aluminum alloys show a similar uniform elongation value, however AA6016 has a higher ductility than AA5182. Regarding the hardening behavior, as expected, it is seen an increase in strength for an initial deformation stage followed by a saturation behavior.

Figure 3.2 shows the obtained stress-strain curves of the two AHSS grades.



(a) Engineering stress-strain curves



(b) True stress-strain curves

Figure 3.2: Flow curves for aluminum alloys DP500 (left) and DP780 (right).

Regarding mechanical properties, the dual-phase steels presents a higher strength than aluminum alloys, but on the other hand, the ductility of steels is lower, as shown in figure 3.2. Also, as expected the material DP780 exhibits a higher strength than DP500, which is in accordance to supplier datasheet. Although the selected dual-phase steels have different ultimate tensile strength values, the flow stress curves show a relatively high slope at lower strains, meaning that this AHSS exhibit a higher initial work hardening.

Table 3.4 contains a summary of the identified mechanical properties of the selected metallic materials under study.

Table 3.4: Uniaxial tensile test material properties.

Material	Angle [^{o}]	$Rp_{0.2}$ [MPa]	Rm [MPa]	e_u [%]	A80 [%]
AA5182-0	0	149.0	293.6	20.7	23.1
	22.5	148.8	292.9	22.0	23.9
	45	150.6	290.1	22.7	25.2
	67.5	148.6	288.8	22.3	25.0
	90	151.3	289.7	22.5	23.9
AA6016-T4	0	155.4	274.2	23.1	28.6
	22.5	155.1	273.2	23.2	26.9
	45	152.9	270.7	24.8	28.7
	67.5	151.3	268.5	24.8	28.7
	90	154	270.5	22.6	25.4
DP500	0	379.7	558.7	16.4	22.3
	22.5	403.8	580.6	15.0	21.0
	45	408.5	585.9	14.8	20.1
	67.5	401.3	583.9	15.0	21.3
	90	390.6	577.8	15.3	21.8
DP780	0	521.2	818.2	13.1	16.9
	22.5	540.8	852.1	12.9	16.2
	45	537.6	847.5	13.8	18.0
	67.5	543.7	861.3	12.2	15.1
	90	550.0	872.3	11.7	14.3

3.2.1.2 Hydraulic bulge test

To fully characterize the material's behavior at higher strain values, it is essential to address the plastic instability observed during uniaxial tensile tests, as it often leads to lower limits in true strain values. Performing biaxial hydraulic bulge tests can be an alternative solution to better understand the material behavior and improve its mechanical hardening characterization. This type of loading provides more experimental information compared to the uniaxial tensile test, with higher values of plastic deformation.

The biaxial hydraulic bulge test induces a biaxial stress state in the material by sealing and restricting a circular sheet around its perimeter and injecting oil under pressure into the central underside zone. This test configuration allows for the characterization of the biaxial stress-strain curve of the material and provides valuable information on the material's ability to withstand biaxial deformation, its formability limits, and the occurrence of other failure modes.

Figure 3.3 presents a scheme of the hydraulic bulge test principles. The experimental setup includes a circular die and a circular blank holder that restrains the specimen at its

outer edge during the test. A drawbead is used to restrain the specimen in its perimeter and also to prevent any oil leakage. The experimental tools dimensions are present in table 3.5.

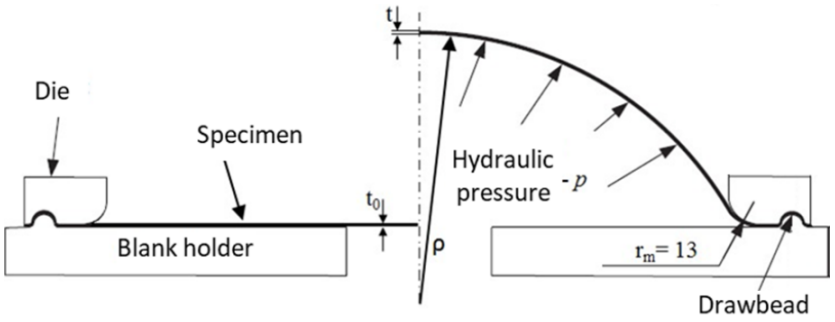


Figure 3.3: Hydraulic bulge test scheme and its key variables (dimensions in mm) - adapted from [90].

Table 3.5: Tools dimensions of the hydraulic bulge test.

Parameter	Value [mm]
Die diameter - ϕ_{die}	150
Die radius - r_m	13
Drawbead diameter - $\phi_{drawbead}$	190 Hz
Specimen diameter	250 mm

A measurement system is used to collect essential data during the deformation process for material characterization. The membrane theory is employed to calculate the biaxial stress-strain curve from the experimental data. The biaxial bulge test is particularly suitable for characterizing thin materials, such as metal sheets with typical thicknesses below 2 mm. To ensure accurate results, it is recommended that the diameter ratio of the die to the sheet thickness be greater than 100 or higher than 50 [91, 92]. This ensures that bending effects are negligible, and the stresses along the thickness (σ_3) are assumed to be zero.

Furthermore, the biaxial hydraulic test has the benefit of eliminating contact and associated friction in the region of interest during characterization. This simplifies the analytic solution.

Expanding the previous assumptions, a relationship is established between the variables of hydraulic pressure (p), sheet thickness at a specific moment (t), radius of curvature (ρ), and biaxial stress (σ_b). Assuming equal stresses in the principal directions

($\sigma_1 = \sigma_2$) and equal radii of curvature ($\rho_1 = \rho_2$) in the axissymmetric scenario, the resulting equation can be formulated as follows:

$$\sigma_b = \frac{p \cdot \rho}{2 \cdot t} \tag{3.1}$$

In order to determine the radius of curvature (ρ) and thickness (t) of the specimen at the pole, various measurement techniques can be employed. One approach involves using a measurement system, as shown in the figure, or utilizing digital image correlation, as outlined in the ISO standard [93]. Alternatively, the radius of curvature can be computed using a basic geometric construction, which can be expressed as

$$\rho = \frac{\left(\frac{Dcv}{2}\right)^2 + h^2}{2 \cdot h} - \frac{t}{2} \tag{3.2}$$

where the distance between the displacement transducer and the support of the spherometer is denoted by h, and the spherometer establishes the diameter Dcv [94].

The variables are obtained from the outer surface of the sheet metal, but the membrane theory applies only to the neutral axis. Therefore, the thickness is divided in half at the calculated radius. To determine the sheet metal's thickness, equation 3.3 is utilized, which involves measuring the initial thickness (t_0) and calculating the thickness strain (ε_t). This leads to a reduction in the material's thickness (t), which can be determined using the following formula:

$$t = t_0 \cdot e^{\varepsilon_t} \tag{3.3}$$

The thickness reduction in the specimen is primarily concentrated in the center, and this region can be seen as a geometric constraint since fractures occur there. If it is assumed that the material is incompressible, meaning that the of all strains is zero and the material's volume remains constant during the test, it can determined the thickness strain (ε_t) or biaxial strain (ε_b) using the following expression, taking into account the strains in the sheet plane ($\varepsilon = \varepsilon_1 = \varepsilon_2$):

$$\varepsilon_b = \varepsilon_t = -2 \cdot \varepsilon \tag{3.4}$$

ε corresponds to the membrane strain.

To determine the membrane strain value, the expansion of a circle with an initial diameter of D_{st0} is measured. A strain gauge is incorporated into the measurement system to track the plastic deformation of the sheet metal throughout the experimental test. By observing the increase in the circle's diameter to D_{st}, the membrane strain can be computed.

$$\varepsilon = ln\left(\frac{D_{st}}{D_{st_0}}\right) \tag{3.5}$$

3.2.1.3 Equi-biaxial stress-strain curve

The biaxial stress-strain curve is obtained from equations 3.1 and 3.4. The experimental characterization tests were conducted under controlled ambient temperature and with a constant pressure increment. Table 3.6 provides details of experiments test conditions.

Table 3.6: Experimental conditions used on the hydraulic bulge test for the AA and AHSS.

Parameter	Value
Specimen diameter	250 mm
Hydraulic pressure increment	1 bar/s
Room temperature	23^oC
Relative humidity	56 %

Figure 3.4 contains the hydraulic pressure evolution with specimen pole height, as well as, the corresponding biaxial stress-strain curves for the different materials.

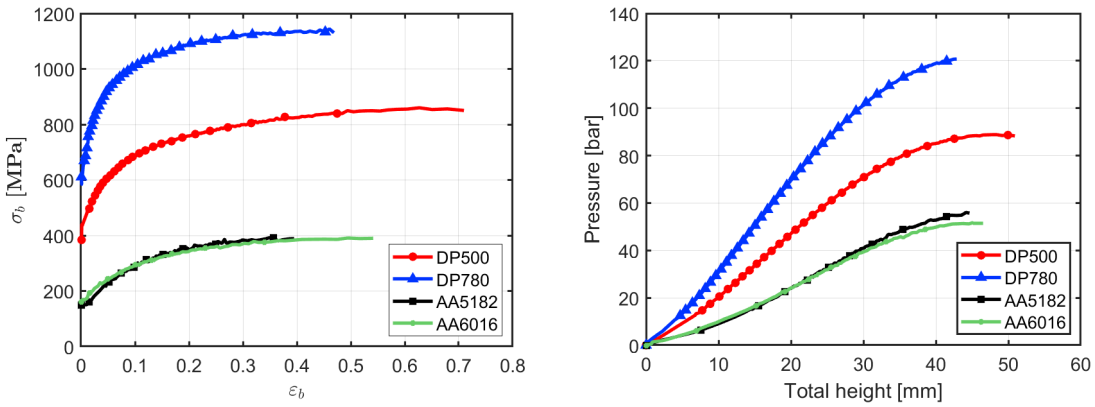


Figure 3.4: Biaxial stress-strain curve (left) and hydraulic pressure-height profiles (right) obtained for the materials in study.

As can be observed in figure 3.4, all the materials reached higher levels of biaixial strain higher than those measured in uniaxial tests. Table 3.7 lists the variables obtained from the experimental tests conducted on each material. The amount of information regarding the material behavior, when compared to the tensile test, increased about 90% and 135% for AA5182 and AA6016, respectively. However, the most notable improvement was observed in the case of DP steels, where the information gained exhibited a remarkable increase of over 400% for DP500 and 280% for DP780.

Additionally, it can be highlighted the fact that DP500 is the material that has the highest strain capacity, something that did not occur in the uniaxial tensile test. Another notable aspect is the higher biaxial ductility presented by DP780 in comparison to AA5182. Overall, these results emphasize the importance of biaxial bulge test for achieving a more precise and accurate characterization of the mechanical behavior of metallic materials, specially the hardening behaviour. Table 3.7 present a summary of the material properties obtain from biaxial hydraulic bulge test.

Table 3.7: Aluminium alloys and dual-phase steels properties obtained form hydraulic bulge test.

Material	Burst pressure [bar]	Total height [mm]	Biaxial stress [MPa]
AA5182-0	55.7	44.6	145.2
AA6016-T4	51.5	46.5	143.8
DP500	88.4	52.7	414.8
DP780	120.8	42.9	585.1

The biaxial hydraulic bulge test offers the advantage of gathering information and data on material behavior at higher levels of plastic deformation compared to the tensile test. This advantage allows for the extension of the material's hardening curve using the biaxial curve [95]. However, the stress-strain curves obtained from these two tests cannot be directly compared or combined due to the different stress states involved in each test.

Consequently, it becomes necessary to transform the biaxial bulge curve into an equivalent curve based on the equivalent plastic work per unit volume (W). This approach has been successfully employed by various researchers [96, 97] with satisfactory results.

The methodology that provides the most favorable outcome is based on the equivalent plastic work corresponding to the maximum stress and strain attained in the tensile test. Based on this assumption the transformation factor can be calculated for using the following equation:

$$\frac{\sigma_{Mx}}{\sigma_b} = \frac{\varepsilon_b}{\varepsilon_{Mx}} = k \tag{3.6}$$

where k is a constant.

The corresponding identified k values are presented in table 3.8 and figure 3.5 shows the obtained stress-strain curves based on the combination of tensile and bulge test hardening data.

Table 3.8: Parameter k value for the transformation of biaxial data.

Material	AA5182-O	AA6016-T4	DP500	DP780
k	0.898	0.983	0.955	0.874

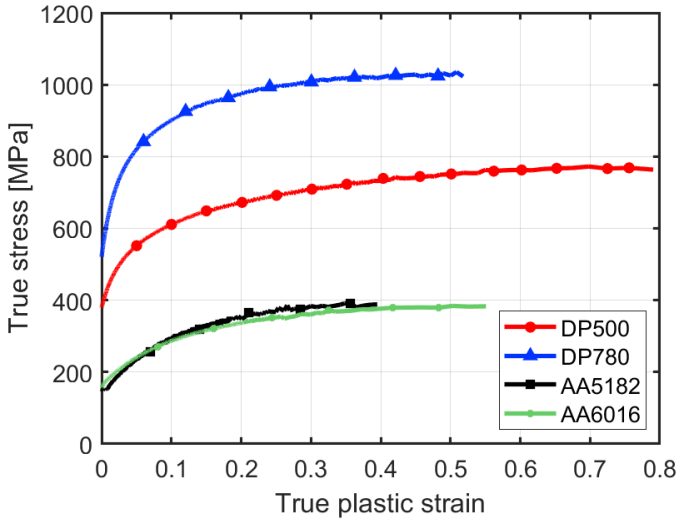


Figure 3.5: Equivalent stress-strain curves for the studied materials by combining the converted biaxial bulge data with results tensile tests.

This transformation facilitates the integration of the converted bulge data into the equivalent stress-strain curve, thereby enabling a more accurate determination of the constitutive law parameters aiming to reproduce the mechanical hardening behavior. By applying this methodology, it is evident that there is a smooth continuation of the hardening curve extension based on the bulge test for the dual-phase steels.

3.3 Anisotropic plastic strain ratios

3.3.1 Anisotropic r-values

Typically, sheet metal materials exhibit mechanical properties that depend on the loading direction, indicating the presence of anisotropy due to the manufacturing rolling process. The anisotropy of plastic strain in a sheet metal can be assessed under plane stress conditions by conducting uniaxial tensile tests on specimens taken at different angles relative to the rolling direction within the sheet plane [98].

The anisotropic behavior is commonly characterized using the r-value, which represents the ratio between the true plastic strain in the width (ε_{22}^p) and the strain in the thickness ε_{33}^p. Using the principle of volume constancy, this relationship is expressed as follows:

$$r = \frac{\frac{w}{w_0}}{\frac{l}{l_0}} = \frac{\varepsilon_{22}^p}{\varepsilon_{33}^p} = -\frac{\varepsilon_{22}^p}{\varepsilon_{11}^p + \varepsilon_{22}^p} \tag{3.7}$$

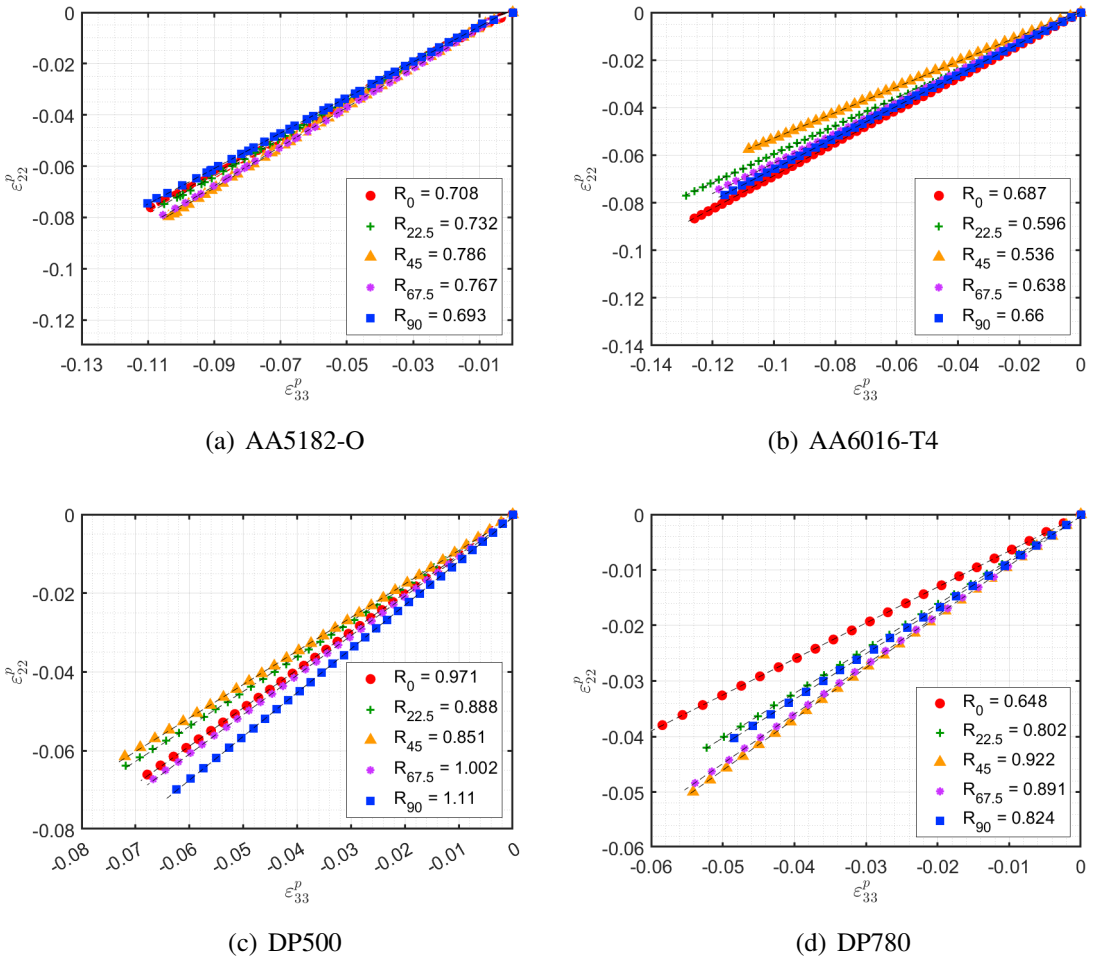
where w_0 and t_0 represent the initial width and thickness of the specimen, w and t represent the width and thickness at the specified moment, and finally ε_{11}^p represents the true plastic strain in the axial direction of the specimen.

In this study, the evaluation of true plastic strains and corresponding r-values are measured by using the digital image correlation (DIC) technique following a standard procedure. DIC enables the measurement of the deformation field evolution within a specified area on the specimen, thereby improving accuracy and providing more comprehensive information on material anisotropic behavior.

To perform the analysis, the specimens need to be prepared for DIC analysis. This involves painting the specimen surface in white and creating a random black speckle pattern. The speckle pattern enables the DIC cameras to detect the black dots and accurately capture their relative displacements. The experiments were conducted using an Instron 5900R universal testing machine with a load cell of 100 kN. The initial strain rate was set at $1.6e^3\ s^{-1}$. Strain measurements were obtained by capturing images at a frequency of 20 Hz using a 5MP camera (Basler acA2440-75um) paired with a high-resolution lens (Fujinon HF50HB-1B, f2.3/50 mm). The commercial software VIC-2D.v6 was utilized to calculate the strain field, specifically logarithmic strains, with a step size of 7 and a set size of 25 within a defined region of interest. Tables 3.9 provide a comprehensive list of the primary experimental conditions applied to determine the anisotropic r-values for the different materials.

Table 3.9: Experimental conditions used to measure anisotropic properties of AA and AHSS.

Loading directions	5
Number of experiments for each direction	3
Crosshead speed (grip)	5 mm/min
Data acquisition	20 Hz
Temperature	20^oC
Relative humidity	54 %



(a) AA5182-O

(b) AA6016-T4

(c) DP500

(d) DP780

Figure 3.6: Evolution of plastic strain transverse and thickness strain for five directions relative to the rolling direction.

Figure 3.6 presents the experimental correlation between thickness strain and transverse strain for each material and loading direction during the tensile test. The data points are fitted using linear regression, and the slope of the line fitting provides the anisotropic

r-value. Table 3.10 presents the measured r-values obtained from the linear fitting in Figure 3.6, along with the corresponding normal anisotropy $\bar{r}$ and planar anisotropy Δr.

Table 3.10: Identified anisotropic properties for the selected materials

Material	r_0	$r_{22.5}$	r_{45}	$r_{67.5}$	r_{90}	$\bar{r}$	Δr
AA5182-O	0.708	0.732	0.786	0.767	0.693	0.743	-0.086
AA6016-T4	0.678	0.596	0.536	0.638	0.66	0.605	0.138
DP500	0.971	0.888	0.851	1.002	1.110	0.946	0.190
DP780	0.648	0.802	0.922	0.891	0.824	0.829	-0.186

3.3.2 Biaxial plastic anisotropy

The biaxial plastic anisotropy coefficient, also referred as r_b, is a measurable material property that can be determined through the stacked disc compression test [38].

$$r_b = \frac{\varepsilon_{22}^p}{\varepsilon_{11}^p} \tag{3.8}$$

This test involves a through-thickness loading and is equivalent to an equibiaxial stress state in terms of work hardening [40]. In this study to obtain the biaxial anisotropy coefficient of the materials, stacked disk compression tests were conducted. These discs were carefully punched to ensure consistent cross-sectional area and concentricity where discs of 10 mm for steels and 11 mm for aluminum alloys were obtained.

The test involved compressing the stacked discs between two polished parallel platens. To ensure smooth contact and minimize friction, all contact interfaces between the disc surfaces and between the upper and lower tools were lubricated with graphite grease. Attention was given to the assembly process to maintain accuracy and reliability in the test setup.

This setup ensures axial compression loading and promotes homogeneous deformation of the specimens under almost frictionless conditions. Figure 3.7 presents the experimental setup used in stacked disc compression tests.

Figure 3.8 displays a stacked specimen assembly composed by five discs. This choice is made to maintain the structural integrity of the specimen. Using a larger number of discs can introduce instability concerns by promoting sliding between the discs. By limiting the stack to five discs, the test setup remains stable and reliable.



Figure 3.7: Experimental setup used for stacked compression test.



Figure 3.8: Experimental assembly with location of specimens for testing.

The respective in-plane strain components (ε_{11}^p and ε_{22}^p) were obtained by measuring the diameters of each disc before and after deformation. In addition, the through-thickness strain (ε_{33}^p) was determined by taking into account the initial and final thickness. All the true plastic strain components were then computed using the following:

$$\begin{cases} \varepsilon_{11}^p = ln\dfrac{d_{RD}}{d_{RD_0}} \\ \varepsilon_{22}^p = ln\dfrac{d_{TD}}{d_{TD_0}} \\ \varepsilon_{33}^p = ln\dfrac{t}{t_0} \end{cases} . \tag{3.9}$$

where, d_{RD} and d_{TD} are the correspondent diameters associated with rolling and transverse direction of the sheet material, respectively.

To optimize the determination of the material's biaxial r_b coefficient, the specimens were subjected to different levels of plastic strain. However, directly measuring the strains proved to be extremely difficult. Therefore, to induce varying degrees of plastic deformation, different maximum load values were used during the experimental tests, which were conducted under load control. Biaxial compression loading was applied using an INSTRON 5900R test machine equipped with a 100 kN load cell.

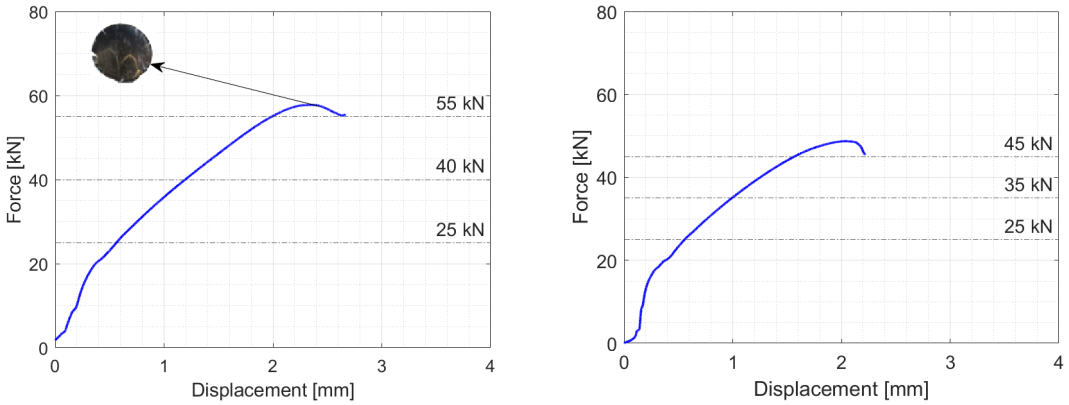
To ensure that the displacement was sufficient to reach the plastic regime, the force range was defined for each material. Table 3.11 outlines the test conditions for aluminum alloys and steels.

Table 3.11: Experimental conditions used on the stacked compression tests.

Parameter	Value
Initial disc diameter	11 mm for AA 10 mm for DP
Number of stacked discs	5
Cross-head speed	1 mm/min
Applied Force	AA5182-O: 25, 40, 55 kN AA6016-T4: 25, 35, 45 kN DP500: 70, 85, 90 kN DP780: 80, 85, 90 kN

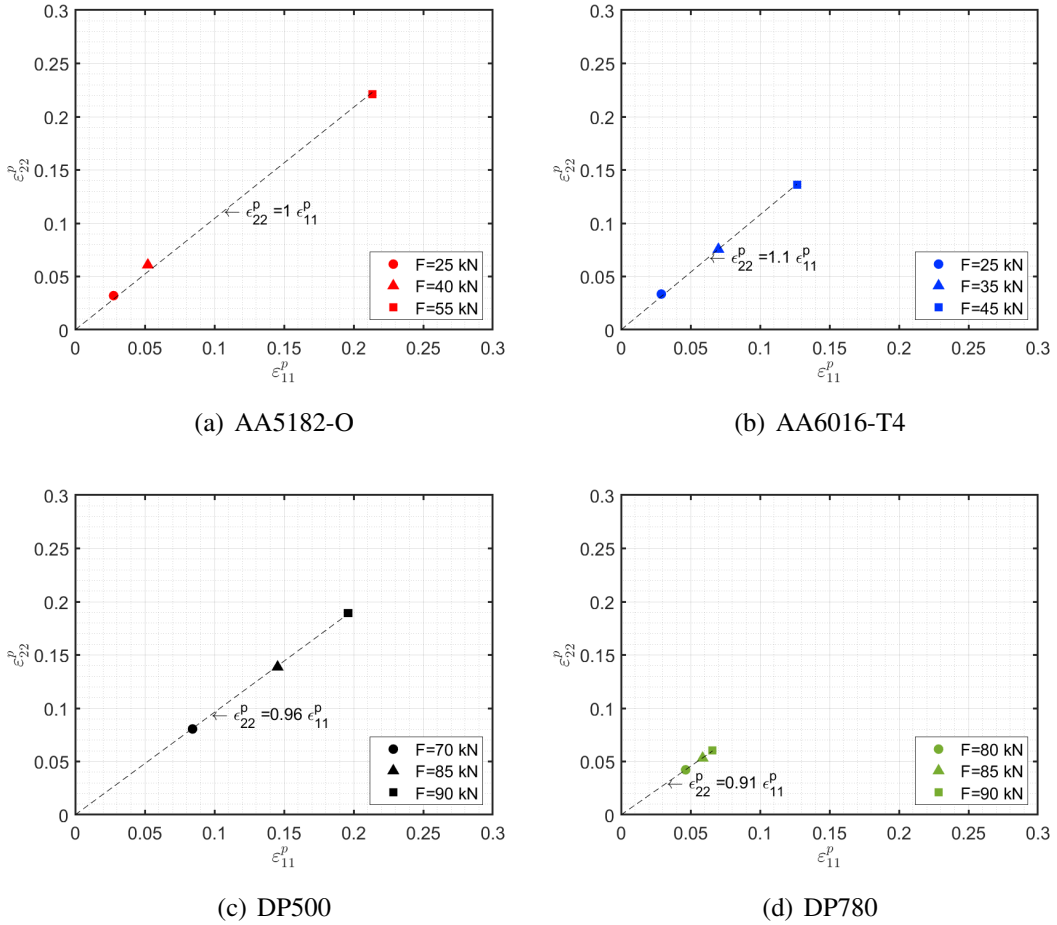
Preliminary compression tests were carried out to analyze and define the load range that should be used to perform the experiments, in order to ensure that the material was in the plastic regime and that the loss of material integrity (fracture) was not reached.

Figure 3.9 shows the corresponding force *vs* displacement evolution curve for the aluminum alloys. The force levels of the dual-phase steels were not determined, since the failure of the specimen could not be reached when the maximum load cell capacity was applied. Figure 3.10 presents the strains measured in the middle specimen for the three load levels applied to the materials in study.



(a) AA5182-O (b) AA6016-T4

Figure 3.9: Force vs. displacement curve used to defined the applied load range for 5 stacked circular disks, 11 mm diameter.



(a) AA5182-O (b) AA6016-T4

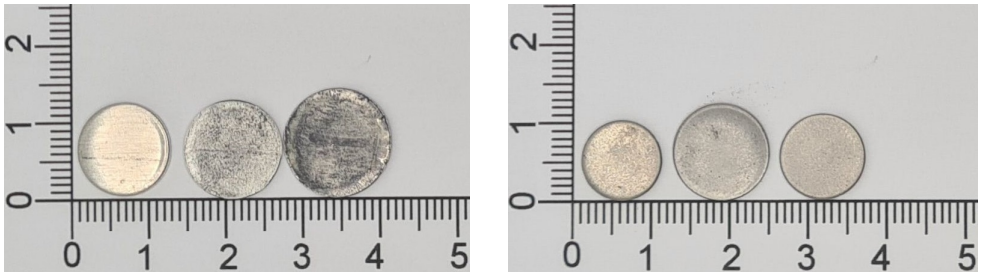
(c) DP500 (d) DP780

Figure 3.10: Relationship between longitudinal and transverse strain by axial compression tests on five stacked circular disks for the aluminum and steel specimens in the study.

According to figure 3.10, a linear fit was applied to reproduce the experimental data for transverse strains (ε_{22}^{p}) plotted against longitudinal strains (ε_{11}^{p}) for all load cases. The slope of the linear fit was defined as the value of r_b. Results indicated that the aluminum alloy AA6016 tend to increase more in transverse direction than the rolling direction since the r_b value is higher than 1.

On the other hand, the dual-phase steels exhibit an opposite behavior, the circular specimen tend to an ellipse shape where the major dimension is aligned with the rolling direction. In case of AA5182, the results show isotropic tendency.

Figure 3.11 presents the disk compression specimen after the application of the maximum load level.



(a) Aluminum alloys: AA5182 (middle), AA6016(right)

(b) Dual-phase steels: DP500 (middle), DP780 (right)

Figure 3.11: Comparison of disk compression specimens (before and after) the forming test.

3.4 Material modeling

The field of materials modeling is as extensive as the range of materials available. Predicting the behavior of metallic materials under given loads during the forming process operations has been the primary focus of numerical approaches in the literature. These existing approaches are comprehensive and generally produce accurate results for classical materials under reasonably complex strain paths. However, the pursuit of technological advancements and understanding of complex materials and processes has created new

challenges, prompting scientists to explore novel mathematical and computational tools [99, 100].

The primary objectives of materials research include modeling various phenomena, predicting material behavior under different conditions, and developing cost-effective materials with improved or desired properties. While significant progress has been made in understanding physical phenomena in materials over the past few decades, empirical models have often been relied upon for predicting process behaviors.

In order to accurately replicate experimental results using advanced constitutive models, it is often necessary to utilize complex finite element models that incorporate advanced structural elements, intricate loading conditions, contact and friction, as well as both static and dynamic analyses. This section gives the description of the experimental identification methodologies employed for the constitutive modeling of two different aluminum alloys and two grades of dual-phase steel.

3.4.1 Hardening

Describing a material's behavior using constitutive models relies on correctly identifying the associated parameters. To anticipate how a material will harden at plastic strain values higher than those observed in experimental stress-strain curve, hardening laws are employed. These laws respond to changes in the yield surface, which is defined by the equivalent stress and influenced by the material's internal variable evolution.

In this research, data from the hydraulic bulge test is used, leading to a more accurate description of the hardening curve and reducing extrapolation errors. The resulting flow curve, obtained by combining data from the uniaxial tensile test with the bulge test, will serve as the reference for identifying hardening law parameters.

To identify parameters for a constitutive model, the optimization method implemented in the MATLAB® tool is employed. This involves adjusting the numerical prediction results to the experimental data using optimization methods, where the primary aim is to minimize an objective function. The function determines the minimum mean square error (*MSE*) between the experimental stress-strain curve, and the predicted data from the hardening law. This is achieved by modifying the constitutive parameters.

Tables 3.12 through 3.15 display the correspondent identified parameters for each material. It is important to highlight that a limited number of hardening laws were taken into account, with some of them selected based on their extensive usage.

Table 3.12: Hardening laws parameters of AA5182 using uniaxial and biaxial stress-strain data.

Hardening law	Parameters				$\sigma_{Y(\bar{\varepsilon}^p=0)}$ [MPa]
Hollomon	K=557.52		n=0.2805		—
Swift	K=579.40	ε_0=0.0131	n=0.3153		147.63
Voce	A=147.66	B=246.74	C=8.895		147.66
Swift-Voce	α=0.2693	K=-18.35	ε_0=0	n=0.3324	147.33
		A=201.63	B=340.29	C=9.057	

Table 3.13: Hardening laws parameters of AA6016 using uniaxial and biaxial stress-strain data.

Hardening law	Parameters				$\sigma_{Y(\bar{\varepsilon}^p=0)}$ [MPa]
Hollomon	K=485.03		n=0.2276		—
Swift	K=495.58	ε_0=0.0093	n=0.2475		155.71
Voce	A=159.30	B=210.48	C=9.287		159.3
Swift-Voce	α=0.4294	K=428.14	ε_0=0.0092	n=0.1811	157.57
		A=138.32	B=251.34	C=8.935	

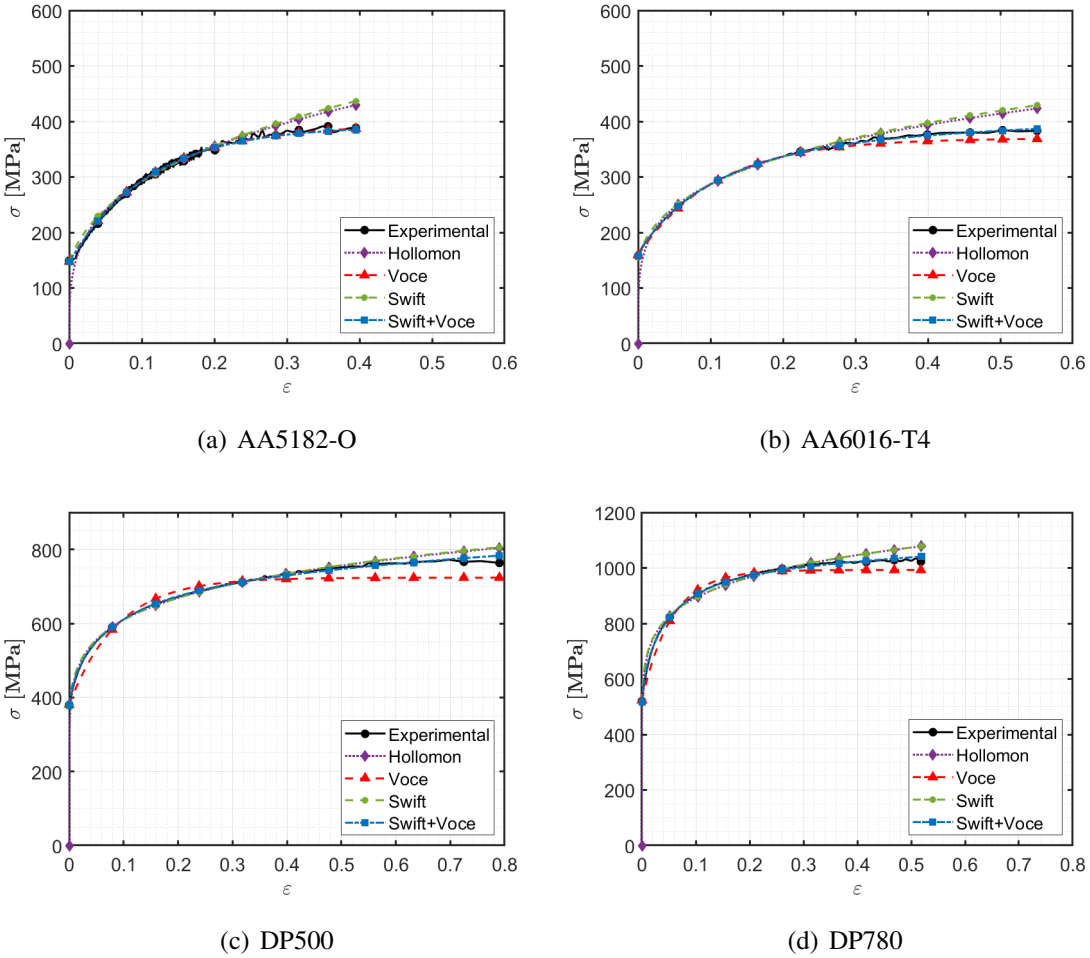
Table 3.14: Hardening laws parameters of DP500 using uniaxial and biaxial stress-strain data.

Hardening law	Parameters				$\sigma_{Y(\bar{\varepsilon}^p=0)}$ [MPa]
Hollomon	K=826.60		n=0.1336		—
Swift	K=832	ε_0=0.0032	n=0.1370		378.6
Voce	A=380.8	B=343.03	C=11.303		380.8
Swift-Voce	α=0.4502	K=1297.14	ε_0=0.003	n=0.1455	379
		A=232.87	B=165.13	C=12.065	

Table 3.15: Hardening laws parameters of DP780 using uniaxial and biaxial stress-strain data.

Hardening law	Parameters				$\sigma_{Y(\bar{\varepsilon}^p=0)}$ [MPa]
Hollomon	K=1162.69		n=0.1150		—
Swift	K=1162.65	ε_0=0.0009	n=0.1151		516.84
Voce	A=523.26	B=469.49	C=18.107		523.26
Swift-Voce	α=0.5280	K=2837.35	ε_0=0.0018	n=0.0479	517.41
		A=-1248.73	B=377.73	C=18.094	

The figure 3.12 illustrates that the hardening behavior of materials in study. For all the materials, all the laws are capable of describing the material behavior under strain levels of 0.3, after this point there is a variation on the results where the Swift-Voce combination hardening law shows a better fit for the combination of biaxial and uniaxial data.



(a) AA5182-O

(b) AA6016-T4

(c) DP500

(d) DP780

Figure 3.12: Comparison between the equivalent stress-strain curves generated by combining the converted biaxial data with uniaxial tensile test and hardening laws for the different materials.

3.4.2 Yield criteria

In order to closely replicate the mechanical behavior of the material, three different yield criteria were chosen: Hill'48, Yld91 and Yld2004-18p. Additionally, a non-associated flow rule (NAFR) approach based on Hill'48 and Yld91 function were considered for both yield and potential surfaces. To identify the corresponding parameters for the Hill'48 criterion, expressions 2.26 and 2.25 were used for stresses, while equation 2.27 was employed for r-values. For the NAFR approach, the yield surface parameters were

determined based on stresses (Hill'48 s-based), while the plastic anisotropic coefficients were used to describe the potential surface (Hill'48 r-based). For the other yield criteria a Genetic Algorithm (GA) was implemented to minimize the objective function. During the identification stage, the following material properties were considered, table 3.16.

Table 3.16: Parameters used in yield criteria.

Parameters	H48-R	H48-S	H48-NAFR	Yld91	Yld91-NAFR
σ_0, $\sigma_{22.5}$, σ_{45} $\sigma_{67.5}$, σ_{90}	-	✓	✓	✓	✓
r_0, $r_{22.5}$, r_{45} $r_{67.5}$, r_{90}	✓	-	✓	✓	✓
σ_b	-	✓	✓	✓	✓
r_b	-	-	✓	✓	✓

Table 3.17: Summary of experimental data used for yield criteria parameters identification.

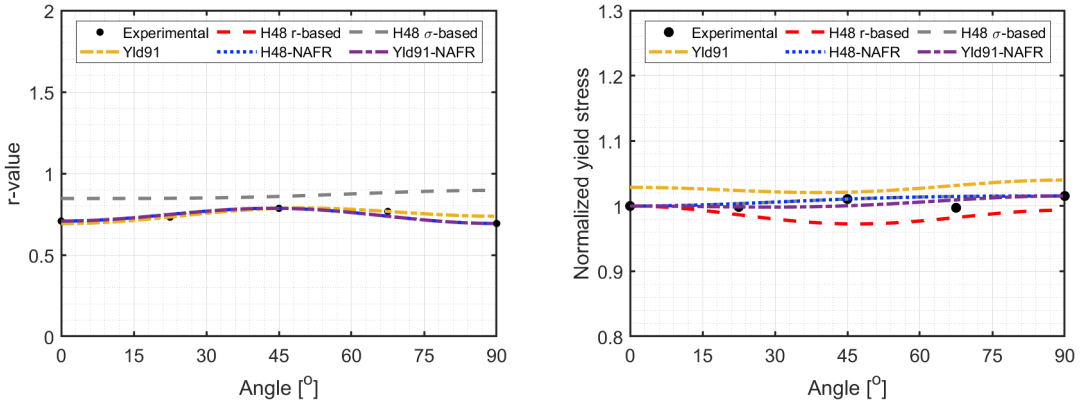
	AA5182-O	AA6016-T4	DP500	DP780
Yield stress				
σ_0	149.0	155.4	379.7	521.2
$\sigma_{22.5}$	148.8	155.1	403.8	540.8
σ_{45}	150.6	152.9	408.5	537.6
$\sigma_{67.5}$	148.6	151.3	401.3	543.7
σ_{90}	151.3	154	390.6	550
σ_b	145.2	143.8	414.8	585.1
Plastic anisotropic coefficient				
r_0	0.708	0.678	0.971	0.648
$r_{22.5}$	0.732	0.596	0.888	0.802
r_{45}	0.786	0.536	0.851	0.922
$r_{67.5}$	0.767	0.638	1.002	0.891
r_{90}	0.693	0.66	1.110	0.824
r_b	1	1.1	0.96	0.91

During the identification process for each criterion, certain assumptions were made. The parameters related to through-thickness material properties, which are difficult to determine in metallic sheets, were assumed to be equal to the isotropic condition value (L and M equal to 1.5 for Hill'48, and f and g equal to 1 for Yld91). The remaining four unknown parameters of Yld91 criterion were identified within a range 0 to 5, since parameter m is 8 for aluminum (face centered cubic - FCC) and 6 for steel (body centered

cubic - BCC). Tables 3.18 to 3.21 contain identified constitutive model parameters. Additionally, figures 3.13 to 3.16 contain the yield surface and the predicted normalized yield stresses and r-values evolutions for different angles relative to the rolling direction.

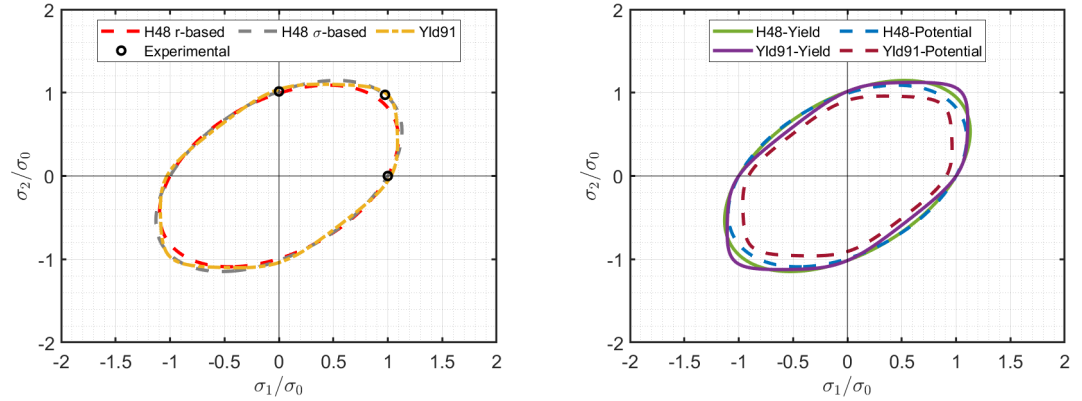
Table 3.18: Identified yield criteria parameters for AA5182.

Hill48	F	G	H	N				
r-based	0.598	0.585	0.415	1.522				
σ-based	0.511	0.542	0.458	1.431				
Yld91	a	b	c	h	a^p	b^p	c^p	h^p
AFR	1.003	1.024	0.919	0.977				
NAFR	0.994	1.013	1.005	1.005	1.037	1.043	0.934	0.993



(a) r-value evolution

(b) Stress evolution



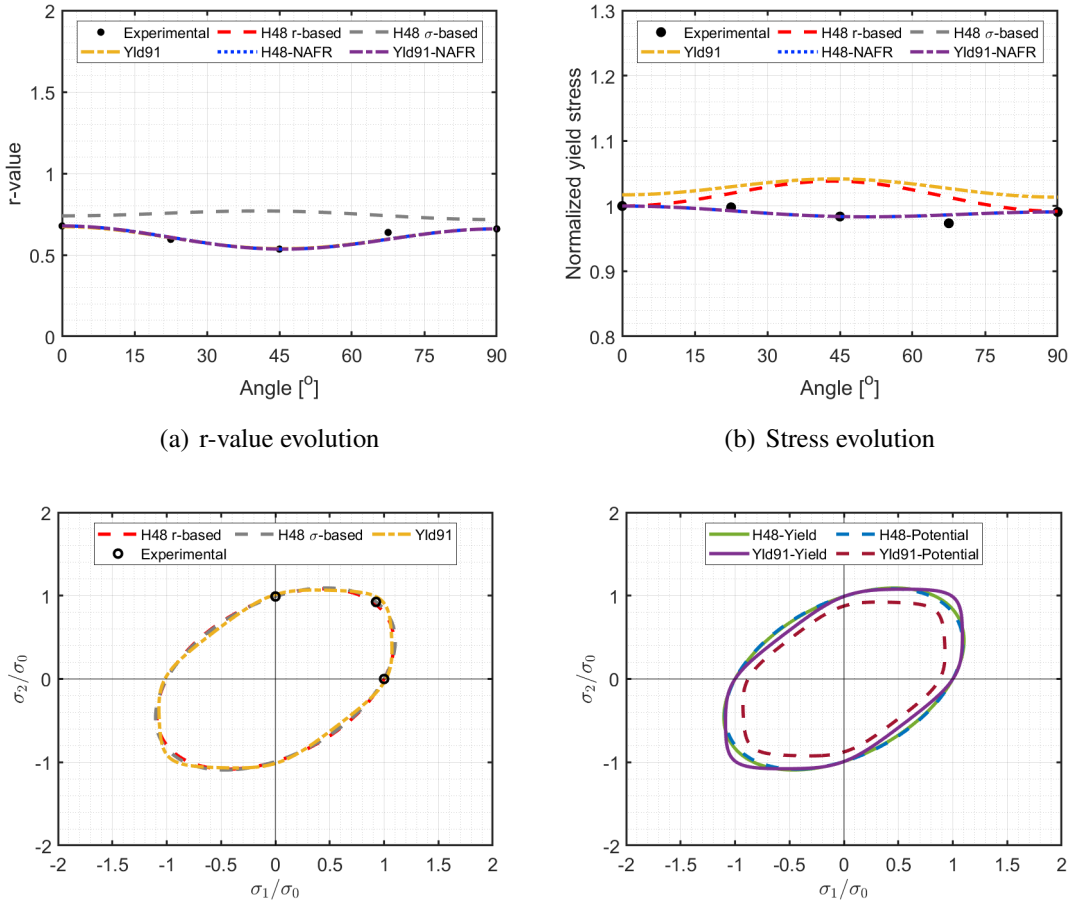
(c) Yield surface

(d) Yield potential

Figure 3.13: Predicted yield surfaces and evolution of yield stresses and r-values of Hill'48 and Yld91 models for AA5182.

Table 3.19: Identified yield criteria parameters for AA6016.

Hill48	F	G	H	N					
r-based	0.612	0.596	0.404	1.252					
σ-based	0.593	0.575	0.425	1.482					
Yld91	a	b	c	h	a^p	b^p	c^p	h^p	
AFR	1.045	1.038	0.926	0.929					
NAFR	1.015	0.980	0.991	1.010	1.063	1.059	0.946	0.946	
Yld2004 [101]	c_1	c_2	c_3	c_4	c_5	c_6	c_7	c_8	c_9
	1.062	0.859	0.619	-0.193	0.745	1.045	1.000	1.000	0.452
	c_{10}	c_{11}	c_{12}	c_{13}	c_{14}	c_{15}	c_{16}	c_{17}	c_{18}
	0.804	1.201	0.831	0.892	-0.059	-0.891	1.000	1.000	1.188



(a) r-value evolution

(b) Stress evolution

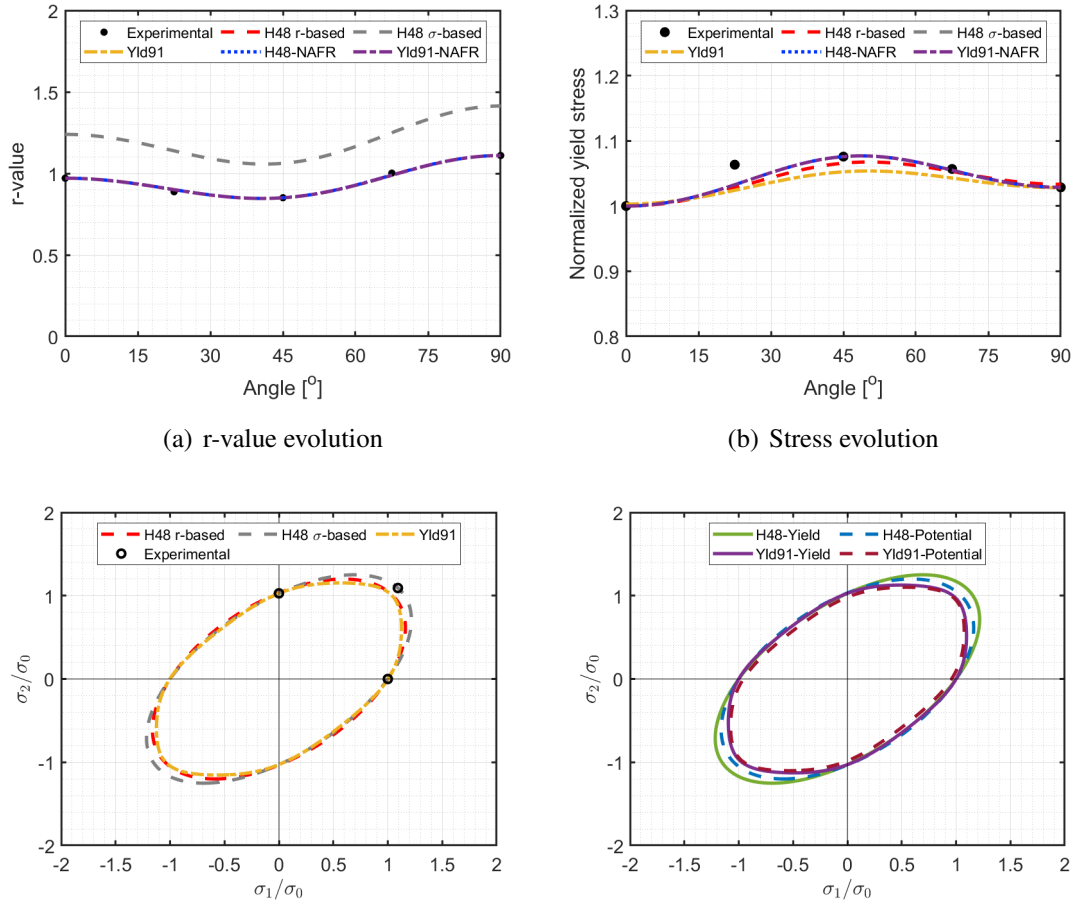
(c) Yield surface

(d) Yield potential

Figure 3.14: Predicted yield surfaces and evolution of yield stresses and r-values of Hill'48 and Yld91 models for AA6016.

Table 3.20: Identified yield criteria parameters for DP500.

Hill48	F	G	H	N				
r-based	0.5056	0.59	0.41	1.5721				
σ-based	0.4543	0.4878	0.5122	1.5215				
Yld91	a	b	c	h	a^p	b^p	c^p	h^p
AFR	1.009	1.062	0.936	1.019				
NAFR	0.990	1.021	1.032	0.935	0.984	1.026	1.016	0.974



(a) r-value evolution

(b) Stress evolution

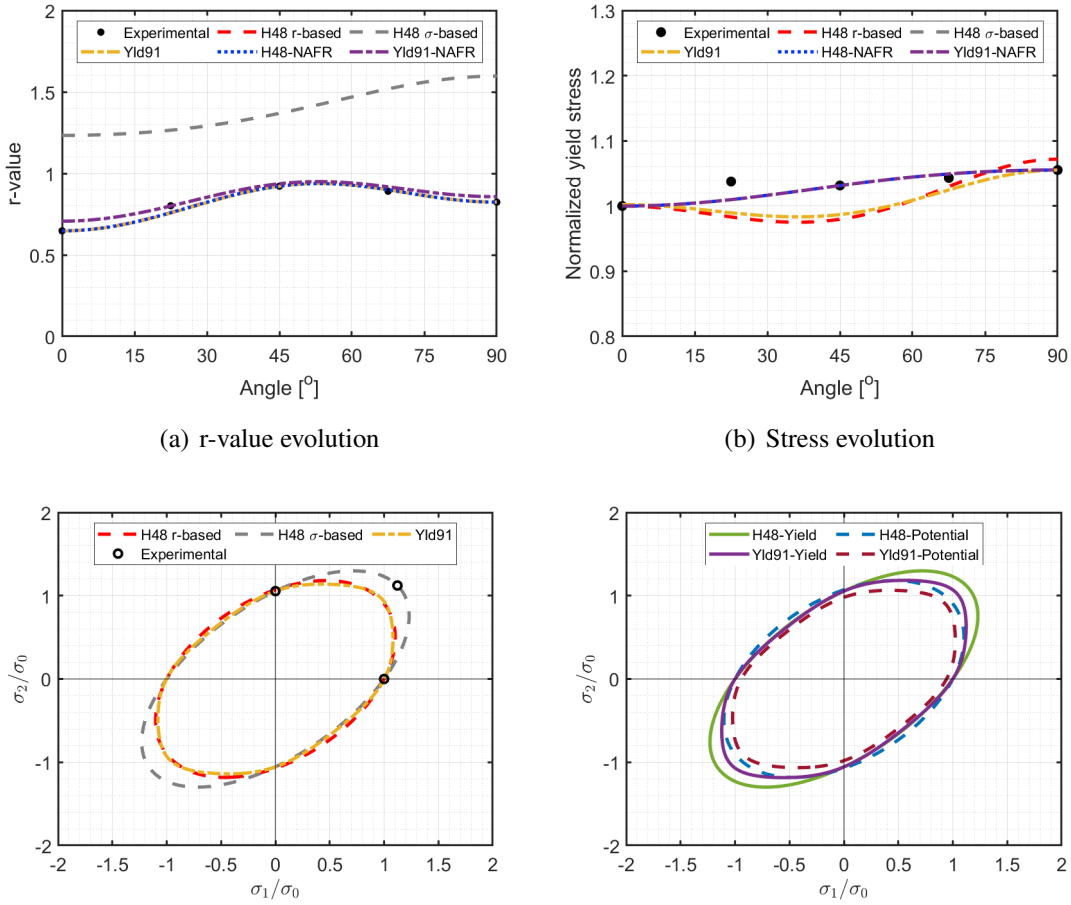
(c) Yield surface

(d) Yield potential

Figure 3.15: Predicted yield surfaces and evolution of yield stresses and r-values of Hill'48 and Yld91 models for DP500 stress.

Table 3.21: Identified yield criteria parameters for DP780.

Hill48	F	G	H	N					
r-based	0.4772	0.6068	0.3932	1.5414					
σ-based	0.3458	0.4477	0.5523	1.4831					
Yld91	a	b	c	h	a^p	b^p	c^p	h^p	
AFR	0.980	1.077	0.915	1.01					
NAFR	0.984	1.063	1.038	1.024	1.001	1.048	0.947	1.009	
Yld2004 [102]	c_1	c_2	c_3	c_4	c_5	c_6	c_7	c_8	c_9
	1.000	1.000	1.096	0.999	0.728	0.263	0.684	0.857	1.024
	c_{10}	c_{11}	c_{12}	c_{13}	c_{14}	c_{15}	c_{16}	c_{17}	c_{18}
	0.846	0.762	0.775	0.599	1.281	1.338	1.239	1.076	0.998



(a) r-value evolution

(b) Stress evolution

(c) Yield surface

(d) Yield potential

Figure 3.16: Predicted yield surfaces and evolution of yield stresses and r-values of Hill'48 and Yld91 models for DP780 stress.

The reproduction of the anisotropic plastic strain ratio coefficients for different angles relative to the rolling direction can be obtained for all selected criteria, with the exception of the Hill'48 criterion whose parameters are identified based on the yield stresses, for all materials. In the case of the normalized yield stress evolution, only the stress-based Hill'48 model and the criteria based on non-associated flow rule approach are able to reproduce more accurately the experimental points. When it comes to yield surfaces, Hill'48 σ-based and Yld91 yield criteria can match the considered experimental data points. However, the Hill'48 σ-based approach was the only criterion able to pass through the σ_b point, for dual-phase steels.

As all experimental data have the same weight in the identification process of yield criteria parameters, especially in the Yld91 criterion, it is expected that the observed differences will occur, since the identification algorithm will try to minimize the objective function, privileging certain experimental data.

To sum up, the non-associated flow rule approach, using either the simple Hill'48 model or Yld91 criterion, appears to be an excellent choice as it can independently and simultaneously reproduce normalized yield stresses and r-values evolutions.

Chapter 4

Experimental benchmark tests

This chapter is dedicated to a conducted set of experimental benchmark tests proposed in this thesis. The acquired results will be used as a reference data for assessing the prediction performance of the selected constitutive models to describe the behavior of materials during sheet metal forming operations.

(This page was deliberately left blank)

4.1 Swift test

The objective of this benchmark is to obtain reference data to evaluate the predictive capabilities of constitutive models, previously mentioned, to reproduce the behavior of materials during sheet metal forming processes. Among the data collected, the focus is the evolution of the earing profiles, as well as the thickness distribution along the cup wall, for several orientations relative to the rolling direction.

To acquire such information, Swift tests were carried out for the four different metal alloys on hydraulic universal sheet metal testing machine [97]. The experimental setup is composed by four axisymetric tools (die, blank holder, punch and stopper) and their geometry is given in figure 4.1.

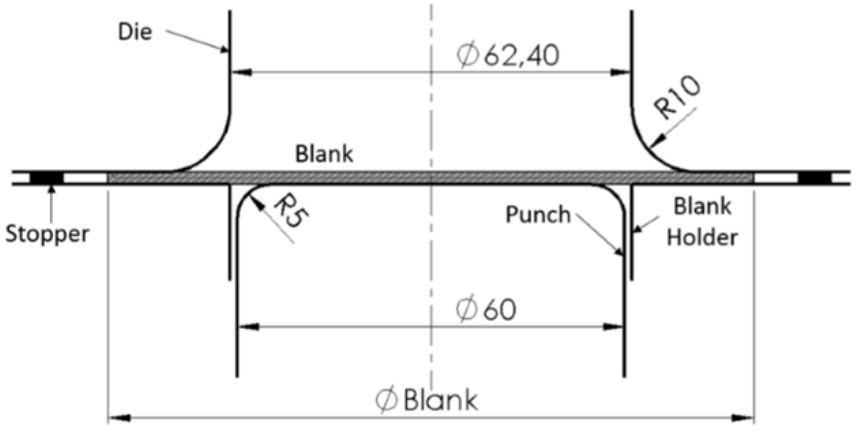


Figure 4.1: Cylindrical cup test schematic representation and tool dimensions.

Based on the limit drawing ratio of the selected materials [62, 103], the circular blanks have different initial diameters, which means that only a punch displacement of 60 mm is required to fully draw the cup, considering also a constant punch travel speed. The applied blank holder force is maintained from the beginning of the deep drawing operation until the cup is fully drawn. At the beginning of the test, an oil lubricant (Ferrocoat N6130, properties at appendix A) is applied manually on both sides of the blanks.

The experimental conditions of the cylindrical cup tests are summarized in table 4.1. In order to minimize the ironing of blank flanges during the final stage of deep drawing, the stopper ring was produced using the same sheet blank material. The blank dimensions were measured (diameter and thickness) by using a micrometer, as shown in figure 4.2.

Table 4.1: Experimental conditions of deep drawing cylindrical cup tests.

Material	AA5182	AA6016	DP500	DP780
Diameter [mm]	ϕ120	ϕ110	ϕ125	ϕ125
Thickness [mm]	1.014 $\pm$ 0.002	0.996 $\pm$ 0.001	0.814 $\pm$ 0.001	0.82 $\pm$ 0.001
Blank holder force [kN]	40	40	100	115
Punch speed [mm/s]	5			
Lubricant conditions	84 g/m^2 of oil (FERROCOAT N6130)			
Temperature [ºC]	23 $\pm$ 1			
Humidity [%]	52 $\pm$ 1			
Data acquisition [Hz]	50			

The blank diameters were selected based on the limiting drawing ratio (LDR) of each material, so the maximum deformation can be reached without the material fracture, highlighting the material anisotropic effects. In case of DP500 and DP780, the corresponding LDR is 2.15 and 2.09 [97]. For the AA5182, the LDR varies between 1.7 - 2 [104]. The AA6016 LDR is lower than the AA5182, since after some experimental trials, the maximum diameter allowed to draw without fracture was 110 mm.

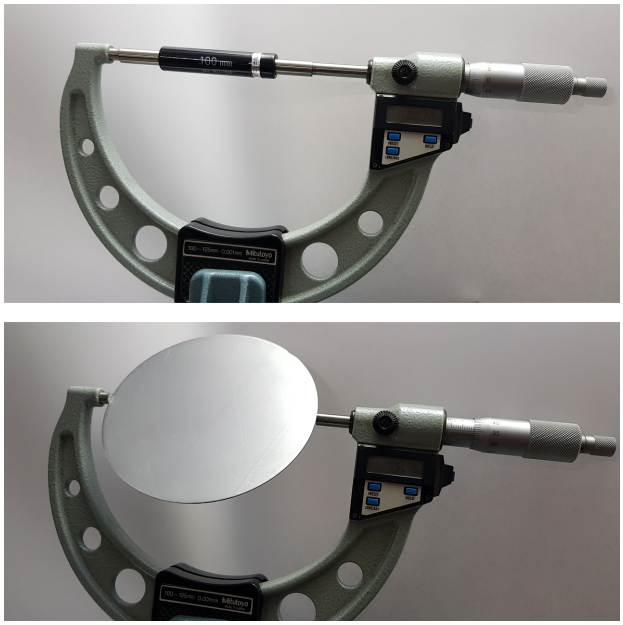
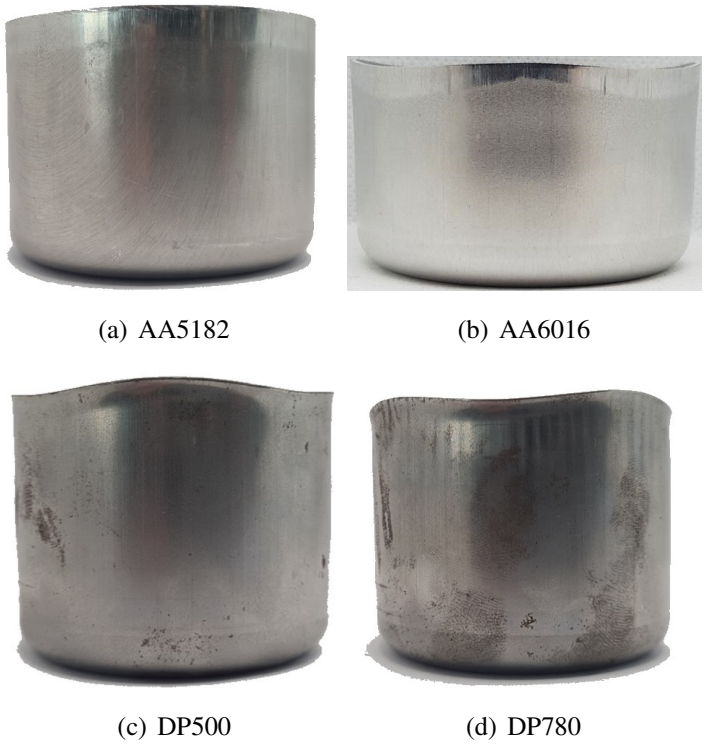


Figure 4.2: Procedure used for measuring the sheet blank diameter.

The fully drawn cups can been seen in figure 4.3. As expected the AA6016 cup has the lowest height because of the initial blank diameter. Moreover, the dual-phase

steels clearly show a pronounced anisotropic earing profiles. To evaluate the earing and thickness profiles, 3D sections data points are obtained using an Industrial 3D Measuring System (ATOS Triple Scan). This equipment is a non-contact high-resolution optical measurement system.



(a) AA5182 (b) AA6016

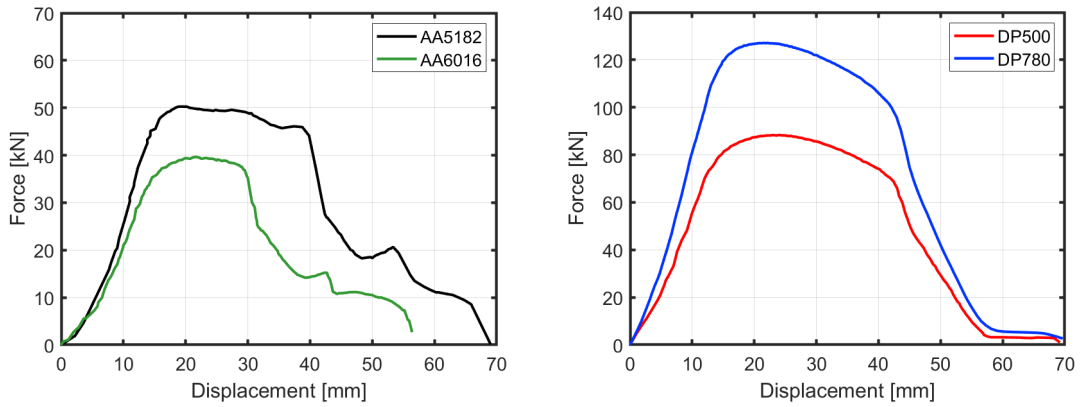
(c) DP500 (d) DP780

Figure 4.3: Obtained experimental cylindrical cups.

4.1.1 Punch force

The punch force required for deep drawing a cylindrical cup depends on several factors, such as the material properties, sheet thickness, cup dimensions, and punch geometry, but also can be affected by some factors such as friction between the sheet and the die, lubrication, and the deformation mode (e.g., whether it is a pure stretching or a combination of stretching and bending).

Figure 4.4 presents the experimental result of the punch force evolution as a function of punch displacement. The dual-phase steels require a higher punch force to deform the circular blank, which, despite having the higher strength, also have a larger initial diameter. In the case of aluminum alloys, although the hardening behavior is very similar for both materials, the smaller initial diameter of AA6016 aluminum implies a lower punch force to draw the cup.



(a) Aluminum alloys (b) Dual-phase steels

Figure 4.4: Experimental punch force vs. displacement for the materials under study.

Nevertheless, the obtained results reveal two different stages. An initial stage that corresponds to the typical increase of punch force in cylindrical cup deep drawing where the force steadily rises until reaching a maximum value (point 2 in figures 4.5 and 4.6). Subsequently, the force gradually decreases, eventually reaching a null value. However, for the aluminum alloys, a second stage emerges at approximately 40 and 50 mm of punch displacement for AA6016 and AA5182, respectively. This stage is characterized by a stabilization and even a small increase in punch force, which continues until reaching a maximum value at around 43 and 54 mm, respectively. After that the force gradually decreases until the end of the drawing process.

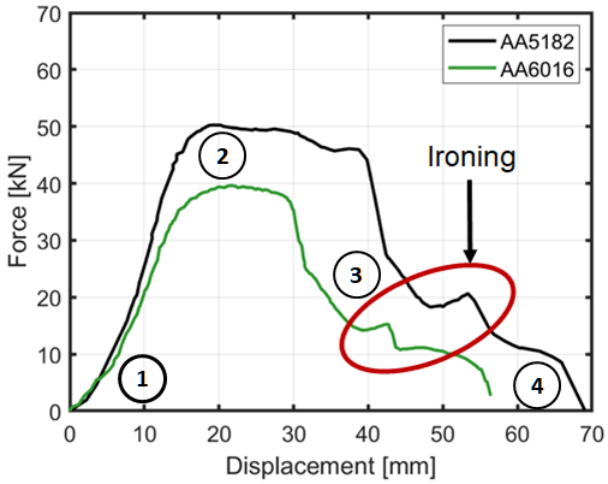


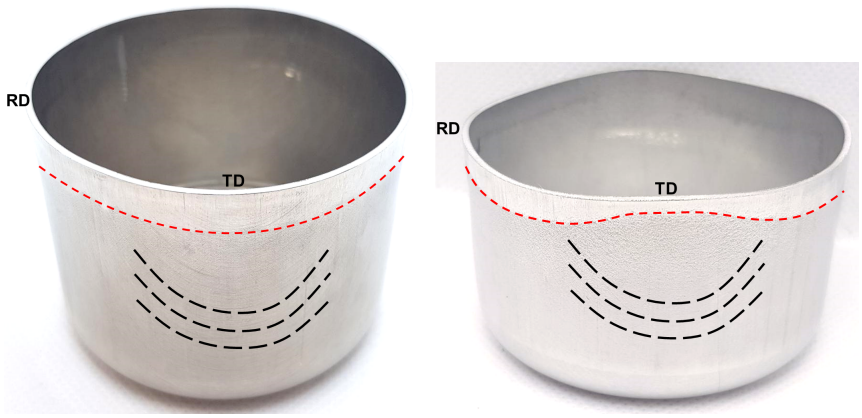
Figure 4.5: Ironing effect on punch force curve for aluminum alloys.

The occurrence of the second stage, marked by an increase in punch force, can be attributed to the ironing process. During the process of deep drawing, the material located between the die and the blank holder undergoes an increase in thickness, exceeding the nominal value of tool clearance. As this material reaches the location where the gap between the die and the punch is lower than the cup wall thickness, a sudden rise in punch force develops. This phenomenon can be observed at point 3 of figures 4.5 and 4.6, which corresponds to the beginning of the ironing stage of these aluminum alloys.



Figure 4.6: Stages of deep drawing cylindrical cup forming process.

At the end of the deep drawing process it is clearly visible a more brighter area close to the cup border (marked in figure 4.7 in red dashed line). This area corresponds to the zone where the ironing effect took place. It can also be seen that AA5182 has a uniform area along the perimeter of the cup, unlike AA6016, which follows the cup ear profile. Another interesting phenomenon that can be observed in these two aluminum alloys is how the material flows during the forming process (black dashed lines). This effect if visible because it is possible to see at naked eye the material rolling direction.



(a) AA5182 (b) AA6016

Figure 4.7: Ironing and the material flow representation.

4.1.2 Earing profile

Earing is a common phenomenon observed in sheet metal forming processes, particularly in deep drawing operations. It refers to deformation of the material, which results in the formation of ears along the circumference of the drawn component, typically near the top edge of the cup, due to the anisotropic nature of sheet metal, where the material exhibits different mechanical properties in different directions.

The height of a deep drawing cylindrical cup will depend on various factors, such as the depth of the draw, the thickness of the material and the initial diameter of the blank. Generally, an increased draw depth corresponds to a greater cup height. However, in deep drawing, there is generally an inverse relationship between cup height and material thickness. As the material thickness increases, the achievable cup height tends to decrease. This is because thicker materials are less ductile and more resistant to deformation, making it harder for the material to stretch and form into a deeper cup shape. Additionally, the diameter of the blank also plays a role in determining the height of the cup because a larger diameter blank can be drawn into a taller cup than a smaller diameter blank, all other factors being equal.

Figure 4.8 presents the methodology for measuring the earing profile, using evolution profiles, with a 3D measuring system post-processing program. The obtained corresponding results, for the selected materials, are presented in figure 4.9. Due to the symetry only a quarter of the results measured is presented, figure 4.9.

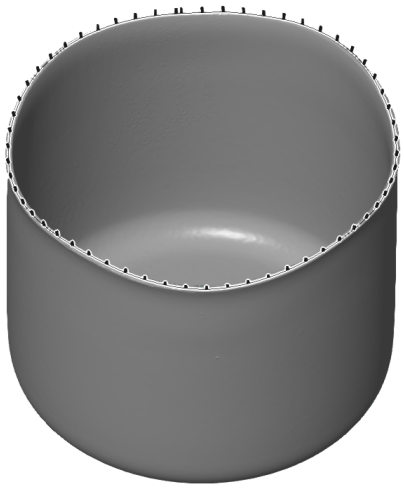
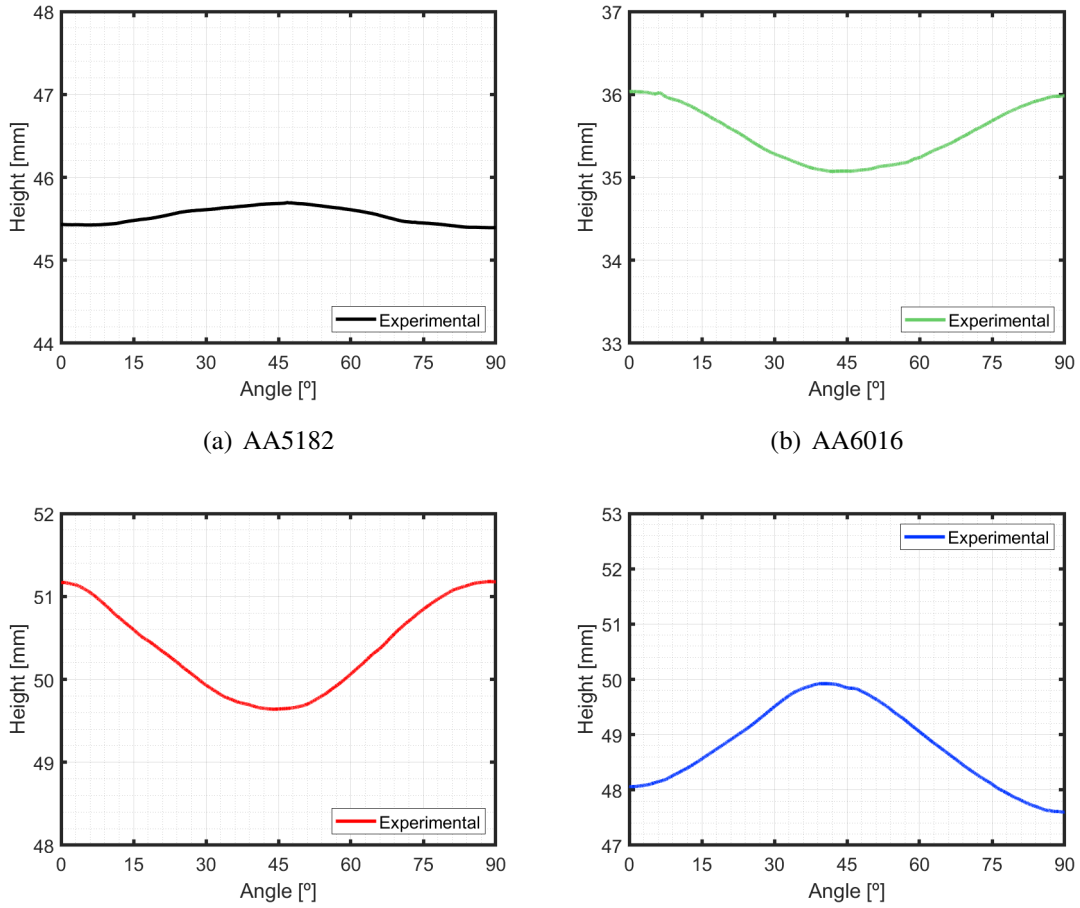


Figure 4.8: Selected points to obtain the earing profiles of the cylindrical cups.



(a) AA5182 (b) AA6016

(c) DP500 (d) DP780

Figure 4.9: Earing profiles for the aluminum alloys and dual-phase steel cups.

As expected from the evolution of anisotropic plastic strain ratios, the AA5182 and DP780 show a similar behavior, i.e., they exhibit a higher ear height at a 45° angle relative to the rolling direction, which is in agreement with the negative planar anisotropy. On the other hand, AA6016 and DP500 have an opposite tendency. What is also noticeable is that the magnitude of the ears is higher in the dual-phase steels, with AA5182 aluminum having almost isotropic behavior.

4.1.3 Cup wall thickness profiles

In deep drawing cylindrical cup, thickness distribution refers to the variation in material thickness across the formed cup. As the material is deformed and stretched during deep drawing, variations in thickness can occur. These variations can manifest as thinner areas, typically near the bottom of the cup, and thicker areas, often at the cup's walls or flange

region. Inconsistent thickness distribution of the cylindrical cup is caused by the material anisotropy.

This section presents the experimental evaluation of the cup wall thickness distribution after the deep drawing process. The approach employed (figure 4.10), involved measuring sections on planes that intersect the cup axis at various angles, including rolling, transverse and diagonal. The obtained wall thickness distribution and profiles for each section and material are presented in figures 4.11 e 4.12, respectively.

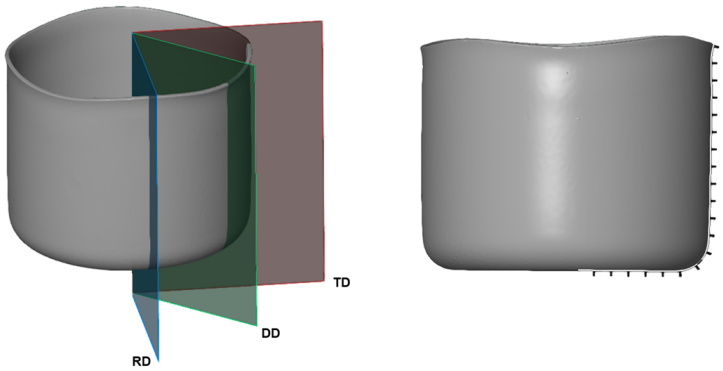
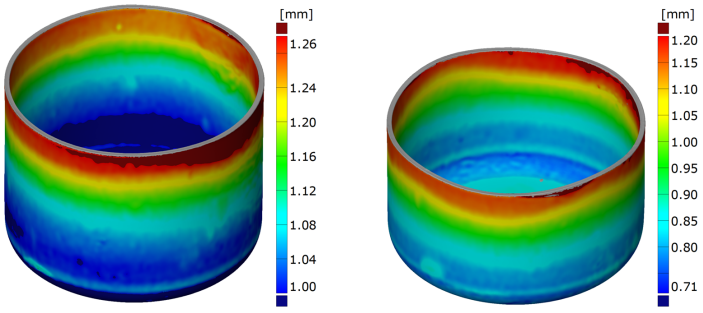
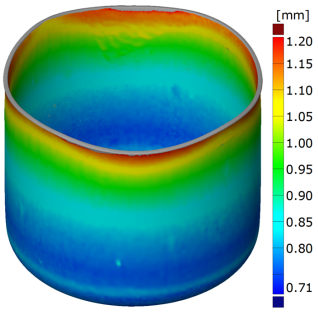


Figure 4.10: Cup thickness profile sections and measurement strategy utilized.

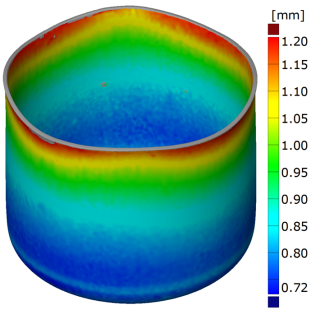


(a) AA5182-O

(b) AA6016-T4

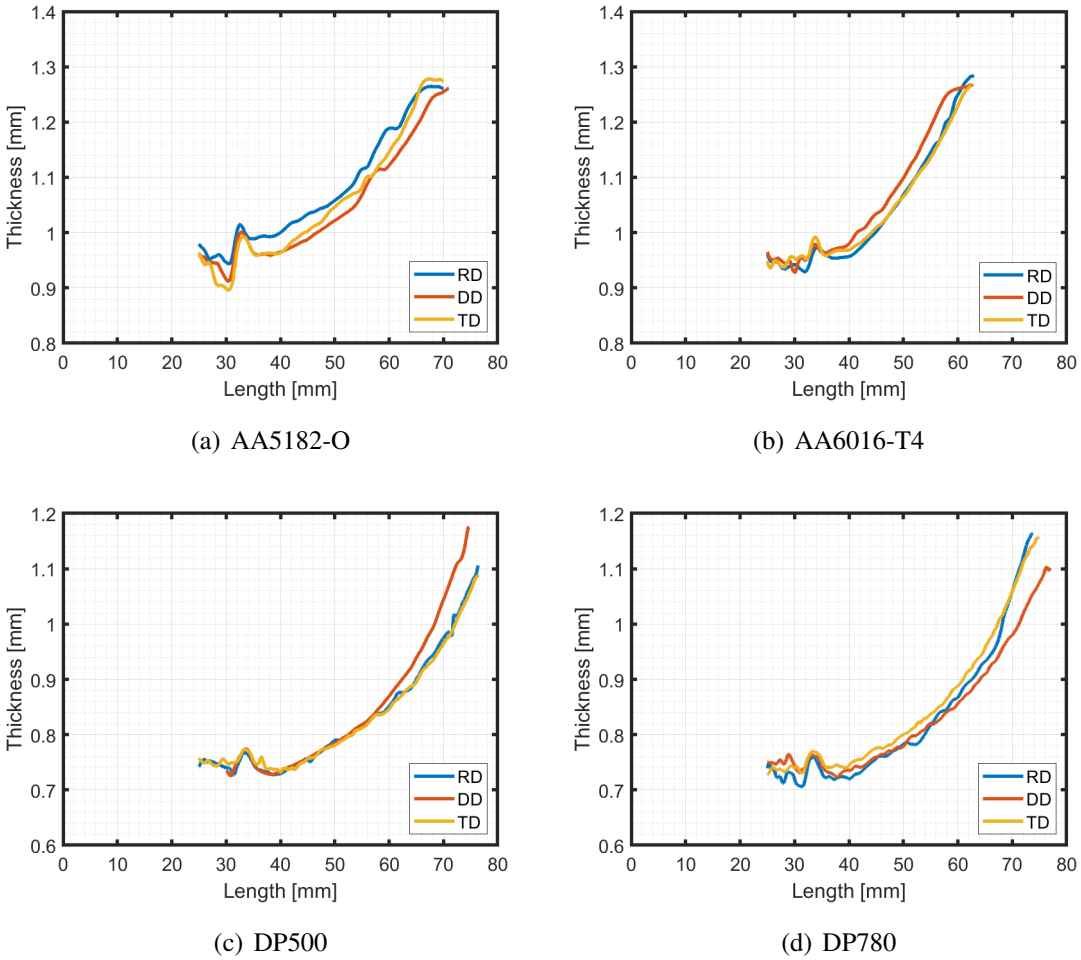


(c) DP500



(d) DP780

Figure 4.11: Cup thickness measurements for vertical section for the aluminum alloys and steel.



(a) AA5182-O

(b) AA6016-T4

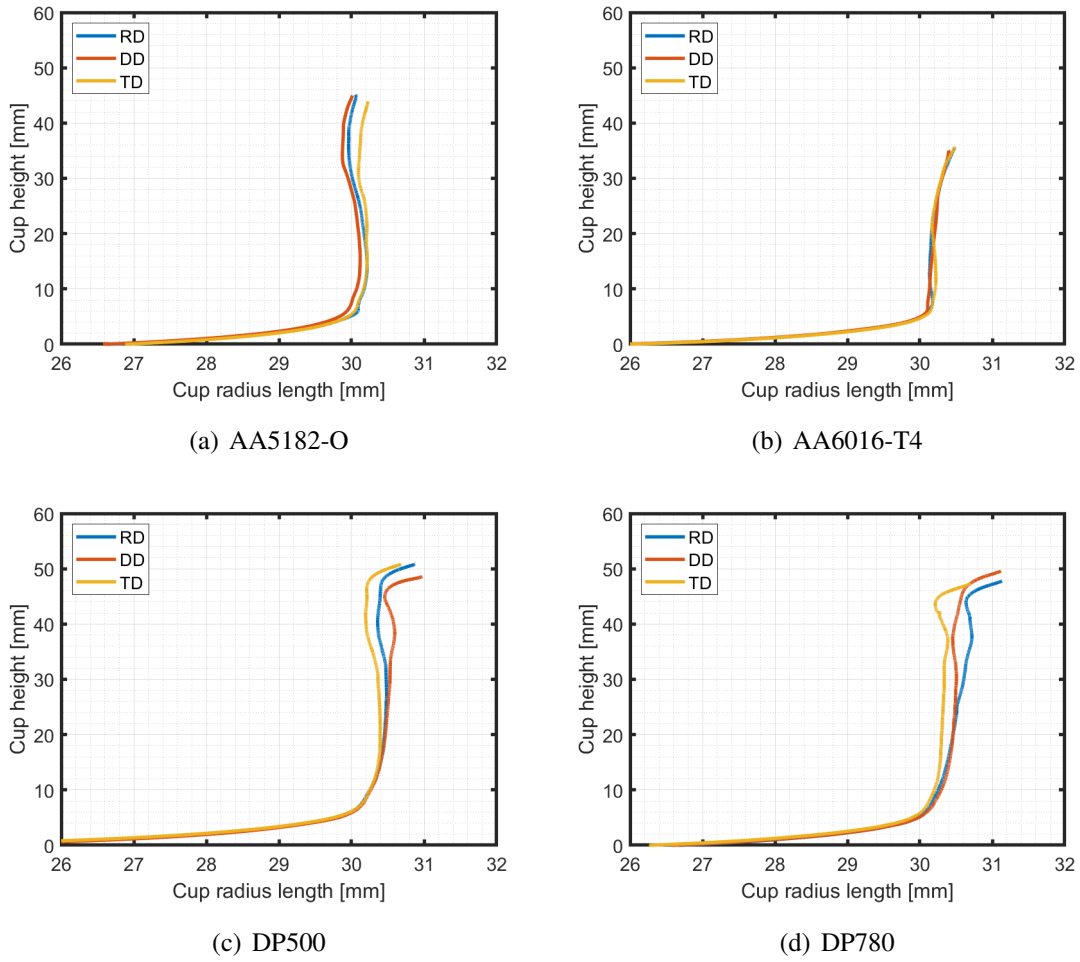
(c) DP500

(d) DP780

Figure 4.12: Cup thickness measurements for vertical section for the aluminum alloys and steel.

As can be seen in figure 4.12, the thickness evolution for all considered materials and sections exhibits a typical profile after deep drawing a cylindrical cup, consistent with findings from various studies. The increase in cup wall thickness initiates after the bottom cup radius and culminates in a peak value near the border. Additionally, there is a noticeable anisotropic behavior among the analyzed sections. A higher ear value typically corresponds to a lower thickness near the cup border. For instance, in DP780, a higher ear is observed at a 45º angle relative to the rolling direction, resulting in the lowest thickness when compared to the RD and TD directions. In contrast, DP500 shows the opposite tendency in terms of thickness distribution profiles. Unlike the consistent thickness evolution in steels, the aluminum alloys undergo an ironing phase towards the end of the deep drawing process. This phase occurs when the cup thickness exceeds the clearance between the punch and the die, which in this setup is 1.2 mm. Such effect is visible, not only by the punch force evolution curve, but also by the plateau present at the

end of the thickness distribution curves, for three the measured directions. Even in the aluminums, the anisotropic behavior is observed, which is in contrast with the dual-phase steels. Figure 4.13 presents the profiles sections obtained for the Swift test.



(a) AA5182-O

(b) AA6016-T4

(c) DP500

(d) DP780

Figure 4.13: Profile sections measured for the cylindrical cup test.

4.2 Modified Demeri Benchmark test (Split Ring test)

Measuring springback continues to be a challenging task and in some cases there is room for enhancements and improvements concerning accuracy and precision. This is because in order to obtain precise measurements of springback, it is crucial that the measuring device does not restrict the movement of the formed part, which would impact the actual springback values. Most of the parts that were studied for springback had to be either constrained by the measuring fixtures or measured at arbitrary locations that were difficult to determine [67].

To analyze the elastic recovery of deep drawing component after forming, the Demeri test was considered [60]. To achieve this objective, the springback is determined through the measurement of the opening of a ring extracted from the sidewall of a drawn cylindrical cup, as presented in figure 4.14. This method presents a simple and effective approach for predicting the forming and springback properties under complex deformation paths of metallic materials based on prior experimental measurements. The change in the outer diameter of the ring from its original unsplit diameter indicates the amount of elastic recovery.

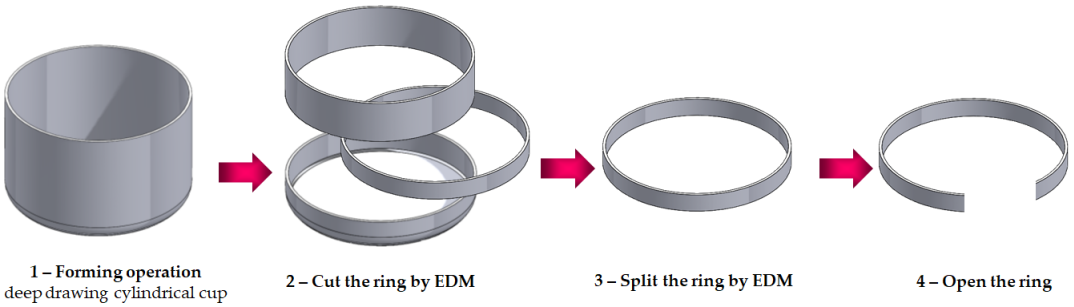


Figure 4.14: Strategy of split ring test.

This test involves the precise trimming of a ring from the vertical wall of a cup that were presented in previous section, followed by a subsequent cut along the rolling direction (RD). The opening of the ring allows for direct measurements of the resulting springback, thereby providing valuable insights into the release of internal stresses. Figure 4.15 displays the gap that is formed in the split ring due to the difference in diameters.

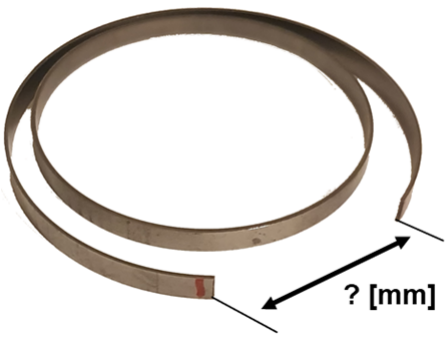


Figure 4.15: Measurement of the opening, before and after vertical cut, the split ring.

The rings were trimmed at a distance of 10 mm from the bottom of the cup, with a fixed height and cutting increments of 5 mm, as shown in figure 4.16. The amount of extracted rings from the cylindrical cup depends on its total height. Table 4.2 indicates the obtained rings that where analyzed in terms of springback, for the different materials.

The machining operation is made by a wire electrical discharge machine and the gap generated by the wire was carefully considered, having a value of 0.25 mm. The gaps in the rings were measured along straight lines that connected the two ends of the split rings. This meticulous process guarantees the accurate assessment of springback and enables the comprehensive analysis of material behavior under the testing conditions.

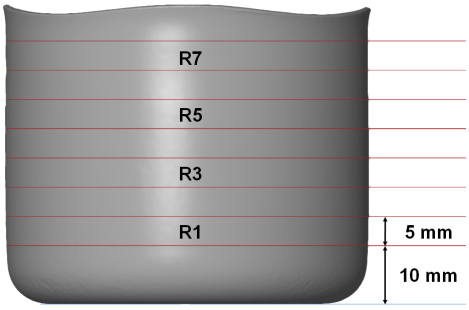


Figure 4.16: Location of the rings for analysis on the cylindrical cup drawing.

Table 4.2: Rings extracted from the cylindrical cups.

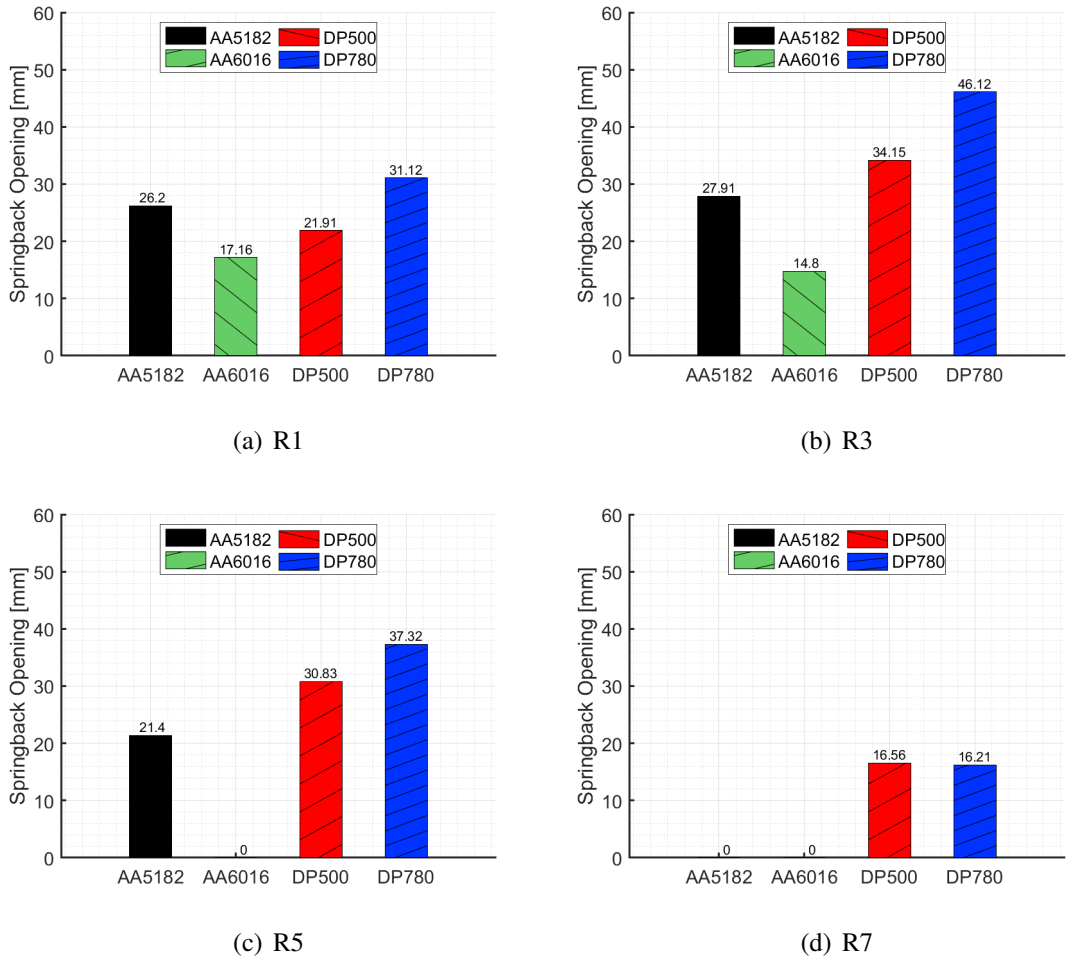
Material	Split Ring opening			
	R1	R3	R5	R7
AA5182	X	X	X	-
AA6016	X	X	-	-
DP500	X	X	X	X
DP780	X	X	X	X

4.2.1 Split ring opening

After the rings were cut vertically so that they can open, measurements were taken between their ends. Table 4.3 contains the opening values for each material and ring. For a better visualization of the trend along the height of the cup, figure 4.17 shows a comparison between the different rings for the different materials.

Table 4.3: Split ring opening measurements.

Material	Split Ring opening			
	R1	R3	R5	R7
AA5182	26.20	27.91	21.40	-
AA6016	17.16	14.80	-	-
DP500	21.91	34.15	30.83	16.56
DP780	37.12	46.12	37.32	16.21



(a) R1

(b) R3

(c) R5

(d) R7

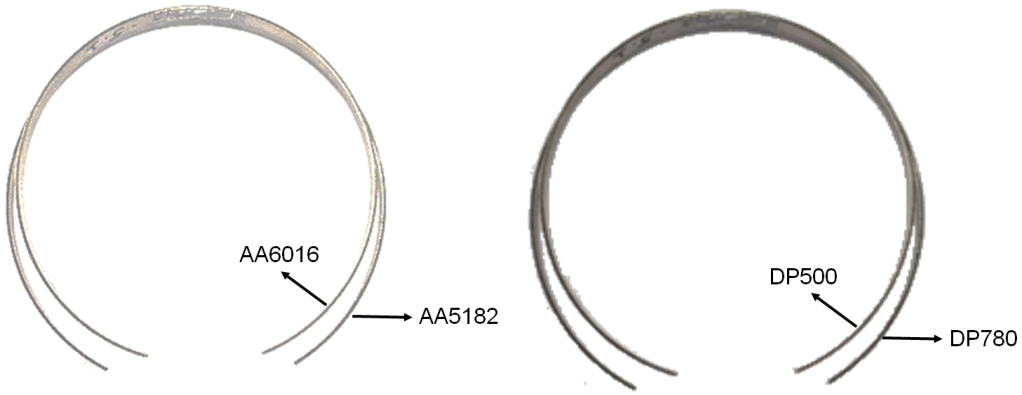
Figure 4.17: Springback opening measured in the rings cutted for the different materials in study.

The comparison of the ring opening values presented in figure 4.17 shows that the springback for the DP steels increases significantly, about 50%, from ring R1 to ring R3, followed by a decrease until the last ring, representing about 24% and 48% of the ring R1 value for DP500 and DP780, respectively. Similar behavior is observed in the case of

AA5182 aluminum as well, however the opening value of the R3 ring only suffers a small increase, about 7%, compared to the R1 ring.

Moreover, the variation of AA5182 springback along the cup wall is also more stable, not showing as many oscillations as the DP500 and DP780 steels. In the case of AA6016, the observed behavior is the opposite, i.e, there is a decrease in the elastic recovery from ring R1 to R3. This phenomenon may be related to the fact that rings close to the edge of the cup have lower springback than those closer to its base, which is in line with the cup obtained for AA6016 being the one with the lowest height.

Additionally, figure 4.18 presents a comparison of the all openings for the first ring obtained for the materials in this study.



(a) Aluminum alloys (b) Dual-phase steels

Figure 4.18: Comparison of rings R1 after springback for the different materials.

The stretching and deformation processes that take place during material flow are one of main causes for the springback phenomena seen in a split ring test on a deep drawn cup. After the occurrence of the elastic recovery, an additional phenomenon known as twist can manifest.

Twist refers to the rotational deformation or misalignment observed in the formed sheet metal component. As a result, the originally flat or planar shape of the sheet metal may become distorted, with sections rotating relative to each other.

Figure 4.19 and 4.20 contains all the analyzed split rings. The ring near to the cup edge (last ring) exhibits not only a linear opening but also some twist along the ring. This phenomenon is more notorious for DP780, as expected due to the higher strength. On the other hand, the aluminum alloys present a smaller twist effect and since the aluminum cups undergo some ironing at the end of the drawing process, the twisting effect may be influenced in some way, minimizing it.



(a) R1



(b) R3



(c) R5

Figure 4.19: Opening rings for the AA5182 and AA6016, left and right respectively.



(a) R1



(b) R3



(c) R5



(d) R7

Figure 4.20: Opening rings for the DP500 and DP780, left and right respectively.

4.3 Cross die test

Due to its inherent advantages over conventional deep drawing benchmarks, the cross die test has emerged as an adopted experiment within the sheet metal forming industry [105]. Its primary purpose is to evaluate the forming characteristics of sheet metals, in which the results obtained include the specimen height, maximum strain values and blank draw-in. As expected, the interaction between blank and tools is complex in any industrial deep drawing process and this test is performed to investigate a wide range of stress loading states and reproduce fundamental strain paths that occur in industrial deep drawing processes.

The cross die benchmark tests were performed on a servo-hydraulic press machine INSTRON 1000KPX (figure 4.21) with a load capacity of 1 MN. The experimental tool setup consists of three active parts (die, punch and blank-holder) with a cross-shaped geometry as shown in figure 4.22. The blank holder force is ensured by six Quiri RG 5000/100 gas springs (50 kN load capacity and 100 mm stroke) connected to each other, in order to minimize any variation in the application of the clamping force. This force can be adjusted according to the geometry and/or the material to be tested. The system contains also a load cell and a displacement transducer that allows the force curve to be obtained as a function of displacement.

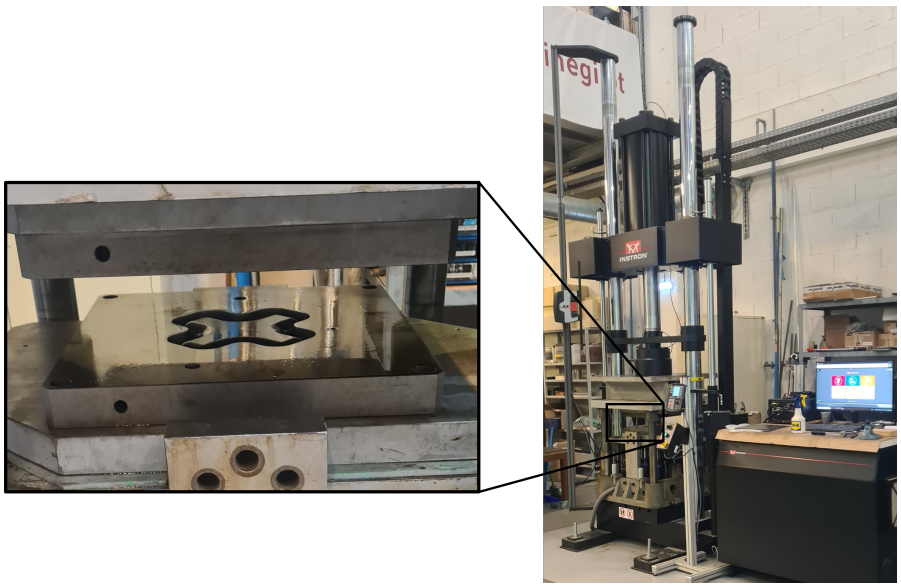


Figure 4.21: Press machine and tools used in Cross die test.

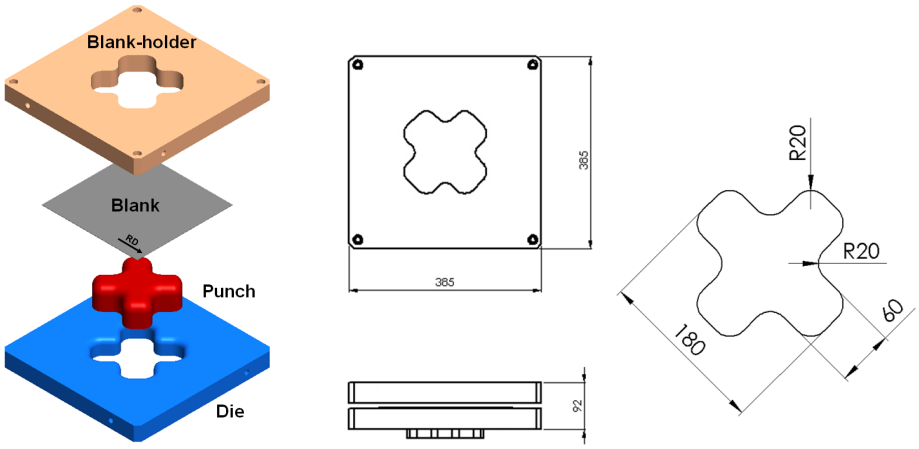
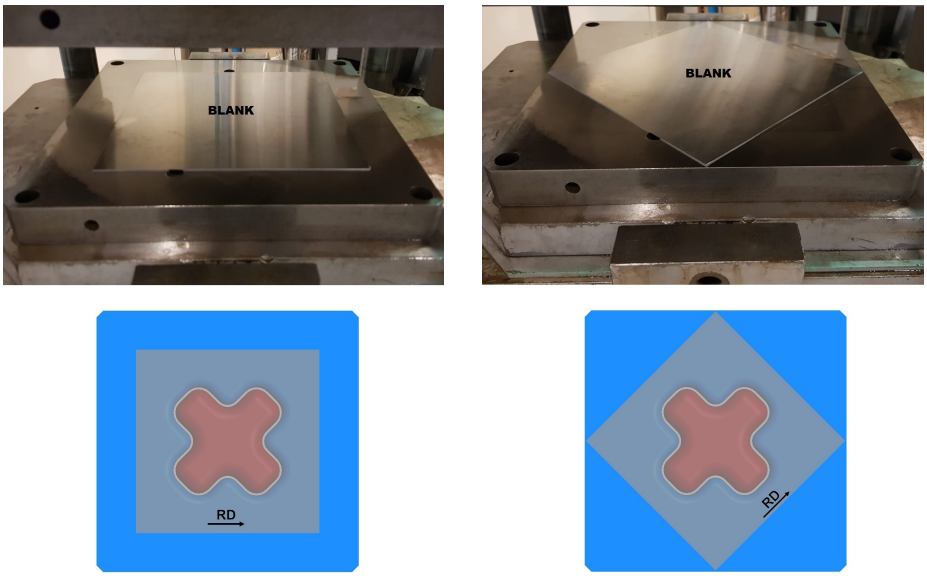


Figure 4.22: Cross-die test assembly and tool dimensions.

A square blank with 270x270 mm^2 was used for all the established experiments. Additionally, the blank was positioned in both rolling and diagonal direction, accordingly to figure 4.23, to analyze the impact of blank orientation. Although the tools are designed for a punch displacement of 70 mm, the experiments were conducted until the moment before the fracture occur. In table 4.4 are summarized all the conditions used in the cross die test.



(a) Cross (b) Plus

Figure 4.23: Different obtained component shapes based on blank orientation.

Table 4.4: Experimental conditions of cross die forming test.

Material	AA5182	AA6016	DP500	DP780
Thickness [mm]	1.014 $\pm$ 0.002	0.996 $\pm$ 0.001	0.814 $\pm$ 0.001	0.820 $\pm$ 0.001
Blank holder force [kN]	60	60	120	120
Punch speed	200 mm/min			
Lubricant conditions	37 g/m^2 of oil (FERROCOAT N6130)			
Temperature [ºC]	23 $\pm$ 1			
Humidity [%]	52 $\pm$ 1			

The experiments were carried out at a constant crosshead speed of 200 mm/min. To minimize the friction between the blank material and the tools, an oil lubricant (Ferrocoat N6130) was applied manually on both blank surfaces. Regarding the blank holder force, the gas springs have a linear increasing behavior with the displacement. Figure 4.24 contains the force evolution considered in the experiments for the aluminum alloys and dual-phase steels.

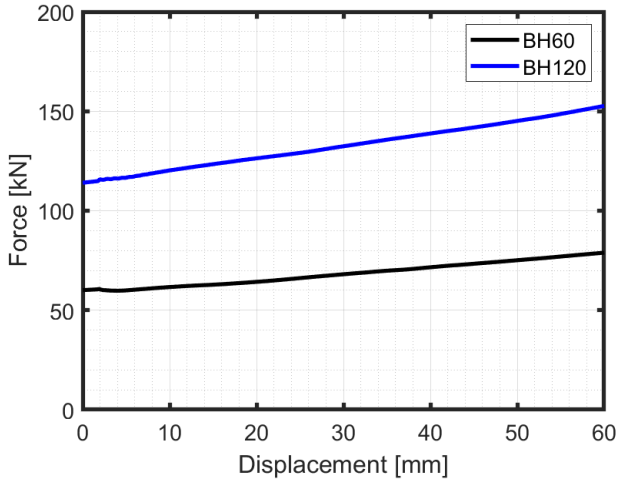


Figure 4.24: Cross die test blank-holder force behavior.

The thickness distribution, as well as, the draw-in of the deformed cross shaped blanks were measured utilizing and Industrial 3D Measuring System (ATOS Triple Scan), as depicted in figure 4.25. The methodology used is similar to the one described in section 4.1.

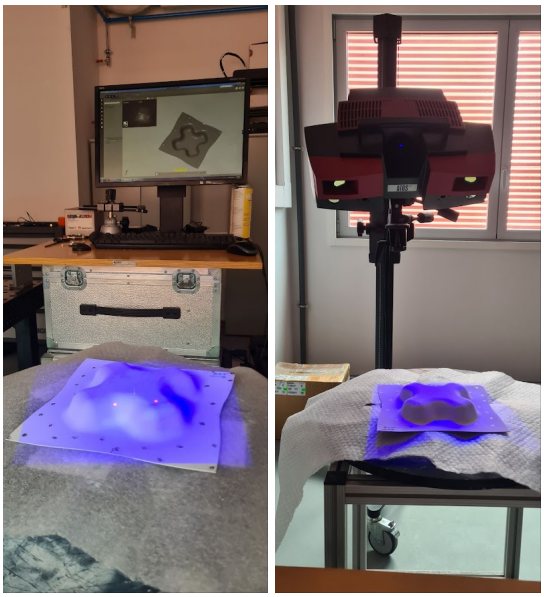
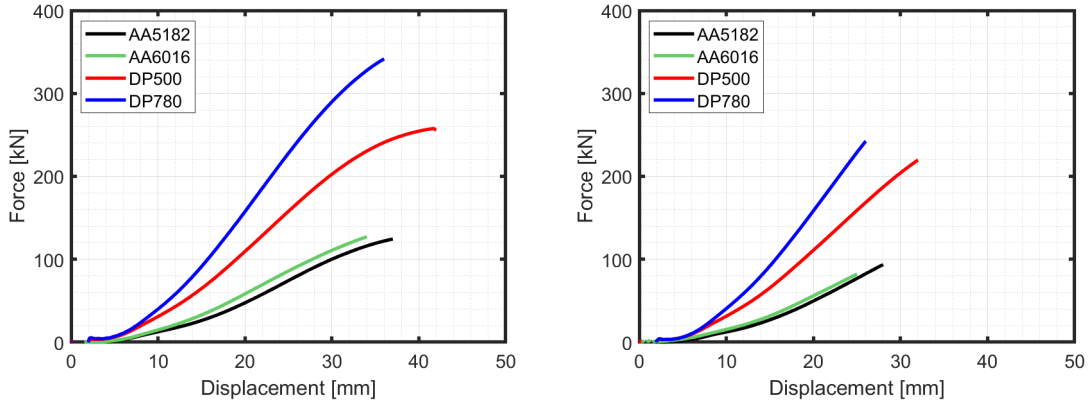


Figure 4.25: Measurement system used to obtain the three-dimensional coordinates of the deformed cross shaped components.

4.3.1 Punch force evolution with displacement

The drawing punch force was measured as a function of displacement. The obtained evolution curves are shown in figure 4.26, for both cross and plus shaped components.



(a) Cross shape - X

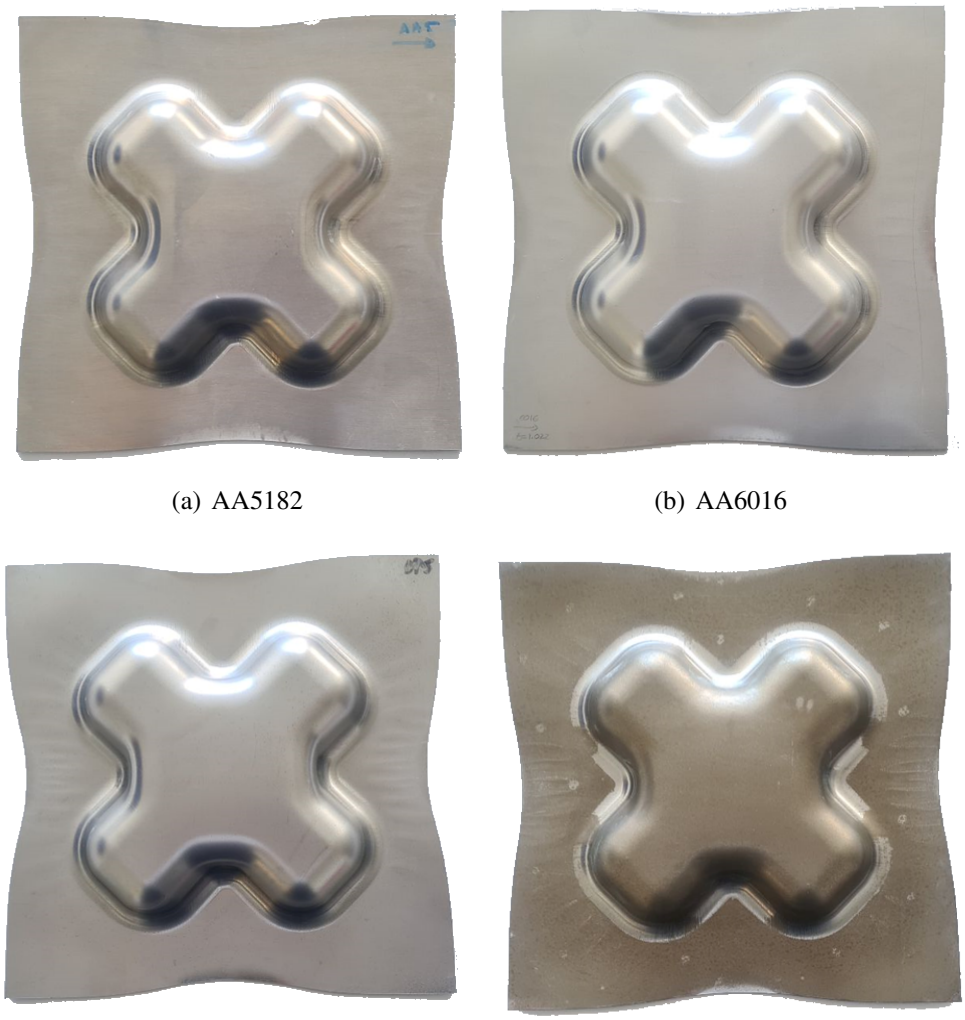
(b) Plus shape - +

Figure 4.26: Comparison of experimental results of punch force *vs.* displacement for the materials in study for cross die forming test.

The different sample orientations resulted in noticeably different drawing characteristics. The punch displacement required to obtain a fully drawn component without failure is lower for the plus shape tests. However, the required force to deform the blank material

for a specific displacement value is identical for both orientations. Figure 4.27 and figure 4.28 present the deformed specimens obtained from the cross die test for rolling and diagonal blank orientations.

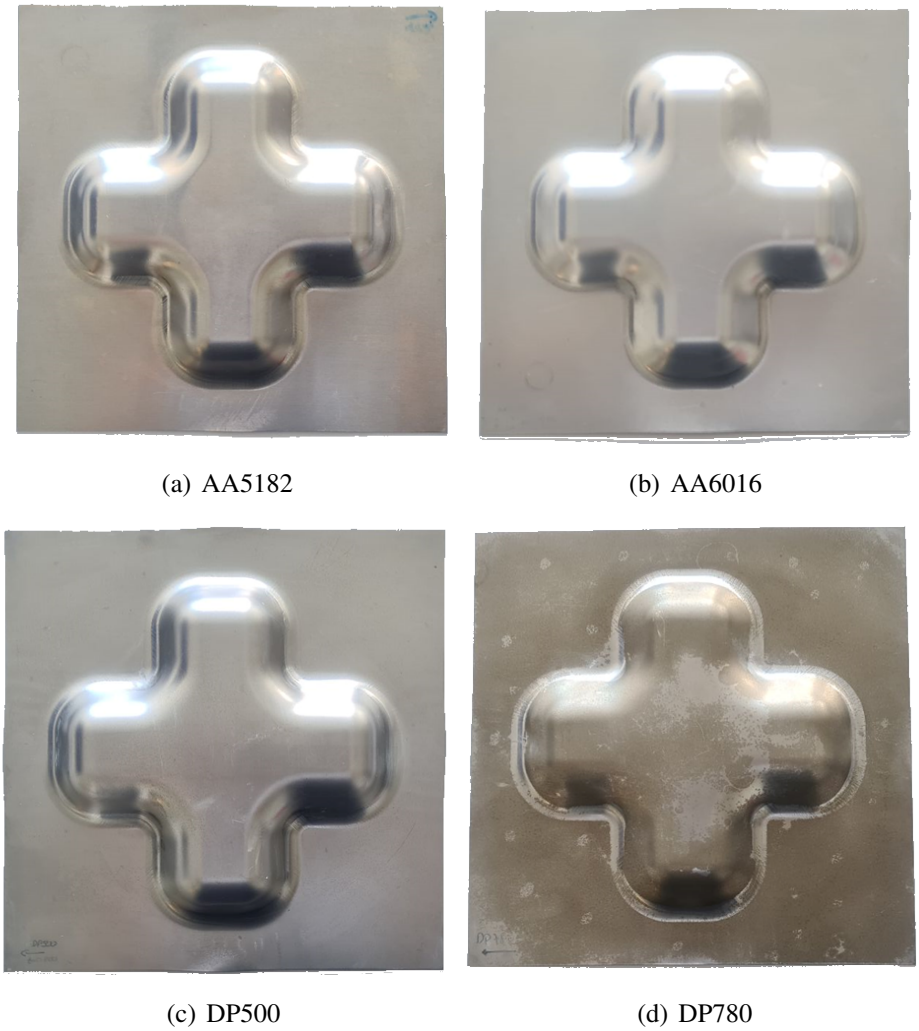
By using different orientations in cross die deep drawing tests, it is possible to gain insight into the effects of material properties, such as anisotropy, and process parameters on the drawing process and final product. This information can be used to optimize the constitutive model parameters and improve the quality and efficiency of the deep drawing process numerical simulation.



(a) AA5182 (b) AA6016

(c) DP500 (d) DP780

Figure 4.27: Obtained samples from cross die test in the rolling direction - cross shape ("X").



(a) AA5182 (b) AA6016

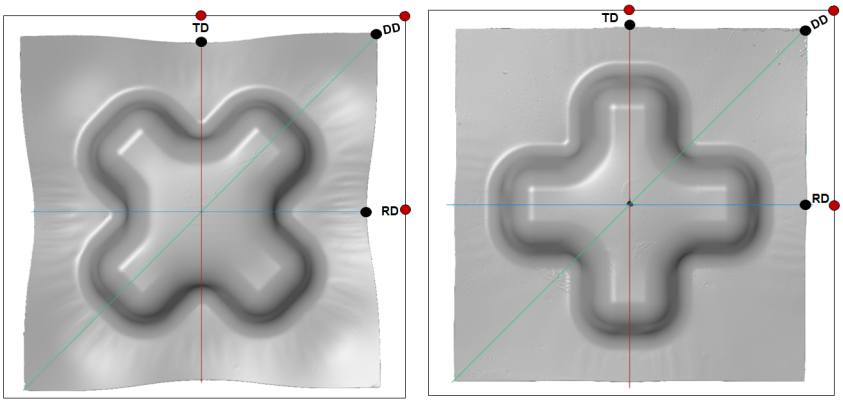
(c) DP500 (d) DP780

Figure 4.28: Obtained samples from cross die test in the rolling direction - plus shape ("+").

4.3.2 Blank draw-in

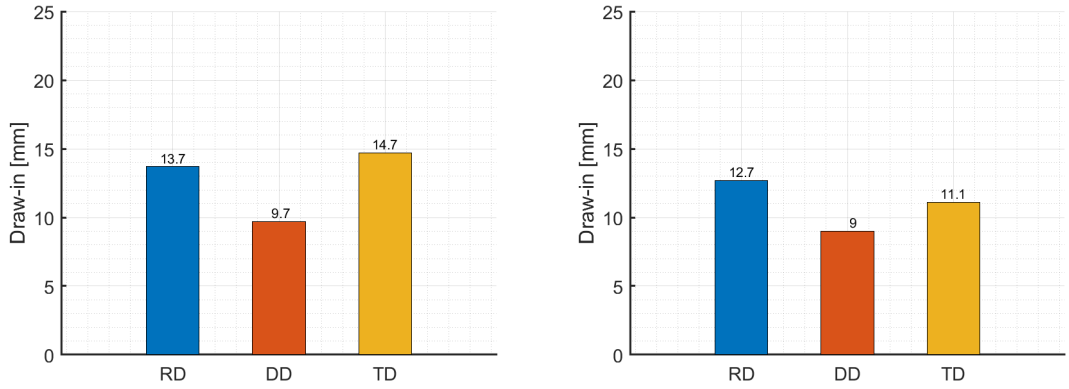
Draw-in is a common effect that can occur during deep drawing tests. It refers to the reduction in length of the blank material at the outer border, i.e, it is the difference between the final and initial shape at a defined position. It is caused by the compressive forces that are generated in the sheet metal as it is drawn through the die, which can cause the material to flow inward and reduce the dimension of the part. The severity of draw-in depends on several factors, including the material properties, size, lubrication between the blank and tools, and the drawing speed.

Figure 4.29 shows the strategy and points used to measure the blank outer border draw-in and figures 4.30 and 4.31 present the final results of cross and plus shape geometries, respectively.

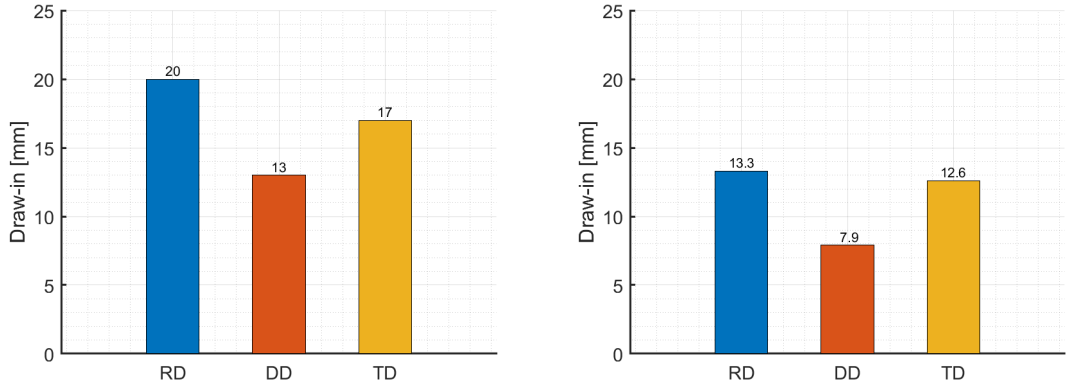


(a) Cross shape (b) Plus shape

Figure 4.29: Points used to measure the blank draw-in.



(a) AA5182 (b) AA6016

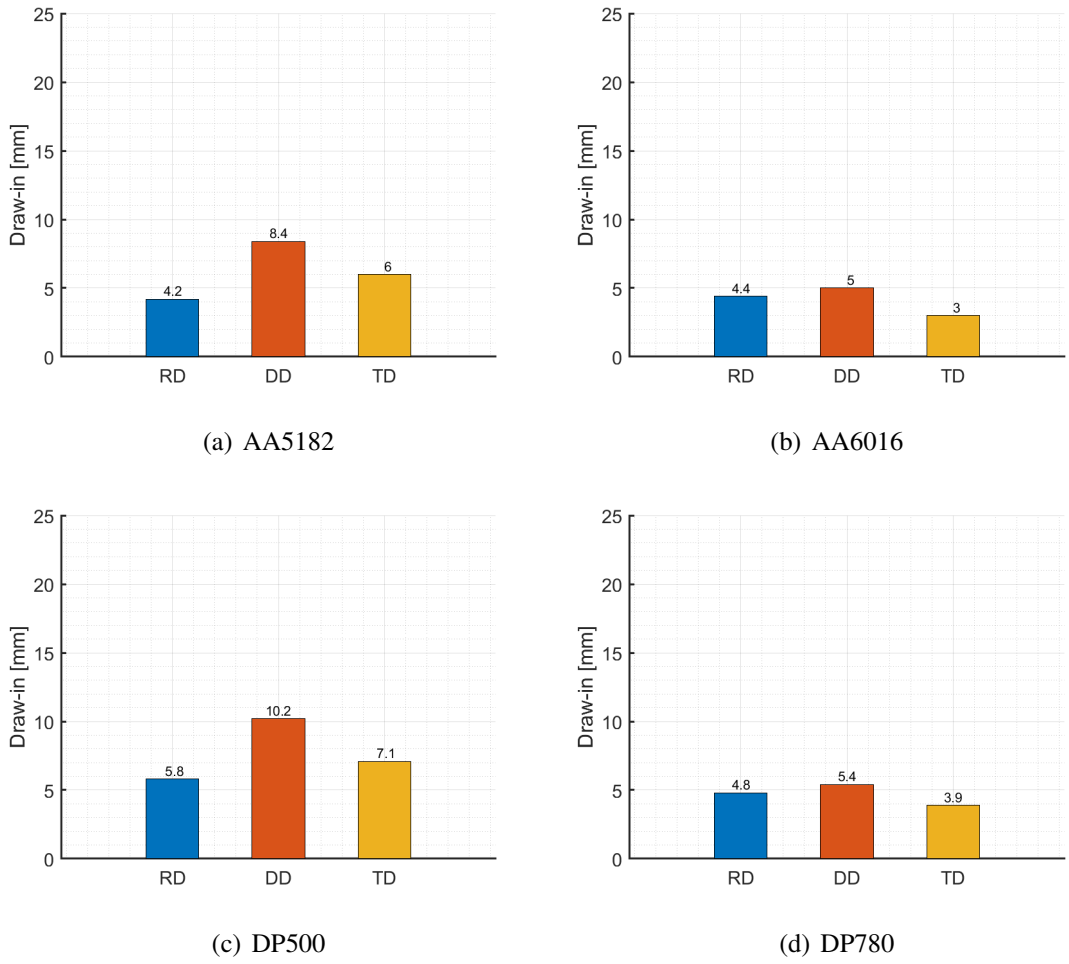


(c) DP500 (d) DP780

Figure 4.30: Measured draw-in in cross-die forming test using aluminum alloys and dual-phase steels for the cross "X" specimen.

The amount of draw-in is directly related with the punch displacement employed. It is evident that the cross shape geometry has a higher draw-in for all materials when compared with the plus shape. This difference in terms of behavior can be justified by the ability of the blank to undergo a higher plastic deformation since the cross orientation does not have the material flow restrictions as the plus shape orientation.

Furthermore, the measured values are in agreement with the experiments present in previous section. For a cross shape the blank corners present a lower draw-in value (diagonal direction) than the other locations. On the other hand, the plus shape specimens, present an opposite behavior. The maximum draw-in value is measured for the rolling direction for all the materials, except for AA5182.



(a) AA5182

(b) AA6016

(c) DP500

(d) DP780

Figure 4.31: Measured draw-in in cross-die forming test using aluminum alloys and dual-phase steels for the plus "+" specimen.

4.3.3 Thickness distribution

To acquire the experimental thickness distribution of the several tests, different sections were defined according to figure 4.32 and 4.34. The obtained evolution is present in figure 4.33 for cross shape geometry and in figure 4.35 for the plus shape geometry.

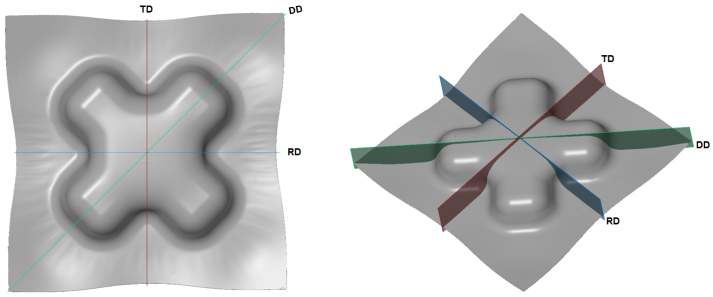
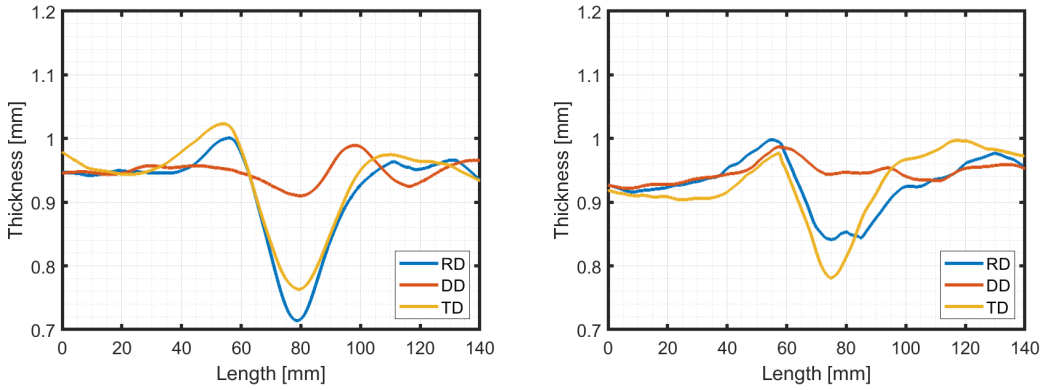
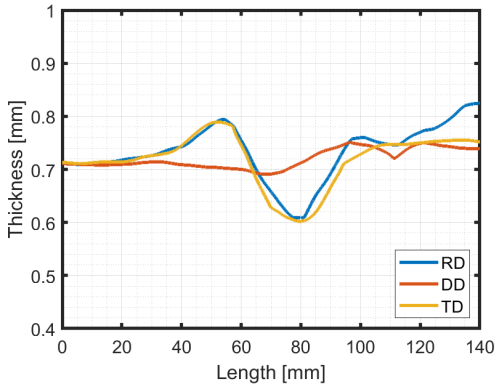


Figure 4.32: Measured strategy followed for the thickness distribution in cross die forming test for the "x" shape.

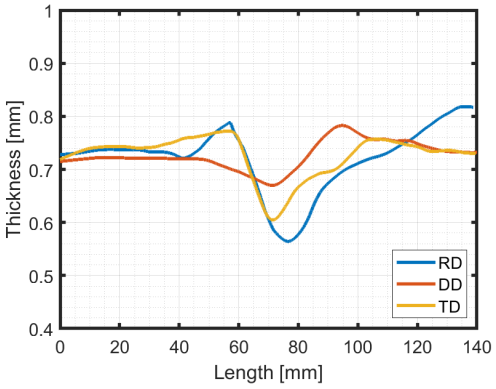


(a) AA5182

(b) AA6016



(c) DP500



(d) DP780

Figure 4.33: Thickness distribution in cross-die forming test for the "X" specimen.

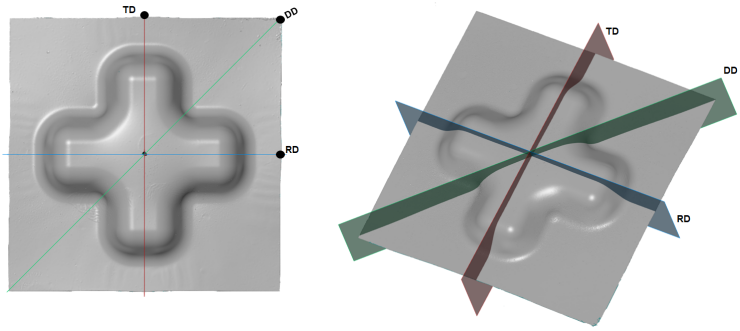
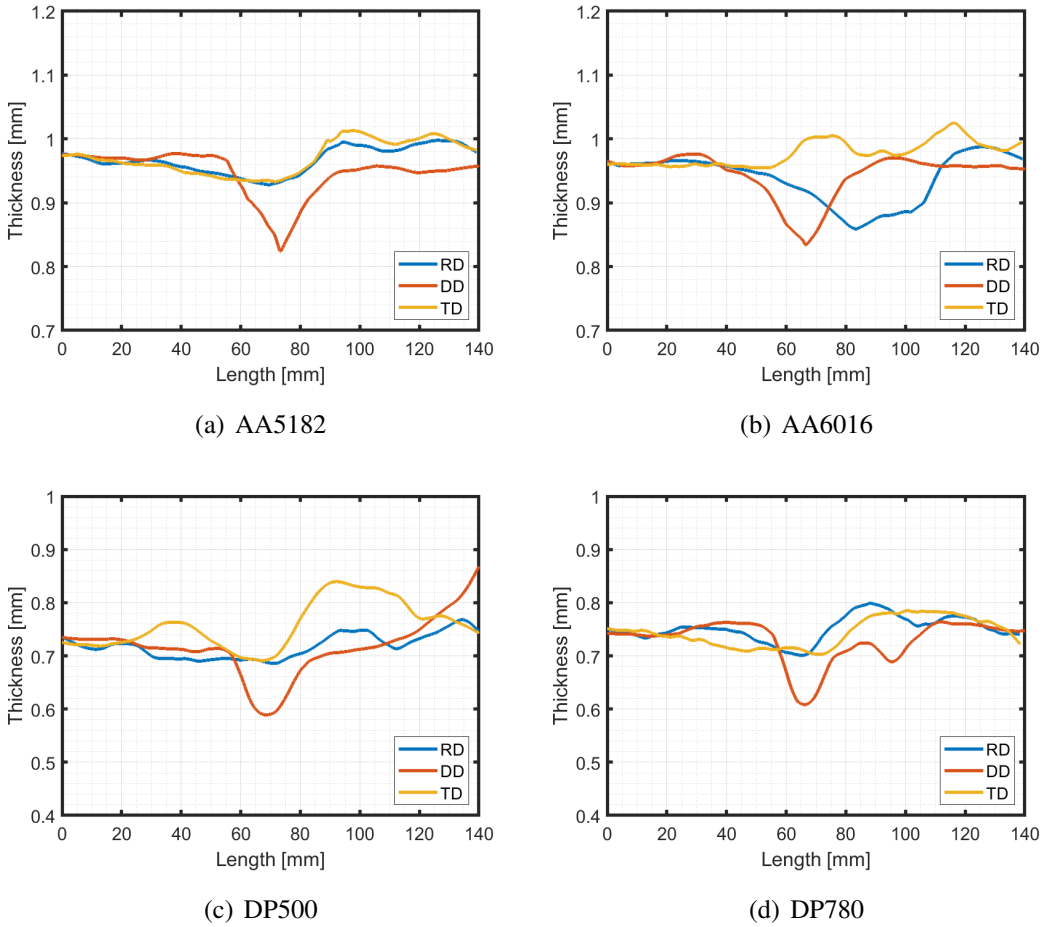


Figure 4.34: Measured strategy followed for the thickness distribution in cross die forming test for the plus "+" shape.



(a) AA5182

(b) AA6016

(c) DP500

(d) DP780

Figure 4.35: Thickness distribution in cross-die forming test for the plus "+" specimen.

In all predictions it is found that the 0° and 90° orientations show a greater thickness reduction than the diagonal direction, and whose thickness distribution profile is very similar given the present symmetry of the tools. Of course, there are differences between

these two orientations due to the anisotropic properties of the materials. Regarding the thickness reduction zones, in the 0° case (the same is valid for 90°), the decrease occurs at the cross component wall (between the punch radius and the die radius), having installed, fundamentally, plane strain stress state. After this reduction, there is a gradual increase until reaching a maximum near the border that is located in a flat area of the component and where there is more draw-in due to the compressive stresses installed in that zone.

In the case of the 45° orientation, the main thickness reduction occurs in the punch radius area, which corresponds to a biaxial stress state. After this reduction, there is still a slight change in the thickness profile located on the side wall of the component that can be linked to the transition between the biaxial to an uniaxial state, since the depth of the component is in general lower. However, the profile does not show significant increases in thickness. Additionally, the critical zones of thickness reduction are not reflected by the sections analyzed here since they are located at the corners of the punch radius and where material fracture usually occurs.

For the plus shaped component, the behavior is the opposite. It is for the 45° orientation that the greatest thickness variation is observed, as expected since between the cross shape geometry and this one there was a 45° rotation.

It is important to recognize that the experimental values have a range of variation. Deviations can arise from factors such as equipment, operator, environmental conditions, etc. Considering the thickness values and the component overall size (thickness variation is around 0.07% of total length of the component), the impact can be more pronounced and small variations should be considered, since the resolution of the equipment used plays a crucial role in achieving precision measurements.

Chapter 5

Numerical simulation benchmark tests

Within this chapter, the validation and evaluation of the constitutive models are performed. Different finite element numerical simulations are carried out under various forming conditions, including deep drawing of cylindrical cups, cross-die forming tests and the application of a modified Demeri split ring for springback analysis. The objective lies in predicting material behavior through the used of previously acquired experimental data and the corresponding identified parameters of the constitutive model. Additionally, a comparison between the results of the numerical simulations and the experimental data is carried out.

(This page was deliberately left blank)

5.1 Numerical models

To evaluate the accuracy and reliability of the studied yield criteria in the numerical simulation, a validation study is conducted based on the comparison with experimental data. For that, two finite element models were created based on experimental benchmark test setups: the deep drawing cylindrical cup test, followed by a split ring analysis, and cross die forming test. Despite the similar configurations of forming tools (punch, die, and blank-holder) in both benchmark tests, distinct differences are observed in the final geometry resulting from the two processes. Also, in case of cylindrical cup test an additional tool, called stopper ring made from the same sheet material and thickness, is used to prevent or reduce the thinning effect at the end of the cup drawing stage, thus maintaining a minimum gap between the die and blank-holder.

Since the two benchmark tests exhibited geometrical symmetry, only a quarter of the real experimental setup was considered to create a 3D finite element model, as shown in figure 5.1. A 3D finite element explicit analysis was considered when carrying out the numerical simulations, with the Abaqus/Explicit code.

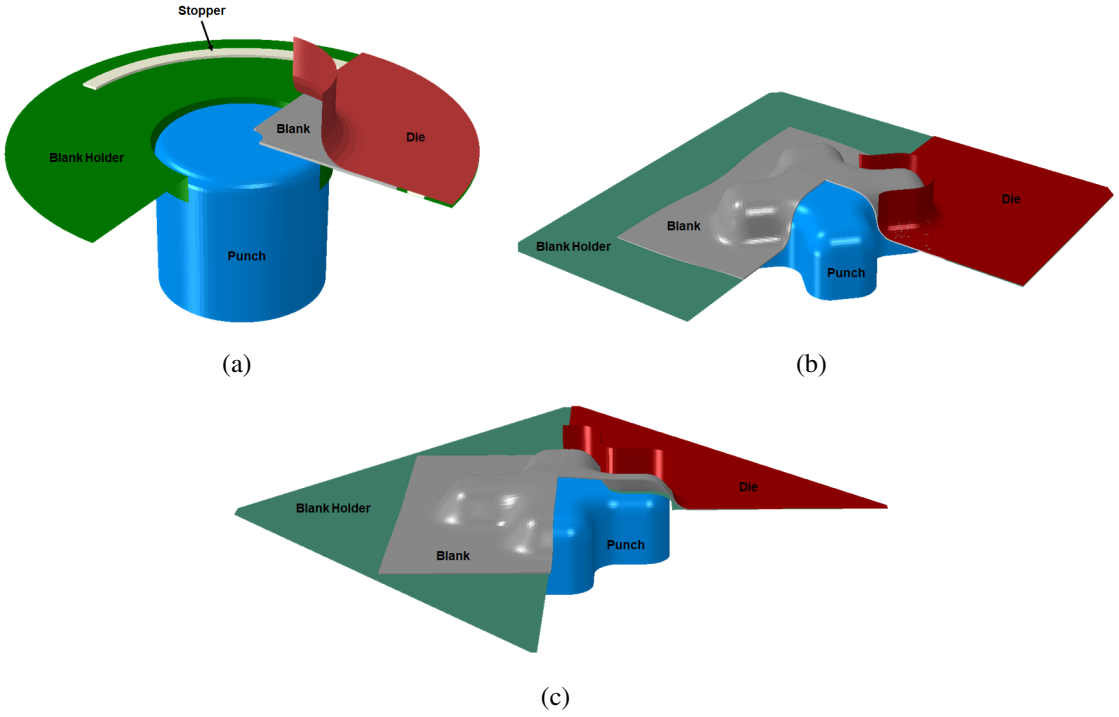
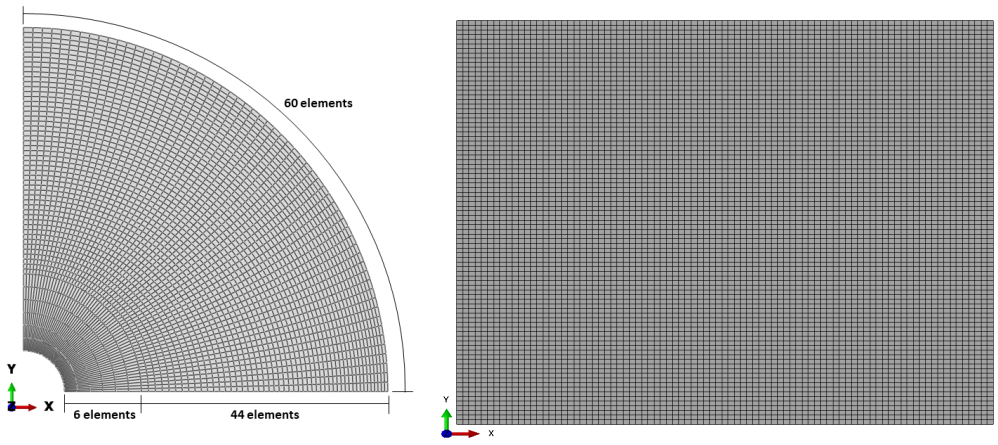


Figure 5.1: Finite element 3D models: Swift test (a); Cross die forming test - cross shape (b) and plus shape (c).

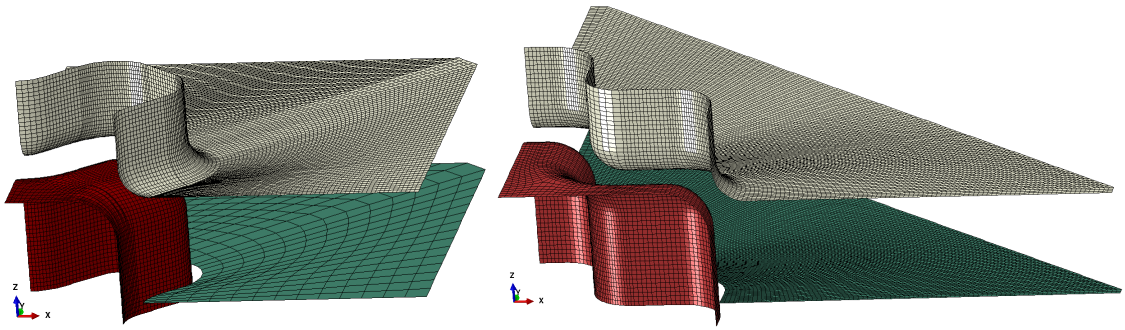
To create the finite element model, the blank, as well as the stopper ring for cylindrical cup test, were discretized by three layers of eight node deformable elements with reduced integration (C3D8R type of Abaqus library). The spatial elements arrangement in XY plane can be seen in figure 5.2. Based on the limiting drawing ratio of the studied materials, the initial blank diameter varies from 110 mm to 125 mm. Regarding the cross die forming, the blank has a fixed dimension, having a square shape with 270x270 mm^2. The tools were modeled as rigid surfaces for both benchmark tests. However, taking advantage of the cylindrical cup geometric characteristics, analytical rigid surfaces were employed. On the other hand, the cross die presented a more complex configuration, demanding a different approach, since the analytical available option in ABAQUS does not have the capability to represent the tools shape. Therefore, discretized rigid surfaces were considered to effectively model its form. For the boundary conditions, the die was fixed and the punch and blank holder move upward.



(a) (b)

Figure 5.2: Considered blank discretization: a) Swift test; b) cross die forming test.

Moreover, as previously addressed in section 4.3, the benchmark test allows to obtain distinct final geometries, such as an “X” or a “+” relative to rolling direction. In order to ensure comparable results between these two approaches, the discretization and position of the blank was kept constant while the tools positions were changed. Consequently, two separate sets of numerical tools were used (figure 5.1), leading to different discretizations. Figure 5.3 illustrates the discretizations used for the two sets of tools employed in the numerical simulations.



(a) Cross shape "X" (b) Plus shape "+"

Figure 5.3: Finite element cross die test tools discretization.

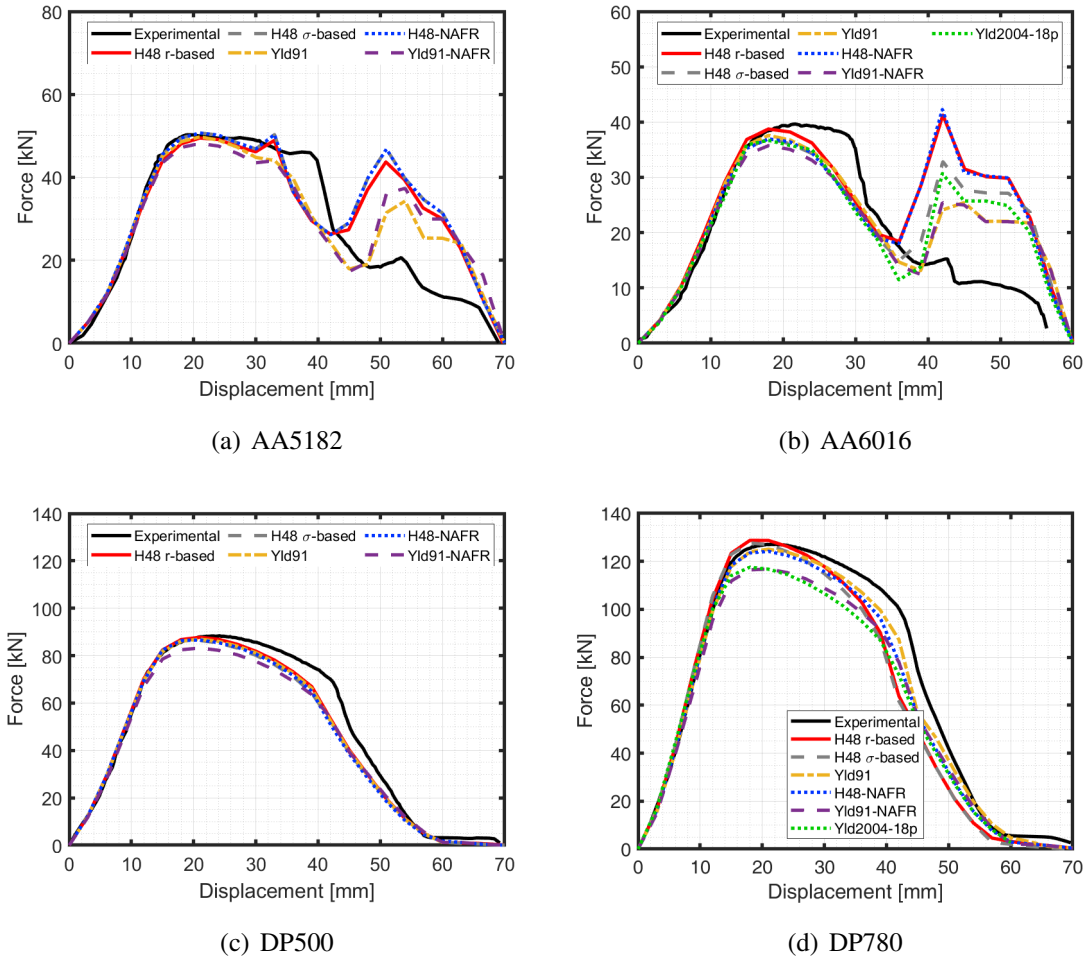
The interacting surfaces were assigned a constant Coulomb friction coefficient. The material modeling took into account the constitutive parameters identified and discussed in the previous chapter. The elastoplastic behavior of the blank was characterized by using various yield criteria, namely Hill'48, Yld91 and Yld2004-18p, in conjunction with isotropic hardening defined by the Swift+Voce constitutive model. To implement these constitutive models, a user material subroutine was implemented. Detailed numerical conditions for each benchmark test are provided in their respective sections, outlining the specific parameters used.

5.2 Swift test

The following sections present the obtained numerical results and corresponding analysis of the deep drawing cylindrical cup test, regarding the evolution of punch force with its displacement, the cup total height and consequent earing profiles, and also the thickness distribution along the cup cross-section. These numerical outcomes provide a comprehensive understanding of the implemented yield criteria concerning the prediction performance based on a comparison with the experimental findings.

5.2.1 Evolution of punch force

The numerical simulations of the deep drawing of the cylindrical cup were performed, considering the Hill'48 and Yld91 yield criteria for AFR and NAFR approaches, and also the application of Yld2004. Figure 5.4 illustrates the comparison of punch force evolution with displacement between the experimental data and the results obtained from numerical simulation.



(a) AA5182 (b) AA6016

(c) DP500 (d) DP780

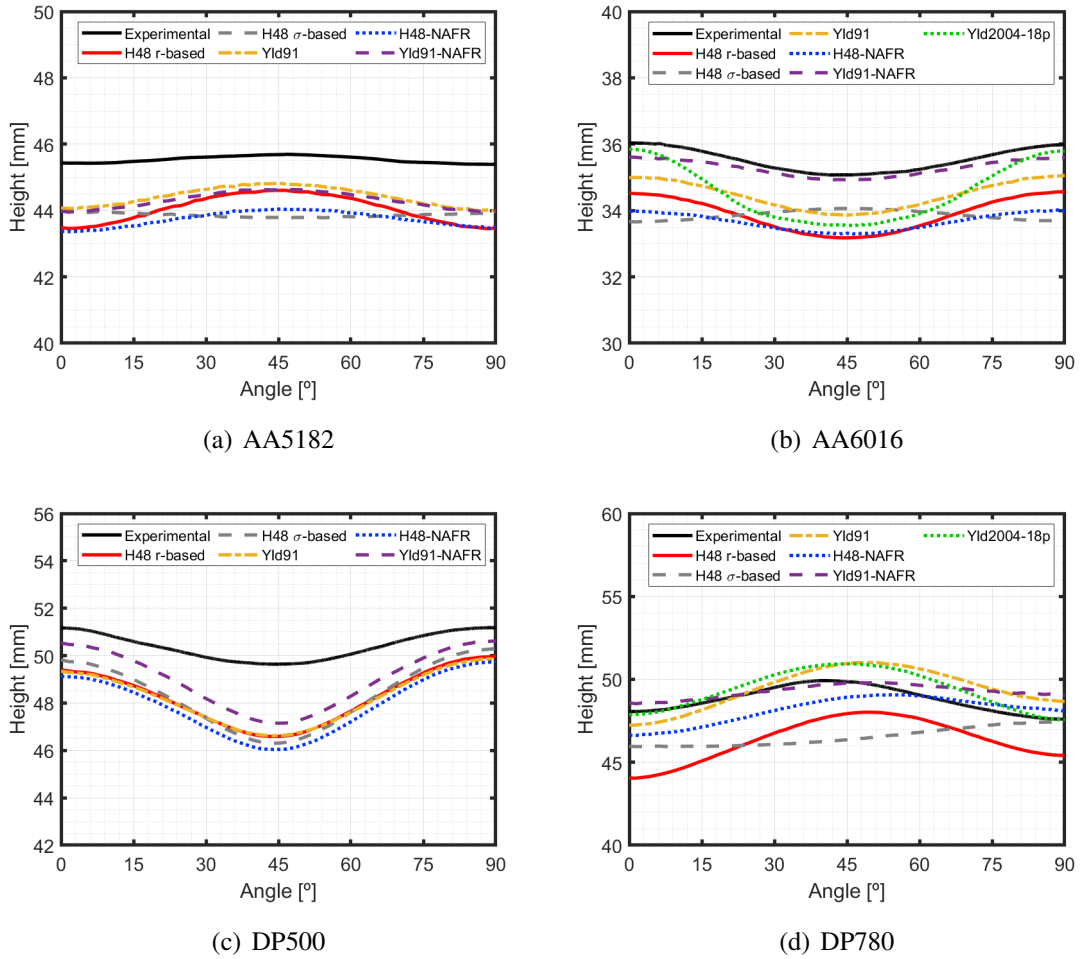
Figure 5.4: Punch force vs displacement for the materials in study using different yield criteria.

As can be seen in figure 5.4, the numerical simulation result predictions show a close correlation with the experimental punch force evolution for both dual-phase steels. However, in case of the aluminum alloys, it can be highlighted a difference in the final drawing stage, which is related with the blank ironing that occurs between the punch and die. For AA5182, the punch force predictions for the ironing stage that starts for a punch displacement of approximately 50 mm, are overestimated for all the considered yield criteria, but the Hill'48 based models show a higher value tendency that Yld91. The same is observed for the AA6016, where a peak value is attained after the initiation of the ironing stage (around 40 mm). Moreover, it is important to note that the maximum punch force is attained for a similar punch displacement of approximately 20 mm across various materials. This occurrence coincides with the stage at which the die and punch shoulder radii are completely shaped within the cylindrical cup. Concerning the Barlat yield criteria family,

it became evident that the results were consistently and remarkably similar across all the models.

5.2.2 Earing evolution - cup height

For the ear height, the resulting predictions from numerical simulation were compared to experimental measurements taken for 90 degrees of the cylindrical cup, starting from the rolling direction orientation up to the transverse direction. The total height was measured using the same methodology applied in the experiments, where the flat bottom of the cup served as the reference point. Figure 5.5 presents a comparison using the different yield criteria proposed.



(a) AA5182

(b) AA6016

(c) DP500

(d) DP780

Figure 5.5: Comparison of numerical earing height profiles of the materials in study with experimental data using different implemented yield criteria.

From figure 5.5 it is evident that all yield criteria predict the same number of ears as observed in the experiments, except for the Hill'48 strain-based criterion for DP780, and an opposite behavior for both aluminum alloys.

Even though AA5182 exhibits almost an isotropic behavior, it has a small ear that occurs at 45° relative to the rolling direction. As the amplitude is very low, only the Yld91 criterion for both formulations and the Hill'48-NAFR reproduce a similar profile. However, being the material aluminum, the Yld91 criterion is the one that comes closest to experimental data. The same occurs for AA6016, both flow rule formulations of Yld91 present a closer prediction, being the Yld91-AFR, the constitutive model that gave better results. The Yld2004 present an higher amplitude ($\Delta R > 0$) than the other constitutive models since the parameters used, reproduce a higher variation, visible at 45º.

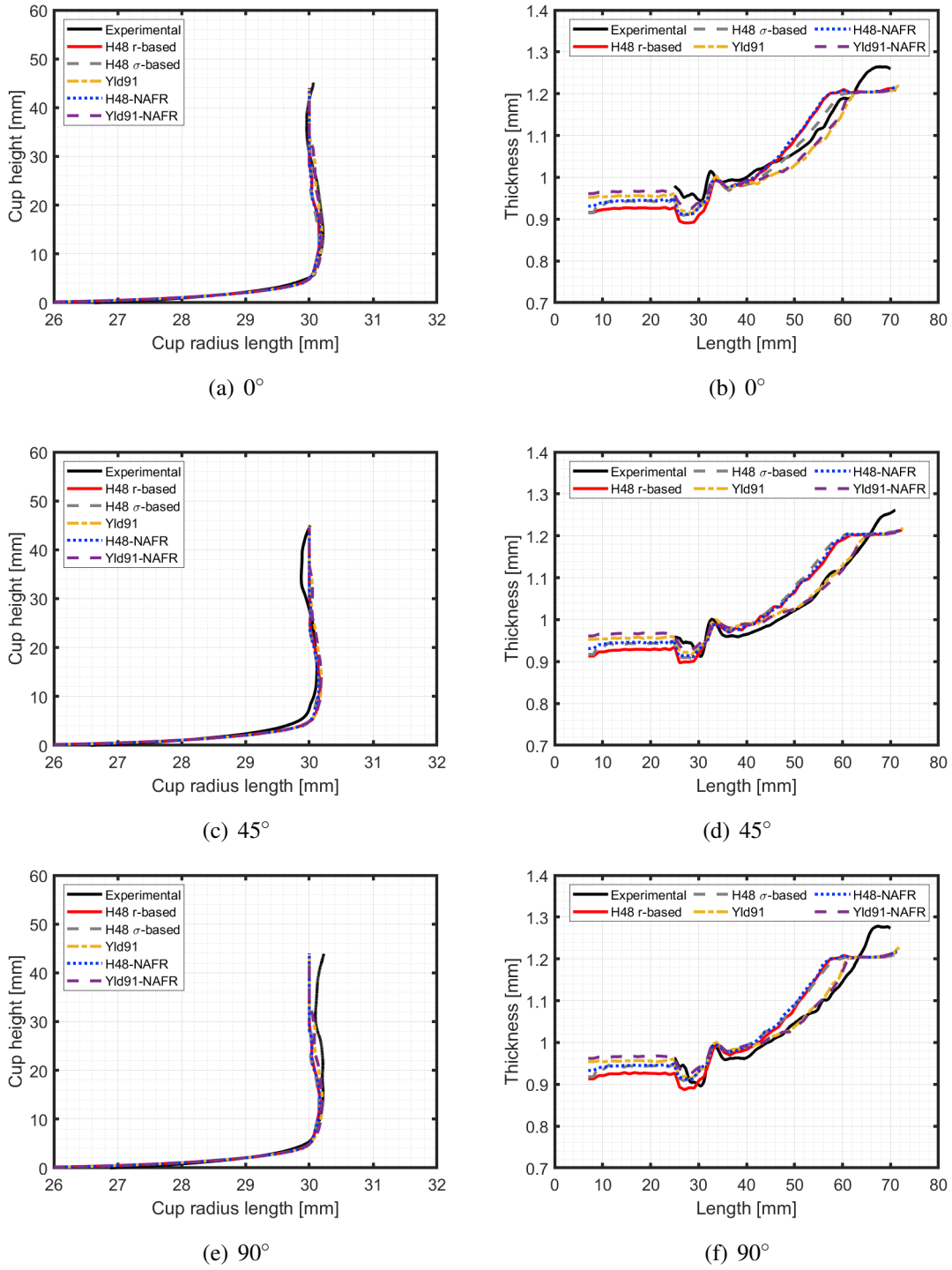
In the case of DP500, the predicted earing profile shows a consistent evolution of ear height from 0° to 90° relative to the rolling direction, aligning with the observed experimental behavior. Notably, at 45° a lower ear valley is observed and it is important to mention that there are significant differences in the magnitude of the ear height values. The disparity between the maximum and minimum ear height values is well pronounced for all the considered yield criteria, where the value for 45º is overestimated. Regarding the predictions of the DP780 behavior, the variation between the results obtained is evident. The Hill'48 yield criteria family was not capable to replicate the experimental measurements, yet, the Yld91-NAFR criterion was able to reproduce and predict the experimentally observed behavior considerably well, being in general the best earing profile prediction. Also, there is an improvement in ears height prediction for 0º and 90º when using Yld2004 instead of Yld91.

In summary, when comparing the numerical predictions to the experimental data, the non-associated flow rule (NAFR) approach demonstrates a closer similarity to the observed earing behavior for all the considered materials. Between the two yield criteria, Hill'48 and Yld91, the Yld91-NAFR approach provides more accurate predictions in terms of ear height distribution, thus exhibiting a higher level of agreement with the experimental results than the Hill'48-NAFR. Although, there is still room for improvement in achieving higher accuracy, particularly for specific angles, since the aluminum experience an ironing and the tools are modeled as rigid surfaces.

5.2.3 Cup wall thickness profiles

In this section, a comprehensive comparison between the experimental data and numerical thickness distribution along the cup wall (from the center up to the top border) was made. The measurements were conducted along three distinct directions: parallel to the

material rolling direction (0°), diagonal (45°) and transverse (90°). The analysis specifically focuses on establishing a correlation between the cup section length and the cup section thickness. Figures 5.6 to 5.9 present the obtained results, as well as the section geometrical profiles.

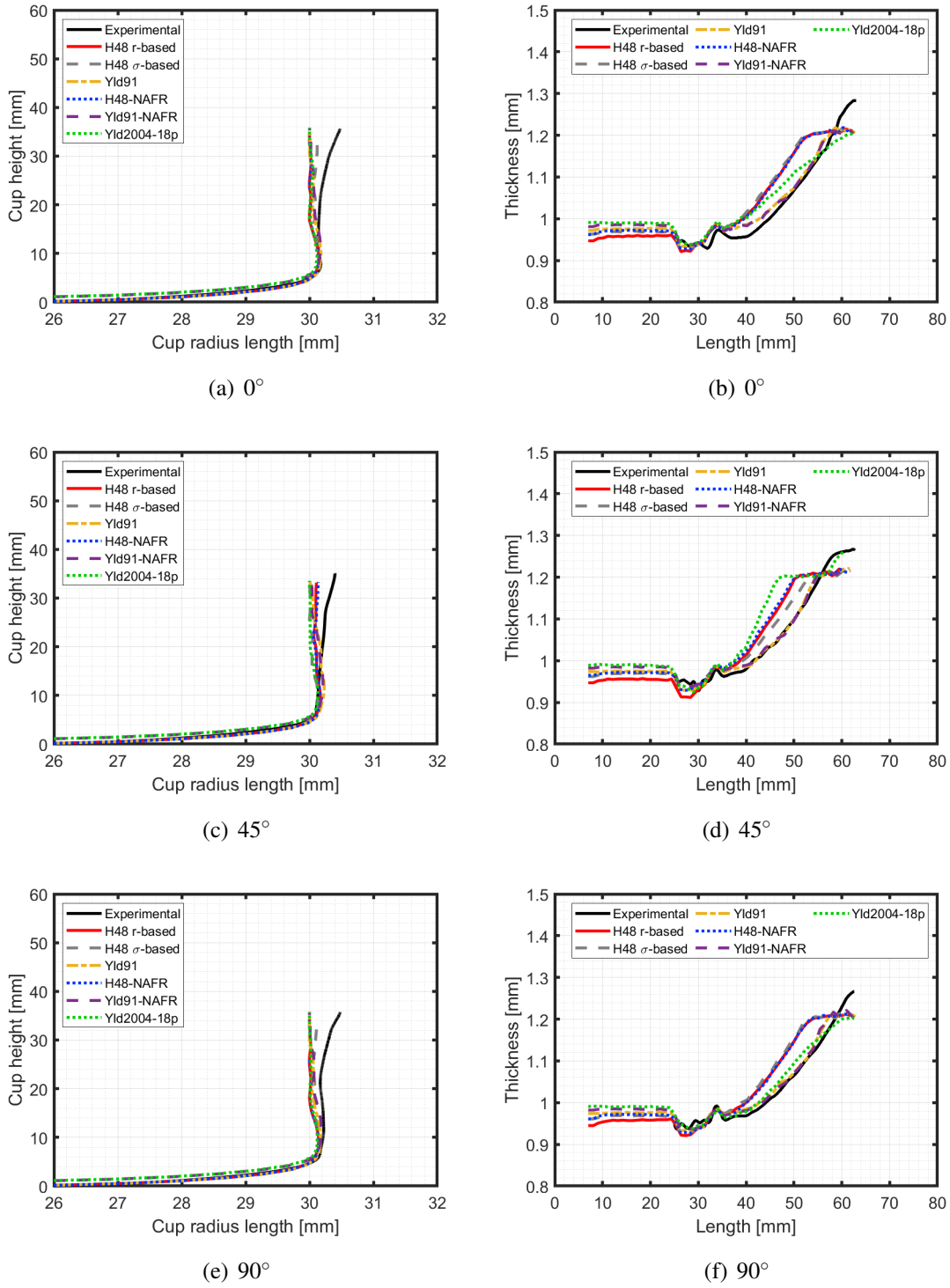


(a) 0° (b) 0°

(c) 45° (d) 45°

(e) 90° (f) 90°

Figure 5.6: Comparison of profile geometry and wall thickness distribution for the AA5182 aluminum alloy using different yield criteria.

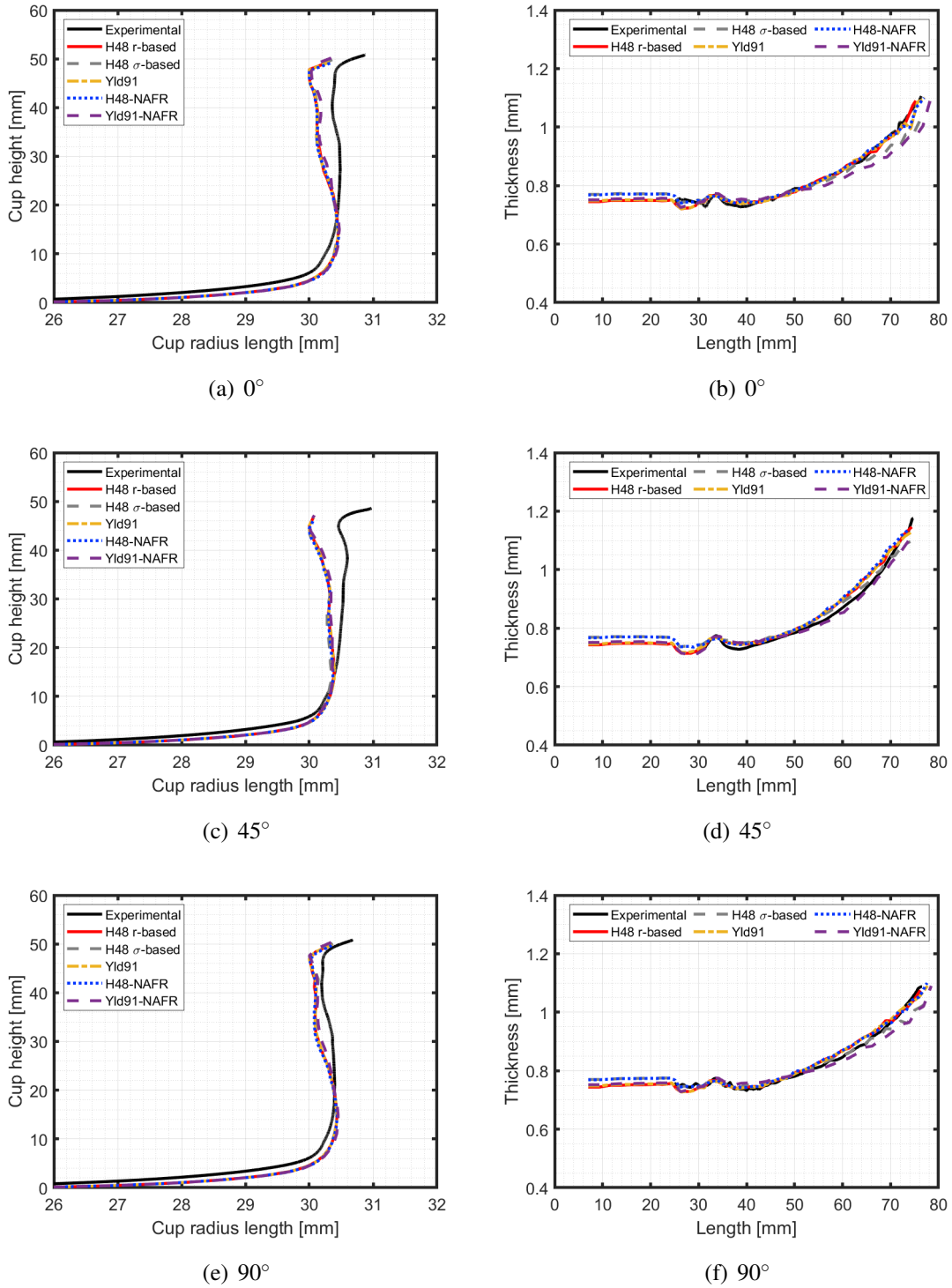


(a) 0° (b) 0°

(c) 45° (d) 45°

(e) 90° (f) 90°

Figure 5.7: Comparison of profile geometry and wall thickness distribution for the AA6016 aluminum alloy using different yield criteria, with rigid tools.

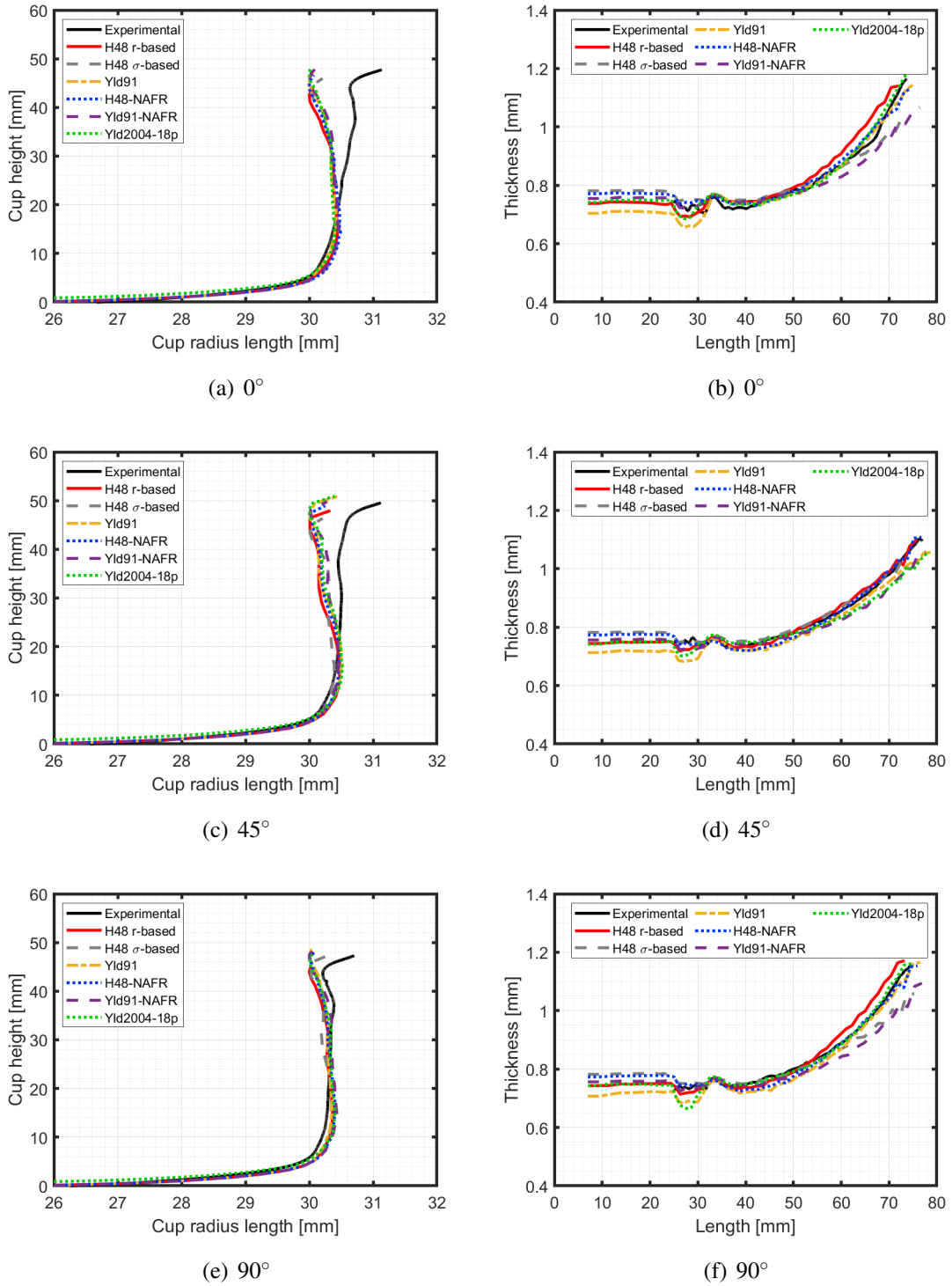


(a) 0° (b) 0°

(c) 45° (d) 45°

(e) 90° (f) 90°

Figure 5.8: Comparison of profile geometry and wall thickness distribution for the DP500 steel alloy using different yield criteria.



(a) 0° (b) 0°

(c) 45° (d) 45°

(e) 90° (f) 90°

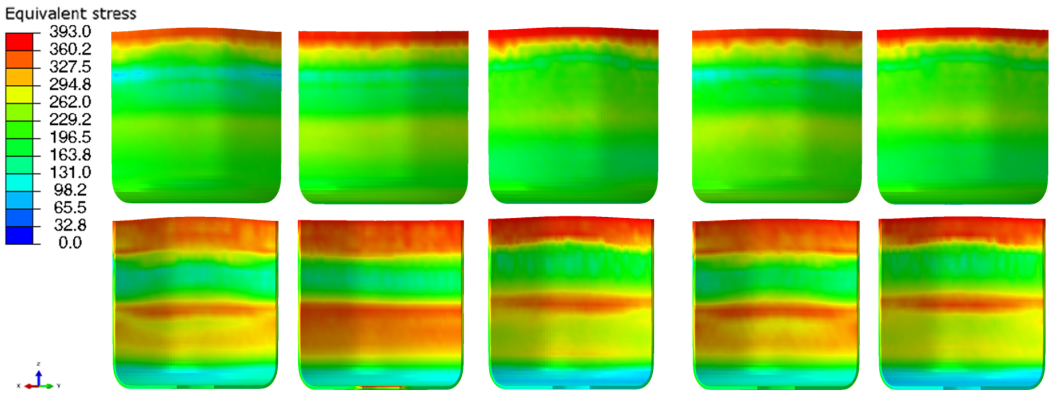
Figure 5.9: Comparison of profile geometry and wall thickness distribution for the DP780 steel alloy using different yield criteria.

The previous results present a comprehensive evaluation of the wall thickness distribution along the cup wall length, comparing the numerical predictions obtained using different yield criteria with the corresponding experimental data profiles. The analysis focuses on evaluating the overall tendency of the wall thickness and its agreement with experimental observations. In general, the numerical simulations capture the trend of the wall thickness distribution, where the obtained thickness values consistently exceed the initial thickness, indicating the presence of a compressive stress state in the circumferential direction. However, some constitutive models have a better prediction performance than others.

As expected, the thickness for the aluminum cups near the border has the maximum value of 1.2 mm, which corresponds to the existent clearance between the die and punch. Although, the experimental value is a slightly higher than the numerical prediction, a difference that could be attributed to tools modeling as rigid surfaces. Also, the Hill'48 yield criteria for both considered flow rule formulations overestimate the increase in thickness along the cup wall and consequently a higher ironing region than the Yld91 model for the different analyzed cross sections. Moreover, the increase in cup wall thickness for AA6016 is notably higher at 45º relative to the rolling direction, reaching the ironing stage earlier. This can be related to the lower ear height, which note only was observed in the numerical predictions but also in experiments. Also, when observing the punch force evolution of the aluminum alloys in figure 5.4, it is possible to see a correlation between the Yld91 criterion and experimental result. The fact that the punch force curve predicted by the Yld91 (AFR and NAFR) is closer to the experimental curve is also reflected in the evolution of the thickness distribution along the cup wall.

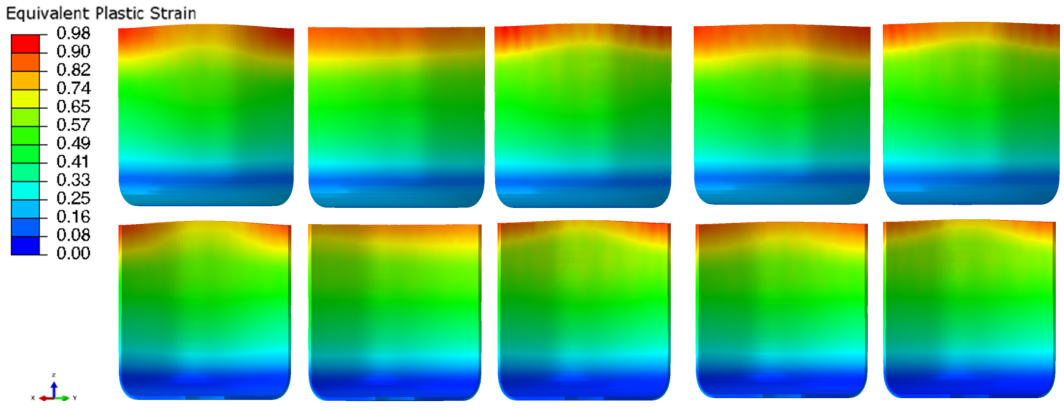
On the other hand, for DP500, of all the yield criteria considered, none could fully predict the thickness distribution profile. For 0° and 90°, the Hill'48 criterion based on strain ratios and the NAFR are able to describe the thickness evolution along the cup, however it overestimates the thickness increase in the median zone of the cup wall for 45°, being this profile better described by both formulations (AFR and NAFR) of Yld91 criterion. In the case of DP780, the cup thickness distributions obtained using the Yld91 yield criteria and the non-associated flow rule approach based on Hill'48 model exhibit a good correlation with the experimentally measured data. However, the Hill'48 NAFR has a better prediction accuracy for all evaluated cup sections, because for 45º the Yld91 underestimate the thickness increase during the final stage of the deep drawing process.

Figures 5.10 to 5.17 provide comprehensive insights into the contour distribution of equivalent stress and equivalent plastic strain for each yield criteria considered. These figures have a specific emphasis on the materials AA5182, AA6016, DP500 and DP780, respectively. The outer cup surface is present on top of the figure and the inner cup surface in the bottom.



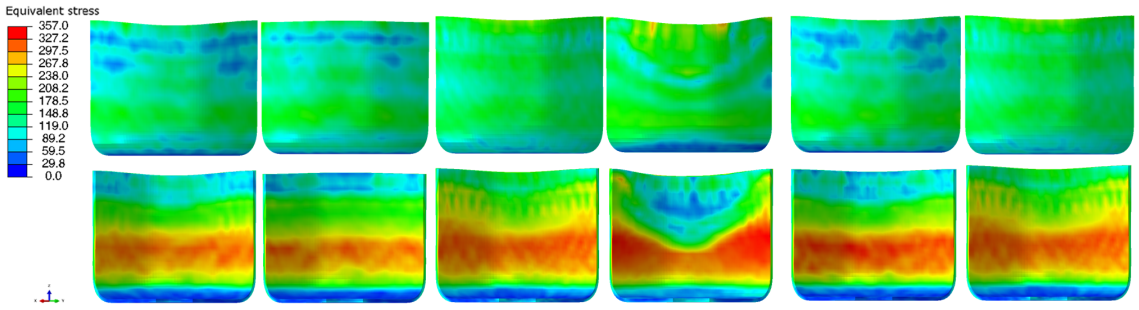
(a) AFR (b) NAFR

Figure 5.10: Outer (top) and inner (bottom) equivalent stress contours for AA5182 cylindrical cup using the different yield criteria: a) Hill'48 r-based, Hill'48 s-based, Yld91; b) Hill'48, Yld91 (from left to right, respectively).



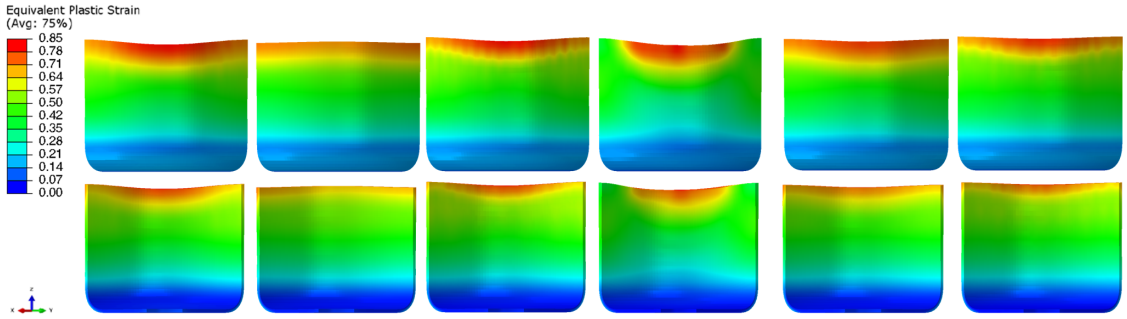
(a) AFR (b) NAFR

Figure 5.11: Outer (top) and inner (bottom) equivalent plastic strain contours for AA5182 cylindrical cup using the different yield criteria: a) Hill'48 r-based, Hill'48 s-based, Yld91; b) Hill'48, Yld91 (from left to right, respectively).



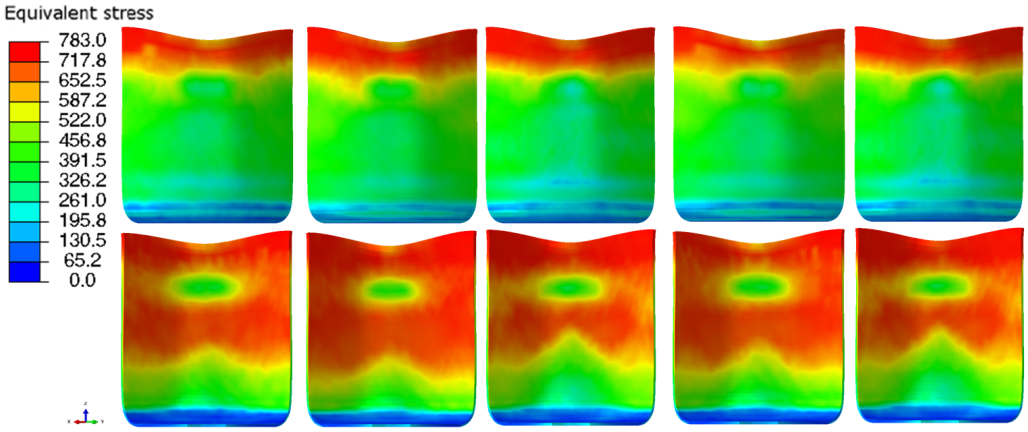
(a) AFR (b) NAFR

Figure 5.12: Outer (top) and inner (bottom) equivalent stress contours for AA6016 cylindrical cup using the different yield criteria: a) Hill'48 r-based, Hill'48 s-based, Yld91, Yld2004; b) Hill'48, Yld91 (from left to right, respectively).



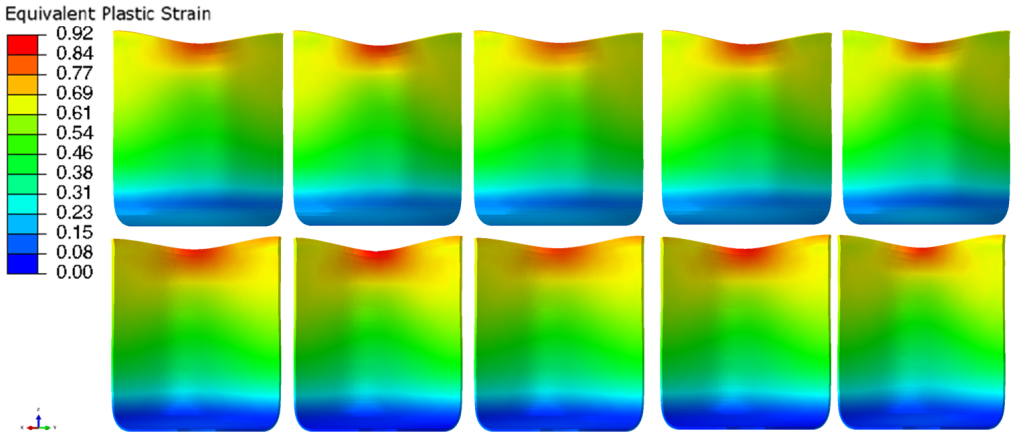
(a) AFR (b) NAFR

Figure 5.13: Outer (top) and inner (bottom) equivalent plastic strain contours for AA6016 cylindrical cup using the different yield criteria: a) Hill'48 r-based, Hill'48 s-based, Yld91, Yld2004; b) Hill'48, Yld91 (from left to right, respectively).



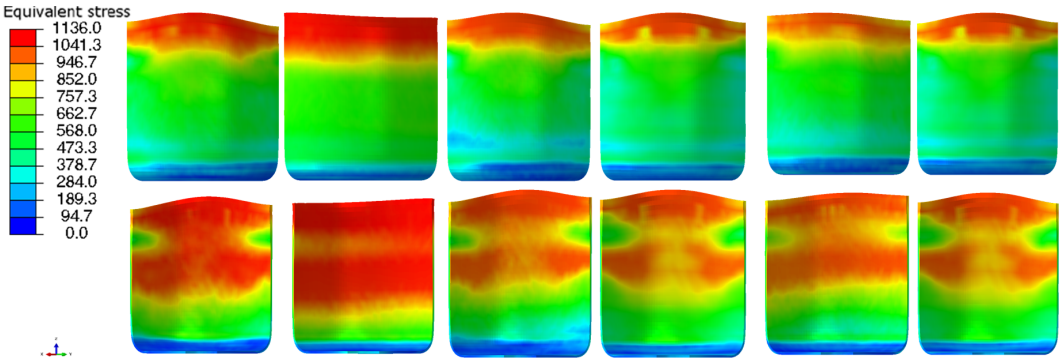
(a) AFR (b) NAFR

Figure 5.14: Outer (top) and inner (bottom) equivalent stress contours for DP500 cylindrical cup using the different yield criteria: a) Hill'48 r-based, Hill'48 s-based, Yld91; b) Hill'48, Yld91 (from left to right, respectively).



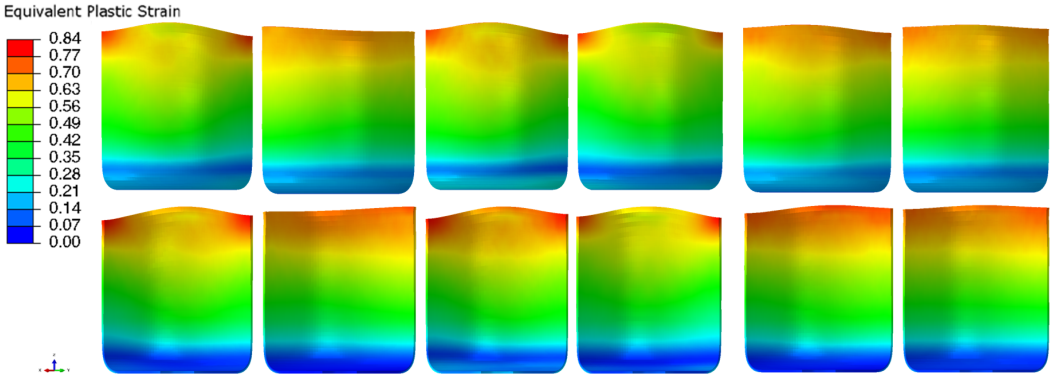
(a) AFR (b) NAFR

Figure 5.15: Outer (top) and inner (bottom) equivalent plastic strain contours for DP500 cylindrical cup using the different yield criteria: a) Hill'48 r-based, Hill'48 s-based, Yld91; b) Hill'48, Yld91 (from left to right, respectively).



(a) AFR (b) NAFR

Figure 5.16: Outer (top) and inner (bottom) equivalent stress contours for DP780 cylindrical cup using the different yield criteria: a) Hill'48 r-based, Hill'48 s-based, Yld91; b) Hill'48, Yld91, Yld2004 (from left to right, respectively).



(a) AFR (b) NAFR

Figure 5.17: Outer (top) and inner (bottom) equivalent plastic strain contours for DP780 cylindrical cup using the different yield criteria: a) Hill'48 r-based, Hill'48 s-based, Yld91; b) Hill'48, Yld91, Yld2004 (from left to right, respectively).

5.2.4 Modeling elastic tools

In numerical simulation, the behavior of tools can be either rigid or elastic, depending on the nature of the analysis and the accuracy required. While rigid tools simplify calculations by assuming no deformation, modeling elastic tools introduces a higher level of realism and accuracy to the simulation process. The use of elastic tools becomes even more obvious when analyzing processes that involve contact between tools and sheet metal blank. In these cases, the ability of the tool to deform itself and adapt to the conditions becomes fundamental, resulting in a more precise description of the interaction between contact surfaces. Modeling the tools elasticity provides insights into stress distribution and contact forces that are inherently linked to the tools behavior and the structural response. This level of realism is indispensable in fields such as material forming, where the shape and mechanical behavior of the tool play a crucial role in the final shape of the component

Since an ironing phase is evident in the case of aluminum, the tools are modeled with eight node deformable elements with reduced integration (C3D8R type of Abaqus library). The tools material have a purely elastic behavior. Figure 5.18 shows the used numerical model in this analysis.

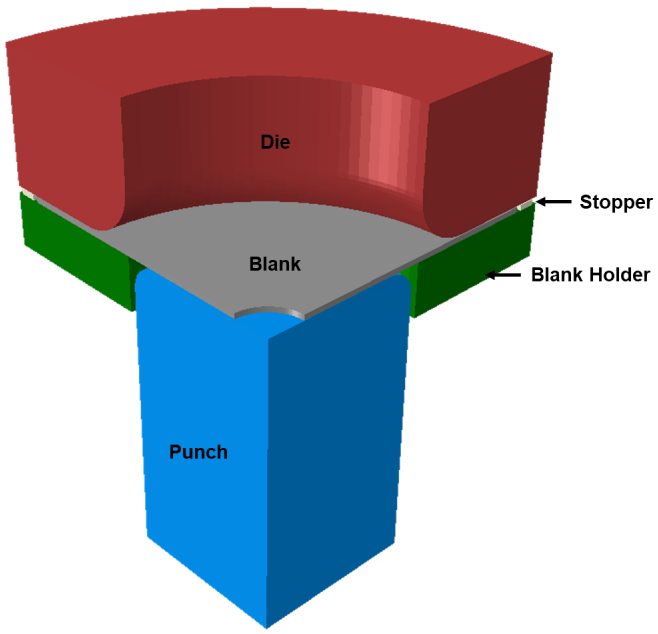
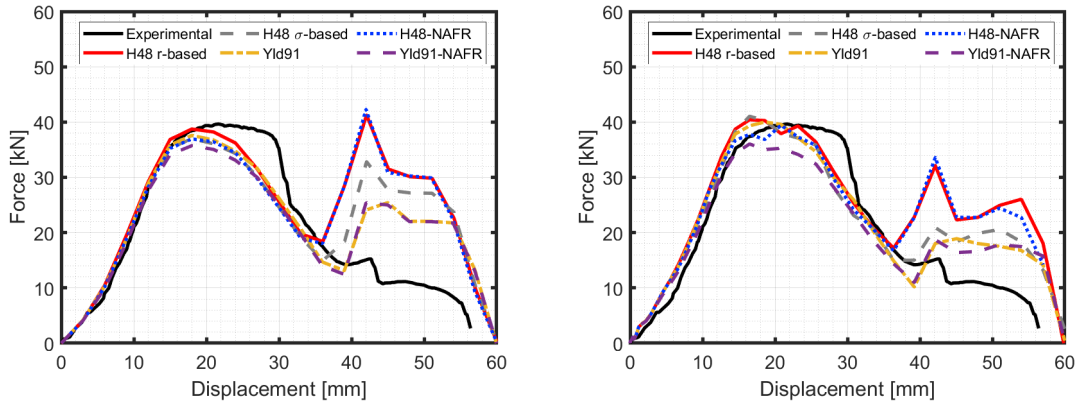


Figure 5.18: Swift test numerical model with deformable tools.

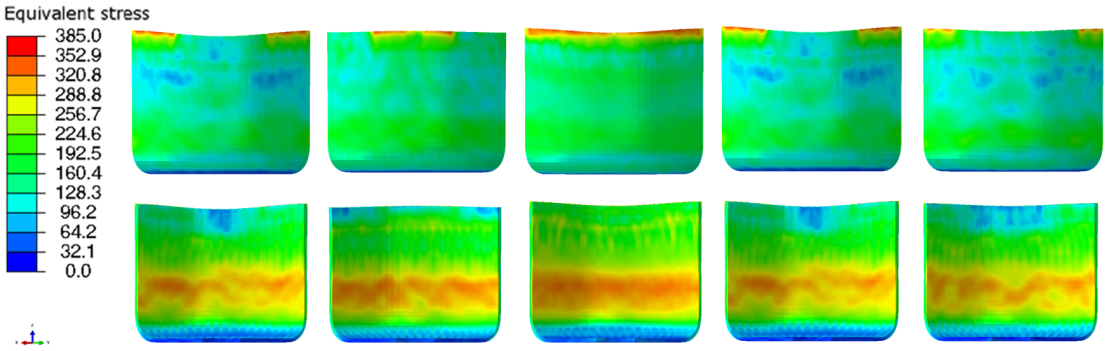
To compare the results between using rigid or elastic tools, a similar analysis was made (punch *vs* displacement evaluation, earing profiles and wall thickness distribution). Figure 5.19 presents the punch force with displacement for the aluminum AA6016.



(a) Rigid (b) Elastic

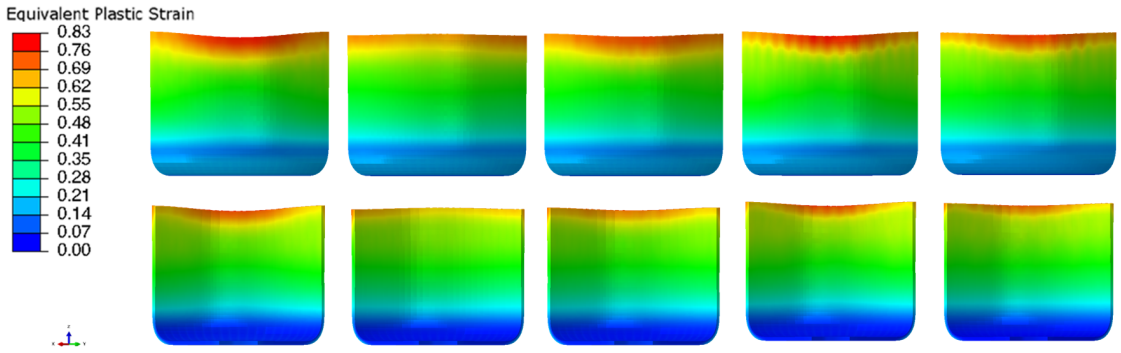
Figure 5.19: Punch force *vs* displacement for the AA6016 using different yield criteria.

As can be seen from the evolution of the punch force, with the use of elastic tools there is a clear improvement in the final stage of the drawing process, where the ironing takes place. The force applied during this stage is much lower compared to rigid tool modeling, in general a 20% reduction is achieved. Also, the Yld91 criterion provided better predictions than the Hill'48 criterion for the AA6016 and with reduction of the required force, there is a clear approximation to the behavior obtained experimentally. Figures 5.20 and 5.21 provides insights into the contour distribution of equivalent stress and equivalent plastic strain for each yield criteria considered using the elastic tools.



(a) AFR (b) NAFR

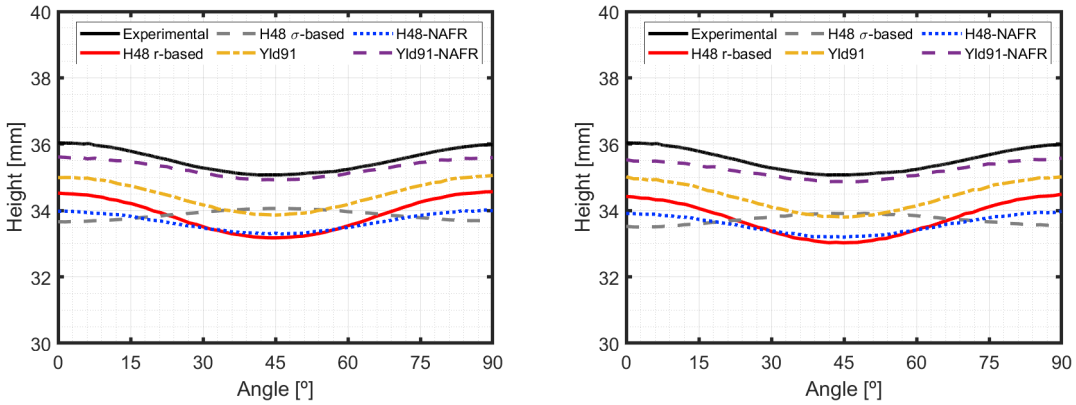
Figure 5.20: Outer (top) and inner (bottom) equivalent stress contours for AA6016 for elastic tools using the different yield criteria: a) Hill'48 r-based, Hill'48 s-based, Yld91; b) Hill'48, Yld91 (from left to right, respectively).



(a) AFR (b) NAFR

Figure 5.21: Outer (top) and inner (bottom) equivalent plastic strain contours for AA6016 for elastic tools using the different yield criteria: a) Hill'48 r-based, Hill'48 s-based, Yld91; b) Hill'48, Yld91 (from left to right, respectively).

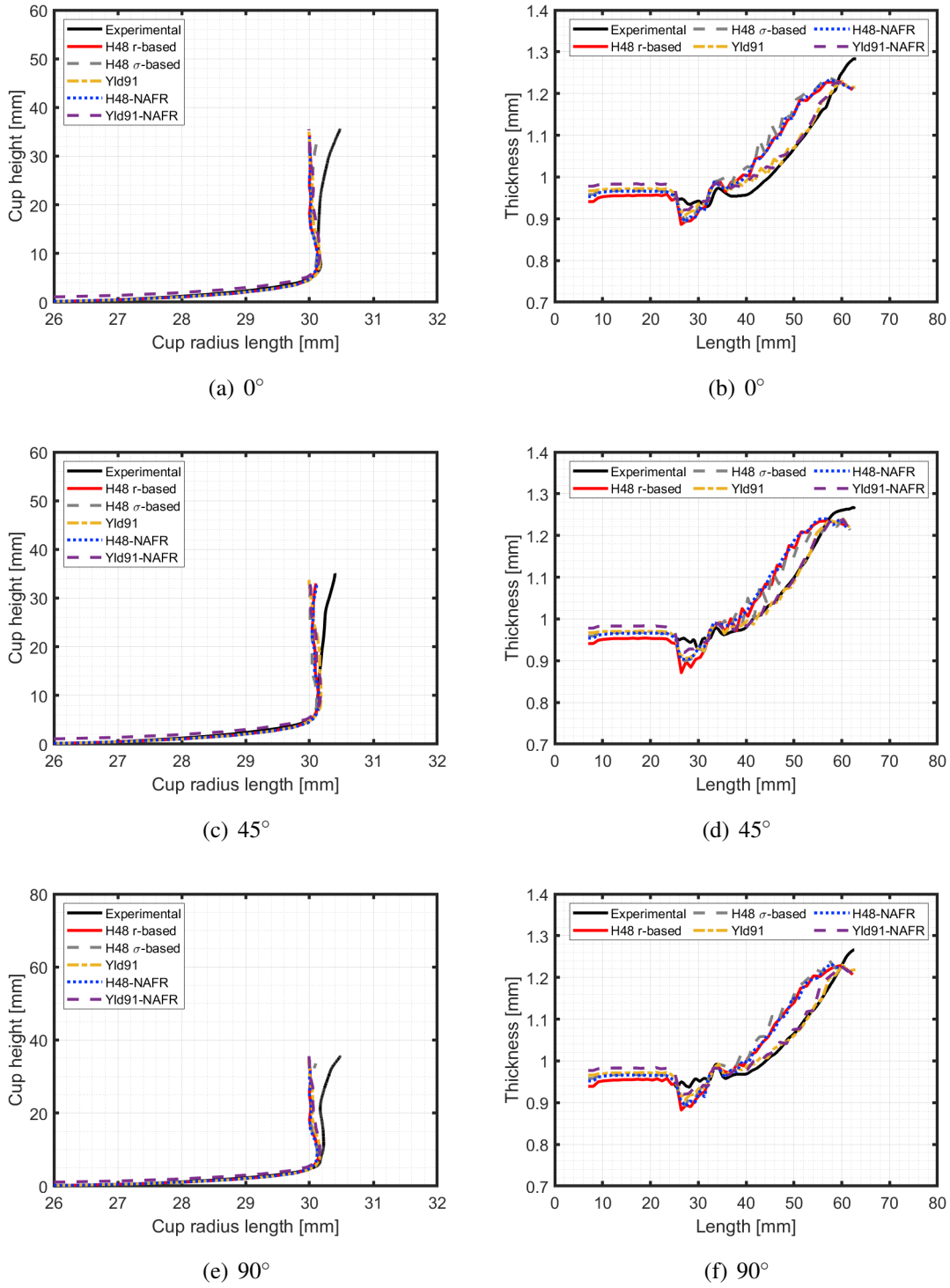
Figure 5.22 presents a comparison of numerical earing height profiles using rigid and elastic modeling tools for AA6016.



(a) Rigid (b) Elastic

Figure 5.22: Comparison of numerical earing height profiles of the AA6016 in study with experimental data for the different implemented yield criteria.

As opposed to what was observed in the evolution of the punch force, the profile of the ears does not show significant changes. In general, for all used plasticity criteria, there is a slight decrease in the predicted cup height. This can be due to the fact that the elastic deformation of the tools slightly increases the clearance between them. Regarding the cup wall thickness distribution (figure 5.23), a similar trend and results are obtained.



(a) 0° (b) 0°

(c) 45° (d) 45°

(e) 90° (f) 90°

Figure 5.23: Comparison of profile geometry and wall thickness distribution for the AA6016 aluminum alloy for the different yield criteria, with elastic tools.

5.2.4.1 Pressure dependent contact

In many cases, the friction force is proportional to the normal force or pressure between the surfaces by the friction coefficient (μ). The friction coefficient is a constant that depends on the nature of the surfaces in contact and the conditions under which they interact. However, in some situations, the coefficient of friction can change with variations in the normal force. For instance, in some cases, like the deep drawing cylindrical test, the tools might deform under higher pressure, causing changes in the microscopic interactions between the contact surfaces. This can lead to changes in the friction behavior. In such cases, the friction force is not solely determined by the normal force and the relationship becomes pressure-dependent [55, 58].

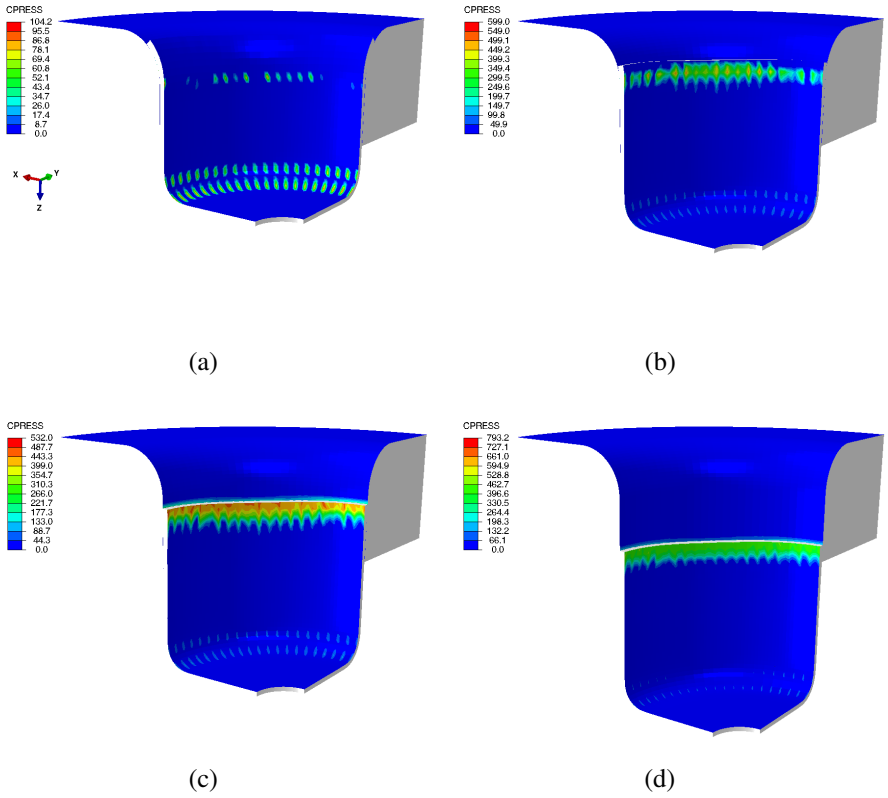


Figure 5.24: Contact pressure distribution in a AA6016 cylindrical cup for different moments of the ironing phase.

Considering the previous research works findings [55, 57, 59] and the levels of contact pressure present in figure 5.24, as well as a frictionless numerical simulation result (as a base reference), the coefficient of friction was modeled as a function of contact pressure. Its evolution for AA6061 is shown in figure 5.25.

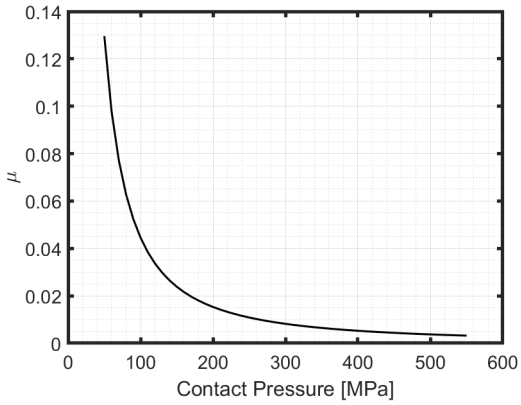
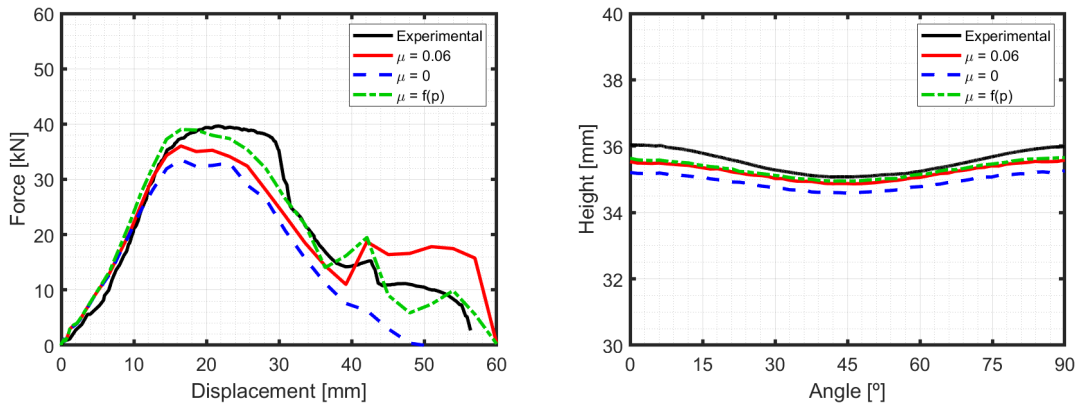


Figure 5.25: Contact pressure distribution in a AA6016 cylindrical cup for different moments of the ironing phase.

To evaluated the impact of using a pressure-dependent friction behavior, additional numerical simulations were performed for the alloy AA6016 using the Yld'91-NAFR criterion. Figure 5.26 presents the obtained punch force and earing height profile. It was considered the same friction coefficient used in numerical simulations with rigid and elastic tools, and also a frictionless analysis, as a basis of comparison.



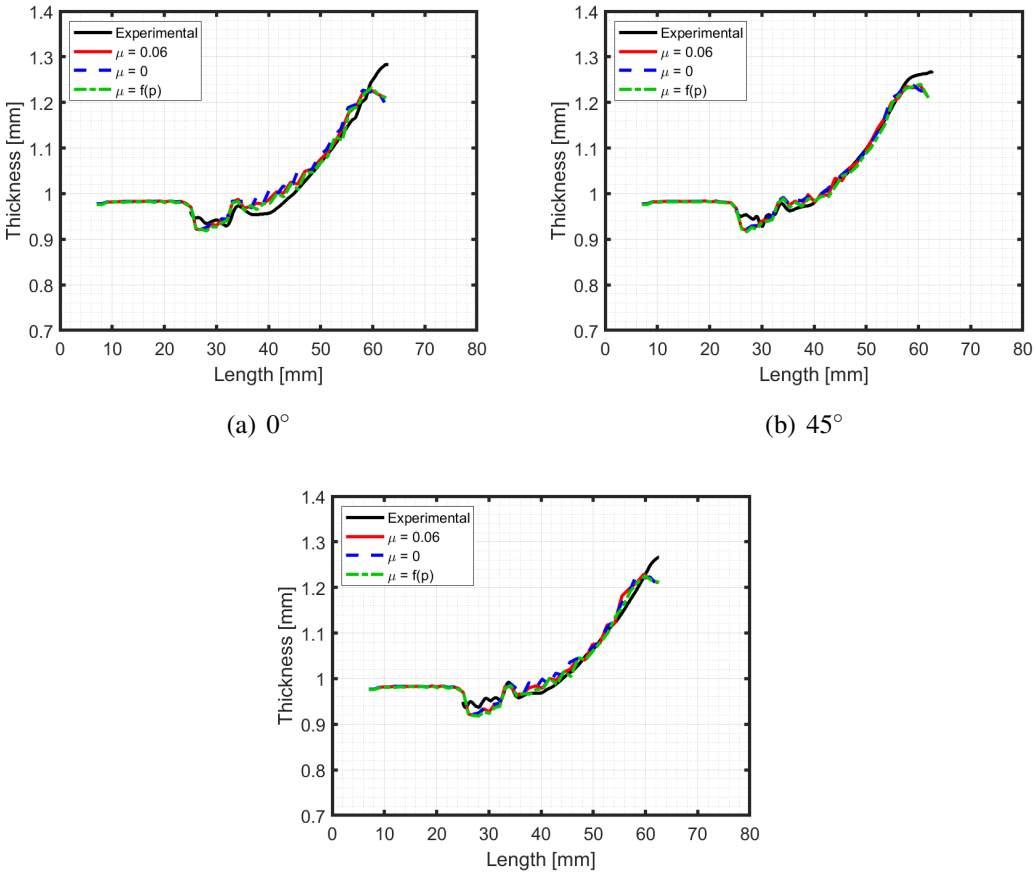
(a) Punch force vs displacement

(b) Earing height profile

Figure 5.26: Comparison of numerical punch force and earing height profiles of the AA6016 for elastic tools, with a constant and pressure dependent friction coefficient.

By using a friction coefficient dependent on the contact pressure imposed, the predictions obtained by numerical simulation are closer to the experimental. In the case of the punch force, there is a clear reduction in the ironing phase, as recorded in the experimental test. On the other hand, the different contact conditions do not change the behavior of the wall thickness distribution, as can be seen in the figure 5.27. Also in the case of

the cup ear height there is an approximation to the experimental measured value. This indicates that the use of this approach has a much higher impact than the use of elastic tools instead of rigid ones, as shown in figure 5.28.

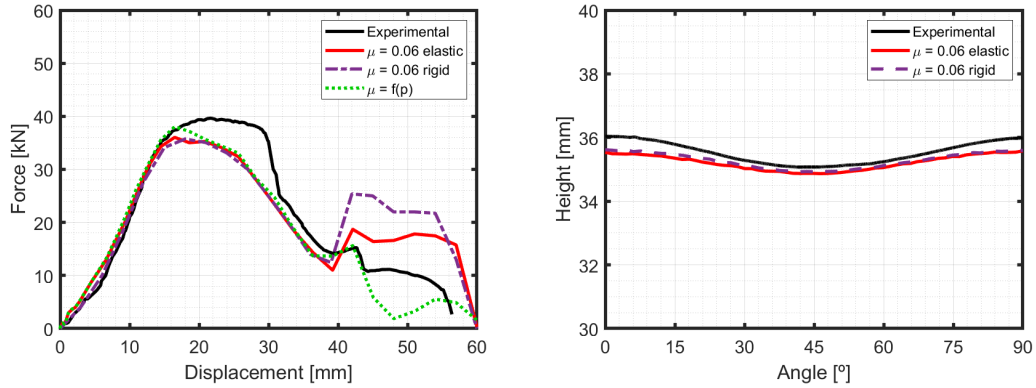


(a) 0°

(b) 45°

(c) 90°

Figure 5.27: Comparison of wall thickness distribution of the AA6016 for elastic tools, with a constant and pressure dependent friction coefficient.



(a) Punch force vs displacement

(b) Earing height profile

Figure 5.28: Comparison of numerical punch force and earing height profiles of the AA6016 using rigid and elastic tools, with a constant and pressure dependent friction coefficient.

Figures 5.29 and 5.30 provides insights into the contour distribution of equivalent stress and equivalent plastic strain for the different friction conditions.

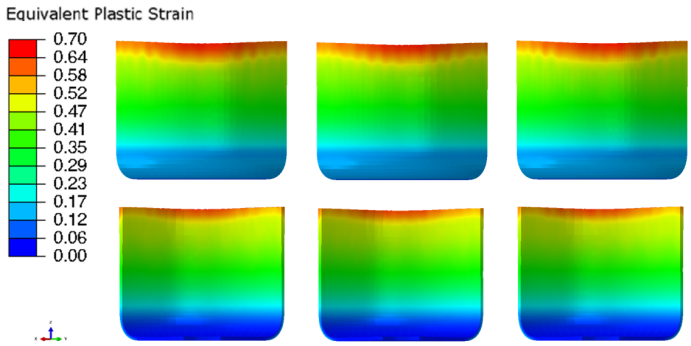


Figure 5.29: Outer (top) and inner (bottom) equivalent plastic strain contours for AA6016 for elastic tools using the different friction conditions, $\mu = 0.06$, $\mu = 0$ and $\mu = f(P)$.

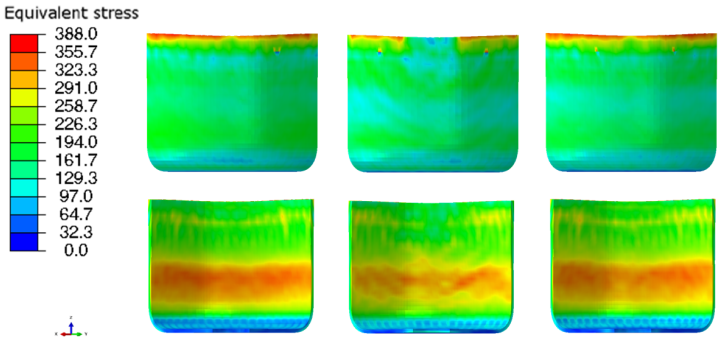


Figure 5.30: Outer (top) and inner (bottom) equivalent stress contours for AA6016 for elastic tools using the different friction conditions, $\mu = 0.06$, $\mu = 0$ and $\mu = f(P)$.

5.3 Split ring test

Deep drawing cups contain a significant amount of residual stress that leads to a higher springback when the elastic recovery is allowed. This springback not only enhances measurement precision but also minimize experimental discrepancies. The rings have a standard position and size, identical to the conditions considered in the experimental benchmark.

To evaluate the springback phenomenon, numerical simulations were performed based on a modified Demeri split ring test, which takes into account the material deformation history from cup forming. Figure 5.31 shows a scheme with the splitting procedure and correspond springback that was applied in the numerical simulations, which allow for stress relief.

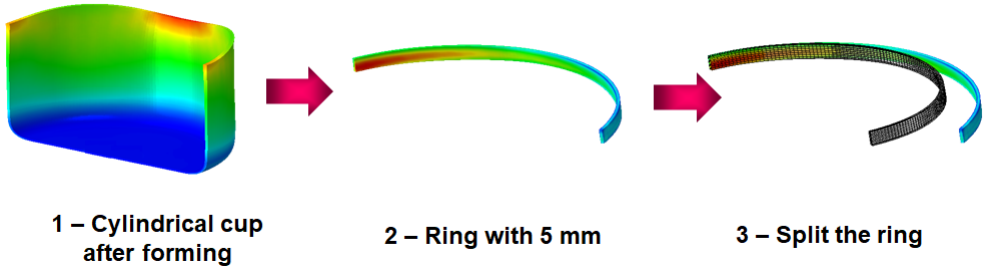


Figure 5.31: Adopted numerical strategy of split ring springback analysis.

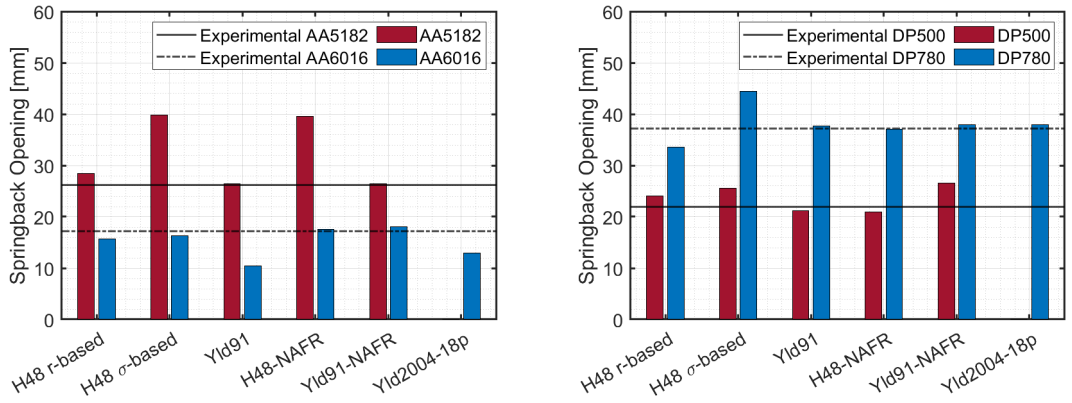
Table 5.1 lists springback results obtained by the numerical simulations for the four materials and all implemented yield criteria. To observe the trend between the different constitutive models, the obtained values were graphically represented. Figure 5.32 presents such values, as well as, the experimentally measured split ring opening and the figure 5.33 a qualitative comparison between the numerical and experimental R1 ring.

Table 5.1: Results of split ring.

Material	Ring	Experimental	H48 r-based	H48 s-based	Yld91	H48 NAFR	Yld91 NAFR	Yld04
AA5182	1	26.20	28.4	39.82	26.44	39.60	26.47	—
	3	27.91	30.32	32.78	27.76	30.79	27.85	
AA6016	1	17.16	15.72	16.34	10.45	17.56	18.06	12.95
	3	14.71	3.74	8.92	4.88	6.32	8.28	8.83
DP500	1	21.91	24.06	25.52	21.14	20.95	21.60	—
	3	34.15	29.12	29.94	19.71	33.17	34	
DP780	1	37.13	33.62	44.48	37.74	37.09	37.91	37.99
	3	46.12	40.3	52.66	34.57	47.31	46.12	46.95

As can be seen in figure 5.32, the Yld91 criterion, for both AFR and NAFR formulations, is the one that predicts springback values closest to the experimentally measured for AA5182. However, for AA6016, both Hill48 and Yld91 criteria provide identical behaviors when considering a NAFR formulation. For DP500 steel, two criteria, Yld91-AFR and Hill'48-NAFR, predict a ring opening close to the experimental one, but slightly below. For DP780, the springabck prediction with the Hill'48-NAFR criterion gives a result equal to the experimental one, with an error lower than 1%. However also the Yld91 criterion, for both flow rule formulations, as well as Yld2004 give satisfactory results. It

is also verified that the Hill'48 s-based criterion presents a tendency to overestimate the elastic recovery after forming.

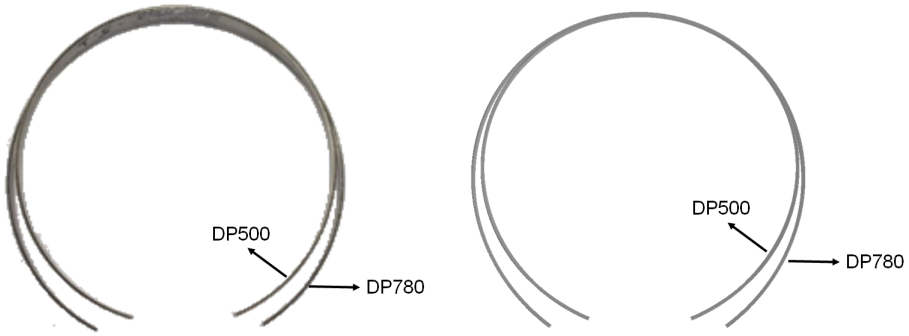


(a) Aluminum alloys (b) Dual-phase steels

Figure 5.32: Split ring springback comparison using the first ring (R1) for the aluminum alloys and dual-phase steels.



(a) Aluminum alloys



(b) Dual-phase steels

Figure 5.33: Split ring experimental (left) and numerical (right) comparison of the first ring (R1) for the materials in the study.

In order to have a complementary analysis of previously obtained results, the equivalent stress contour distributions (appendix B), before and after springback, were analyzed (figure 5.34). For a better visualization of the permanently plastic region, a limit value was established in the stress contour after elastic recovery whose value corresponds to the yield stress of the respective material.

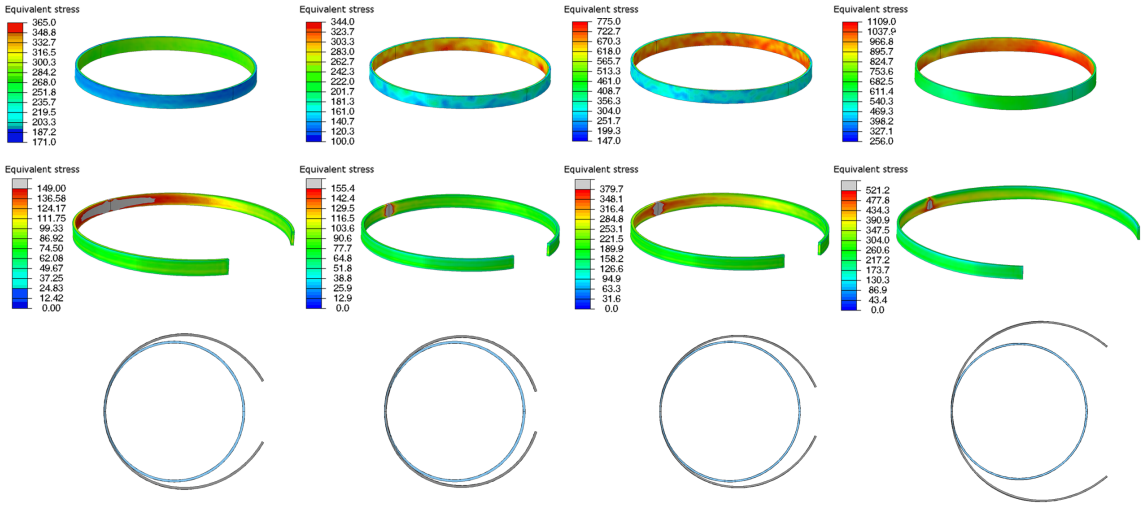


Figure 5.34: Split ring equivalent stress contours for AA5182 (Yld91), AA6016 (Hill'48-NAFR), DP500 (Yld91-NAFR) and DP780 (Hill'48-NAFR), left to right, respectively.

5.4 Cross die forming test

To assess the ability to predict material behavior by different criteria, numerical simulations of the cross die forming test were performed, given the existence of different strain paths, similar to those of industrial processes. In this section, the results obtained in terms of punch force, draw-in and blank thickness distribution will be presented for the two blank orientations, as illustrated in figures 5.35 and 5.36.

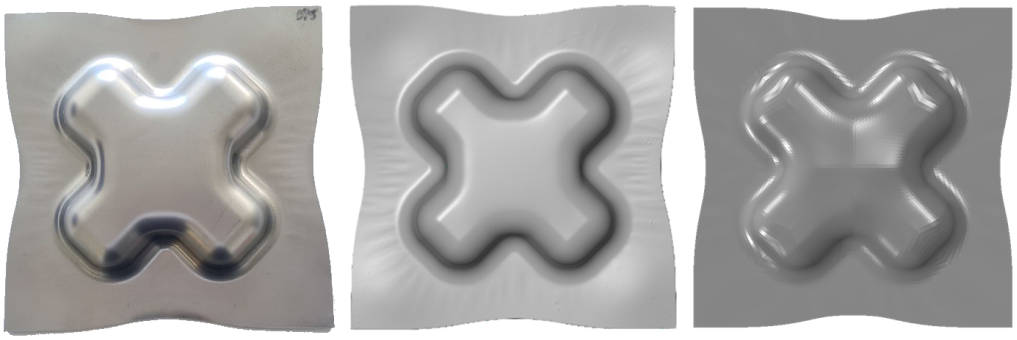


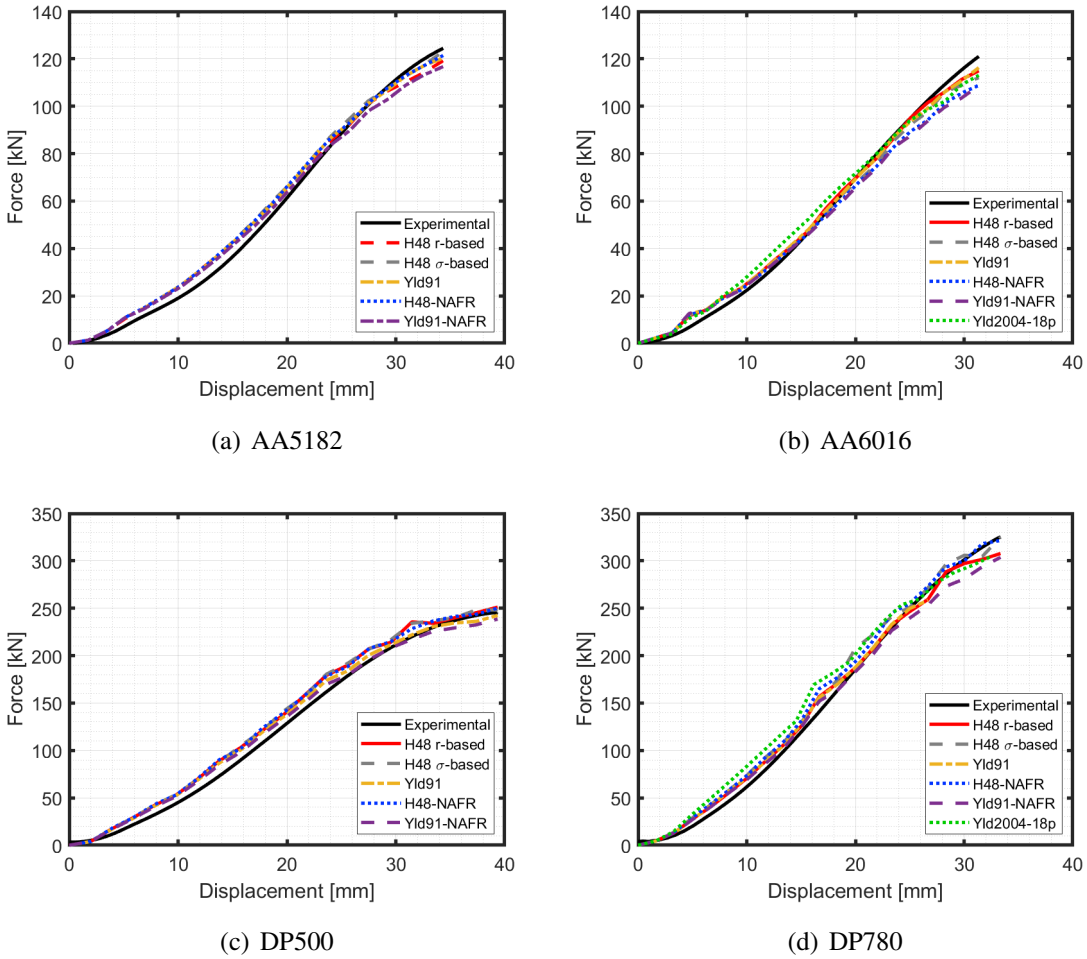
Figure 5.35: Comparison of cross shape between experimental, 3D scan and numerical simulation.



Figure 5.36: Comparison of plus shape between experimental, 3D scan and numerical simulation.

5.4.1 Punch force evolution

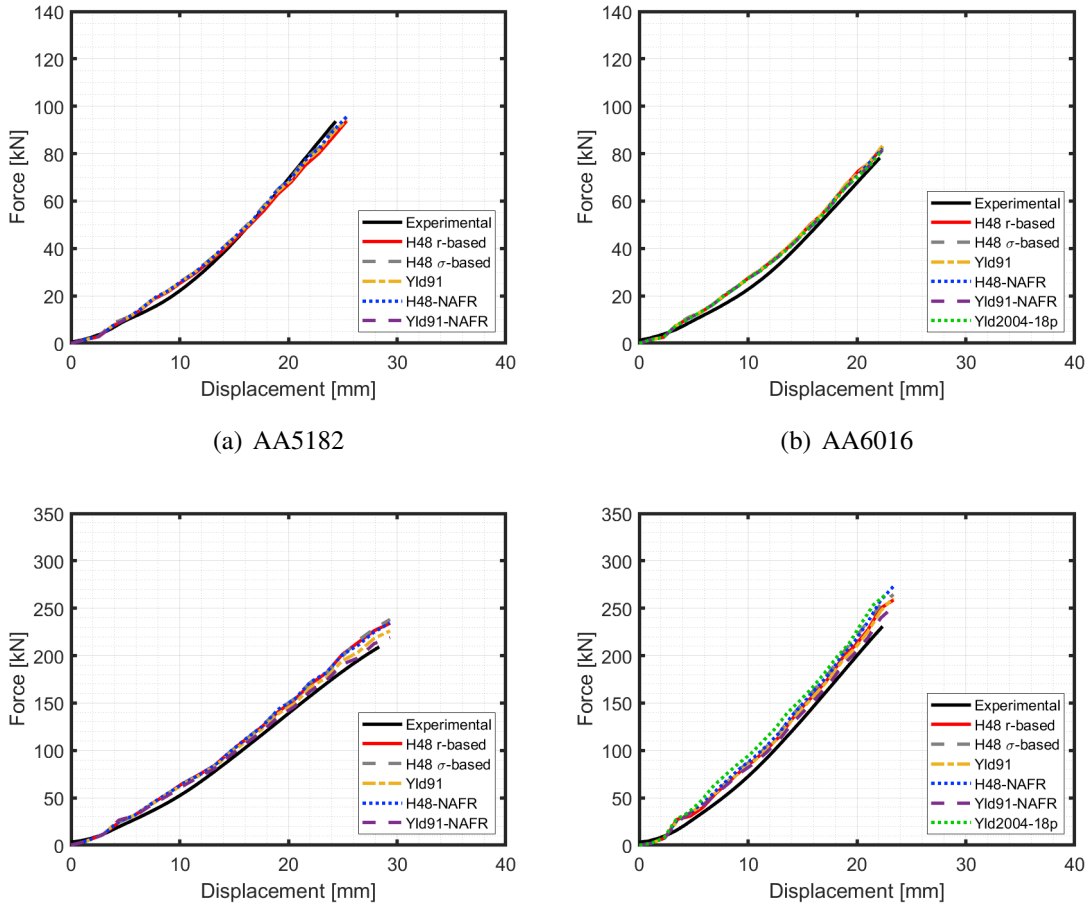
The punch force *vs* displacement curves obtained from numerical simulation using different yield functions are shown in figure 5.37 and figure 5.38, for the cross and plus shape components, respectively.



(a) AA5182 (b) AA6016

(c) DP500 (d) DP780

Figure 5.37: Punch force-displacement curves of the cross die test, for 'X' shape component.



(a) AA5182 (b) AA6016

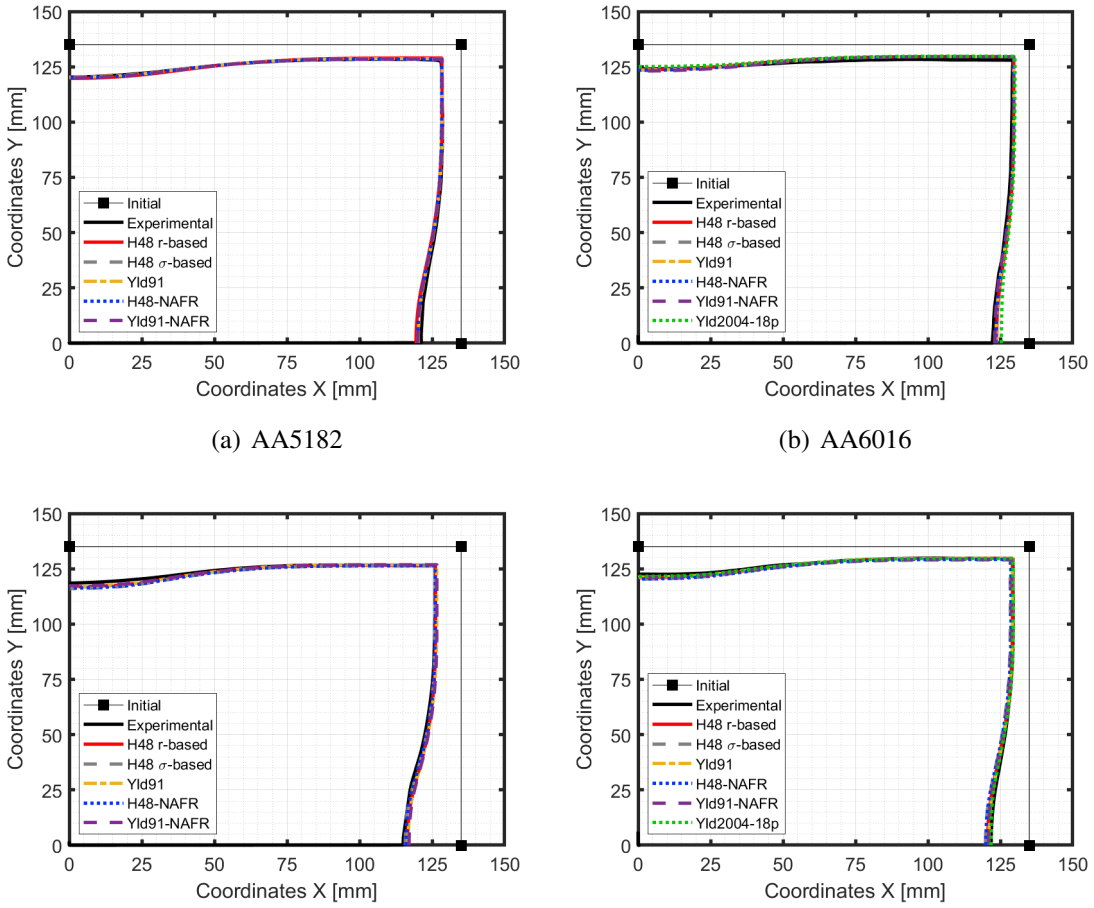
(c) DP500 (d) DP780

Figure 5.38: Punch force-displacement curves of the cross die test, for the plus shape '+' component.

In general, for both blank orientations, all the yield criteria demonstrate a remarkable consistency with experimental data, capturing the general trend of the punch evolution force with displacement. However, the Yld91-NAFR formulation predict a more accurate force vs displacement curve than those based on Hill'48 model, when comparing with experimental results. Additionally, for the cross shape component there is a slightly decrease in the punch force observed in the end of the experiment for all the yield criteria. This can be related with the begging of necking, since the considered punch displacements are near the material failure, which was not the objective of this study. Another observed aspect is the reduced influence of the yield criteria on punch force evolution. For example, although the parameters of Yld2004 model are not optimized for the materials behavior, the predictions manage to reproduce the experimental tendency. This only reinforces the importance of a good definition of the material hardening, as well as the contact and friction conditions between the involved surfaces.

5.4.2 Draw-in

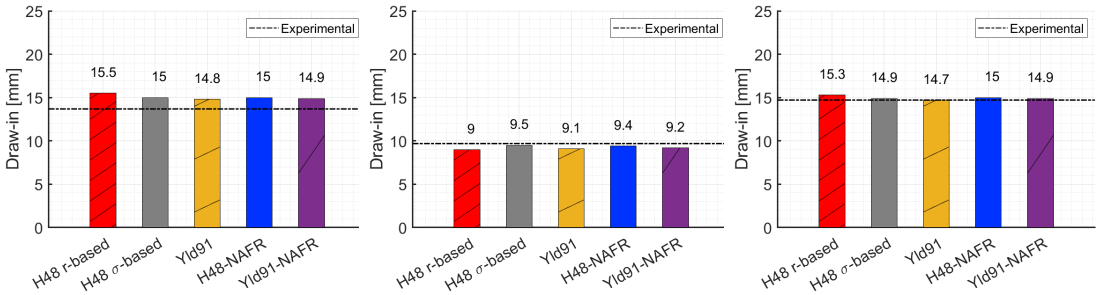
During the deep drawing process, the blank undergoes various forms of deformation. As the punch applies force, the blank material is drawn into the die cavity, causing it to change it shape. This results in a situation where the material near the edges of the blank gets pulled inward along with the movement of the punch. The predicted final cross shape and the draw-in amount for three different section are presented in figure 5.39 to 5.43.



(a) AA5182 (b) AA6016

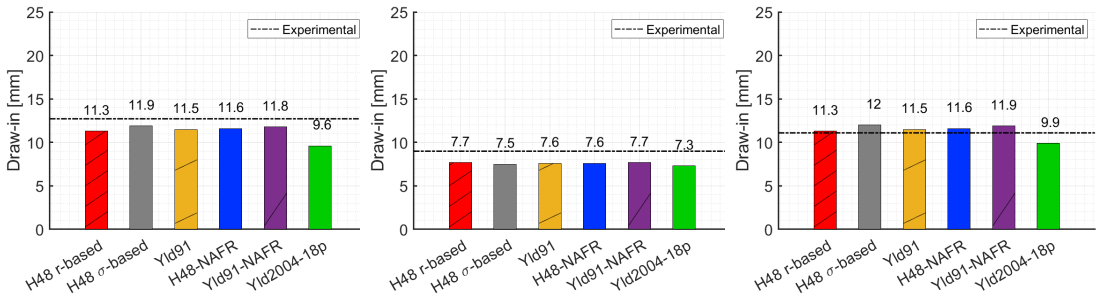
(c) DP500 (d) DP780

Figure 5.39: Draw-in results of the cross die test, for the 'X' shape component



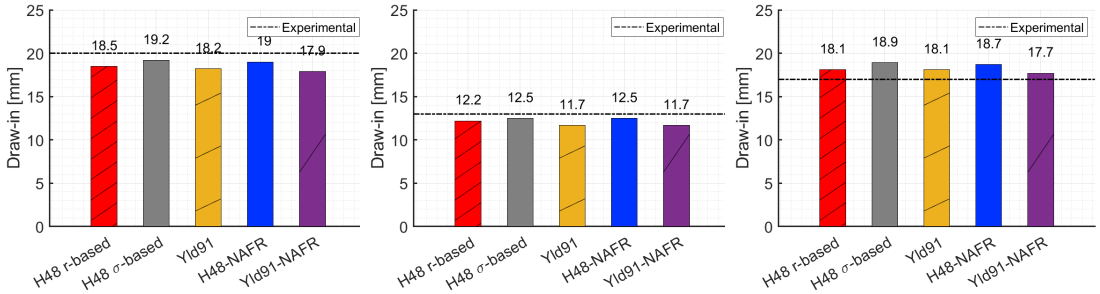
(a) 0° (b) 45° (c) 90°

Figure 5.40: Draw-in 'X' shape results of cross die test, for the AA5182.



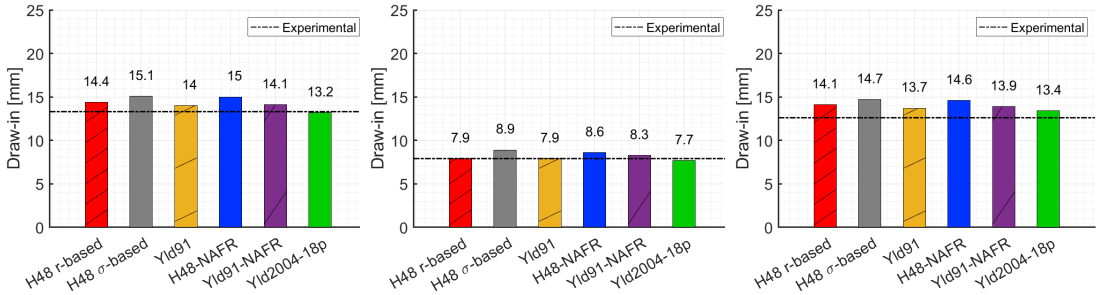
(a) 0° (b) 45° (c) 90°

Figure 5.41: Draw-in 'X' shape results of cross die test, for the AA6016.



(a) 0° (b) 45° (c) 90°

Figure 5.42: Draw-in 'X' shape results of cross die test, for the DP500.



(a) 0° (b) 45° (c) 90°

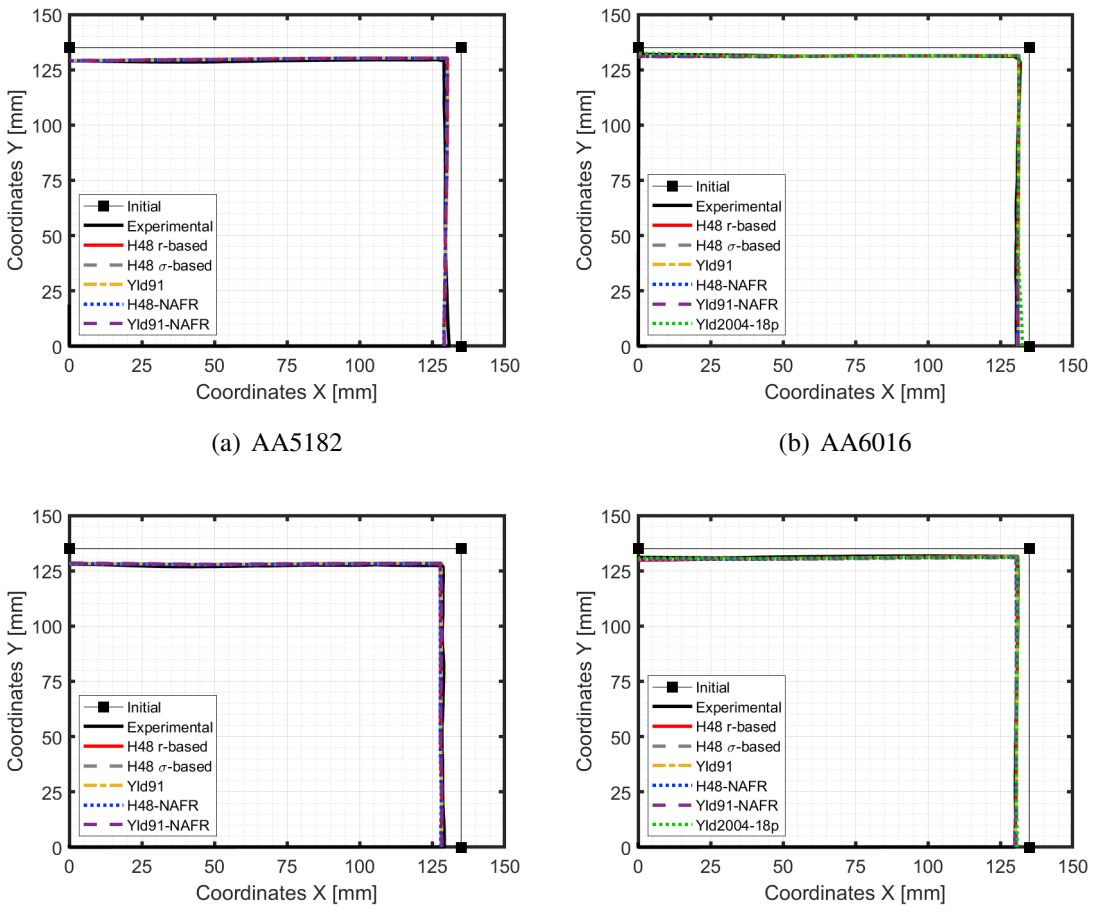
Figure 5.43: Draw-in 'X' shape results of cross die test, for the DP780.

As can be seen in figure 5.39, the numerical simulation final shape result predictions show a good agreement with the experimental measured. However, the maximum amount of draw-in achieved is lower that 7% of the total length of initial blank shape. In case of AA5182, the Yld91 with an AFR formulation gave, in overall, the best results. For along the rolling direction (0°) all the yield criteria overestimate the amount of draw-in, but underestimate for 45°. For the transverse direction (90°) the Yld91-AFR could predict

exactly the amount of draw-in experimentally measured. For AA6016, the observed behavior is opposite. A underestimation of the amount of draw-in for 0° and overestimation for 90°. Regarding the diagonal direction, although the results were uniform and without much variation, the predictions also fell short when compared to the experimental value.

Concerning the dual-phase steel DP500, the Hill'48 stress-based approach show the closer results to the experiments, expect for the transverse direction, having the higher overestimation draw-in prediction. For DP780, like the AA5182, the Yld91-AFR had the better performance. For all the section evaluated, the draw-in amount prediction where higher than those observed experimentally, except for diagonal direction, in which Hill'48 r-based and Yld91 predict the same value.

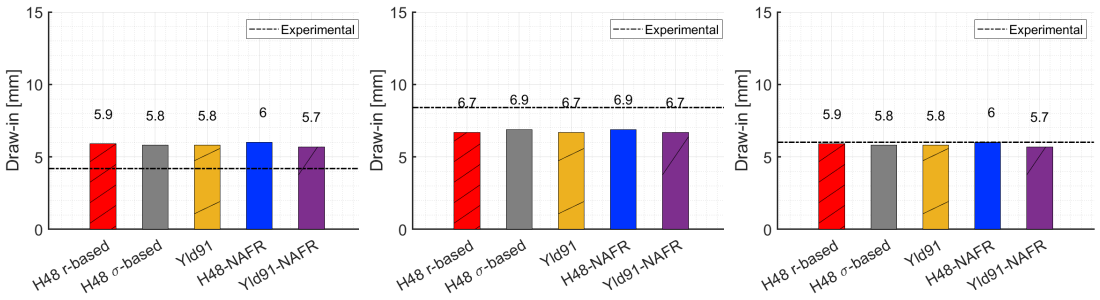
Furthermore, Figure 5.44 to 5.48 illustrate the predicted final plus shape and draw-in amount for three distinct sections.



(a) AA5182 (b) AA6016

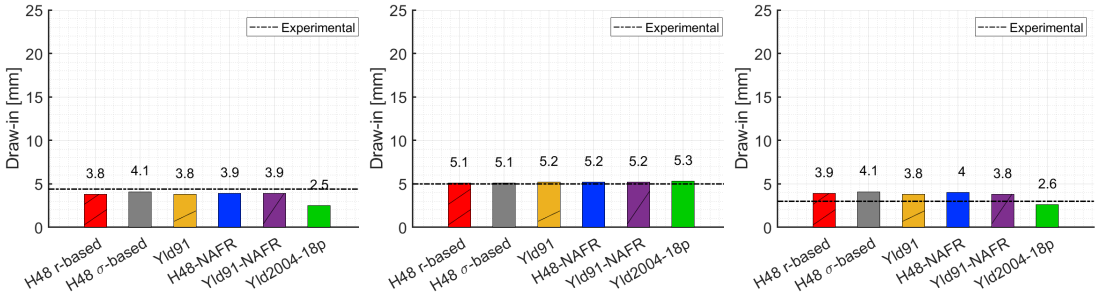
(c) DP500 (d) DP780

Figure 5.44: Draw-in results of the cross die test, for the '+' shape component



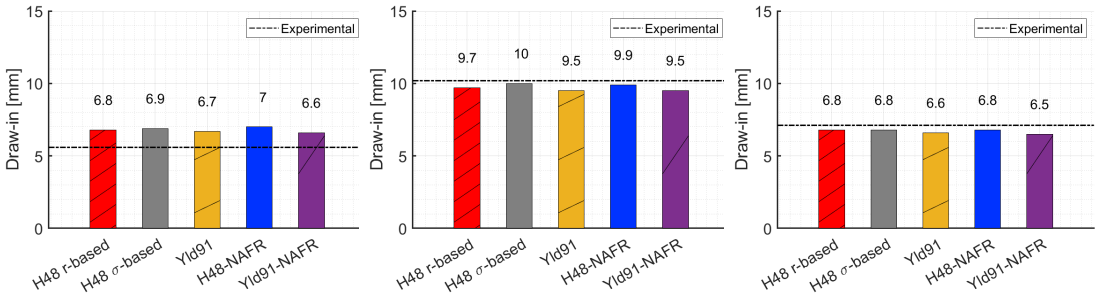
(a) 0° (b) 45° (c) 90°

Figure 5.45: Draw-in '+' shape results of cross die test, for the AA5182.



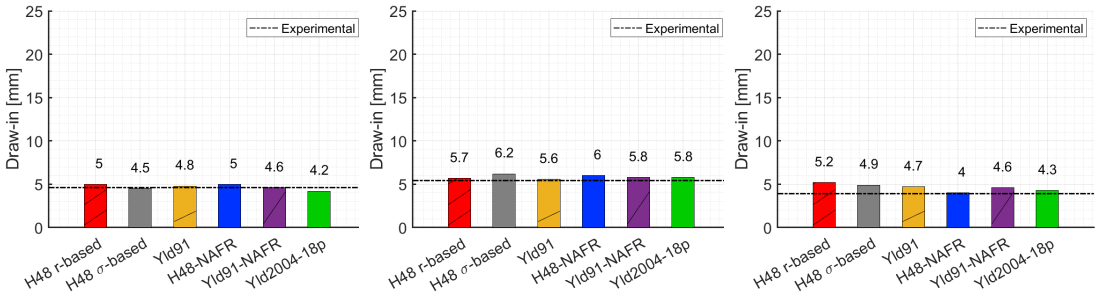
(a) 0° (b) 45° (c) 90°

Figure 5.46: Draw-in '+' shape results of cross die test, for the AA6016.



(a) 0° (b) 45° (c) 90°

Figure 5.47: Draw-in '+' shape results of cross die test, for the DP500.



(a) 0° (b) 45° (c) 90°

Figure 5.48: Draw-in '+' shape results of cross die test, for the DP780.

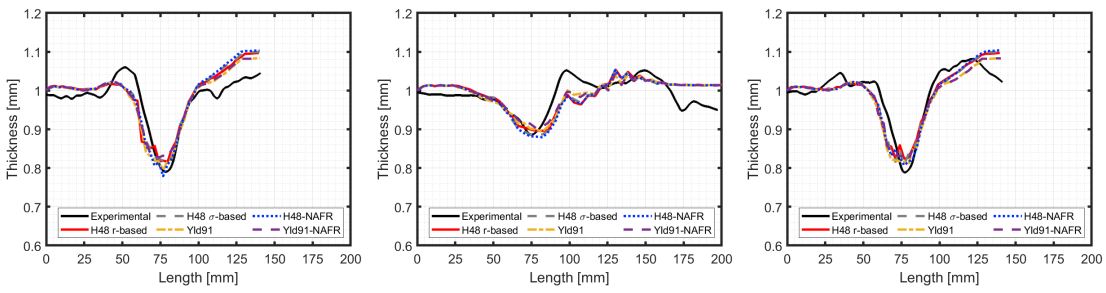
Since the punch displacement for the plus shape experiments is lower than the cross shape case, the amount of draw-in is consequently lower, as can be observed in figure 5.44. The amount of draw-in for AA5182 plus shape component is almost 70% lower when compared to the cross shape geometry. Also, no criterion gave better results than another (in general), as predictions are good for one direction and bad for another.

The same is happening for AA6016, where there is no uniformity between the yield criteria, although all show very close trends with the experimental data and in the same order of magnitude. In case of dual-phase steels, specially for DP780, the Yld91-NAFR shows an overall closer result to the experiment.

The results obtained for this test show small variations and a lower amount of draw-in for all the evaluated sections. Since the draw-in in general is very low, there are also errors associated with the experimental measurement, which also limits the analysis and validation of the ability of the yield criteria to predict the behavior of the material during the deformation process.

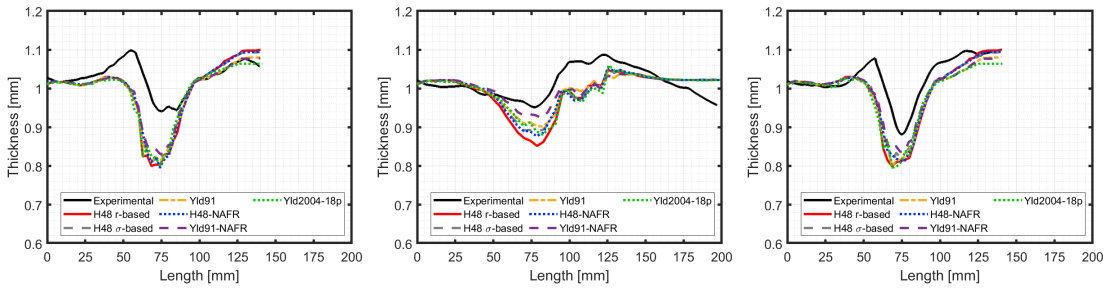
5.4.3 Thickness Distribution

An analysis between the numerical results of the different yield criteria formulations was made and compared with the experimental reference data for all the selected sheet materials. Figures 5.49 to 5.52 show the thickness distribution profiles for the cross shape component.



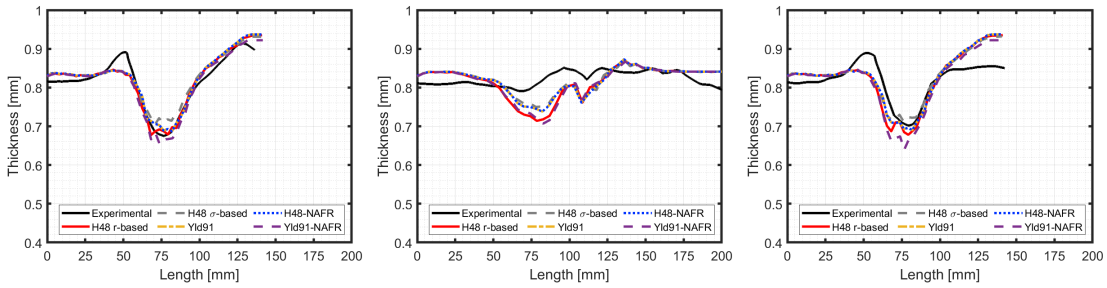
(a) 0° (b) 45° (c) 90°

Figure 5.49: Comparison of profile geometry for the AA5182 aluminum alloy for the different yield criteria for 'X' result.



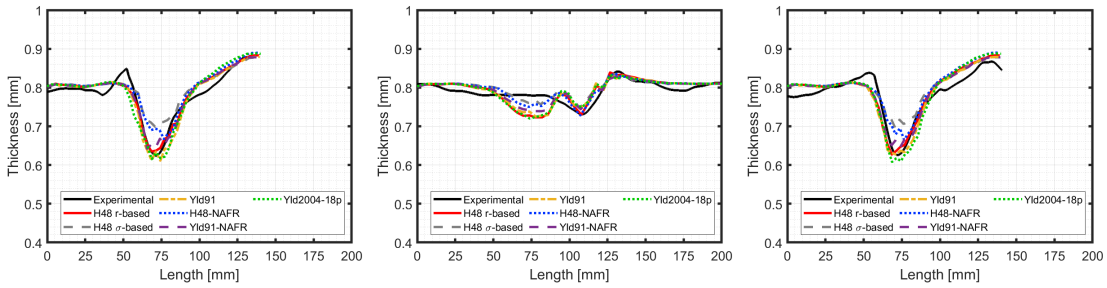
(a) 0° (b) 45° (c) 90°

Figure 5.50: Comparison of profile geometry for the AA6016 aluminum alloy for the different yield criteria for 'X' result.



(a) 0° (b) 45° (c) 90°

Figure 5.51: Comparison of profile geometry for the DP500 dual-phase steel for the different yield criteria for 'X' result.



(a) 0° (b) 45° (c) 90°

Figure 5.52: Comparison of profile geometry for the DP780 dual-phase steel for the different yield criteria for 'X' result.

The analysis of the cross shape component results show a good agreement between numerical thickness distribution and experimental measured values, specially for the section along the rolling and transverse direction. The greatest differences between the constitutive models are observed in the area where the greatest reduction in thickness occurs, while for the rest of the thickness profile the predictions are very similar.

Concerning the AA5182 and DP780, the amplitude of thinning and location are well captured for the three analyzed sections. The difference between the numerical predictions for AA5182, when using the different yield criteria is almost neglected, but in case of DP780, the Hill'48 r-based and both Yld91 formulations give a closer profile when compared to the experiment. On the other hand, in all numerical simulations for the AA6016 material, there is an overestimation of the material thickness reduction, being almost 75% higher than the experimental evidence. However, the Yld91 NAFR criterion is the model that present results closer to the experimental data, mainly for the section oriented at 45º, where a greater dispersion in numerical predicted is obtained.

In correlation with the analysis previously carried out on the experimental results, in fact the zones with the highest equivalent plastic strain values (as can be seen in figures on appendix C) occur at the critical regions of the component, as shown in figure 5.53 (region A is purely stretched and region B is subject to a plain strain loading).

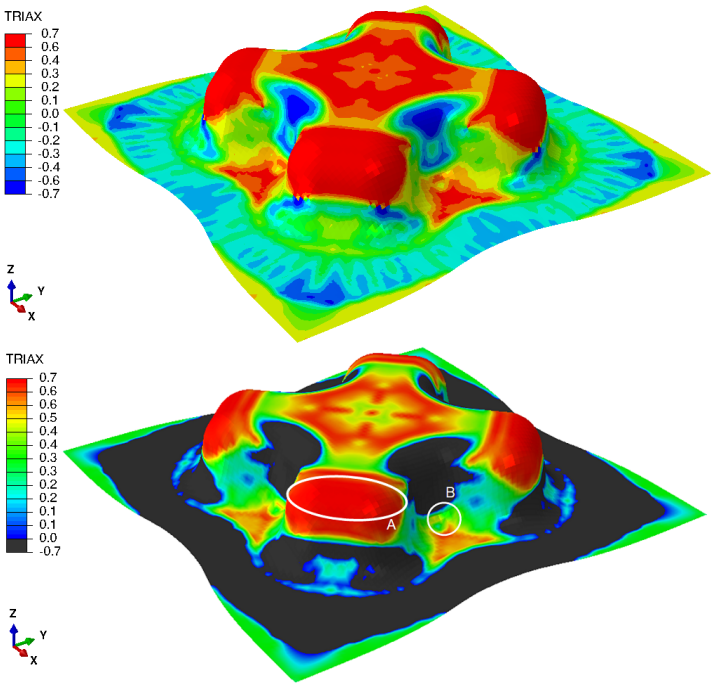
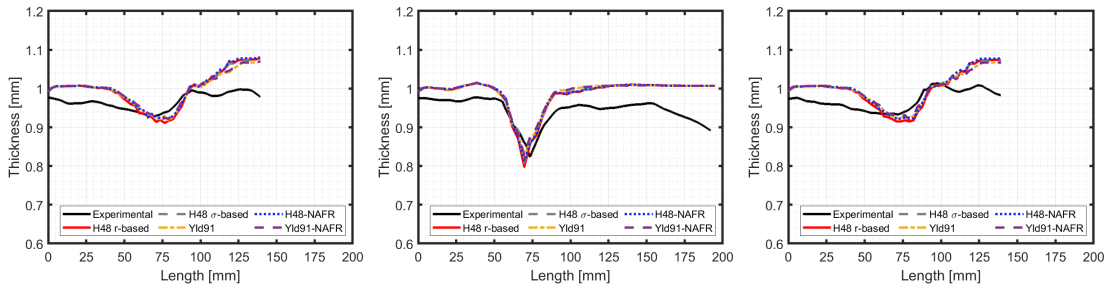


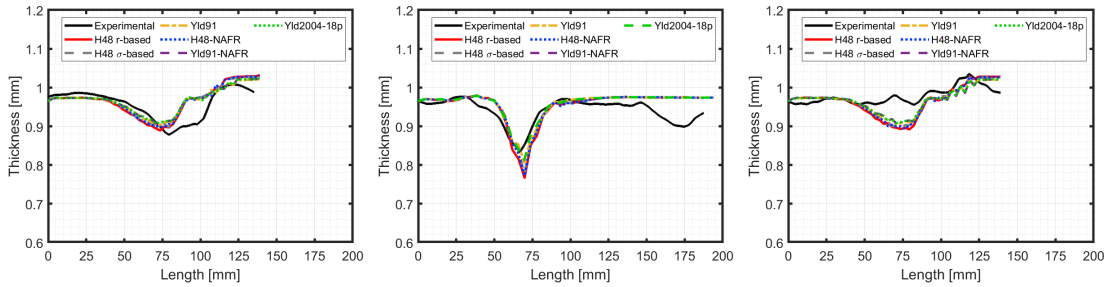
Figure 5.53: Stress triaxility distribution of the DP780 cross shape component.

Figure 5.54 to 5.57 presents the thickness distribution profiles for the plus shape component.



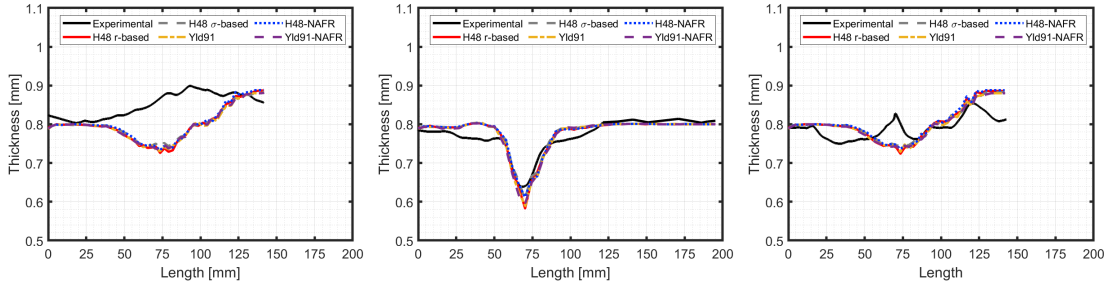
(a) 0° (b) 45° (c) 90°

Figure 5.54: Comparison of profile geometry for the AA5182 aluminum alloy for the different yield criteria for '+' result.



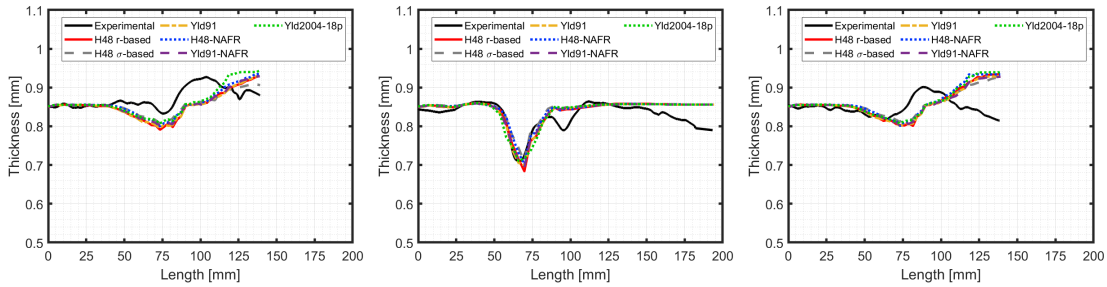
(a) 0° (b) 45° (c) 90°

Figure 5.55: Comparison of profile geometry for the AA6016 aluminum alloy for the different yield criteria for '+' result..



(a) 0° (b) 45° (c) 90°

Figure 5.56: Comparison of profile geometry for the DP500 dual-phase steel for the different yield criteria for '+' result.



(a) 0° (b) 45° (c) 90°

Figure 5.57: Comparison of profile geometry for the DP780 dual-phase steel for the different yield criteria for '+' result.

In the case of the plus shape component, and since its geometry is rotated by 45º with relative to the cross-shaped component orientation, the greatest reduction (about 10% of the initial thickness value) occurs for 45º, located at the components wall. The low thickness reduction may be associated with the low overall height of the component and therefore low levels of plastic deformation. For these reasons, the predictions obtained by the numerical simulation of the various models are very similar, but when compared to the experimental results, they show a greater discrepancy. Furthermore, it is important to note that the experimental measurements carried out, despite the system having a resolution of 10 μm, the thickness values may be subject to small variations.

Chapter 6

Conclusions

This chapter summarizes the main conclusions of this work, as well as some suggestions for future analysis regarding, not only, material behavior modeling and its use in numerical simulation of sheet metal forming processes, but also some identified process variables.

(This page was deliberately left blank)

6.1 Final remarks

The sheet metal forming industry and other sectors have shown significant interest in using numerical tools for simulating their manufacturing processes. The main purpose of these simulations is to predict the material behavior and possible defects that might occur during the design and development phases of formed components. The study of the mechanical behavior of metallic materials holds significant importance, and it has garnered considerable interest over time. Researchers have formulated mathematical constitutive models to describe this behavior as closely as possible to experimental evidence. Such advancements have practical implications for industries, enabling them to gain competitive advantages by better understanding material behavior and its applications, as well as optimizing manufacturing processes.

However, the deep drawing process is highly complex, involving nonlinearity and interactions between various phenomena, which can make it challenging to achieve a good correlation between numerical predictions and experimental observations. To overcome that, there have been substantial advancements in numerical tools to improve their ability to reproduce real world industrial scenarios more reliably. The ultimate goal is to bridge the gap between simulation results and actual experimental outcomes, allowing engineers to make better informed decisions during the product development stages.

Within the scope of this PhD thesis, the finite element method was employed to the numerical simulation of sheet metal forming experiments. These simulations utilized different material anisotropic constitutive models (Hill'48, Yld91 and Yld2004-18p) to accurately reproduce the mechanical behavior of two aluminum alloys (AA5182 and AA6016) and two advanced high strength steels (DP500 and DP780). To obtain the mechanical characteristics of the selected materials under diverse loading conditions, to comprehensively address the stress states encountered in complex sheet metal forming components, a set of experimental data was considered and performed, including tensile tests (yield strength and plastic anisotropic coefficients), biaxial expansion (biaxial yield strength) and biaxial compression (biaxial plastic anisotropic coefficient). To explore the potential of using different flow rules with the different yield criteria, various loading directionalities were considered, allowing for greater accuracy in the description of material behavior.

To assess and evaluate the potential of each approach in the material behavior prediction, three benchmark tests were considered: deep drawing cylindrical cup (Swift test), modified Demeri split ring and cross die forming.

Regarding the cylindrical cup, when the increase of wall thickness is less than the gap between punch and die (the case of DP's), the evolution of the punch force is not

influenced by the choice of plasticity criteria. However, when an ironing phase occurs (the case of aluminum alloys), the constitutive models proposed by Barlat (Yld91 and Yld2004) show a behavior closer to that obtained experimentally, but still with a considerable error. For this situation, the choice of elastically deformable tools showed significant improvements (reduction of the predicted force by 20%) in the region where the ironing phase occurs.

Concerning the earing profiles, the application of the non-associated flow rule revealed a very close similarity to the experimental evidence, especially when combined with the Yld91 criterion. Still, despite the improvements observed in the evolution of the punch force with the use of elastic tools, the prediction of earing profile did not prove to have any influence. On the other hand, the application of a friction model dependent on contact pressure proved to have a much greater impact on the obtained results. In the case of the punch force, there is a clear reduction in the ironing phase, and for the cup ear height there is an approximation to the experimental measured value. This indicates that the use of this approach has a much higher influence than the use of elastic tools instead of rigid ones.

The elastic recovery predictions obtained with the modified Demeri slipt ring test showed a common trend for aluminum alloys and other for steels. The Yld91 criterion gave better results for aluminum alloys and Hill'48 for steels when a NAFR formulation was used. However, in the case of AA6061 and DP500, both criteria give good predictions. In general, the application of a non-associated flow rule clear improve the accuracy of numerical predictions, being quite evident when using Hill'48.

Relatively to cross die forming numerical simulation, it is noteworthy that all the employed yield criteria exhibit a significant consistency with experimental measurements for both blank orientations. They effectively capture the general trend in the evolution of punch force. However, among the various criteria, the Yld91-NAFR formulation stands out for its ability to provide a more precise curve, aligning closely with the experimental data. In particular, it surpasses predictions based on Hill'48 criterion. Furthermore, the numerical simulations of the final cross shape demonstrate a good level of agreement with the experimental evidence. In the case of AA5182, the Yld91 formulation, when coupled with an AFR approach, consistently delivers better results, although for the rolling direction (0°) all the yield criteria overestimate the amount of draw-in, and on the other hand, underestimate for 45°. For AA6016, the observed behavior is opposite. A underestimation of the amount of draw-in for 0° and overestimation for 90°. Concerning the dual-phase steel DP500, the Hill'48 stress-based approach generally gives results that are closer to the experiments, except in the transverse direction. For DP780, like

the AA5182, the Yld91-AFR combination demonstrates a better performance. However, across all evaluated sections, the predicted amount of draw-in tends to exceed the experimental observations, except in the diagonal direction, where Hill'48 and Yld91 gave similar predictions. About the plus shape numerical analysis, it is notable that the amount of draw-in is considerably lower. This is primarily due to the lower punch displacement required to deform the component. In the case of AA5182 plus shapes, the draw-in is lower compared to the cross shape geometry. Particularly, there is no single criterion that consistently outperforms the others. Predictions diverge, providing accurate results for one direction but less precise for another. This lack of uniformity is also observed in AA6016, where yield criteria exhibit variability in their predictions. In the case of dual-phase steels, particularly DP780, the Yld91-NAFR formulation arises as the most consistent approach, giving results that align with experimental data across the various orientations and sections.

The analysis of the cross shape component thickness distribution results show a good compromise between numerical and experimental values, particularly evident in the sections along the rolling and transverse directions. The higher differences were observed where the greatest reduction in thickness occurs. However, it is noteworthy that for the remaining thickness profile, the predictions are very similar. Furthermore, it is important to note that the experimental measurements carried out, despite the system having a resolution of 10 μm, the thickness values may be subject to small variations.

6.2 Future work

For a deeper knowledge of the investigated topics of research, it would be interesting to continue this work in different paths. With this in mind, several perspectives for future work are proposed.

- Numerical and experimental analysis and evaluation of the springback behavior and the degradation of the elastic properties with plastic deformation, based on a split-ring test using the deep drawing cylindrical cup component;
- Perform the identification of anisotropy parameters based on the evolution profile of the earing in deep drawing. Traditional identification based on plastic anisotropic coefficients may not be the most appropriate.
- Given the importance of the friction conditions between the surfaces, it is suggested to explore other types of models that reproduce this behavior; in addition, the identification of parameters could be carried out through inverse analysis methodologies

based on the cylindrical cup test, since for cases in which the gap between the die and the punch leads to the appearance of an ironing phase, the friction model considered has a significant impact on the evolution of the punch force;

- Carry out studies for several rings along the height of the cylindrical cup and for materials with higher ear amplitudes, in order to capture the distortion effect observed in the last ring;
- Sensitivity analysis of ring height and its impact on elastic recovery (springback);
- Use of a combined isotropic-kinematic hardening law, which can capture the Bauschinger effect, since strain path reverse is quite common in sheet metal forming processes;
- Use materials with greater plastic forming capacity in the cross die test, to obtain an analysis reference with less dispersion of the variables studied, especially in the thickness distribution, since the materials studied have low amplitudes and in some cases are close to the resolution of the equipment used; additionally and as a complement, it is suggested that a more extensive physical measurement be carried out.

References

[1] Xiaobo Fan, Xianshuo Chen, and Shijian Yuan. Novel forming process for aluminum alloy thin shells at ultra-low temperature gradient. *International Journal of Machine Tools and Manufacture*, 185:103992, 2023.

[2] Omolayo M. Ikumapayi, Sunday A. Afolalu, Joseph F. Kayode, Rasaq A. Kazeem, and Saheed Akande. A concise overview of deep drawing in the metal forming operation. *Materials Today: Proceedings*, 62:3233–3238, 2022.

[3] Tomasz Trzepieciński. Recent developments and trends in sheet metal forming. *Metals*, 10(6):779, 2020.

[4] H. Li, X. S. Liu, Y. S. Zhang, M. T. Ma, G. Y. Li, and J. Senkara. Current research and challenges in innovative technology of joining dissimilar materials for electric vehicles. December 2018.

[5] M. Ghosh, A. Ghosh, and A. Roy. Renewable and Sustainable Materials in Automotive Industry. In *Encyclopedia of Renewable and Sustainable Materials*, pages 162–179. Elsevier, 2019.

[6] Wen Zhang and Jun Xu. Advanced lightweight materials for automobiles: a review. *Materials & Design*, 221:110994, September 2022.

[7] T. P. Hovorun, , K. V. Berladir, V. I. Pererva, S. G. Rudenko, A. I. Martynov, , , and and. Modern materials for automotive industry. *Journal of Engineering Sciences*, 4(2):f8–f18, 2017.

[8] James R. Fekete. Overview of sheet metals for stamping. February 1997.

[9] Xin Yun Wang, Jun song Ji, Lei Deng, and Qiu Zheng. Stamping forging processing of sheet metal parts. October 2012.

[10] Rashmi Dwivedi and Geeta Agnihotri. Study of deep drawing process parameters. *Materials Today: Proceedings*, 4(2):820–826, 2017.

[11] Manikyam Sandeep. Optimization of deep drawing process parameters for cylindrical cup. *Materials Today: Proceedings*, 19:772–777, 2019.

[12] C.-W. Hsu, A.G. Ulsoy, and M.Y. Demeri. Development of process control in sheet metal forming. *Journal of Materials Processing Technology*, 127(3):361–368, 2002.

[13] Olaf Engler, Juergen R. Hirsch, and S. Kalz. *Simulation of Sheet Anisotropy*. Number 13 in II. Wiley-VCH Verlag, Weinheim, 2006.

[14] Takalkar Atul S and M C Lenin Babu. A review on effect of thinning, wrinkling and spring-back on deep drawing process. *Proceedings of the Institution of Mechanical Engineers, Part B: Journal of Engineering Manufacture*, 233(4):1011–1036, 2018.

[15] M. Ikumapayi Omolayo, A. Afolalu Sunday, S. Fatoba Olawale, A. Kazeem Rasaq, A. Adetunla Adedotun, and O. Ongbali Samuel. A concise study on shearing operation in metal forming. *E3S Web of Conferences*, 309:01004, 2021.

[16] D. Swapna, Ch. Srinivasa Rao, and S. Radhika. Formability of lightweight materials-a review. *Materials Today: Proceedings*, 18:426–435, 2019.

[17] D. Swapna, C. S. Rao, and S. Radhika. A review on deep drawing process. *International Journal of Emerging Research in Management and Technology*, 6(6), 2018.

[18] Brathikan Vijayamohan Mankayarkarasi, Gideon Devairakkam Stephen Joseph, Sangeethkumar Babu, and Kavi Scidarth. Effect on deep drawing due to change in sheet metal thickness. 2023.

[19] Pushkar R. Tiwari, Akshay Rathore, and Mohan G. Bodkhe. Factors affecting the deep drawing process – a review. *Materials Today: Proceedings*, 56:2902–2908, 2022.

[20] Nicola Simon, Hannes Erdle, Stefan Walzer, Jens Gibmeier, Thomas Böhlke, and Mathias Liewald. Residual stresses in deep-drawn cups made of duplex stainless steel x2crnin23-4. *Forschung im Ingenieurwesen*, 85(3):795–806, 2021.

[21] M.C. Oliveira and J.V. Fernandes. Modelling and Simulation of Sheet Metal Forming Processes. *Metals*, 9(12):1356, 2019.

[22] W. Volk, P. Groche, A. Brosius, A. Ghiotti, B.L. Kinsey, M. Liewald, L. Madej, J. Min, and J. Yanagimoto. Models and modelling for process limits in metal forming. *CIRP Annals*, 68(2):775–798, 2019.

[23] Peter Mulidrán, Marek Šiser, Ján Slota, Emil Spišák, and Tomáš Sleziak. Numerical prediction of forming car body parts with emphasis on springback. *Metals*, 8(6):435, June 2018.

[24] M. Tisza. Numerical modelling and simulation in sheet metal forming. *Journal of Materials Processing Technology*, 151(1-3):58–62, 2004.

[25] D. U. Furrer and S. L. Semiatin. *Metals Process Simulation*. ASM International, 2010.

[26] Marta C. Oliveira and José V. Fernandes. Modelling and simulation of sheet metal forming processes. *Metals*, 9(12):1356, 2019.

[27] I.N. Vladimirov, M.P. Pietryga, and S. Reese. Anisotropic finite elastoplasticity with nonlinear kinematic and isotropic hardening and application to sheet metal forming. *International Journal of Plasticity*, 26(5):659–687, 2010.

[28] H. Pashazad and M. Kharazi. A peridynamic plastic model based on von Mises criteria with isotropic, kinematic and mixed hardenings under cyclic loading. *International Journal of Mechanical Sciences*, 156:182–204, 2019.

[29] P. Ludwik. *Elemente der Technologischen Mechanik*. VerlagVon Julius, Springer Leipzig, 1909.

[30] J.H. Hollomon. Tensile Deformation. *Transactions of the Metallurgical Society of AIME*, 162:268–290, 1945.

[31] E. Voce. The relationship between stress and strain for homogeneous deformations. *Journal of the Institute of Metals*, 74:537–562, 1948.

[32] H.W. Swift. Plastic instability under plane stress. *Journal of the Mechanics and Physics of Solids*, 1(1):1–18, 1952.

[33] J.E. Hockett and O.D. Sherby. Large strain deformation of polycrystalline metals at low homologous temperatures. *Journal of the Mechanics and Physics of Solids*, 23(2):87–98, 1975.

[34] L. Kessler and J. Gerlach. The impact of materials testing strategies on the determination and calibration of different FEM material models. In *Proceedings of IDDRG 2006*, pages 113–120, 2006.

[35] F. Barlat and K. Lian. Plastic behavior and stretchability of sheet metals. Part I: A yield function for orthotropic sheets under plane stress conditions. *International Journal of Plasticity*, 5(1):51–66, 1989.

[36] F. Barlat, D.J. Lege, and J.C. Brem. A six-component yield function for anisotropic materials. *International Journal of Plasticity*, 7(7):693–712, 1991.

[37] F. Barlat, J.C. Brem, J.W. Yoon, K. Chung, R.E. Dick, D.J. Lege, F. Pourboghrat, S.-H. Choi, and E. Chu. Plane stress yield function for aluminum alloy sheets—part 1: theory. *International Journal of Plasticity*, 19(9):1297–1319, 2003.

[38] F. Barlat, H. Aretz, J.W. Yoon, M.E. Karabin, J.C. Brem, and R.E. Dick. Linear transfomation-based anisotropic yield functions. *International Journal of Plasticity*, 21(5):1009–1039, 2005.

[39] F. Barlat. Constitutive Modeling for Sheet Metal Forming. In *AIP Conference Proceedings*, volume 778, pages 353–358, 2005.

[40] D. Banabicn, T. Kuwabara, T. Balan, and D. S. Comsa. An anisotropic yield criterion for sheet metals. *Journal of Materials Processing Technology*, 157–158:462–465, December 2004.

[41] O. Cazacu, B. Plunkett, and F. Barlat. Orthotropic yield criterion for hexagonal closed packed metals. *International Journal of Plasticity*, 22(7):1171–1194, 2006.

[42] Jeong Yeon Lee, Myoung Gyu Lee, Frédéric Barlat, Kyung Hwan Chung, and Dong-Jin Kim. Effect of nonlinear multi-axial elasticity and anisotropic plasticity on quasi-static dent properties of automotive steel sheets. *International Journal of Solids and Structures*, 87:254–266, June 2016.

[43] H. J. Choi, K. J. Lee, Y. Choi, G. Bae, D. C. Ahn, and M.-G. Lee. Effect of evolutionary anisotropy on earing prediction in cylindrical cup drawing. *JOM*, 69(5):915–921, January 2017.

[44] R. Hill. A theory of the yielding and plastic flow of anisotropic metals. *Proceedings of the Royal Society London A*, 193:281–297, 1948.

[45] Boxun Wu, Koichi Ito, Naomichi Mori, Tetsuo Oya, Tom Taylor, and Jun Yanagimoto. Constitutive equations based on non-associated flow rule for the analysis of forming of anisotropic sheet metals. *International Journal of Precision Engineering and Manufacturing-Green Technology*, 7(2):465–480, February 2019.

[46] Rui Loureiro Amaral. *Development of accurate numerical methodologies applied to the stamping of advanced high strength steels and experimental validation*. PhD thesis, University of Porto, 2020.

[47] F. Barlat, H. Aretz, J.W. Yoon, M.E. Karabin, J.C. Brem, and R.E. Dick. Linear transfomation-based anisotropic yield functions. *International Journal of Plasticity*, 21(5):1009–1039, 2005.

[48] D. Banabic. An improved analytical description of orthotropy in metallic sheets. *International Journal of Plasticity*, 21(3):493–512, 2005.

[49] H. Vegter and A.H. van den Boogaard. A plane stress yield function for anisotropic sheet material by interpolation of biaxial stress states. *International Journal of Plasticity*, 22(3):557–580, 2006.

[50] T.B. Stoughton. A non-associated flow rule for sheetmetal forming. *International Journal of Plasticity*, 18:687–714, 2002.

[51] T.B. Stoughton and J.W. Yoon. Review of Drucker's postulate and the issue of plastic stability in metal forming. *International Journal of Plasticity*, 22:391–433, 2006.

[52] M. Safaei, J.W. Yoon, and W. De Waele. Study on the definition ofequivalent plastic strain under non-associated flow rule for finiteelement formulation. *International Journal of Plasticity*, 58:219–238, 2014.

[53] Heng Yang, Heng Li, Jun Ma, Zhao Zhang, and Jun Chen. Constitutive modeling related uncertainties: Effects on deformation prediction accuracy of sheet metallic materials. *International Journal of Mechanical Sciences*, 157-158:574–598, 2019.

[54] Xiao Yang, Xiaochuan Liu, Heli Liu, Denis J. Politis, David Leyvraz, and LiLiang Wang. Experimental and modelling study of friction evolution and lubricant breakdown behaviour under varying contact conditions in warm aluminium forming processes. *Tribology International*, 158:106934, 2021.

[55] L. Muñiz, J. Trinidad, E. Garcia, I. Peinado, N. Montes, and L. Galdos. On the Use of Advanced Friction Models for the Simulation of an Industrial Stamping Process including the Analysis of Material and Lubricant Fluctuations. *Lubricants*, 11(5):193, 2023.

[56] D. K. Karupannasamy, M. B. de Rooij, and D. J. Schipper. Multi-scale friction modelling for rough contacts under sliding conditions. *Wear*, 308(1-2):222–231, 2013.

[57] Young Suk Kim. Non-uniform Pressure Distribution in Draw-Bend Friction Test and its Influence on Friction Measurement. 2005.

[58] Y. S. Kim, M. K. Jain, and D. R. Metzger. Determination of pressure-dependent friction coefficient from draw-bend test and its application to cup drawing. *International Journal of Machine Tools and Manufacture*, 56:69–78, 2012.

[59] Martin Kraus, Matthias Lenzen, and Marion Merklein. Contact pressure-dependent friction characterization by using a single sheet metal compression test. *Wear*, 476:203679, 2021.

[60] E2492-07: Standard Test Method for Evaluating Springback of Sheet Metal Using the Demeri Split Ring Test, 2012.

[61] Alimi Abdul Ghafar, Ahmad Baharuddin Abdullah, and Johan Ihsan Mahmood. Experimental and numerical prediction on square cup punch–die misalignment during the deep drawing process. *The International Journal of Advanced Manufacturing Technology*, 113(1-2):379–388, 2021.

[62] Rui L. Amaral, Abel D. Santos, Sara S. Miranda, and J. Cesar de Sa. Earing Profile and Wall Thickness Prediction of a Cylindrical Cup for Dual-phase Steels Using Different Yield Criteria in FE Simulation. *AIP Conference Proceedings*, pages 180011–1–180011–6, 2019.

[63] Najmeddin Arab and Abotaleb Javadimanesh. Theoretical and experimental analysis of deep drawing cylindrical cup. *Journal of Minerals and Materials Characterization and Engineering*, 01(06):336–342, 2013.

[64] P. D. Barros, D. M. Neto, R. E. Dick, M. C. Oliveira, J. L. Alves, and L. F. Menezes. Numerical prediction of the earing in the cup drawing of an aa3104 aluminum alloy: process conditions versus yield criterion. *International Mechanical Engineering Congress & Exposition*, 2018.

[65] Emil Evin, Naqib Daneshjo, Albert Mareš, Miroslav Tomáš, and Katarína Petrovčiková. Experimental assessment of friction coefficient in deep drawing and its verification by numerical simulation. *Applied Sciences*, 11(6):2756, 2021.

[66] Rashmi Dwivedi, Ajay Kumar Choubey, Rajesh Purohit, and R. S. Rana. Experimental and numerical analysis of aluminium alloy cylindrical cup using novel deep drawing technique. *Advances in Materials and Processing Technologies*, 8(2):1831–1844, 2021.

[67] Martin Allen, Marta Oliveira, Sumit Hazra, Oluwamayokun Adetoro, Abhishek Das, and Rui Cardoso. Benchmark 2 – Springback of a Jaguar Land Rover Aluminium. *Journal of Physics: Conference Series*, 734:022002, 2016.

[68] Z. C. Xia. Springback Behavior of AA6111-T4 with Split-Ring Test. 2004.

[69] H. Laurent, R. Greze, M. C. Oliveira, L. F. Menezes, P. Y. Manach, and J. L. Alves. Numerical study of springback using the split-ring test for an AA5754 aluminum alloy. *Finite Elements in Analysis and Design*, 46(9):751–759, 2010.

[70] Pierre-Yves Manach, Jeremy Coer, Anthony Jegata Herve Laurent, and Jeong Whan Yoon. Benchmark 3 - Springback of an Al-Mg alloy in warm forming conditions. *Journal of Physics: Conference Series*, 734:022003, 2016.

[71] H. Laurent, R. Grèze, P.Y. Manach, and S. Thuillier. Influence of constitutive model in springback prediction using the split-ring test. *International Journal of Mechanical Sciences*, 51(3):233–245, 2009.

[72] V. M. Simoes, M. C. Oliveira, D. M. Neto, P. M. Cunha, H. Laurent, J. L. Alves, and L. F. Menezes. Numerical study of springback using the split-ring test: influence of the clearance between the die and the punch. *International Journal of Material Forming*, 11(2):325–337, 2017.

[73] Myoung-Gyu Lee, Jeong-Yeon Lee, Hongjin Choi, Yumi Choi, Kijung Lee, and Jinwoo Lee. Effect of deformation induced nonlinear and anisotropic elastoplasticity on sheet forming simulations. *Journal of Physics: Conference Series*, 1063:012029, 2018.

[74] J. Coër, H. Laurent, M. C. Oliveira, P.-Y. Manach, and L. F. Menezes. Detailed experimental and numerical analysis of a cylindrical cup deep drawing: Pros and cons of using solid-shell elements. *International Journal of Material Forming*, 11(3):357–373, 2017.

[75] Ali Khalfallah, José Luís Alves, Marta Cristina Oliveira, and Luís Filipe Menezes. Influence of the characteristics of the experimental data set used to identify anisotropy parameters. *Simulation Modelling Practice and Theory*, 53:15–44, 2015.

[76] A. Nakwattanaset, S. Suranuntchai, and S. Panich. Strain- and stress-based forming limit curves of DP440 steel sheet with application to the cross-die forming test. *AIP Conference Proceedings*, 2279(050004), 2020.

[77] A. Ramazani, M. Abbasi, U. Prahl, and W. Bleck. Failure analysis of DP600 steel during the cross-die test. *Computational Materials Science*, 64:101–105, 2012.

[78] R. A. Lingbeek, T. Meinders, and A. Rietman. Tool And Blank Interaction In The Cross-Die Forming Process. *International Journal of Material Forming*, 1(S1):161–164, apr 2008.

[79] Tales Carvalho-Resende, Tudor Balan, Salima Bouvier, Farid Abed-Meraim, and Simon-Serge Sablin. Numerical investigation and experimental validation of a plasticity model for sheet steel forming. *Modelling and Simulation in Materials Science and Engineering*, 21(1):015008, 2012.

[80] Ojo Sunday Isaac Fayomi, Abimbola Patricia Idowu Popoola, and Nduka Ekene Udoye. Effect of alloying element on the integrity and functionality of aluminium-based alloy. 2017.

[81] Joaquin Rams. Wrought aluminum alloys. pages 132–140, 2022.

[82] J. Li, W.C. Liu, T. Zhai, and E.A. Kenik. Comparison of recrystallization texture in cold-rolled continuous cast AA5083 and 5182 aluminum alloys. *Scripta Materialia*, 52(3):163–168, feb 2005.

[83] Daniel Marinho Filizzola, Thaís da Silva Santos, Adalberto Gomes de Miranda, João Carlos Martins da Costa, Nayra Reis do Nascimento, Marcos Dantas dos Santos, Roger Hoel Bello, Gilberto Garcia del Pino, and José Costa de Macêdo Neto. Annealing effect on the microstructure and mechanical properties of AA 5182 aluminum alloy. *Materials Research*, 2021.

[84] J. Bottema, C. Lahaye, R. Baartman, L. Zhuang, P. De Smet, and F. Schoepen. Recent developments in aa6016 aluminium type body sheet product. *JOURNAL OF MATERIALS & MANUFACTURING*, 107(5):900 – 907, 1998.

[85] Ömer Necati and Muammer Koç. Promises and problems of ultra/advanced high strength steel (u/ahss) utilization in auto industry. 2014.

[86] Dierk Raabe, Binhan Sun, Alisson Kwiatkowski Da Silva, Baptiste Gault, Hung-Wei Yen, Karo Sedighiani, Prithiv Thoudden Sukumar, Isnaldi R. Souza Filho, Shyam Katnagallu, Eric Jägle, Philipp Kürnsteiner, Navyanth Kusampudi, Leigh Stephenson, Michael Herbig, Christian H. Liebscher, Hauke Springer, Stefan Zaefferer, Vitesh Shah, Su-Leen Wong, Christian Baron, Martin Diehl, Franz Roters, and Dirk Ponge. Current challenges and opportunities in microstructure-related properties of advanced high-strength steels. *Metallurgical and Materials Transactions A*, 51(11):5517–5586, 2020.

[87] H. Ghadbeigi, C. Pinna, and S. Celotto. Failure mechanisms in DP600 steel: Initiation, evolution and fracture. *Materials Science and Engineering: A*, 588:420–431, 2013.

[88] Miklós Tisza and Zsolt Lukács. Formability investigations of high-strength dual-phase steels. *Acta Metallurgica Sinica (English Letters)*, 28(12):1471–1481, 2015.

[89] ASTM E8 / E8M-16ae1. Standard Test Methods for Tension Testing of Metallic Materials, 2016.

[90] L.C. Reis, M.C. Oliveira, A.D. Santos, and J.V. Fernandes. On the determination of the work hardening curve using the bulge test. *International Journal of Mechanical Sciences*, 105:158–181, 2016.

[91] M. Atkinson. Accurate determination of biaxial stress—strain relationships from hydraulic bulging tests of sheet metals. *International Journal of Mechanical Sciences*, 39(7):761–769, 1997.

[92] X. Lemoine, A. Iancu, and G. Ferron. Flow Curve Determination at Large Plastic Strain Levels: Limitations of the Membrane Theory in the Analysis of the Hydraulic Bulge Test. volume 1353, pages 1411–1416, 2011.

[93] ISO 16808:2022(en)Metallic materials — Sheet and strip — Determination of biaxial stress-strain curve by means of bulge test with optical measuring systems, 2022.

[94] Hugo Campos, Abel D. Santos, and Rui Amaral. Experimental and analytical evaluation of the stress-strain curves of aa5754-t4 and aa6061-t6 by hydraulic bulge test. *Ciência & Tecnologia dos Materiais*, 29(1):e244–e248, January 2017.

[95] K.C Chan and W.B Lee. A prediction of equibiaxial stress-strain curves of sheet metals. *Scripta Metallurgica et Materialia*, 29(7):949–954, 1993.

[96] L. Lazarescu, I. Nicodim, I. Ciobanu, D. S. Comsa, and D. Banabic. Determination of material parameters of sheet metals using the hydraulic bulge test. *Acta Metallurgica Slovaca*, 19(1):4–12, 2013.

[97] R. L. Amaral, A. D. Santos, and S. S. Miranda. *Limiting Drawing Ratio and Formability Behaviour of Dual Phase Steels - Experimental Analysis and Finite Element Modelling*, volume 98 of *Materials Design and Applications II: Advanced Structured Materials*. Springer, Cham, 2019.

[98] ASTM E517-19. Standard Test Method for Plastic Strain Ratio r for Sheet Metal, 2019.

[99] Frédéric Barlat. Advanced Constitutive Modeling for Application to Sheet Forming. *Journal of Physics: Conference Series*, 1063:012002, 2018.

[100] Pedro Prates and André Pereira. Recent advances and applications of machine learning in metal forming processes. *Metals*, 12(8):1342, 2022.

[101] D. Vysochinskiy, T. Coudert, O. S. Hopperstad, O.-G. Lademo, and A. Reyes. Experimental study on the formability of AA6016 sheets pre-strained by rolling. *International Journal of Material Forming*, 11(4):541–557, 2017.

[102] Minsu Wi, Jae Hyun Choi, and Fredéric Barlat. Prediction of plastic flow localization with shell element in thick AHSS sheets. *Procedia Manufacturing*, 15:861–868, 2018.

[103] J.F. Duarte, F. Simões, P. Teixeira, and A.D. Santos. Experimental Benchmark nº7 (Cylindrical Cup) - Internal report of "3DS" project. Technical report, INEGI, 2002.

[104] You Gen Wang, Guang Sheng Huang, Ding Kai Liu, Lin Cheng, Ting Zhuang Han, Jian Peng, and Fu Sheng Pan. Influence of blank holder type on drawability of 5182o aluminum sheet at room temperature. *Transactions of Nonferrous Metals Society of China*, 26(5):1251–1258, May 2016.

[105] Jenny Venema, Gerben Botman, Tu Phan, and Theo Kop. Formability of AlSi and zn coating during hot stamping. *IOP Conference Series: Materials Science and Engineering*, 651(1):012042, 2019.

(This page was deliberately left blank)

Appendix A

Lubricant conditions - FERROCOAT N6130

(This page was deliberately left blank)

A.1 Applications

This oil-based rust preventive provides in-process or final protection for medium to long-term indoor storage of metal surfaces, both ferrous and non-ferrous.

Meets South Coast Air Quality Management District (SCAQMD) 2012 requirements under Rule 1144, ASTM E1868-10 (TGA) for metal protecting, general (corrosion preventives).

- Flood;
- Flow-on;
- Imemersion;
- Wipe-on;
- Eletrostatic.

A.2 Properties

Table A.1: FERROCOAT N6130

Properties	Typical Value
Appearence	Clear Ambar
Pounds per gallon at 60 ºF	7.44 lbs/gal
Flash Point via COC	425 ºF/218 ºC
VOC (EPA Method 24)	0.0 lbs/gal
VOC (SCAQMD ASTM E1868-10)	6.42 g/l
Viscosity at 100º F	20.0 cSt

A.3 Benefits

- Specified and used by steel mills and automotive manufacturers;
- Protection against normal humidity and acidic atmospheres found in industrial environments;
- Excellent resistance to stain and varnish where metal-to-metal contact is present, especially with high temperature and humidity;

- Rapidly displaces moisture and can be used to treat wet parts with no loss of protection, passes MIL-C-16173 requirements;
- Provides versatility in a single product to protect many metals and simplifies overall operations and reduces costs.

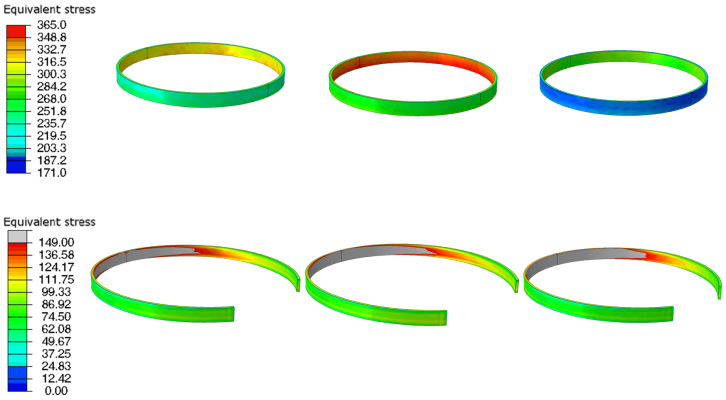
Appendix B

Split-ring test

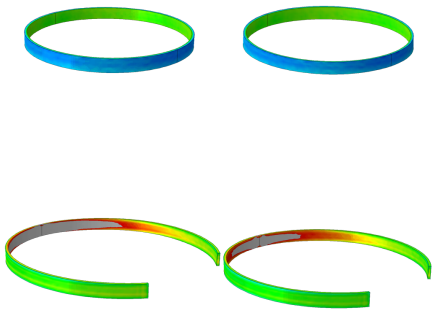
(This page was deliberately left blank)

B.1 Split-ring test

B.1.1 AA5182

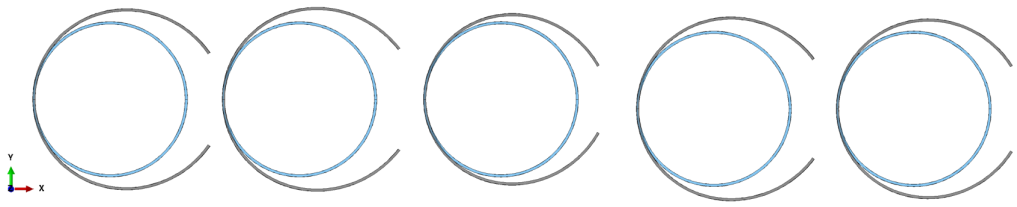


(a) AFR



(b) NAFR

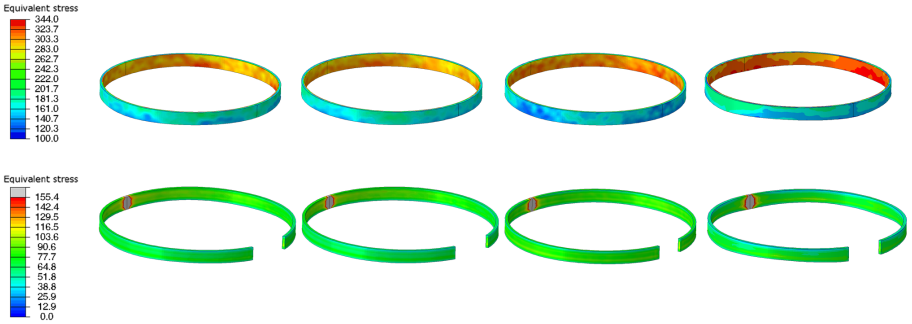
Figure B.1: Split-Ring equivalent plastic stress contours for AA5182 using the yield point as a limit for different yield criteria a) Hill'48 r-based, Hill'48 s-based, Yld91; b) Hill'48 and Yld91(left to right, respectively).



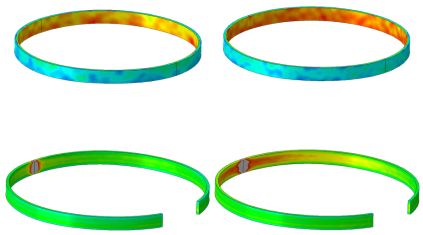
(a) AFR (b) NAFR

Figure B.2: Split-Ring opening evaluation for different yield criteria a) Hill'48 r-based, Hill'48 s-based, Yld91; b) Hill'48 and Yld91(left to right, respectively).

B.1.2 AA6016

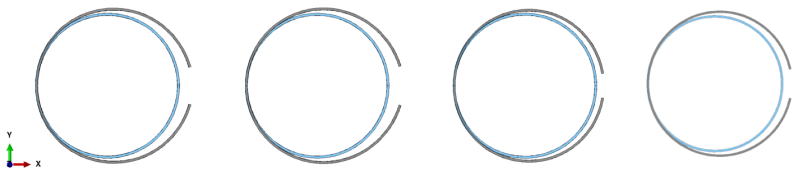


(a) AFR

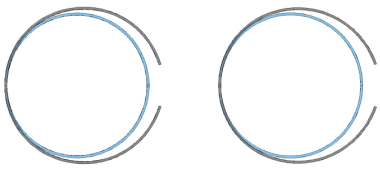


(b) NAFR

Figure B.3: Split-Ring equivalent plastic stress contours for AA6016 using the yield point as a limit for different yield criteria a) Hill'48 r-based, Hill'48 s-based, Yld91; b) Hill'48 and Yld91(left to right, respectively).



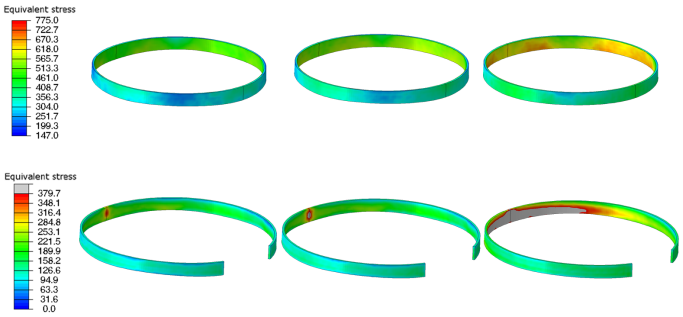
(a) AFR



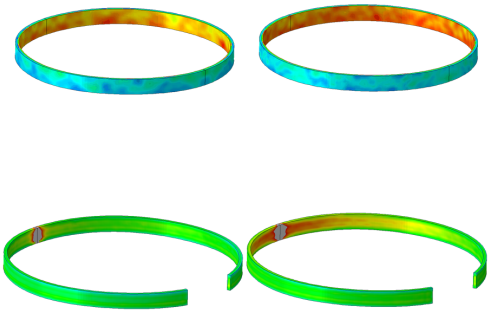
(b) NAFR

Figure B.4: Split-Ring opening evaluation of AA6016 for different yield criteria a) Hill'48 r-based, Hill'48 s-based, Yld91; b) Hill'48 and Yld91(left to right, respectively).

B.1.3 DP500

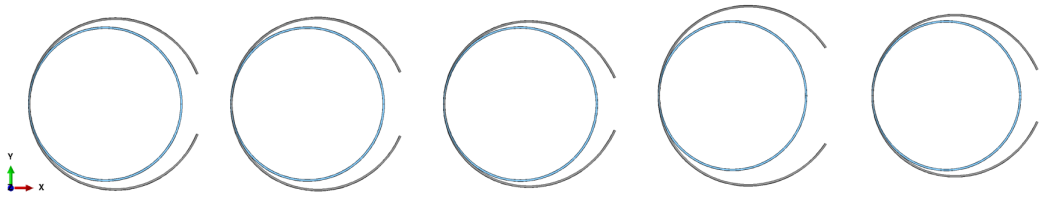


(a) AFR



(b) NAFR

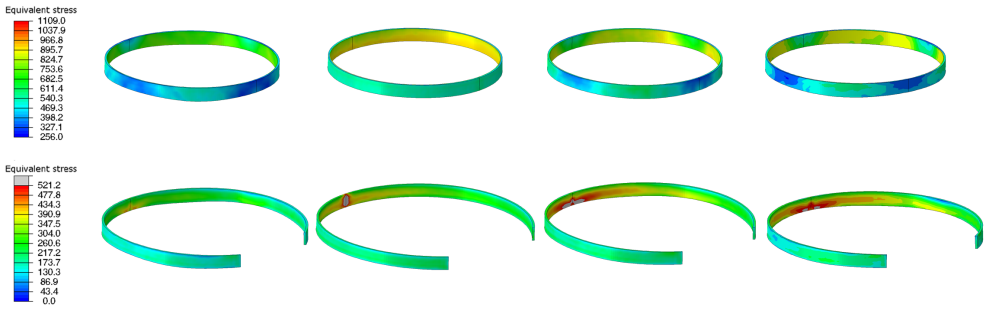
Figure B.5: Split-Ring equivalent plastic stress contours for DP500 using the yield point as a limit for different yield criteria a) Hill'48 r-based, Hill'48 s-based, Yld91; b) Hill'48 and Yld91(left to right, respectively).



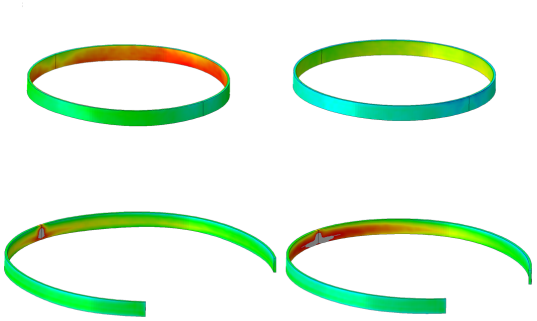
(a) AFR (b) NAFR

Figure B.6: Split-Ring opening evaluation of DP500 for different yield criteria a) Hill'48 r-based, Hill'48 s-based, Yld91; b) Hill'48 and Yld91(left to right, respectively).

B.1.4 DP780

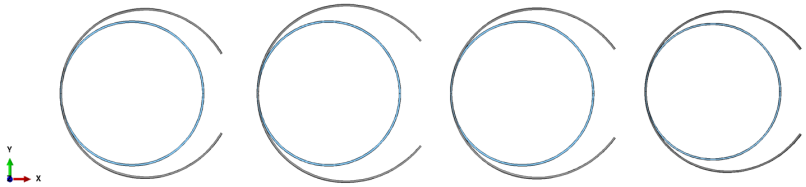


(a) AFR

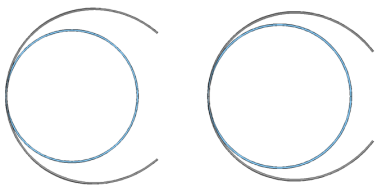


(b) NAFR

Figure B.7: Split-Ring equivalent plastic stress contours for DP780 using the yield point as a limit for different yield criteria a) Hill'48 r-based, Hill'48 s-based, Yld91; b) Hill'48 and Yld91(left to right, respectively).



(a) AFR



(b) NAFR

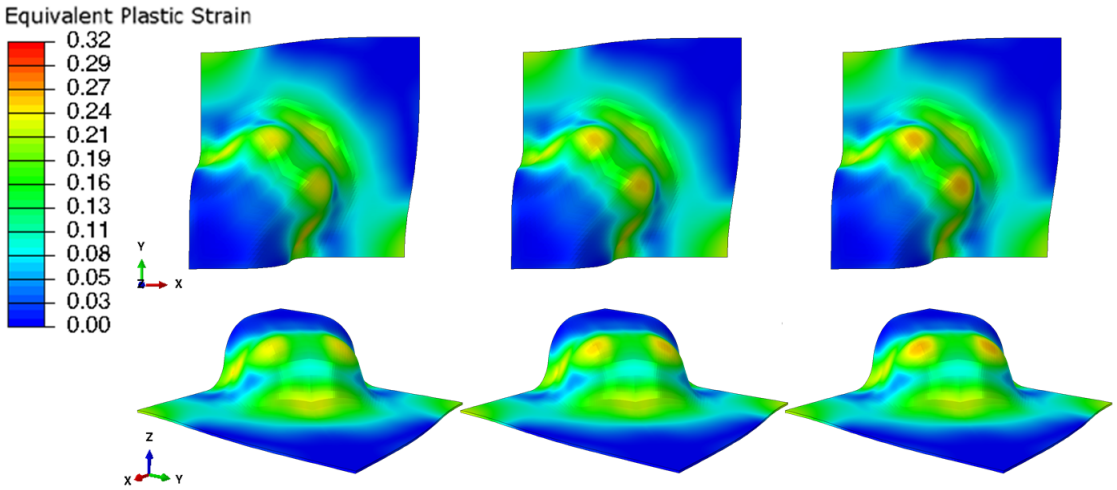
Figure B.8: Split-Ring opening evaluation of DP780 for different yield criteria a) Hill'48 r-based, Hill'48 s-based, Yld91; b) Hill'48 and Yld91(left to right, respectively).

Appendix C

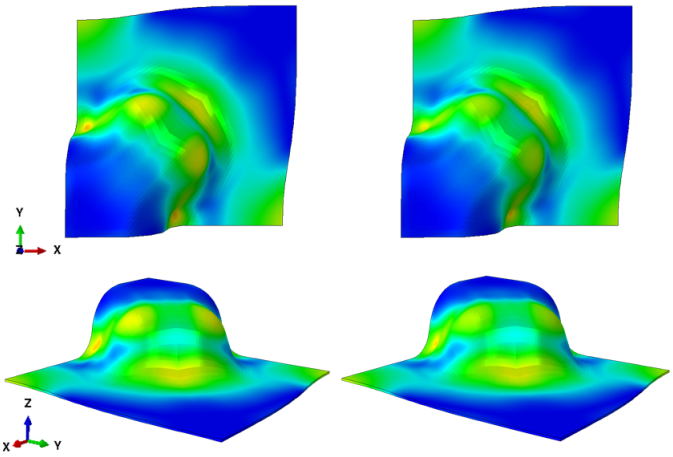
Cross die forming test

(This page was deliberately left blank)

C.1 Cross shape component

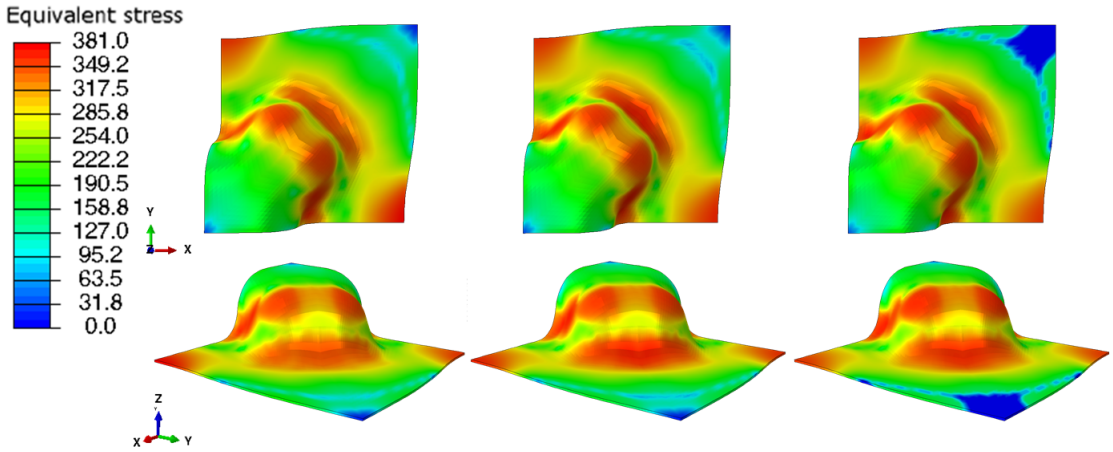


(a) AFR

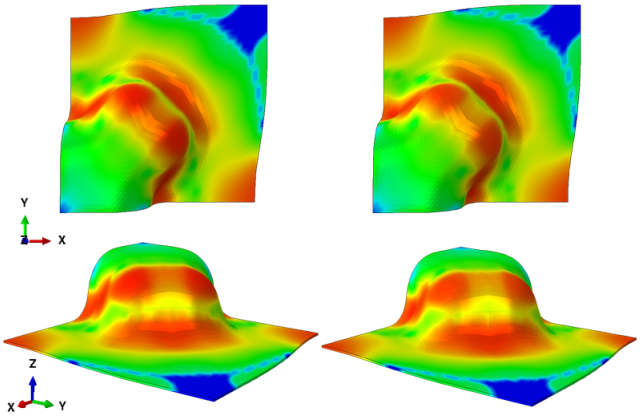


(b) NAFR

Figure C.1: Equivalent plastic strains contours for AA5182 X shape of cross die, using the different yield criteria: a) Hill'48 r-based, Hill'48 s-based, Yld91; b) Hill'48, Yld91 (from left to right, respectively).

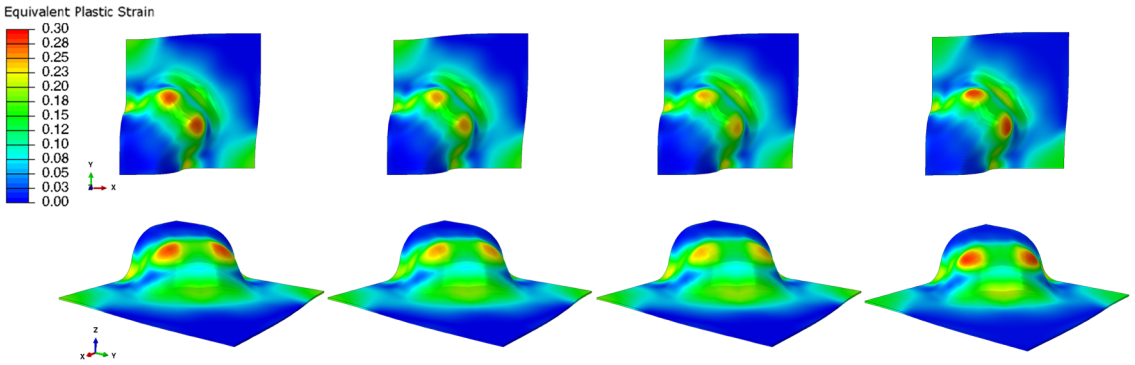


(a) AFR

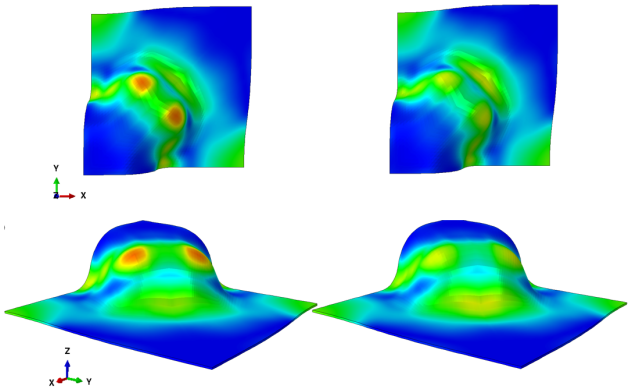


(b) NAFR

Figure C.2: Equivalent stress contours for AA5182 X shape of cross die, using the different yield criteria: a) Hill'48 r-based, Hill'48 s-based, Yld91; b) Hill'48, Yld91 (from left to right, respectively).

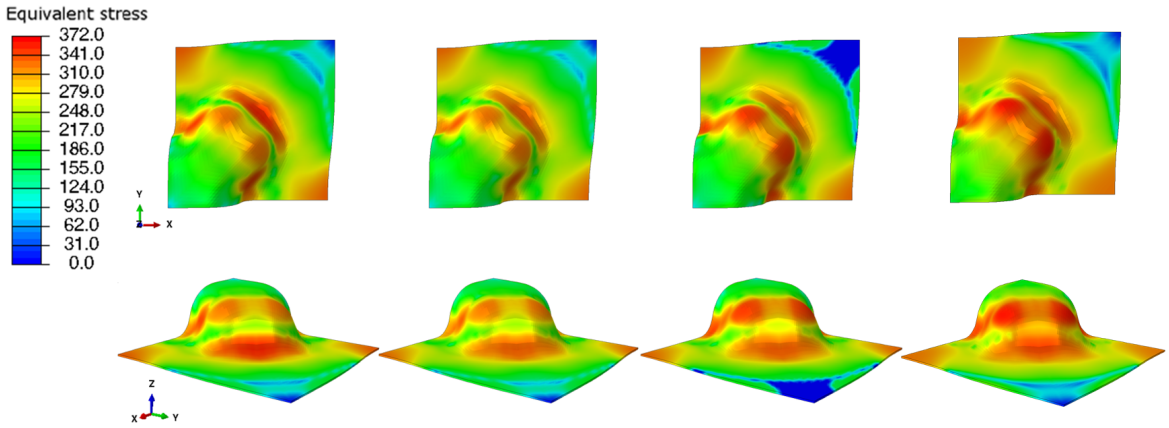


(a) AFR

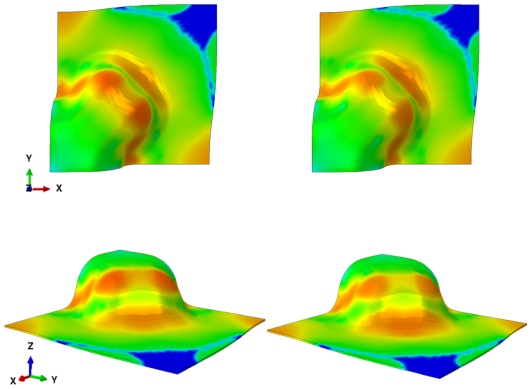


(b) NAFR

Figure C.3: Equivalent plastic strains contours for AA6016 X shape of cross die, using the different yield criteria: a) Hill'48 r-based, Hill'48 s-based, Yld91; b) Hill'48, Yld91 (from left to right, respectively)

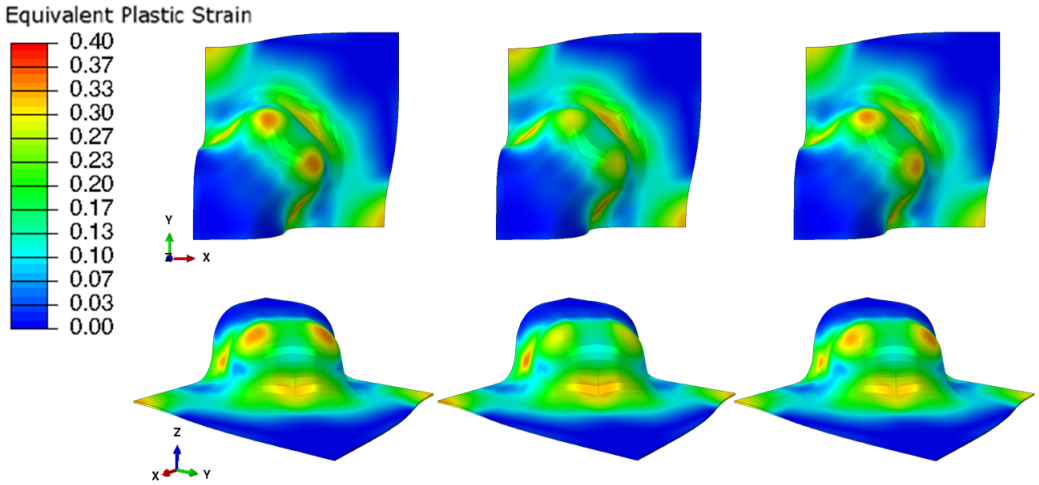


(a) AFR

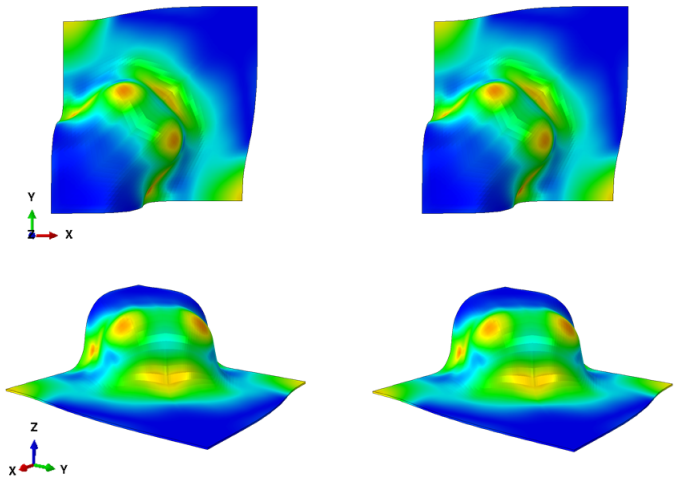


(b) NAFR

Figure C.4: Equivalent stress contours for AA6016 X shape of cross die, using the different yield criteria: a) Hill'48 r-based, Hill'48 s-based, Yld91; b) Hill'48, Yld91 (from left to right, respectively).

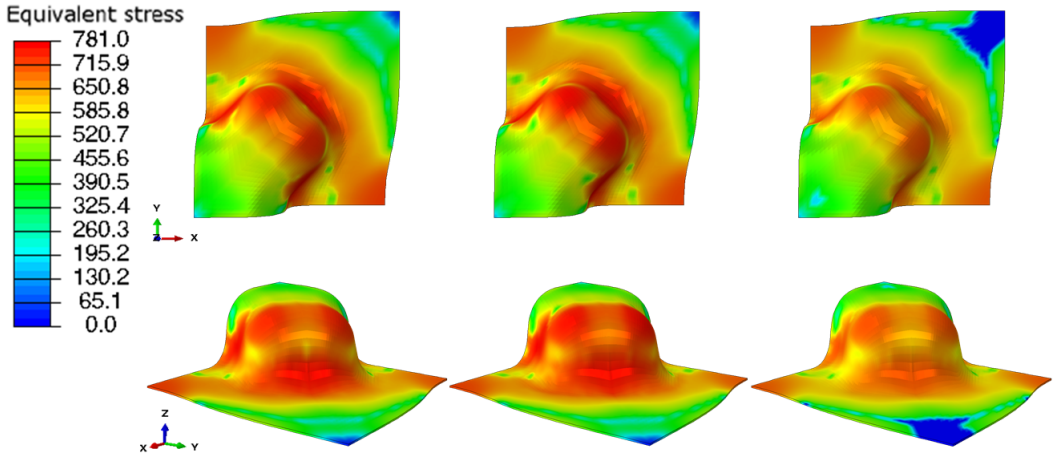


(a) AFR

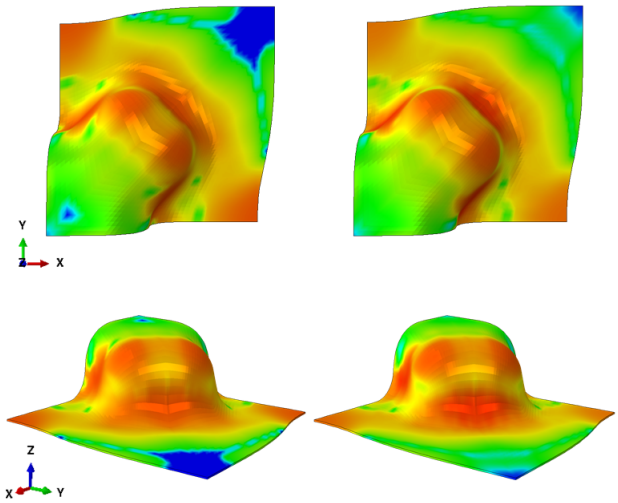


(b) NAFR

Figure C.5: Equivalent plastic strains contours for DP500 X shape of cross die, using the different yield criteria: a) Hill'48 r-based, Hill'48 s-based, Yld91; b) Hill'48, Yld91 (from left to right, respectively).

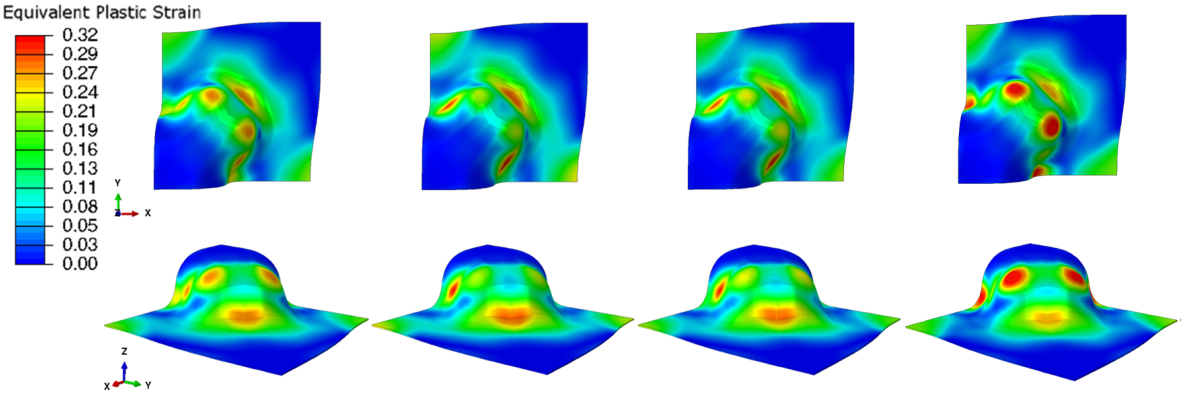


(a) AFR

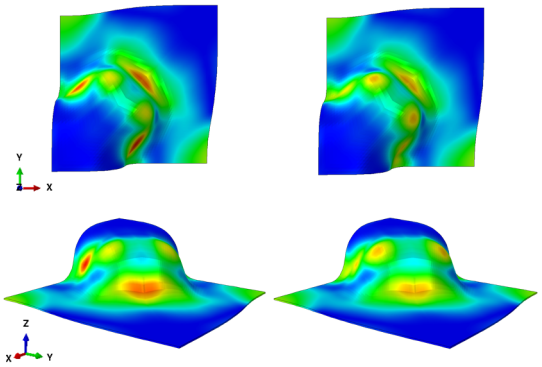


(b) NAFR

Figure C.6: Equivalent stress contours for DP500 X shape of cross die, using the different yield criteria: a) Hill'48 r-based, Hill'48 s-based, Yld91; b) Hill'48, Yld91 (from left to right, respectively).

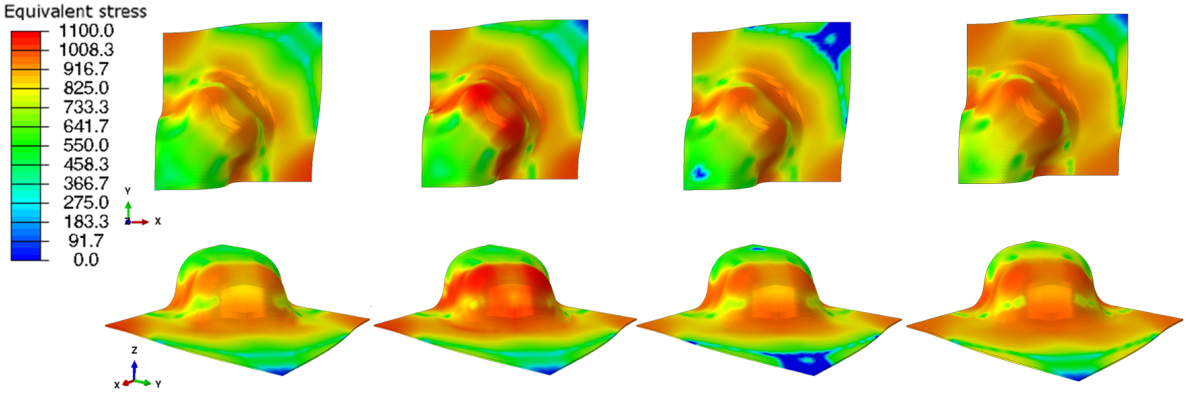


(a) AFR

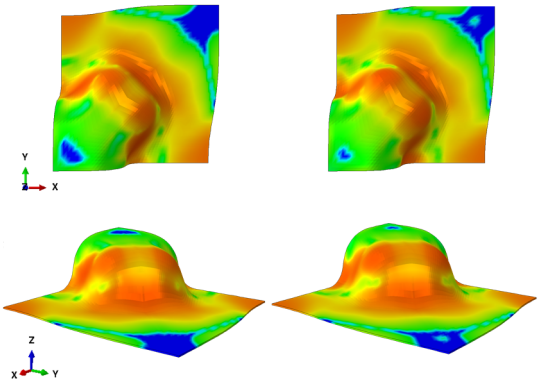


(b) NAFR

Figure C.7: Equivalent plastic strains contours for DP780 X shape of cross die, using the different yield criteria: a) Hill'48 r-based, Hill'48 s-based, Yld91; b) Hill'48, Yld91 (from left to right, respectively).



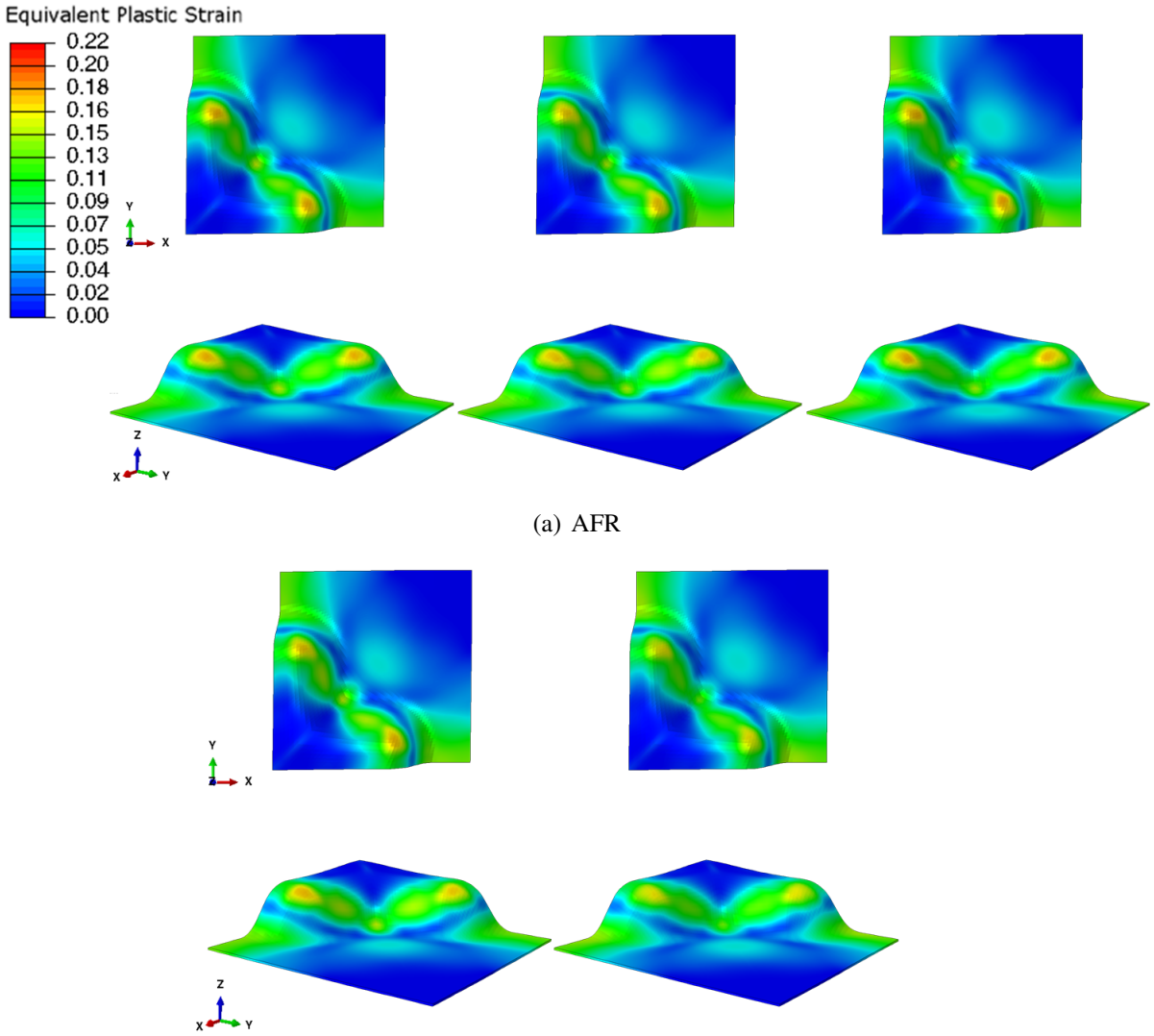
(a) AFR



(b) NAFR

Figure C.8: Equivalent stress contours for DP780 X shape of cross die, using the different yield criteria: a) Hill'48 r-based, Hill'48 s-based, Yld91; b) Hill'48, Yld91 (from left to right, respectively).

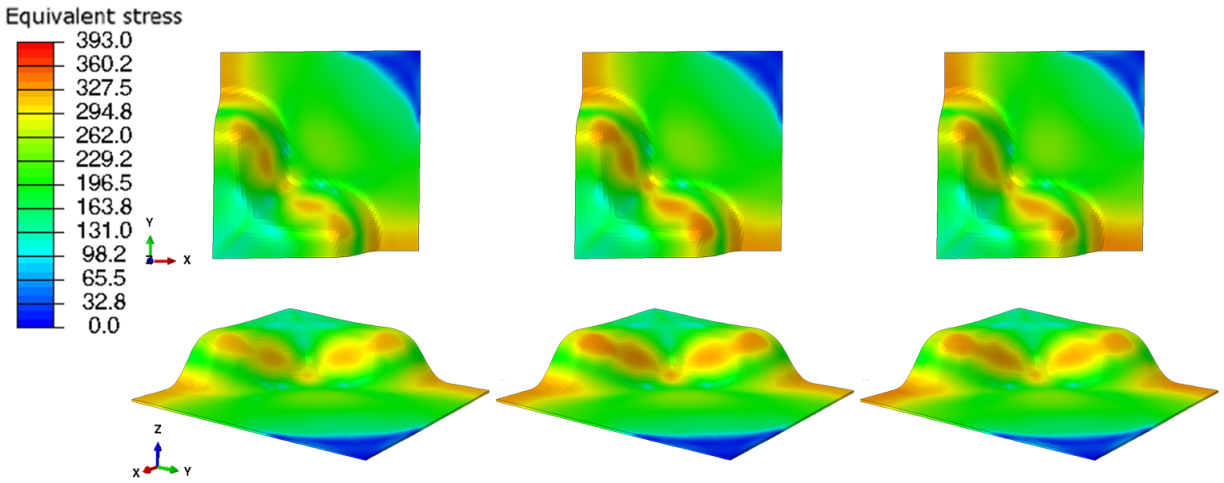
C.2 Plus shape component



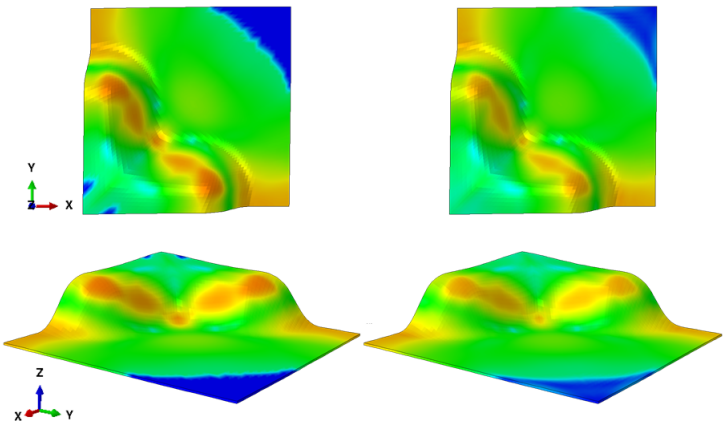
(a) AFR

(b) NAFR

Figure C.9: Equivalent plastic strains contours for AA5182 plus shape ("+") of cross die, using the different yield criteria: a) Hill'48 r-based, Hill'48 s-based, Yld91; b) Hill'48, Yld91 (from left to right, respectively).

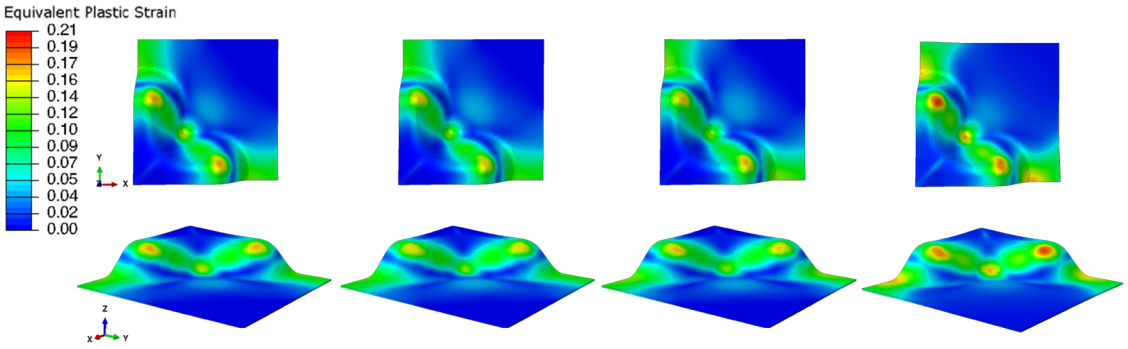


(a) AFR

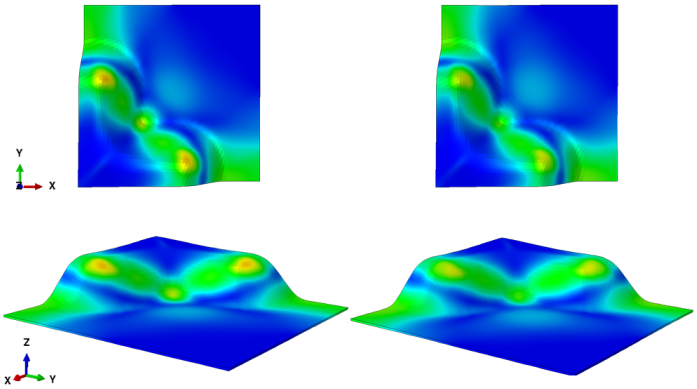


(b) NAFR

Figure C.10: Equivalent stress contours for AA5182 plus shape ("+") of cross die, using the different yield criteria: a) Hill'48 r-based, Hill'48 s-based, Yld91; b) Hill'48, Yld91 (from left to right, respectively).

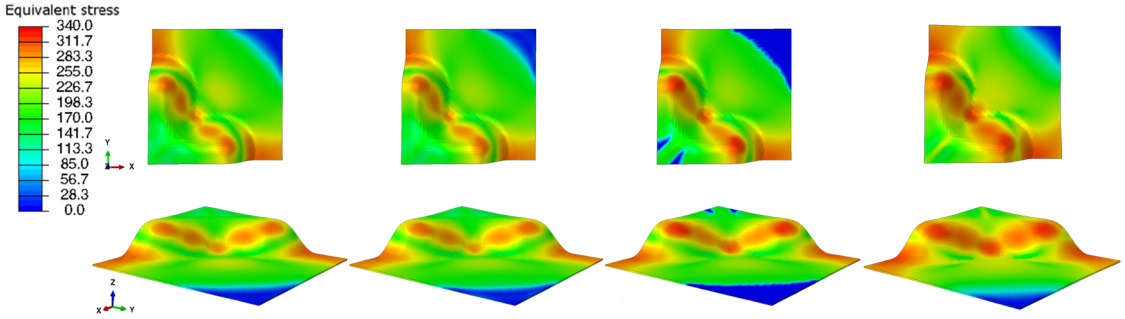


(a) AFR

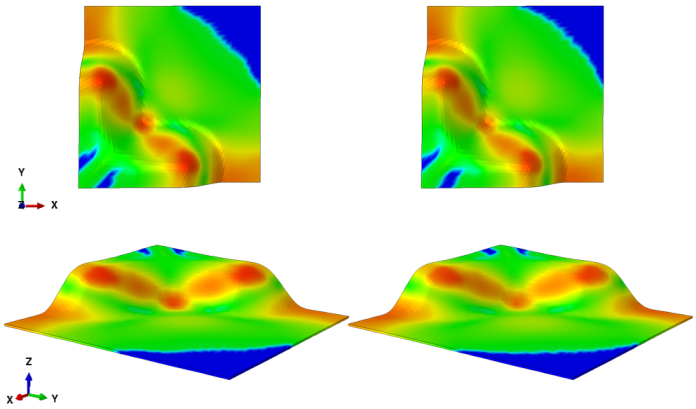


(b) NAFR

Figure C.11: Equivalent plastic strains contours for AA6016 plus shape ("+") of cross die, of cross die using the different yield criteria: a) Hill'48 r-based, Hill'48 s-based, Yld91; b) Hill'48, Yld91 (from left to right, respectively).

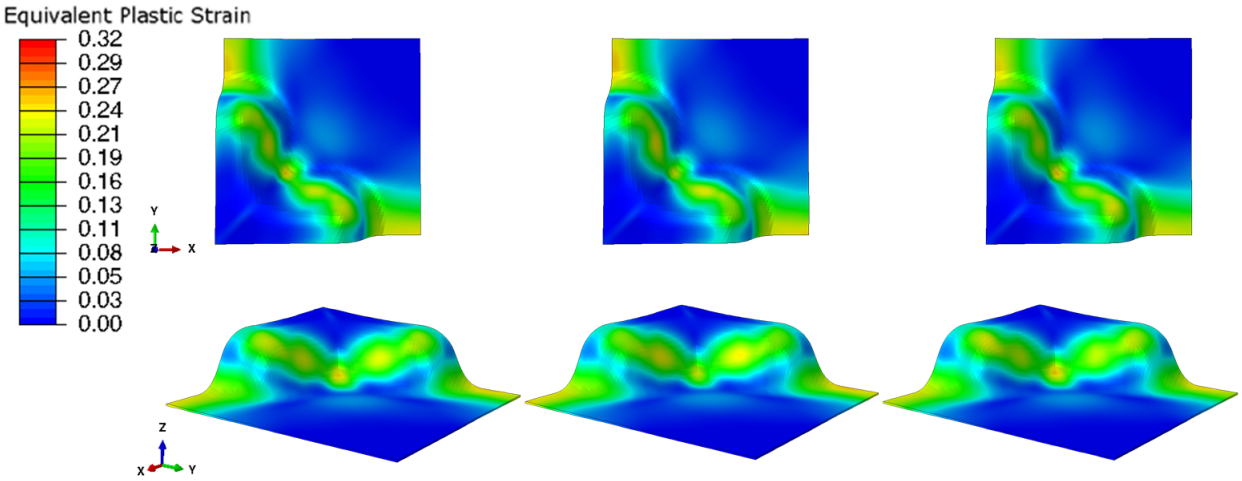


(a) AFR

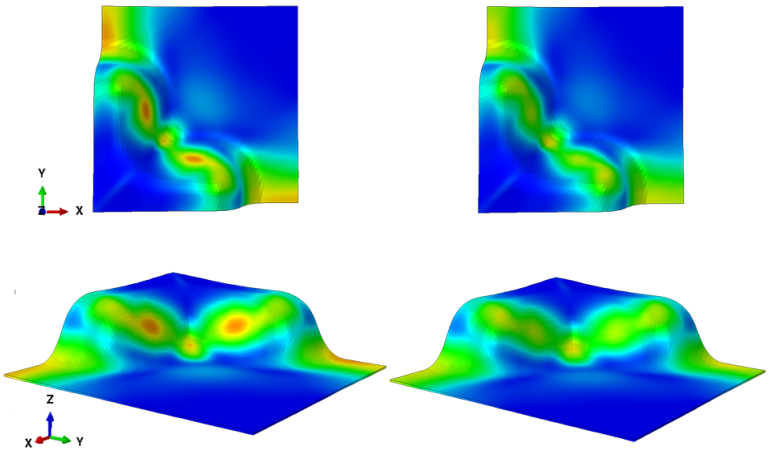


(b) NAFR

Figure C.12: Equivalent stress contours for AA6016 plus shape ("+") of cross die, using the different yield criteria: a) Hill'48 r-based, Hill'48 s-based, Yld91; b) Hill'48, Yld91 (from left to right, respectively).

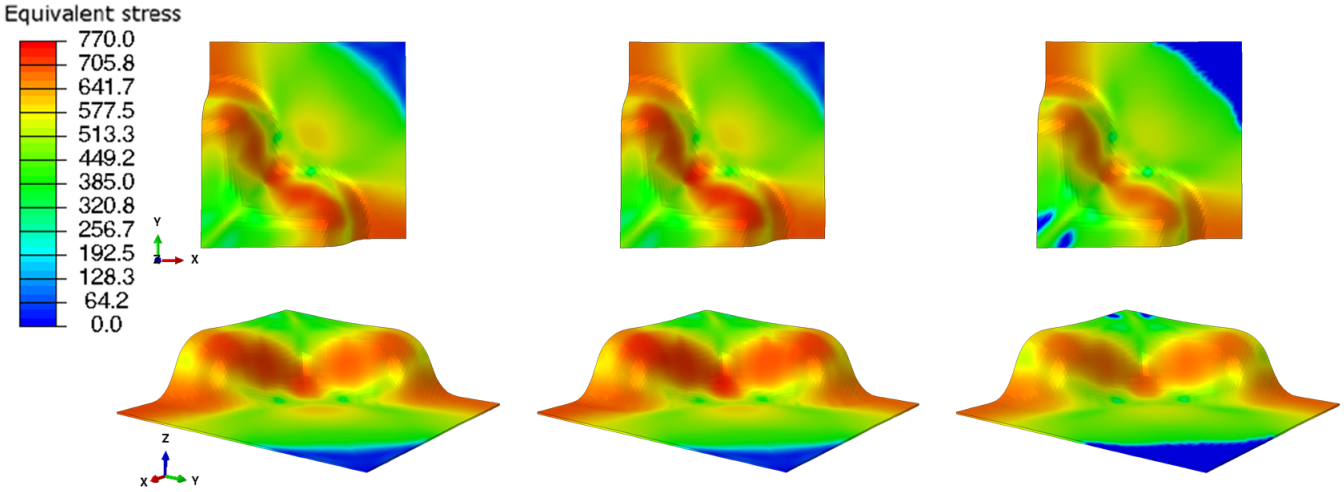


(a) AFR

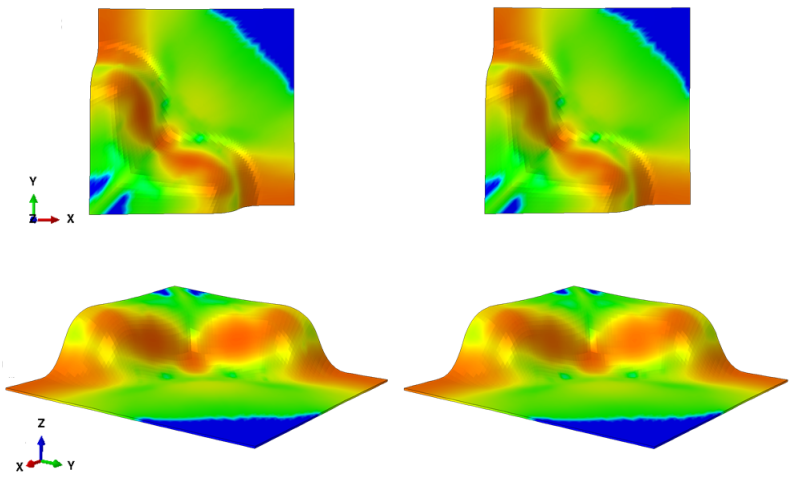


(b) NAFR

Figure C.13: Equivalent stress contours for DP500 plus shape ("+") of cross die, using the different yield criteria: a) Hill'48 r-based, Hill'48 s-based, Yld91; b) Hill'48, Yld91 (from left to right, respectively).

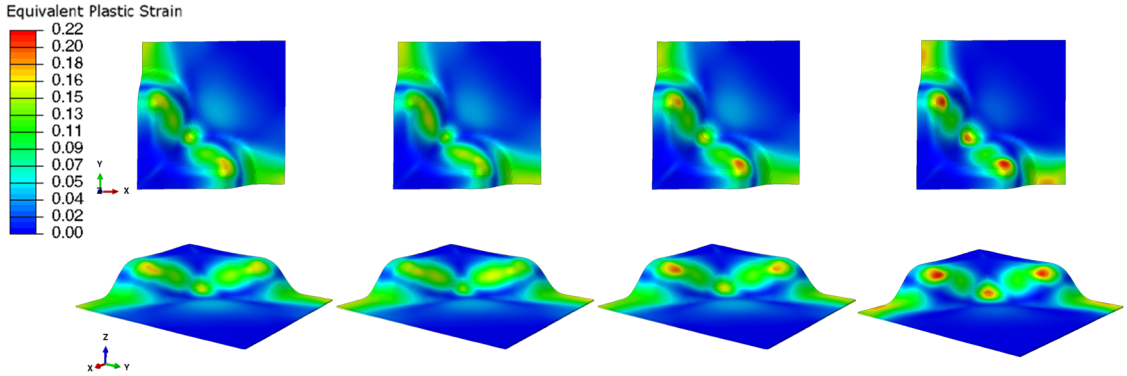


(a) AFR

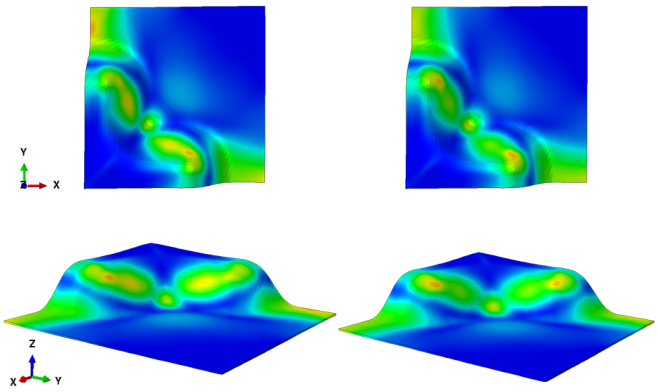


(b) NAFR

Figure C.14: Equivalent stress contours for DP500 plus shape ("+") of cross die, using the different yield criteria: a) Hill'48 r-based, Hill'48 s-based, Yld91; b) Hill'48, Yld91 (from left to right, respectively).

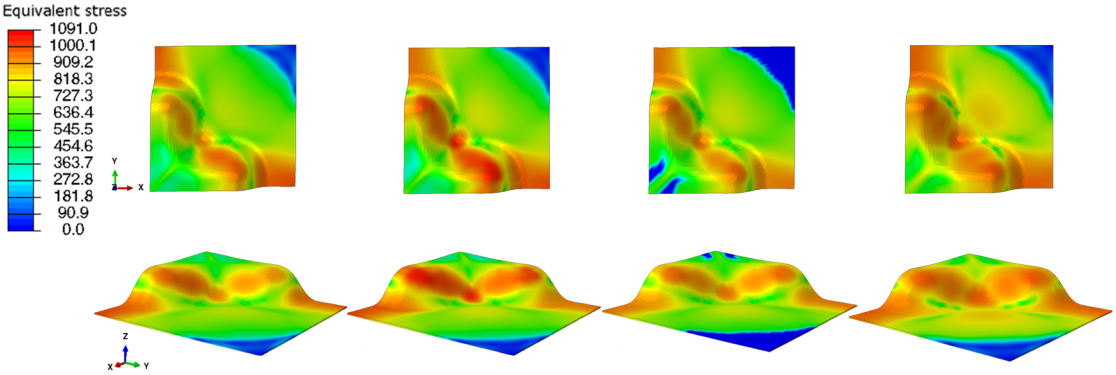


(a) AFR

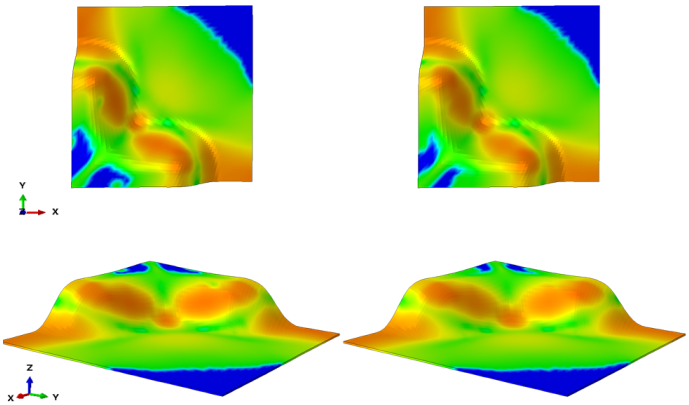


(b) NAFR

Figure C.15: Equivalent stress contours for DP780 plus shape ("+") of cross die, using the different yield criteria: a) Hill'48 r-based, Hill'48 s-based, Yld91; b) Hill'48, Yld91 (from left to right, respectively).



(a) AFR



(b) NAFR

Figure C.16: Equivalent stress contours for DP780 plus shape ("+") of cross die, using the different yield criteria: a) Hill'48 r-based, Hill'48 s-based, Yld91; b) Hill'48, Yld91 (from left to right, respectively).